



Access Granted  
! Landing Dock

Volume 20 Spring 2018  
Volume 20 Spring 2018  
Volume 20 Spring 2018  
Volume 20 Spring 2018



# (ur) DIMENSIONS

The Journal of Undergraduate Research  
in Natural Sciences and Mathematics

Volume 20  
Spring 2018

[ur] DIMENSIONS

The Journal of Undergraduate Research in Natural Sciences and Mathematics  
Volume 20 | Spring 2018

## **Marks of a CSUF graduate from the College of Natural Sciences and Mathematics**

### **GRADUATES FROM THE COLLEGE OF NATURAL SCIENCES AND MATHEMATICS:**

Understand the basic concepts and principles of science and mathematics.

Are experienced in working collectively and collaborating to solve problems.

Communicate both orally and in writing with clarity, precision, and confidence.

Are adept at using computers to do word processing, prepare spreadsheets and graphs, and use presentation software.

Possess skills in information retrieval using library resources and the internet.

Have extensive laboratory, workshop, and field experience where they utilize the scientific method to ask questions, formulate hypotheses, design and conduct experiments, and analyze data.

Appreciate diverse cultures as a result of working side by side with many people in collaborative efforts in the classroom, laboratory, and on research projects.

Have had the opportunity to work individually with faculty members in conducting research and independent projects, often leading to the generation of original data and contributing to the research knowledge base.

Are capable of working with modern equipment, instrumentation, and techniques.

## **DIMENSIONS**

DIMENSIONS: The Journal of Undergraduate Research in Natural Sciences and Mathematics is an official publication of California State University, Fullerton. DIMENSIONS is published annually by CSUF, 800 N. State College Blvd., Fullerton, CA 92834. Copyright ©2018 CSUF. Except as otherwise provided, DIMENSIONS grants permission for material in this publication to be copied for use by non-profit educational institutions for scholarly or instructional purposes only, provided that 1) copies are distributed at or below cost, 2) the author and DIMENSIONS are identified, and 3) proper notice of copyright appears on each copy. If the author retains the copyright, permission to copy must be obtained directly from the author.

## **ABOUT THE COVER**

There comes a time when we begin to imagine that our technological progress would take us beyond our known solar system. We explore an imaginary world where we setup a research station near a planetoid for science students to conduct specialized projects and observations. This is sheer fantasy, but it serves to motivate our goal to excel and accomplish our academic endeavors. In other words, reach for the stars.

## **DIMENSIONS Editorial Staff and Thanks**

### **EDITOR-IN-CHIEF**

Mikayla Mays - Physics

### **EDITORS**

Breanna Mcbean - Mathematics

Bianca Diaz - Physics

Desirée Marshall - Geological Sciences

Marlene Hernandez - Biological Science

Randall Ortega - Chemistry and Biochemistry

### **ADVISOR**

Dr. Colleen McDonough - Assistant Dean for Student Affairs

### **GRAPHIC DESIGN**

Gabriel Martinez - Layout Editor and Cover Designer

### **COLLEGE OF NATURAL SCIENCES & MATHEMATICS**

Dr. Marie Johnson - Dean

Dr. Mark Filowitz - Associate Dean

Dr. Sean E. Walker - Chair, Department of Biological Science

Dr. Peter de Lijser - Chair, Department of Chemistry and Biochemistry

Dr. Diane Clemens-Knott - Chair, Department of Geological Sciences

Dr. Dr. Martin Bonsangue - Chair, Department of Mathematics

Dr. Ionel Tifrea - Chair, Department of Physics

### **Special Thanks To**

The CNSM administrative staff for their support, the faculty for advising students and providing them with valuable research opportunities, and Dr. Colleen McDonough for her guidance and oversight.



## Table of Contents

### 10 Biological Science

- 10 Using Cementum Annuli And Tooth Wear To Determine The Age Of Coyotes In Southern California  
- **Ariana Mc Kenzie**  
- Advisor: Paul Stapp, Ph.D.
- 16 Biology Student Exposure and Comfort Across Multiple Graph Types  
- **Benjamin Verboonen**  
- Advisor: Joel K. Abraham, Ph.D.
- 17 Life Through The Microscope: A Collection Of Images From Biol 418L  
- **Instruction by Merri Lynn Casem, Ph.D.**
- Performance And Perceived Difficulty Of English Language Learners And Native English Speaking Undergraduate Biology Students  
- **Erick Valdez**  
- Advisor: Joel K. Abraham, Ph.D.
- 21 Determining Zygosity in *Sauromalus ater* (=obesus) Twins  
- **Maureen Kelley**  
- Advisor: Christopher R. Tracy, Ph.D.
- 22 Phenotypic And Genomic Differentiation In Experimentally Evolved Populations Of *Drosophila melanogaster*  
- **Melanie Garcia and Madison Cheek**  
- Advisor: Parvin Shahrestani, Ph.D.
- 30 Interaction Between Clinical *Acinetobacter baumannii* and *Staphylococcus aureus* Strains Recovered from the Same Site of Infection  
- **Nancy Castellanos, Jun Nakanouchi, Sammie Fung, Claudia Barberis, Lorena Tuchscher, and Sean Doorly**  
- Advisor: Maria Soledad Ramirez, Ph.D.

- 31 Quantitative Trait Locus Mapping Identifies Candidate Fungal Resistance Genes in *Drosophila melanogaster*  
- **Melissa Riddle and Neeka Farnoudi**  
- Advisor: Parvin Shahrestani, Ph.D.
- 41 Relaxed Selection of Experimentally-Evolved *Drosophila* Shows Transient Evolutionary Trade-Offs  
- **Neeka Farnoudi, Cristina Narvaza, Melissa Riddle, Silvia Orozco, and Stephen Gonzalez**  
- Advisor: Parvin Shahrestani, Ph.D., and Sam Behseta, Ph.D.
- 48 Gonadal Development of the Black-belly Dragonfish (*Stomias atriventer*)  
- **Sean Zulueta and Kristy Forsgren, Ph.D.**  
- Advisor: Kristy Forsgren, Ph.D.
- 55 No Apparent Effect of Elevated Atmospheric CO<sub>2</sub> On Growth Response or Competition Between Native and Non-Native California Grasses in a Growth Chamber Study  
- **Tilly M. Duong, Kyle L. Gunther, Jillian J. Stephens, Darren R. Sandquist, Ph.D., and Joel K. Abraham, Ph.D.**  
- Advisor: Joel K. Abraham, Ph.D.
- 56 Intestinal Barrier Dysfunction as a Possible Predictor of Death in *Drosophila melanogaster*  
- **Yasamin Hajy Heydary and Sabeeca Vadakkann**  
- Advisor: Parvin Shahrestani, Ph.D.

### 57 Chemistry and Biochemistry

- 57 Probing Rare Earth Concentration Quenching in Doubly Ordered Double Perovskites  
- **Aida Dadashzadeh**  
- Advisor: Allyson M. Fry-Petit, Ph.D.

- 58 Understanding How Two Similar Rna Binding Domains Of Paralogous Proteins Mediate Different Protein-Protein Interactions  
 - **Collin M. Marshall and Jeffrey Pina**  
 - Advisor: Niroshika M. Keppetipola, Ph.D.
- 59 Adsorption Potential Energy of Ascorbic Acid Enantiomers on Pd (111)  
 - **Jacqueline Estrada**  
 - Advisor: Michael Groves, Ph.D.
- 68 Synthesis of Proposed System of Ionic-Conducting Materials  
 $X\text{AgTa}_{4-y}\text{Mo}_y\text{O}_{11}$  (X: Na, K, Rb, Cs)  
 - **Karen Tom**  
 - Advisor: Allyson M. Fry-Petit, Ph.D.
- 69 The Effect of Synthesis Conditions on the Formation and Crystal Structure of Perovskite Oxygen Transport Membranes  
 - **Liz Hitch**  
 - Advisor: Allyson M. Fry-Petit, Ph.D.
- 70 Fitting of Perovskite Structure Using PDFgui & Determination of Structure Transition of  $\text{Sr}_3\text{Pb}_n\text{WO}_6$  ( $n=0, 1, 1.5, 2, 3$ )  
 - **Luis Gamez**  
 - Advisor: Allyson M. Fry-Petit, Ph.D.
- 71 Improvement of the Evolutionary Algorithm on the Atomic Simulation Environment Though Intelligent Starting Population Creation and Clustering  
 - **Nicholas Kellas**  
 - Advisor: Michael Groves, Ph.D.
- 72 The Decomposition of Ethylamine on Pt(111)  
 - **Waseefa Ahmed**  
 - Advisor: Michael Groves, Ph.D.
- 78 Geological Sciences**
- 78 Ground Source Heat Pump Potential Characterization for California State University Fullerton  
 - **Adrian Escobar**  
 - Advisor: Richard Laton, Ph.D.
- 81 Testing Relations Between Volcanic and Plutonic Rocks on the Kern Plateau, Sierra Nevada  
 - **Brian Magumcia**  
 - Advisor: Diane Clemens-Knott, Ph.D.
- 82 Geochemical and Petrographic Analysis of Salt Dome Associated Calcite Phases in Gulf Coast Cap Rocks: Implications for Carbon Sources and Paragenetic Evolution  
 - **Connor Frederickson**  
 - Advisor: Sean Loyd, Ph.D.
- 83 Using a Virtual Field Trip to Teach the Plutonic History of Yosemite  
 - **Isabel A. Guinto**  
 - Advisor: Natalie Bursztyn, Ph.D.
- 84 Stratigraphic Variability in Response to Environmental Changes Across Short and Long Time Scales Along the Southern Monterey Bay Continental Shelf  
 - **Jamie Hayward**  
 - Advisor: Joe Carlin, Ph.D.
- 88 Investigating The Causes Of Compositional Variation In The Half Dome Granodiorite, Tuolumne Intrusive Complex, Yosemite National Park, Ca: Big Or Small Magma Chambers?  
 - **John Ayers**  
 - Advisor: Valbone Memeti, Ph.D.
- 89 Manageable Molecular Mineralogy: Developing a User-Friendly Interactive Mineralogy Game for Mobile Devices  
 - **Leah Witablake**  
 - Advisor: Natalie Bursztyn, Ph.D.

- 90 Are the “Cretaceous” High-Silica Granites Associated with the Low-silica Summit Gabbro Actually Late Jurassic age?  
 - **Rodrigo Aviles**  
 - Advisor: Diane Clemens-Knott, Ph.D.
- 91 Investigating Volcanic and Plutonic Connections at Iron Mountain Pendant, Sierra National Forest, CA  
 - **Sabrina Green**  
 - Advisor: Valbone Memeti, Ph.D.
- 92 Basalt Correlation in the Sylvania Mountains, California, by X-ray Fluorescence Spectroscopy (XRF)  
 - **Shayna Avila**  
 - Advisor: Jeffrey R. Knott, Ph. D.
- 102 13 Year Analysis of Water Pressure and Chemical Changes from Well CSF-1, Fullerton, CA  
 - **Terrinda Alonso**  
 - Advisor: Richard Laton, Ph.D.
- 103 Interpreting Recent Stratigraphic Changes for the Northern Monterey Bay Continental Shelf  
 - **Victoria Severin**  
 - Advisor: Joe Carlin, Ph.D.

## 107 Mathematics

- 107 Shapes of Giant Soap Bubbles  
 - **Angelica Arredondo and Breanna McBean**  
 - Advisor: Nicholas Brubaker, Ph.D.
- 108 Alternating Hamiltonian Cycles  
 - **Christian Do and James Shade**  
 - Advisors: Adam Glessner, Ph.D., and Matt Rathbun, Ph.D.
- 115 Linearizing the Repressilator Model  
 - **Killian Wood**  
 - Advisor: Anael Verdugo, Ph.D.

- 124 Don’t Walk and Text!: An Investigation of Cell Phone Usage by Pedestrians on CSUF’s Campus  
 - **Crystal Rodela, Kimberly M. Zavala, and Natalie Lincoln**  
 - Advisor: Alison S. Marzocchi, Ph.D.
- 129 Mathematical Model to Noninvasively Detect Dry-eye Diseases  
 - **Trini Nguyen<sup>1</sup>**  
 - Advisors: Charles Lee, Ph.D.<sup>1</sup>, Mr. Stanley Huth<sup>2</sup>, and Nattapol Ploymaklam, Ph.D.<sup>3</sup>

## 150 Physics

- 150 Building a Custom Microscope – An Advanced Lab to Study Brownian Motion  
 - **Hunter Seyforth**  
 - Advisor: Wylie Ahmed, Ph.D.
- 151 Nonequilibrium Dynamics of Active Colloids  
 - **Paris Blaisdell-Pijuan<sup>1</sup>, Mauricio Gomez<sup>1</sup>, and Ngoc La<sup>1,2</sup>**  
 - Advisor: Wylie Ahmed, Ph.D.<sup>1</sup>
- 152 Visualizing Fluid Physics of Microswimmers  
 - **Sarah Al Bassri**  
 - Advisor: Wylie Ahmed, Ph.D.

## 153 Authors and Editors



# **Using Cementum Annuli And Tooth Wear To Determine The Age Of Coyotes In Southern California**

**Ariana Mc Kenzie**

**Advisor: Paul Stapp, Ph.D.**

*Department of Biological Science, California State University, Fullerton*

## **ABSTRACT**

Although coyotes (*Canis latrans*) are a natural component of southern California ecosystems, they are sometimes considered a nuisance because their opportunistic habits and tolerance for urbanization brings them into conflict with people. Recent attacks on people and pets have increasingly led to lethal control of nuisance animals, yet it is unclear whether the demographic distribution of these individuals are representative of the coyote population as a whole and is information that could be used to guide coyote management. I used two methods, cementum annuli analysis and tooth wear, to estimate the age from the mandibles of 100 coyotes collected as nuisance animals and as roadkills in southern California. Age estimates based on tooth wear, a non-lethal method, were broadly similar to those from cementum annuli analysis, although tooth wear estimates produced more variation and would tend to overestimate age, especially for younger individuals. The demographic structure of coyotes collected as nuisance animals was biased toward juveniles, young adults, and males, which is a pattern typical of exploited populations elsewhere. Although fewer road-killed individuals were examined, the fact that younger animals were overrepresented in the sample of nuisance individuals suggests that younger age classes (and males) may be more likely to be the target of control efforts, possibly because their behavior creates opportunities for greater conflict with people.

## **INTRODUCTION**

Coyotes (*Canis latrans*) are opportunistic predators that can live in a variety of habitats, including urban and

suburban environments (Bekoff, 1977; Bateman and Flemming, 2012). Habitat fragmentation caused by the expanding urban environment has altered coyote movements and foraging behavior (Tigas *et al.*, 2002). In addition, an abundance of anthropogenic foods, e.g., pets, pet food, unattended garbage, fallen fruit, has contributed to the increasing numbers of coyotes in urban and suburban areas. These factors have created opportunities for conflict between coyotes and people, including the killing of pets and even attacks on children (Green *et al.*, 1994; Baker and Timm, 1998; Grinder and Krausmann, 1998; Murray *et al.*, 2015). As a result, many communities in southern California have resorted to using private trappers to remove nuisance coyotes, a practice that may not be sustainable long-term (Bateman and Flemming, 2012).

Because the behavior of coyotes varies among demographic classes (Bekoff, 1977), it is reasonable to expect that age and sex will affect the likelihood that a coyote will interact with people. In agricultural settings, older, territorial coyotes are more likely to be a nuisance and therefore be controlled (Houben and Mason, 2004). On the other hand, younger, subordinate individuals may wander more or be forced into poorer quality habitat and may be more desperate for food and shelter associated with the urban environment (Gese *et al.*, 1988). Little information exists on the demographic structure of urban coyote populations, or how age affects the potential for conflict with humans (Way and Strauss, 2004). Knowledge of the age distribution these coyotes will allow a better understanding on how urbanization affects coyote populations in southern California, and

may help identify those individuals that are more likely to encounter people, which, in turn, might minimize conflict and reduce the need for lethal control.

Cementum annuli (CA) analysis, the most common method used to age mammals, involves extracting and sectioning a canine tooth to count cementum layers (annuli) that are deposited approximately yearly. Among canids, CA has been used to estimate the age of coyotes, gray wolves (*Canis lupus*), and red foxes (*Vulpes macrotis*; Allen, 1974; Landon *et al.*, 1998; Scrivner *et al.*, 2014). Although the CA technique is considered to be accurate, it can only humanely be used on dead animals because it is considered unethical to remove a canine tooth from a live animal. Visual inspection of tooth wear (TW) has also been used to estimate age, although it is not considered to be as precise or consistent as CA analysis (Bowen, 1982). Recently, Gipson *et al.* (2000) used TW to estimate age of known-aged gray wolves and suggested improvements that could improve the reliability of this technique. However, the effectiveness of TW for aging coyotes, which eat a more variable diet, has not been established.

I used CA and TW methods to estimate the age of 100 coyotes killed in southern California as a result of control efforts or as roadkill and compared the two methods to determine if TW could be used to age coyotes non-lethally. I then estimated the age distribution of coyotes in the sample to determine if particular age classes or sexes were overrepresented among those killed as nuisance animals.

## MATERIAL AND METHODS

Mandibles were collected during gross necropsy from 100 coyotes that were euthanized by private trappers or animal control agents, or killed by vehicles in urban areas throughout southern California. Most samples came from Orange County (n = 48) and Los Angeles County (n = 39), although a few (n = 13) were collected from other urban areas in San Bernardino, Fresno, Riverside and San Diego counties. Coyote carcasses were necropsied at the South Coast Research and Extension

Center in Irvine, California, and mandibles were removed and stored in a -20°C freezer. I categorized age classes as follows: juveniles, < 1 year old; young adults, 1-2 years old; adults, 3-5 years old; and older adults, > 6 years old.

### Tooth Extraction

I removed large amounts of remaining tissue from the mandible and inserted it into a mesh bag to prevent any teeth from being lost. The mandible was placed into a water bath at 85°C for approximately 6-8 hours to loosen the teeth. I extracted one undamaged lower canine (usually the left) using pliers, and cleaned any excess marrow from the tooth root using a nylon net fabric to minimize damage to the cementum layers. Extracted teeth were set aside to air dry for >10 minutes. Tooth samples were sent to Matson's Laboratory (<http://matsonslab.com/>) for processing and CA age determination. If, after cleaning, visual inspection of the mandibles identified the presence of milk teeth and underdeveloped carnassial teeth, the mandible was assigned an age of 0-6 months (Linhart and Knowlton, 1967; Nellis *et al.*, 1978) and the tooth was not sent off for analysis. The age determined by CA analysis was considered to be the most accurate estimate of true age.

### Visual Determination of Tooth Wear

After the canine was removed, I cleaned the entire mandible to the bone using a toothbrush and nylon net fabric. Using a Sony Canon Cyber Shot 20.1 megapixel camera, I took frontal and lateral images of each mandible. The camera was placed at the same level as the sample, zoomed in so that the mandible filled the screen, and shot with an exposure value (E.V.) set at -2.0 with flash to maximize the contrast and make the tooth wear easier to examine. The top of the flash bulb was covered to minimize reflection and to ensure a dark background.

Age was estimated by inspecting the condition of three types of teeth (incisors, canine, and carnassial tooth), using Gipson *et al.* (2000) as a guide to tooth wear (TW). I estimated age based on each type of tooth

and took the average of these estimates as the TW age estimate for that individual. If estimates from the different tooth types varied greatly, I gave more weight to the condition of the incisors, which have been shown to have a more consistent rate of wear and tear (Gipson *et al.*, 2000). Mandibles were aged by TW prior to obtaining result from CA analysis to avoid any bias.

## RESULTS

Coyotes ( $n = 100$ ) were collected between March 2016 and January 2017. It was not possible to formally compare the age distributions between those euthanized as nuisance animals and those killed accidentally by vehicles because only 20 (20%) were roadkills, although patterns were noted. Eighteen individuals were determined to be <6 months old based on the presence



**Figure 1.** Variations in coyote tooth wear patterns based on age class. ( $A = < 1$ ,  $B = 1-2$ ,  $C = 3-5$ ,  $D = 6-9$  years old).

of milk teeth and underdeveloped carnassial teeth. The teeth for the remaining 82 individuals were examined using both CA and TW analysis.

Examples of tooth wear were created for each age class, and representative mandibles were chosen based on CA age and consistency of tooth wear (Fig. 1). Results from TW and CA analysis were positively correlated (Fig. 2), although TW tended to overestimate coyote age, especially for younger animals (< 2 years old), which often had damaged or heavily worn teeth. In two instances, TW underestimated coyote age (Fig. 3). CY155 had fully formed teeth with minimal wear and its tooth wear more closely resembled that seen in a younger animal (~ 2 years old), but CA analysis showed its actual age as 7 years old. Similarly, 3-year-old CY85 was estimated using TW to be 1 year old.

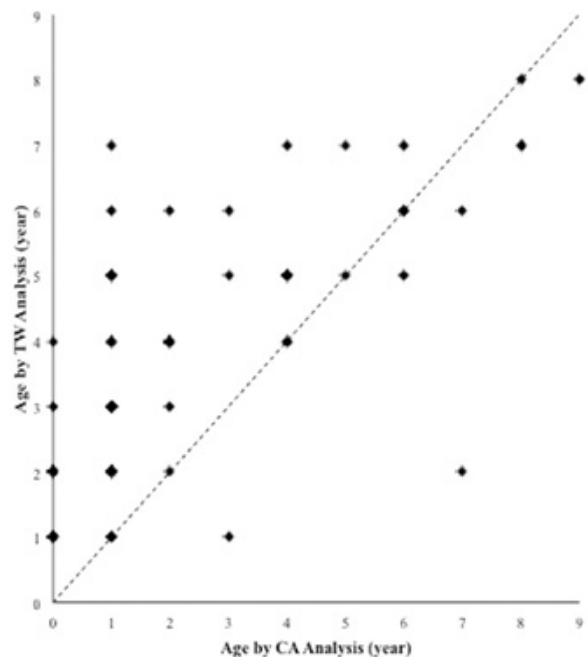


**Figure 2.** Comparison of estimated age of coyote teeth using tooth wear (TW) to those from cementum annuli (CA) analysis ( $n = 82$ ;  $r = 0.72$ ;  $P < 0.001$ ;  $y = 0.61x + 2.26$ ). Eighteen individuals with milk teeth were not analyzed using the CA method and were assigned an age of 0-6 months. Dashed line represents a 1:1 ratio.

Based on the results of the CA analysis, most coyotes examined were young adults (46%) and juveniles (33%; Fig. 4). Adults (13%) made up the smallest fraction of the sample, followed closely by older adults



**Figure 3.** Examples of unexpected patterns of tooth wear of coyote teeth. A: CY155 was estimated to be 2 years old based on TW, but was actually 7 years old (CA analysis). B: Three-year-old CY85 was estimated to be only 1 year old based on TW analysis.

(9%; Fig. 4). The age distribution was similar for the 20 individuals collected as roadkills: most were juvenile (45%) or young adults (30%), with adult coyotes aged >

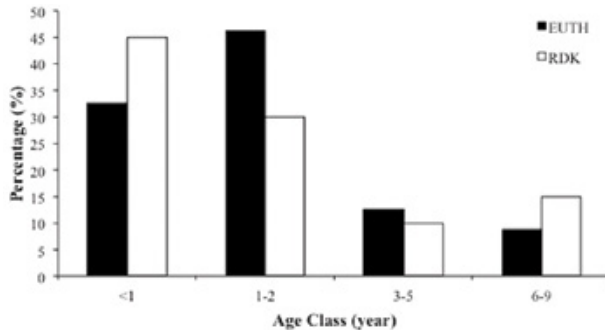


**Figure 4.** Age distribution between euthanized (EUTH) and roadkill (RDK) coyotes in southern California between March 2016–January 2017 ( $n = 80, 20$ ), based on CA analysis.

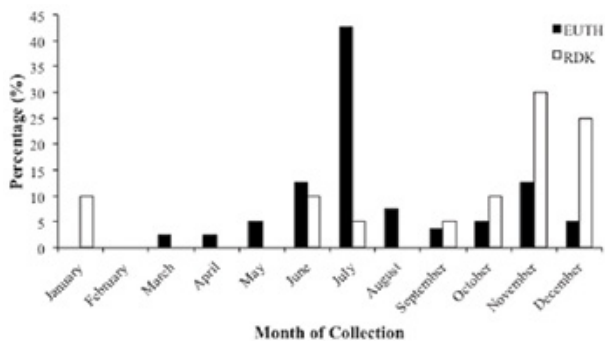


**Figure 5.** Collection dates of euthanized (EUTH) and roadkill (RDK) coyotes in southern California ( $n = 80, 20$ ).

3 years old making up the last 25%. Young adults tended to comprise a greater fraction of those controlled as nuisance animals (46%) than those killed by vehicles (30%).

A large fraction (35%) of coyotes in the sample were collected during July 2016. Excluding roadkills, however, a greater proportion of euthanized coyotes collected in July were juveniles (41%) than those collected in other months (26%; Fig. 5). This could explain the relatively large number of juveniles in the sample if juveniles happen to be very common in the population at this time, although, the age distribution of individuals collected in July was roughly similar to that in other months (Fig. 6).

Males were overrepresented in the sample across

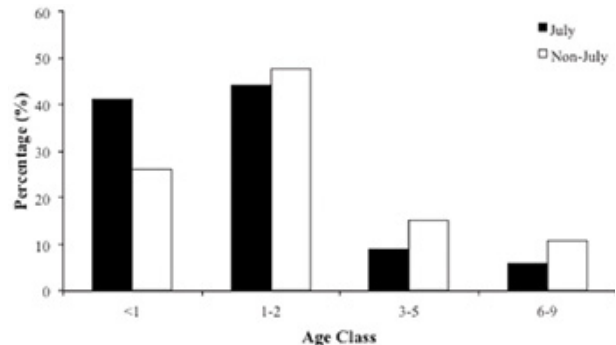


**Figure 6.** CA analysis-derived age distribution of euthanized coyotes collected during July, compared to the distribution of samples from other months ( $n = 80$ ; July = 34; other months = 46).

all age classes, with an overall sex ratio (M:F) of 61:39 (Fig. 7). Sex ratios among nuisance coyotes were also skewed towards males (51:29), although both sexes were equally represented among roadkills (10:10). The skewed ratio among euthanized coyotes was particularly evident in the adult segment of the population, where males outnumbered females nearly four-fold.

## DISCUSSION

The two methods of age estimation, CA and TW, gave roughly similar results; although, coyote ages tended to be overestimated using the non-lethal TW method, especially for young animals. The high variability in

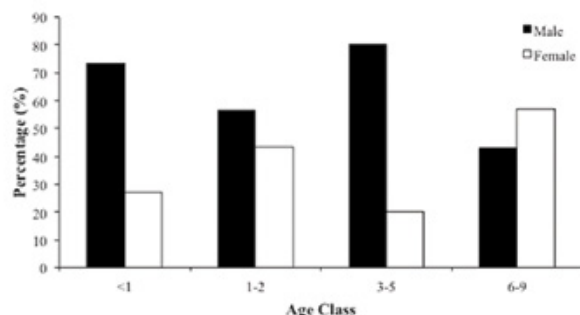


**Figure 7.** Sex ratios of euthanized coyotes within each age class in southern California. Age based on CA analysis ( $n = 80$ ; M = 51; F = 29). Males were 64%, 50%, and 61% of euthanized, road-killed, and all coyotes, respectively.

the tooth wear for younger coyotes may reflect the opportunistic diet of urban coyotes, where access to ample anthropogenic food may contribute to an unusual pattern of tooth wear. In addition, a large fraction (63%) of juveniles and young adults in the sample were estimated by TW to be > 2 years older than their known age. While the TW method was able to distinguish among the ages of older coyotes and could be used to complement other gross measures of coyote age, e.g., size, weight, TW is unlikely to be a consistently reliable method to estimate the age structure of most urban coyote populations.

Based on CA analysis, the age distribution of the 100 coyotes I sampled was largely dominated by younger age classes. Approximately 78% of coyotes were < 2 years old, and this demographic pattern was broadly similar between nuisance and road-killed individuals. A larger sample of roadkills would help to determine if the age structure of euthanized coyotes does indeed differ from those in the broader population. This pattern seems to be typical of exploited populations; for example, Nelson and Lloyd (2005) reported that 70% of the coyote population in Illinois was < 2 years old. The relatively large number of juveniles seen in urban environments might reflect the effects of human activity on the age distribution of coyote populations. Habitat fragmentation forces coyotes to expand their territories and travel among multiple fragments (Tigas *et al.*, 2002), which may facilitate intraspecific contact and, possibly, more breeding. Female coyotes may also reproduce during their first year in times (or locations) of food abundance (Gier, 1968). Alternatively, the large number of young individuals in my sample may reflect the fact that young coyotes are more likely to behave in ways that make them a nuisance to people or more vulnerable to control activities due to their inexperience. While my data are limited, if the age distribution of coyotes accidentally killed by vehicles reasonably reflects the age distribution of the population as a whole, then the disproportionate number of young animals that are euthanized suggests that these young animals are more at

risk. Younger individuals are more likely to be transient and susceptible to exclusion by territory-holding adults (Gese *et al.*, 1989). They may also be more likely to seek out anthropogenic resources, particularly those that put them in closer proximity to people (Bateman and Flemming, 2011; Murray *et al.*, 2016), although this problem merits further study.

A balanced sex ratio is expected in coyote populations found in lightly exploited, rural environments, whereas populations in urban environments tend to be female-biased because males, which are wide-ranging and have larger territories, may be more vulnerable to control efforts (Gese *et al.*, 1988; Nelson and Lloyd, 2005). My results suggest that this is the case in southern California (Fig. 7), suggesting that the behavior of males makes them more likely to be perceived as a nuisance. Detailed studies of the movements and spacing behavior of coyotes in southern California are needed to determine if the behavior of males makes them more likely to be controlled.

Most coyotes in my sample were collected in July, which may reflect the emergence of pups born in April and May from natal dens that falls around this time (Green *et al.*, 1994). Because pups are still traveling with their mothers, entire family units might be removed by control efforts. People are also likely to be outdoors more during the summer, which might bring them into contact with coyotes more and result in more nuisance complaints.

My study is part of a larger project to study the diet and ecology of coyotes in southern California that takes advantage of the large number of coyotes that are controlled each month. To date, > 400 coyotes have been euthanized over the past 2 years. Culling coyote populations can actually reduce intraspecific competition between females and increase litter size, resulting in higher population densities (Gese *et al.*, 1996; Bateman and Flemming, 2011). There may be alternative methods to reduce conflict between coyotes and people without the need for lethal control. One possible solution is better management of natural open space, including

creating corridors that allow coyotes to move between fragments with minimal contact with people (Tigas *et al.*, 2002). Non-lethal control methods, such as sterilization, might reduce coyote numbers slowly, and change the behavior of individuals (Seidler *et al.*, 2014). Lastly, educating the public on how to manage their property better by removing anthropogenic foods, securing trash, and keeping pets indoors may discourage coyotes from coming into their yards.

## REFERENCES

- Allen, S. H. 1974. Modified techniques for aging red fox using canine teeth. *Journal of Wildlife Management* 38:152-154.
- Baker, R. O., and R. M. Timm. 1998. Management of conflicts between urban coyotes and humans in southern California. Pp. 299-312 in Proceedings of the 18th Vertebrate Pest Conference (R. O. Baker and A. C. Crabb, eds.). University of California, Davis, CA.
- Bateman, P. W., and P. A. Fleming. 2011. Big city life: carnivores in urban environments. *Journal of Zoology* 287:1-23.
- Bekoff, M. 1977. Coyote (*Canis latrans*). *Mammalian Species* 79:1-9.
- Bowen, W. D. 1982. Determining age of coyotes, *Canis latrans*, by tooth sections and tooth-wear patters. *Canadian Field-Naturalist* 96:339-341.
- Gese, E. M., O. J. Ronstad, and W. R. Mytton. 1988. Home range and habitat use of coyotes in southeaster Colorado. *Journal of Wildlife Management* 52:640-646.
- Gese, E. M., O. J. Ronstad, and W. R. Mytton. 1989. Population dynamics of coyotes in southeastern Colorado. *Journal of Wildlife Management* 53:174-181.
- Gier, H. T. 1968. Coyotes in Kansas. Kansas Agricultural Experiment Station, Kansas State University, Manhattan.
- Gipson, P. S., L. D. Mech, R. M. Norwalk, and W. B. Ballard. 2000. Accuracy and precision of estimating age of gray wolves by tooth wear. *Journal of Wildlife Management* 54:752-758.
- Green, J. S., F. R. Henderson, and M. D. Collinge. 1994. *Canis latrans*. Pp. C51-C53 in Prevention and Control of Wildlife Damage (G. E. Larson, R. M. Timm, and S. E. Hygnstrom, eds.). University of Nebraska-Lincoln.
- Houben, J. M., and J. R. Mason. 2004. Weight and age of coyotes captures in Virginia, USA. USDA National Wildlife Research Center, Staff Publications Paper 365:75-76.
- Landon, B. D., C. A. Waite, L. D. Mech, and R. O. Peterson. 1998. Evaluation of age determination techniques for gray wolves. *Journal of Wildlife Management* 62:674-682.
- Linhart, S. B., and F. F. Knowlton. 1967. Determining age of coyotes by tooth cementum layers. *Journal of Wildlife Management* 31:362-365.
- Minter, L. J., and T. J. DeLiberto. 2008. Seasonal variation in serum testosterone, testicular volume, and semen characteristics in the coyote (*Canis latrans*). *Theriogenology* 69:946-952.
- Murray, M., A. Cembrowski, A. D. M. Latham, V. M. Lukasik, S. Pruss, and C. C. St Clair. 2015. Greater consumption of protein-poor anthropogenic food by urban relative to rural coyotes increases diet breadth and potential for human-wildlife conflict. *Ecography* 38:1235-1242.
- Murray, M., J. Hill, P. Whyte, and C. C. St. Clair. 2016. Urban compost attracts coyotes, contains toxins, and may promote disease in urban-adapted wildlife. *EcoHealth* 13:285-292.
- Nellis, C. H., S. P. Whetmore, and L. B. Keith. 1987. Age-related characteristics of coyote canines. *Journal of Wildlife Management* 42:680-683.
- Nelson, T. A., and D. M. Lloyd. 2005. Demographics and conditions of coyotes in Illinois. *The American Midland Naturalist* 153:418-427.
- Scrivner, J. H., C. A. Johnson, and C. A. Sego. 2014. Use of cementum annuli and eye-lens weight for aging coyotes. *Wildlife Society Bulletin* 38:874-877.
- Seidler, R. G., E. M. Gese, and M. M. Conner. 2014. Using sterilization to change predation rates of wild coyotes: a test case involving pronghorn fawns. *Applied Animal Behaviour Science* 154:83-92.
- Snacks, B. N. 2005. Reproduction and body condition of California coyotes (*Canis latrans*). *Journal of Mammalogy* 86:1036-1041.
- Tigas, L. A., D. H. Van Vuren, and R. M. Sauvajot. 2002. Behavioral responses of bobcats and coyotes to habitat fragmentation and corridors in an urban environment. *Biological Conservation* 108:299-306.
- Way, J. G., and E. G. Strauss. 2004. Old-aged coyote in an urbanized landscape. *Canid News* 7:2:1-3.

# **Biology Student Exposure and Comfort Across Multiple Graph Types**

**Benjamin Verboonen**

**Advisor: Joel K. Abraham, Ph.D.**

*Department of Biological Science, California State University, Fullerton*

## **ABSTRACT**

Graphs are a key tool in science communication, and thus competency in graph construction and interpretation are core learning goals in most science programs. Some graph forms, such as line graphs or bar graphs, are frequently presented in introductory classes. Although these graph forms can be appropriate for communicating some data, they may not be sufficient for certain data or contexts, and other graph forms, such as box plots, are increasingly common in scientific papers. We surveyed STEM faculty and undergraduate students to determine the frequency and context of exposure of different graph forms in courses as well as student confidence in using different graph types. We found that students have had the most exposure to line graphs, and scatterplots in courses, while graphs like box plots and histograms, and bar graphs were less commonly encountered. Furthermore, we found that the majority of first encounters of graph types to be during class lecture or during reading from a course textbook. This finding applies to when students are asked to construct and interpret the different graph types with most students being asked to construct and interpret them during lectures and during readings. Finally, students report a high confidence in graph usage in all graph types except boxplots. These findings provide insight into the usage of different graph types during courses and can help cement the usage of different graph types in order to broaden exposure to other commonly used graph types in STEM fields, as well as increase the graphing skills of students.

# Life Through The Microscope: A Collection Of Images From Biol 418L

**Instruction by Merri Lynn Casem, Ph.D.**

*Department of Biological Science, California State University, Fullerton*

Biology 418L *Advances in Cell Biology Lab* is an upper division course that provides students with training in the use of various forms of microscopy to capture and analyze images. Throughout the semester, students develop skills in macrophotography, bright field microscopy, phase microscopy, fluorescence microscopy, confocal microscopy and scanning electron microscopy. In addition, students learn the proper use of image analysis software. The following collection of images represents the work of students from the Fall 2017 offering of the course. These images illustrate the range of methods used in the course and highlight the aesthetic qualities of scientific images.

## MACROPHOTOGRAPHY

**By Melanie Garcia**

*Drosophila melanogaster* (Figure 1), also known as fruit flies, are a commonly used model system in biological research. Their relatively short life cycle and well characterized genetics make them a useful research

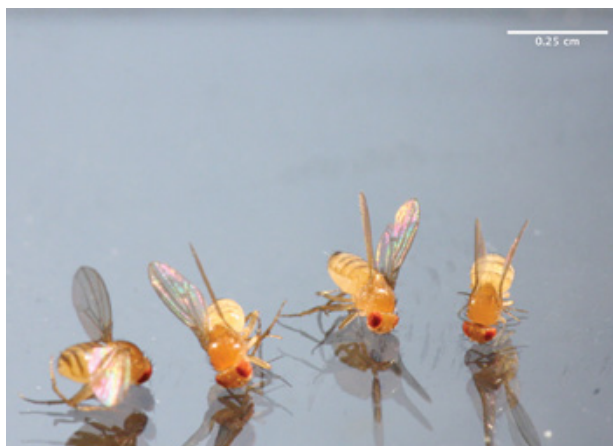


**Figure 1.** *Drosophila melanogaster*

organism. Fruit flies can help us better understand development and social behaviors when they are in groups.

## STEREOMICROSCOPY WITH DEPTH OF FIELD EXPANSION

**By Susan Munguia**

The Rocky Intertidal is one of the most diverse ecosystems primarily used to study marine organisms. The intertidal is home to an array of organisms including barnacles, algae, limpets and chitons. The chiton, *Schizochiton marshallensis*, is part of one of the most mysterious polyplacophoran mollusca family, *Schizochitonidae*. In Figure 2, the radula of a *Schizochiton*

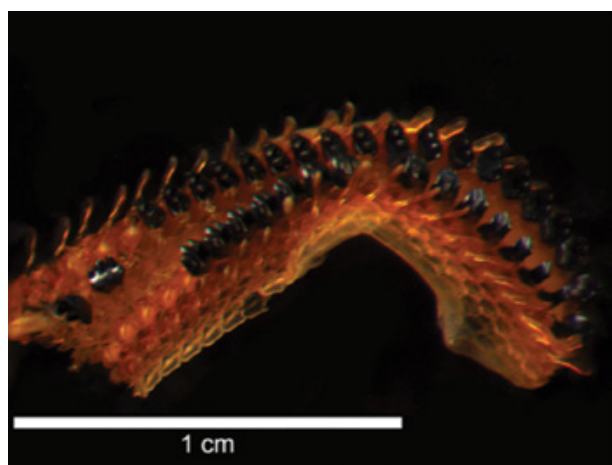


**Figure 2.** Radula of *Schizochiton marshallensis*

was photographed at varying focus distances. With Adobe Photoshop, images were loaded as individual layers and blended into a single image that is in focus throughout. Further editing was done to remove background “noise”. As chitons live in a harsh environment they are grazers, the radula provides teeth like structures that can help them feed.

## BRIGHT FIELD WITH DEPTH OF FIELD EXPANSION

By Evelyn Bond

Lily pads (*Nymphaea sp.*) are often seen floating in ponds, but have you ever wondered what they look like at the cellular level? This is a cross section of a lily pad that was stained with multiple color stains to differentiate between various tissue types. The loose arrangement (right side of Figure 3) is spongy parenchyma, and the more colorful, structurally diverse side (left side) is the palisade parenchyma. The main functions of

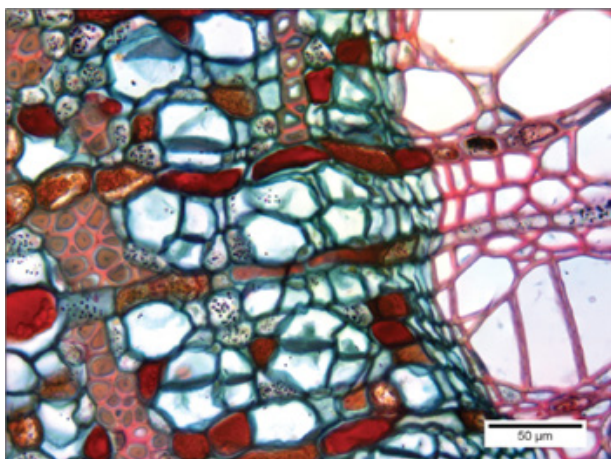


Figure 3. Cross section of a dicot leaf from the genus *Nymphaea* observed at 40X.

parenchyma are to provide the plants with storage and food production. To get this image, several images were taken at varying depths, and then the images were merged using Photoshop. Merging the images together provides us with great detail while maintaining high resolution.

## PHASE MICROSCOPY

By Rebecca Clark

Fibroblasts are commonly referred to as the main cell of the connective tissues in the body. The nucleus of the cells is the oval shape that is observed in the center of each of the cells. Fibroblasts have an elongated shape

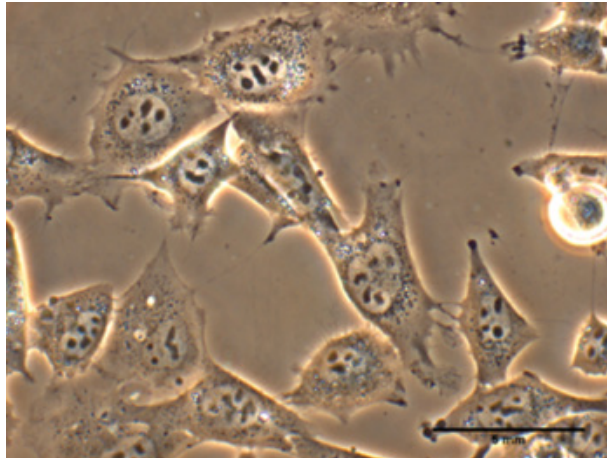


Figure 4. Mouse fibroblast cells.

that can be observed in this image. Fibroblasts play a central role in the production of collagen, and are also very important to the healing process upon injury. The image in Figure 4 was captured using a technique called photomicrography.

## FLUORESCENCE MICROSCOPY

By Sarah Flores

Mitochondria are a vital component of cell physiology responsible for nearly all the ATP production in the cell. Mitochondria are found in all eukaryotic cells, see Figure 5. Mitochondria contain their own DNA. The DNA

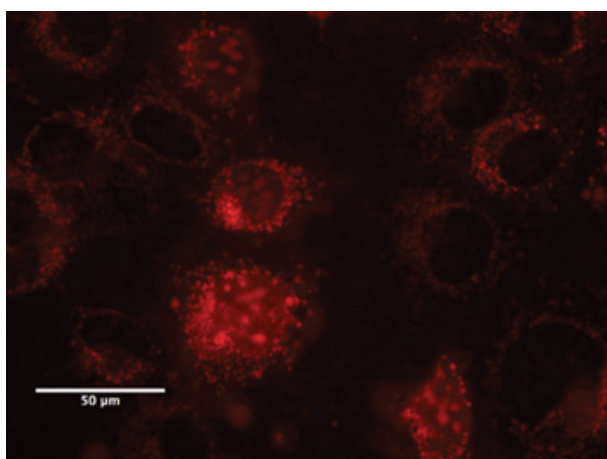


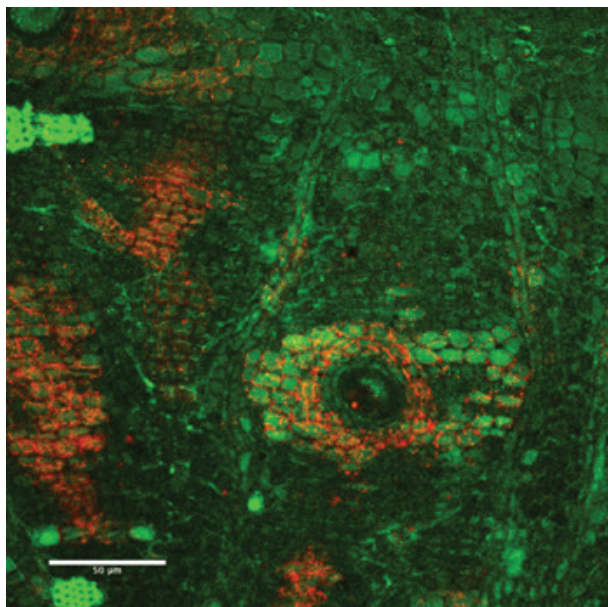
Figure 5. Fluorescence image of mitochondria in T3 mouse cancer cells stained with MitoTracker Red.

found within the mitochondria is non-recombinant and passed exclusively through the mother, meaning that the integrity of the DNA is maintained as it is passed through generations. mtDNA has been used in recent research as a means to tracing the common ancestor which all women shared, known as Mitochondrial Eve. The use of mitochondrial DNA serves as a new platform to explore the evolution of the first female.

## CONFOCAL MICROSCOPY

By Jose Rodriguez

The *Boswellia sacra* is a type of Frankincense tree, see Figure 6. This tree is native in Africa, South America, and Asia and usually resides in very dry regions. The resin of this tree is particularly interesting due to its worldwide economic value. The resin is used to make an oil which can be very expensive. This tree also has historic value as it has been cut down to make incense used by a number of religions for their respective ceremonies. Confocal microscope was used for this



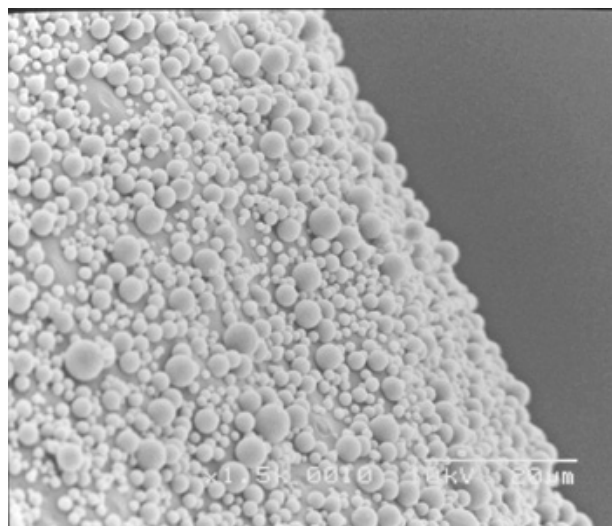
**Figure 6.** Radial section of a micro-core slice from the bark of *Boswellia sacra*. A single resin duct is visible (black oval). Two separate confocal images were merged to produce this image highlighting structural differences in the sample.

image to help identify the structures of resin ducts and canals. The end goal for obtaining these samples from a micro-core processing procedure was to compare their anatomical structures for conservation purposes.

## SCANNING ELECTRON MICROSCOPY

By Patrick Flores

The surface of a single egg belonging to a black widow spider, *Latrodectus hesperus*. The spheres distributed on the surface of the egg are known as chorion granules, which are comprised of various proteins , see Figure 7. This outermost layer of protection is analogous to the shell of a chicken egg. Some of the main functions of this outer shell are to provide protection, prevent



**Figure 7.** Surface of an egg from the black widow spider, *Latrodectus hesperus*. Chorion granules are distributed across the surface of the vitelline

desiccation, and regulate the exchange of materials between the external environment and the interior of the egg. While a single egg can be seen with the naked eye, it is next to impossible to ascertain any information about the surface of the egg with just your eye.

# **Item Format Effects On Performance And Perceived Difficulty Of English Language Learners And Native English Speaking Undergraduate Biology Students**

**Erick Valdez**

**Advisor: Joel K. Abraham, Ph.D.**

*Department of Biological Science, California State University, Fullerton*

## **ABSTRACT**

Students who are considered English Language Learners (ELL) may perceive the difficulty of some test questions higher than native English speakers (NES). This stress may vary across test item format, so an understanding of the varying effects of item format is important when considering test validity. Furthermore, the increased use of computer-based assessment allows for novel, but often unexamined, item formats. In this study, we administered a computer-based test on biology content to ELL and NES students. Each test item had one of three formats: high constraint (i.e. multiple-choice), intermediate constraint (i.e. sentence completion with dropdown menus), or low constraint (i.e. sentence completion with fill in the blanks); all tests include all item formats. We tracked student performance, and asked students about the perceived difficulty and appeal of different test item formats. We predicted that ELL students would perform better on, and prefer, intermediate constraint items, and that both groups of students would perform better on high and intermediate constraint items. Through our preliminary study, we found that both ELL and NES students performed better on high and intermediate constraint items, and both groups perceived low constraint items to be more difficult. We did not find consistent differences in performance or perceived difficulty between ELL and NES students. As we continue this work, we hope to improve understanding of the impacts of test item formats on undergraduate student performance.

## **Determining Zygosity in *Sauromalus ater* (=obesus) Twins**

**Maureen Kelley**

**Advisor: Christopher R. Tracy, Ph.D.**

*Department of Biological Science, California State University, Fullerton*

### **ABSTRACT**

Twining in Iguanid lizards is a rare phenomenon. Using genetic analysis, we explored whether a pair of putative twin common chuckwalla (*Sauromalus ater*) individuals is mono- or di-zygotic using eight polymorphic microsatellite loci. In April 2016, we incubated a clutch of 10 eggs from a captive colony of common chuckwalls at 32°C on vermiculite mixed 1:1 by mass with water. In June 2016, during hatching, we noticed two individuals emerging from a single egg. These hatchlings were approximately half the body mass of the five other surviving siblings (twins: 4.37, 4.25 g; other siblings:  $8.06 \pm 0.20$  g). We compared their genetic similarity with the remaining seven siblings, from which we were able to retrieve useful DNA samples (both alive and deceased), including the parents. We also followed growth of all siblings and found that the surviving twin caught up to the body mass and snout-vent-length of its siblings in approximately four months.

# **Phenotypic And Genomic Differentiation In Experimentally Evolved Populations Of *Drosophila melanogaster***

**Melanie Garcia and Madison Cheek**

**Advisor: Parvin Shahrestani, Ph.D.**

*Department of Biological Science, California State University, Fullerton*

## **INTRODUCTION**

Experimental evolution combined with next generation sequencing has provided scientists a window into the world of genetic adaptations. Researchers have been able to demonstrate the effects of selection in both long term and short term evolution experiments using model organisms. *Drosophila melanogaster*, commonly known as the fruit fly, has been used in experimental evolution projects due to their small genome size, easy maintenance, quick replication cycles, and easy manipulation. These studies have concluded that adaptations within sexually reproducing populations of *D. melanogaster* are continuously driven by the presence of genetic variation and reflect a lack of fixation within the populations (Burke *et al.* 2010, Orozco-terWengel *et al.* 2012). Experimental evolution studies have also shown that evolution in outbred populations is rapid and highly repeatable using groups of long-standing and newly derived *D. melanogaster* populations exposed to the same selection regimes (Graves *et al.* 2017; Burke *et al.* 2016). However, there remain unanswered questions regarding the driving factors behind the rapid evolution observed in the *D. melanogaster* populations. Specifically, in experimental evolution studies, is adaptation primarily dependent on current selection regimes, or also on evolutionary history?

Evolutionary histories of populations are believed to have lingering effects on the populations even when exposed to “new” selection regimes, but in recent studies, findings suggest that although organisms may have long evolutionary histories, their most recent selection pressures may have a stronger impact. Graves *et al.* (2017) and Burke *et al.* (2016) propose that the

driving force behind the phenotypes and patterns of genetic variation are mainly affected by the most recent selection pressures. This idea has been challenged by Simões *et al.* (2017), stating that while recent selection regimes may shape populations at the phenotypic level, evolutionary history may have major effects on outcomes at the genetic level. Furthermore, reverse experimental evolution studies also suggest that the degree to which populations revert to ancestral phenotypic values and allele frequencies is related to evolutionary history to some extent (Teotónio and Rose 2002; Teotónio *et al.* 2009). However, the authors of these studies were unable to rule out the possibility that more generations of reverse evolution might have resulted in complete reversion of phenotypes and genotypes. In response to this issue, the authors from Graves *et al.* (2017) described the inverse relationship present between selection intensity and genetic variation. Higher intensity selection regimes demonstrated to result in greater loss of genetic variation, potentially due to higher possibility of fixation of adaptive alleles. Therefore, the finding that phenotypes and patterns of genetic variation are almost exclusively shaped by most recent selection regime in Graves *et al.* (2017) and Burke *et al.* (2016) could be due to the fact that none of the populations studied were exposed to sufficiently intense selection regimes in their evolutionary histories.

Our study tests this hypothesis using *D. melanogaster* populations with an evolutionary history of being subjected to intense selection pressures for desiccation resistance. Specifically, we examine patterns of phenotypic and genomic differentiation in two five-

fold replicated stocks, known as C and D stocks, which were first described in Rose et al (1992). The D populations were previously intensely selected for desiccation resistance for about 260 generations. Then, for about 200 generations they have been under relaxed selection. In comparison, the C populations were moderately selected for starvation resistance for about 260 generations in parallel to the D population. Both the C and D populations are now on the same selection regime. After 260 generations of directional selection, the D and C populations had become differentiated in functional characters (Djawdan et. al 1998), resulting from the adaptation of the D populations to their hostile environment, which allowed for only 10% (Telomis - Scott et al. 2006) of individuals to survive each generation. We expected that after 200 generations of relaxed selection, the D and C populations will have converged on their phenotypes. Moreover, we expect that genomic comparisons of these populations should show very little, if any, differentiation. This result would be in line with the idea that most recent selection pressures (in this case relaxed selection) shape populations more than their previous evolutionary histories.

## MATERIALS AND METHODS

### Populations

This experiment used large, outbred lab populations of *Drosophila melanogaster* derived from a population sampled from South Amherst, Massachusetts (Ives, 1970). The experimental stocks used in this study were derived from a set of five populations that had been selected for late reproduction (O), and were originally derived from the Ives stock (Rose, 1984). In 1988, two sets of populations were derived from the O populations: one set (D1-5) were selected for desiccation resistance while the other set (C1-5) were handled like the D populations, except flies were given nonnutritive agar instead of desiccant, thus becoming mildly starvation resistant (Rose, 1992). In 2005, these populations were relaxed from selection and kept on a 21-day culture

regime to the present day. In total, the D populations underwent ~260 generations of selection for desiccation resistance, and ~200 generations of relaxed selection.

### Mortality Assay

The C and D population flies were cultivated to adulthood over a span of 14 days in polystyrene vials. From each individual replicate, C1-5 and D1-5, a total of 3,000 flies were obtained and distributed amongst three, six-liter acrylic plastic cages. Every two weeks flies were lightly anesthetized with CO<sub>2</sub> to be transferred to clean cages and were maintained on fresh banana-molasses food administered daily. To control for density, flies were transferred to half sized cages when their density dropped to half of the starting size. Mortality was assessed every 24 hours, flies were sexed after death, and the exact size of all populations was calculated using mortality data to determine that the total cohort size across all replicates was 30,000 flies.

Mean longevity was analyzed using a linear mixed-effects model (LME) in the R-project for statistical computing ([www.R-project.org](http://www.R-project.org)). Mortality rates from the D and C populations were analyzed using a two-stage, three-parameter Gompertz model. The Gompertz model and its variants describe the change in instantaneous mortality rates with age. The model chosen had the lowest Akaike and Bayesian information criterion (Pinhero and Bates, 2000, chapter 8).

### Development Time: Larvae to Adult

This study took a closer look at the developmental phase of the flies, by tracking the time between larvae hatching to adult eclosion from pupae. The C and D populations were given non-nutritive agar and allowed to lay eggs that were allowed to develop into larvae. 50 first-instar larvae from each agar plate, were transferred into polystyrene vials containing banana molasses food. This assay consisted of 13 vials per replicate population. The flies were monitored every six hours after the first flies eclosed. The eclosed flies were sexed and counted. Time to eclosion was analyzed using a linear mixed-effects

model (LME) in the R-project for statistical computing ([www.R.project.org](http://www.R.project.org)).

#### Adult Age-specific Fecundity

The fecundity assay was conducted over a span of 14 days. After allowing fruit flies to develop for 14 days from egg, 60 mating pairs, one male and one female per pair, were obtained from each replicate and transferred to vials containing charcoal food caps, with one mating couple per cap. Charcoal medium is composed of activated carbon, agar, sucrose, baker's yeast, and methyl 4-hydroxybenzoate (an anti-fungal). Fecundity was monitored every 24 hours for 14 days ending on day 28 from egg. Supplemental yeast was added to the caps each day and charcoal caps from the previous day were scanned on a flatbed scanner and the numbers of eggs laid on each cap were counted. Age-specific fecundity was analyzed using a linear mixed-effects model (LME) in the R-project for statistical computing ([www.R.project.org](http://www.R.project.org)).

#### Fungal Resistance

To determine if any difference exists in C and D populations fungal immunity, a fungal assay was completed. Flies were anesthetized with CO<sub>2</sub> and transferred from vials onto a dampened filter paper lying within a Petri dish. This Petri dish was then placed on ice to ensure the flies remained immobilized while fungal inoculations were completed. All populations were inoculated via the Spray Tower (Vandenberg 1996) with 5-mL doses of 0.3 g fungus/25-mL of 0.03 %*Silwet* solution. Once inoculation was complete each population was transferred to their designated cages with densities of approximately 500 flies per cage. Uninfected control flies from each population were handled in an identical manner except that they were sprayed with 5-mL of 0.03% *Silwet* solution. The sleeve of each cage was soaked with deionized water to increase humidity prior to being incubated with a 24-hour light cycle and maintained at 25 degrees Celsius. Humidity was set to 90% for the first 24 hours to ensure fungal

invasion of flies and then dropped down to 50-60% for the remainder of the assay. Each population was tested three times. We used a linear logistic regression function to model mortality probabilities, the parameters of the equation were estimated by the *glm* function in R ([www.R.project.org](http://www.R.project.org)).

#### Starvation Resistance

On day 15 from egg, 30 female flies from each replicate per stock were placed in their own starvation straw with agar. The agar plug provides adequate humidity, but no nutrients. Mortality was checked every four hours, using lack of movement under provocation as a sign of death. Starvation resistance was analyzed using a linear mixed-effects model (LME) in the R-project for statistical computing ([www.R.project.org](http://www.R.project.org))

#### Desiccation Resistance

15 days after eclosion, 30 female flies from each replicate per stock were transferred into individual straws fixed with pipet tips that contained 0.75 grams of anhydrous calcium sulfate (desiccant). Flies were separated from the desiccant by placing a piece of cheesecloth between the end of the straw and the pipet tip. The straws were then sealed and secured using Parafilm. Mortality was monitored hourly and any dead flies or flies showing lack of movement were removed. Female mean longevity in a desiccated environment was analyzed using a linear mixed-effects model (LME) in the R-project for statistical computing ([www.R.project.org](http://www.R.project.org)).

#### Cardiac Arrest Rates

On days 15, 16, and 17 from egg, 30 female flies from each replicate per stock were chosen at random (total of 90 flies per replicate). The flies were anesthetized for three minutes using triethylamine, also known as FlyNap, and then placed on a microscope slide prepared with foil and two electrodes. The two electrodes were attached to a square-wave stimulator in order to produce electric pacing of heart contraction with a shock at 40 volts, six Hertz, and 10 ms pulse duration, for 30

seconds. Anesthetized flies were attached to the slide between the foil gaps using a conductive electrode jelly touching the two ends of the fly body, the head and the posterior abdomen tip. An initial check of the status of the heart was made after completion of the shock, followed by a check after a two-minute “recovery” period. Heart status was scored as either contracting or in cardiac arrest if the heart did not return to a functioning state. The protocol for this assay is outlined in Wessells and Bodmer (2004). Cochran-Mantel-Haenszel (CMH) tests were used to analyze the rates of cardiac arrests between the C1-5 and D1-5 populations.

### Genomic Analysis

Genomic DNA was extracted from samples of 200 female flies collected from each of the 10 individual populations ( $C_{1-5}$  and  $D_{1-5}$ ) using the Qiagen/Gentra Puregene kit. The 30 gDNA pools were prepared as standard 200-300 bp fragment libraries for Illumina sequencing. Libraries were run across PE100 lanes of an Illumina HiSEQ 2000 at the UCI Genomics High throughput Sequencing Facility. Each population was sequenced twice and the reads were mapped using Burrows-Wheeler-Aligner (BWA version 0.7.8) (Li and Durbin 2009) against the *D. melanogaster* reference genome (version 6.14). The SAM files were then organized for reads mapped in adequate pairs while maintaining a minimum mapping quality of 20. Average coverage was above 70X or greater for all populations except C3, which was 67X. A SNP table was created, and brought into consideration sites where coverage was between 30X and 200X, and for a site to be considered polymorphic it was required to have a minimum minor allele frequency of 2% across all 10 populations. To assess broad patterns of SNP variation in C and D populations, heterozygosity was calculated and plotted over 100kb non-overlapping windows directly from the major and minor counts in our SNP table. A t-test was performed to compare mean heterozygosity between the two groups of populations. To assess how closely replicate populations resembled one another,  $F_{ST}$  estimates were also obtained using the formula:  $F_{ST} = \frac{(H_T - H_S)}{H_T}$  where  $H_T$  is heterozygosity based on total population allele frequencies, and  $H_S$  is the average subpopulation heterozygosity in each of the replicate populations (Hedrick, 2009).

$F_{ST}$  estimates were made at every polymorphic site in the data set for a given set of replicate populations.

### SNP Differentiation

Cochran-Mantel-Haenszel (CMH) testing was used to measure levels of SNP differentiation between the two groups of populations (C and D). First, used was the Cochran-Mantel-Haenszel (CMH) test as implemented in the PoPoolation2 software package to compare SNP frequencies between the C and D populations. We subsampled to a uniform coverage of 50X across the genome for each population using PoPoolation2. Only polymorphic sites were taken into consideration if they had a minor allele frequency of 2% across all ten populations. In total, the resulting subsampled sync file contained ~1.2 million SNPs spread across the major chromosome arms. CMH tests between the two groups of populations were performed at each of these polymorphic sites. To correct for multiple comparisons, the permutation method as featured in Graves *et al.* (2017) was used.

## RESULTS

### Mortality and Mean Longevity

The C and D populations differed in their background mortality rates and in their rate of aging. In addition, the D populations show a greater break-day compared to the C populations ( $p<0.0001$ ), suggesting that the onset of the late life phase of adulthood happens later in the D populations. When analyzing mean longevity, the D populations are able to live ~7 days longer than the C populations ( $p=.0009$ ). These significant differences are observed in both males and females.

### Development Time: Larvae to Adult

The D populations take about one hour longer to eclose

from pupa compared to the C populations, however this difference is not significant ( $p=0.66$ ).

#### Adult Age-specific Fecundity

The D populations show a greater number of eggs laid per surviving female compared to the C populations in the interval just prior to these populations' reproductive window ( $p=0.02$ ). All other intervals from the analysis are not significant ( $p>0.05$ ).

#### Fungal-resistance

No difference was observed between the D and C populations for mortality after exposure to a fungal pathogen ( $p= 0.123$ ).

#### Starvation Resistance

No differences were observed in starvation resistance between the C and D populations (see Fig. 5). The average survival time during starvation, or starvation resistance, for the five C populations is 73.54 hours, and for the five D populations, it is 69.05 hours. However, this 4.49 hour difference in starvation resistance is not statistically significant ( $p\text{-value} = 0.152$ ).

#### Desiccation Resistance

No differences were seen in desiccation resistance between the C and D populations (see Fig. 6). The average survival time during desiccation, or desiccation resistance, for the five C populations is 13.26 hours, and for the five D populations, it is 15.04 hours. However, this 1.78 hour difference in survival time is not statistically significant ( $p\text{-value} = 0.164$ ).

#### Cardiac Arrest Rates

There is no difference in the rates of cardiac arrest between the C and the D populations (see Fig. 7). The five C populations had an average cardiac arrest rate of 27.6%. Furthermore, the five D populations had an average cardiac arrest rate of 25.78%, and this small difference between the two sets of populations was not statistically significant ( $p\text{-value} = 0.598$ ).

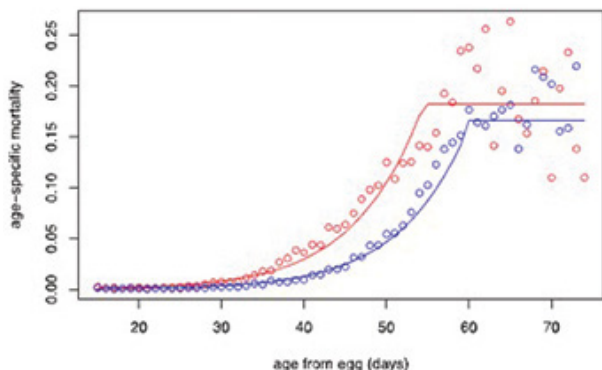


**Figure 1.** Average age-specific mortality rates across the five D and five C replicates shown in blue and red circles respectively. The data was fitted by a two-stage, three-parameter Gompertz model. Fitted lines for the D and C populations are shown in blue and red respectively. Flies from the D populations lived significantly longer than the C population flies.

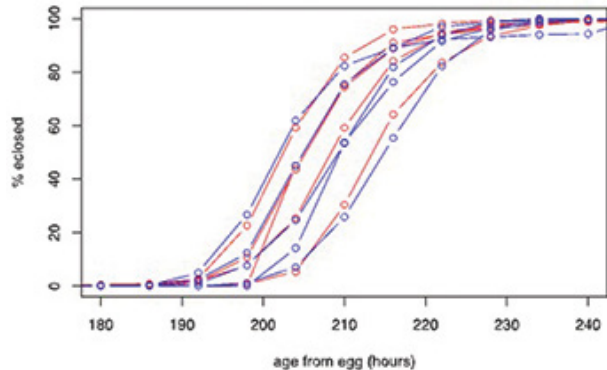


**Figure 2.** Time to eclosion in the D and C populations. Lines and points represent the percentage of the total cohort of flies eclosed each collection interval. C populations are represented by red lines and open red circles, while the D populations are represented by blue lines and open blue circles. The D's are fully converged upon the C's for this development time measure.

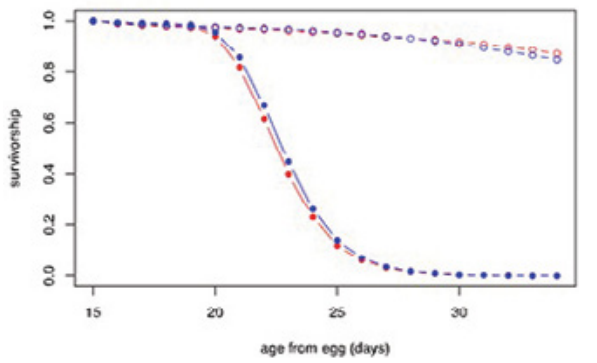


**Figure 3.** Adult survivorship in the D and C fungal resistance experiment. Uninfected treatments are represented by open points and infected treatments (exposed to fungus) are represented by closed points. C and D points are shown in red and blue respectively. Averages across replicates and across experiments are shown. Fungal resistance is not significantly different between the D and C populations.

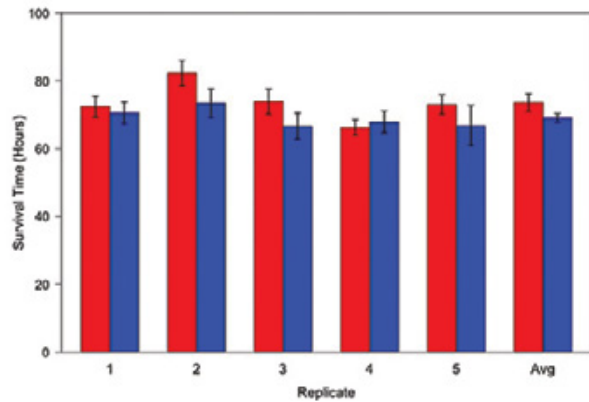


**Figure 4.** The average survival time in a starvation environment of female fruit flies at age 15 days from egg from the two five-fold replicated stocks (mean  $\pm$  1 SEM). There was no significant difference in starvation resistance between the C (red) and D (blue) populations ( $p$ -value = 0.152).

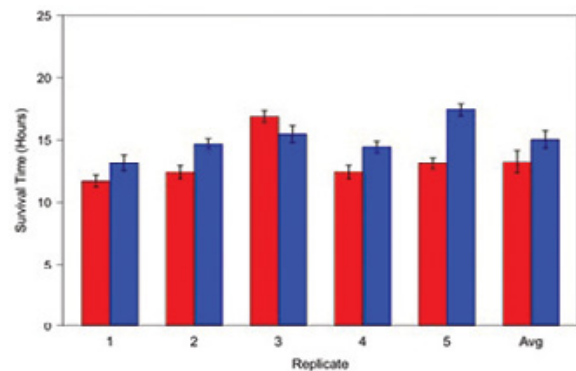


**Figure 5.** The average survival time in a desiccation environment of female fruit flies at age 15 days from egg from the two five-fold replicated stocks (mean  $\pm$  1 SEM). There was no significant difference ( $p$ -value: 0.164) in desiccation resistance between the D (blue) and C populations (red).

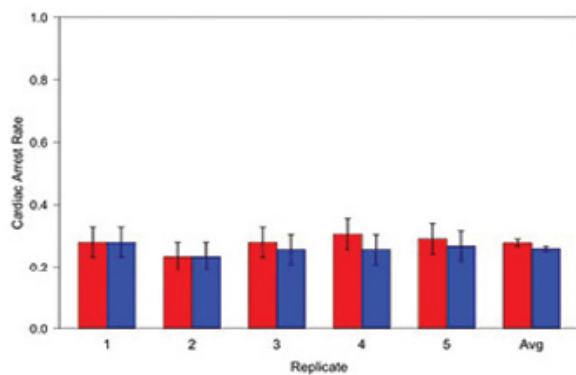


**Figure 6.** The average rate of cardiac arrests of female fruit flies from the two five-fold replicated stocks (mean  $\pm$  1 SEM). There was no statistical difference ( $p$ -value = 0.598) in the rates of cardiac arrests between the five C (red) and five D populations (blue).

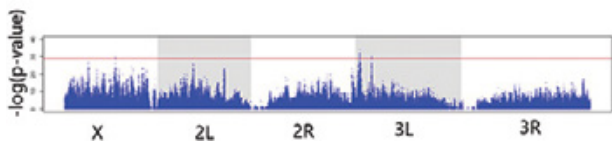


**Figure 7.** Results from statistical test comparing SNP frequencies in the D and C populations. Results from CMH tests plotted along all major chromosome arms as  $-\log(p\text{-value})$ . Our permutation derived significance threshold is shown in red. Points that fall above the red line describe regions of the genome that are differentiated between the D and C populations.

## DISCUSSION

This study aimed to determine if adaptation is dependent on evolutionary history or on the most recent selection pressures. Experimentally evolved *Drosophila melanogaster* populations, called “D” populations, underwent 260 generations of desiccation stress (given no water and no food until most flies died) and were then placed under 200 generations of relaxed selection (given both water and food). Control populations, called “C” populations, underwent 260 generations of mild starvation resistance (given water but no food), and then were placed under 200 generations of relaxed selection (given both water and food). At the height of their differentiation, these populations differed in desiccation resistance and starvation resistance (Djawdan *et al.* 1998) and in a variety of other characteristics, such as body content and cuticular hydrocarbons. However, we found that after 200 generations of relaxed selection, the D and C populations converged on almost all of the characteristics that we tested, despite having historically been differentiated. The populations have converged on fecundity, cardiac function, immune defense against fungal infection, development time, starvation resistance, and desiccation resistance. However, the D populations maintain increased longevity compared to the C populations, even after 200 generations of relaxed selection. Genomic comparison of the D and C populations reveals that across most of the genome, the populations have converged, and they differ in SNP (single nucleotide polymorphism) frequencies at only 17 sites.

The only significant differentiation that remains between D and C populations after relaxed selection is in longevity in which on average D population flies lived 7 days longer than the averaged C population flies. This was not due to a difference in development time, for which there were no differences between the C and D populations. The difference in longevity could be in part due to traits obtained during the desiccation selection regime that were not as costly as the desiccation resistance itself and therefore remained within the population after relaxed selection. The reason for this advantage developing has yet to be thoroughly explained through this study as a relationship between longevity and current or past desiccation stress has yet to be established. The few lingering SNP frequency differentiations remaining in these two populations on a genomic level have yet to be determined as relevant to longevity, but may be found in future studies to hold influence in regards to the D populations living longer than the C populations.

The research presented suggests that the most current selection pressure, relaxed selection, is the driving force for the changes in allele frequency rather than the past selection, desiccation resistance (Simões *et al.* 2017). Although, the study of an organism's evolutionary history may have importance and lingering effects on allele frequencies, the current selection pressures are able to have overpowering effects greater than those of life history (Graves *et al.* 2017; Burke *et al.* 2016). Our results offer support for the most recent selection regime having the greatest impact on shaping allele frequencies. This opens a window for researchers in other fields such as ecology, and conservation due to the wide applications available with this information. This research suggests that if organisms were to have an evolutionary history that allowed them to survive in a specific location and temperature range, they could potentially adapt if they were to be relocated into a new environment, assuming there exists standing genetic variation within the populations. Moreover, this study offers support for the premise that populations that

were once adapted to exposure from a pathogen for multiple generations may no longer have that resistance if they were to be no longer exposed to that pathogen for multiple generations. Essentially, the absence of the pathogen would be the recent selection environment, and may thus shape the population allele frequencies more than their distant evolutionary history. A broader implication of our study is that even during periods of intense selection, such as selection for desiccation resistance, genetic variation is not necessarily lost (none of the alleles in these populations went to fixation). Given a large population with standing genetic variation, adaptation to the most recent conditions can be fast and replicable. In our study, five genetically isolated D populations all responded in the same manner.

## REFERENCES

- Burke, M., Dunham, J., Shahrestani, P., Thornton, K., Rose, M., & Long, A. (2010). Genome-wide analysis of a long-term evolution experiment with *Drosophila*. *Nature*, 467(7315), 587-90.
- Chintapalli, V., Wang, J., & Dow, J. (2007). Using yatas to identify better *Drosophila melanogaster* models of human disease. *Nature Genetics*, 39(6), 715.
- Djawdan, M., Chippindale, A., Rose, M., & Bradley, T. (1998). Metabolic reserves and evolved stress resistance in *Drosophila melanogaster*. *Physiological Zoology*, 71(5), 584.
- Gibbs, A., Chippindale, A., & Rose, M. (1997). Physiological mechanisms of evolved desiccation resistance in *Drosophila melanogaster*. *Journal of Experimental Biology*, 200(12), 1821.
- Graves, J., Hertweck, K., Phillips, M., Han, M., Cabral, L., Barter, T., Rose, M. (2017). Genomics of Parallel Experimental Evolution in *Drosophila*. *Molecular Biology and Evolution*, 34(4), 831-842.
- Graves, J., Toolson, E., Jeong, C., Vu, L., & Rose, M. (1992). Desiccation, Flight, Glycogen, and Postponed Senescence in *Drosophila melanogaster*. *Physiological Zoology*, 65(2), 268-286.
- Hedrick, P. (2009). Conservation Genetics and North American Bison (*Bison bison*). *Journal of Heredity*, 100(4), 411-420.
- Ives, P.T. (1970). Further genetic studies of the South Amherst population of *Drosophila melanogaster*. *Evolution* 24: 507--518.
- Mark A. Phillips, Anthony D. Long, Zachary S. Greenspan, Lee F. Greer, Molly K. Burke, Bryant Villeponteau, Michael R. Rose. (2016). Genome-wide analysis of long-term evolutionary domestication in *Drosophila melanogaster*. *Scientific Reports*, 6(1), 39281.
- Nghiem, D., Gibbs, A. , Rose, M. , & Bradley, T. (2000). Postponed aging and desiccation resistance in *Drosophila melanogaster*. *Experimental Gerontology*, 35(8), 957-969.
- Orozco-terWengel, P., Kapun, M., Nolte, V., Kofler, R., Flatt, T., & Schlötterer, C. (2012). Adaptation of *Drosophila* to a novel laboratory environment reveals temporally heterogeneous trajectories of selected alleles. *Molecular Ecology*, 21(20), 4931-4941.
- Pinheiro, J., & Bates, D. (2000). Mixed-effects models in S and S-PLUS (Statistics and computing). New York: Springer.
- Rose, M. (1984). Genetic Covariation in *Drosophila* Life History: Untangling the Data. *The American Naturalist*, 123(4), 565-569.
- Rose M.R., J.L. Graves, & Hutchinson E.W. (1990). Use of Selection to Probe Patterns of Pleiotropy in Fitness Characters. In: Insect Life Cycles: Genetics, Evolution and Coordination. Springer London, 91-105.
- Simões, P., Fragata, I., Seabra, S., Faria, G., Santos, M., Rose, M., Matos, M.(2017). Predictable phenotypic, but not karyotypic, evolution of populations with contrasting initial history. *Scientific Reports*, 7(1), 1-12.
- Telonis-Scott, M., Guthridge, K., & Hoffmann, A. (2006). A new set of laboratory-selected *Drosophila melanogaster* lines for the analysis of desiccation resistance: Response to selection, physiology and correlated responses. *The Journal of Experimental Biology*, 209(Pt 10), 1837-47.
- Teotónio, H., Chelo, I., Bradić, M., Rose, M., & Long, A. (2009). Experimental evolution reveals natural selection on standing genetic variation. *Nature Genetics*, 41(2), 251-7.
- Teotónio, H., Matos, M., & Rose, M. (2002). Reverse evolution of fitness in *Drosophila melanogaster*. *Journal of Evolutionary Biology*, 15(4), 608-617.
- Vandenberg, J.D. (1996). Standardized bioassay and screening of *Beauveria bassiana* and *Paecilomyces fumosoroseus* against the Russian wheat aphid. *Journal of Economic Entomology* 89,1418-1423.
- Wessells, R., & Bodmer, R. (2004). Screening assays for heart function mutants in *Drosophila*. *BioTechniques*, 37(1), 58-60, 62, 64 passim.

# **Interaction Between Clinical *Acinetobacter baumannii* and *Staphylococcus aureus* Strains Recovered from the Same Site of Infection**

**Nancy Castellanos, Jun Nakanouchi, Sammie Fung, Claudia Barberis, Lorena Tuchscher, and Sean Doorly  
Advisor: Maria Soledad Ramirez, Ph.D.**

*Department of Biological Science, California State University, Fullerton*

## **ABSTRACT**

Many species of bacteria are often found together sharing the same site of infection. Descriptions of co-infections are well documented, and in some cases, polymicrobial infections exhibit increased morbidity. Some organisms can grow in mixed-culture biofilms, which promotes communication among species and could ultimately induce expression of different features..

Four different strains, two *S. aureus* (689 and 1928) and two *A. baumannii* (694 and 1929) strains were used in the present study. Clinically significant samples, from two different infection sites (muscle and secretions) where *A. baumannii* and *S. aureus* were recovered together were used in this study. Both *S. aureus* strains were methicillin susceptible and both *A. baumannii* were extensively drug-resistant.

Our results indicated that when *A. baumannii* and *S. aureus* are co-cultured, both species experience a decrease in growth. However, when we exposed them to the CFCM of each other, only *S. aureus* was observed to have decreased growth. In addition, in co-culture condition and CFCM exposure we observed changes in the susceptibility profiles. Changes in susceptibility to gentamicin, amikacin, imipenem where observed in *A. baumannii* and a change in the susceptibility to ceftazidime and cefoxitin where observed in *S. aureus*. In all cases a decrease in susceptibility was observed. Hemolysis activity was also observed to decrease for *S. aureus* 689 when it grown in the presence of *A. baumannii* 694.

This project is continuing to identify interactions between *A. baumannii* and *S. aureus* to further explore potential outcomes when they are together.

# **Quantitative Trait Locus Mapping Identifies Candidate Fungal Resistance Genes in *Drosophila melanogaster***

**Melissa Riddle and Neeka Farnoudi**

**Advisor: Parvin Shahrestani, Ph.D.**

*Department of Biological Science, California State University, Fullerton*

## **I. ABSTRACT**

Quantitative trait locus (QTL) mapping has become exceptionally useful in understanding genetic variants that contribute to phenotypic effects, such as immune response. By using recombinant fly lines from the *Drosophila* Synthetic Population Resource (DSPR), and infecting them with fungal pathogen *Beauveria bassiana*, we were able to identify and describe novel genomic regions that show significant contributions to the *Drosophila melanogaster* immune system. We also showed that sexual dimorphism in survivability after infection depends on the genomic background of populations and varies greatly among genetically distinct populations.

## **II. INTRODUCTION**

Identifying regions of the genome related to insect immune defense has the potential to elucidate the pathways and genes involved in immune defense, and help uncover the genetic mechanisms underlying risk for diseases. *Drosophila melanogaster*, the laboratory fruit fly, serves as a model for the human innate immune system, with a 40% similarity when comparing protein sequences and a 77% similarity when comparing disease-causing genes (Pandey & Nichols, 2011; Reiter et al., 2001). When *D. melanogaster* is exposed to pathogenic organisms, a humoral response is initiated, resulting in increased production of antimicrobial peptides (AMPs) from the fat body into the hemolymph. AMPs protect their host by providing mechanisms that kill harmful bacteria, fungi, and viruses (Zhang et al., 2016). This immune response is conserved in the mammalian liver (Alarco et al., 2004). There are eight classes of AMPs in *D. melanogaster*, each of which are activated as a response

to a specific type of infection. Bacterial infection will result in production of Ceropin, Drosocin, Defensin and Metchnikowin (Lemaitre et al., 1997). Fungal infection will induce production of Drosomycin through the Toll pathway, which is conserved in the mammalian MYD88-dependent Toll-like receptor (TLR) pathway (Buchon et al., 2014).

Genes previously found to be related to *Drosophila* Toll immune pathway have been associated with responses to fungal pathogens (Buchon et al., 2014). Previous studies have subjected *D. melanogaster* to the natural entomopathogenic fungus *Beauveria bassiana* (*B. bassiana*) and observed four thousand genes that changed in rate of expression before fungal infection and 24 hours after infection (Paparazzo et al., 2015). *B. bassiana* is known to infect its host after penetrating the outer cuticle. Once spores germinate, they are penetrated within the insect's body and toxins are produced that then drain the insect of nutrients. The fungus subsequently induces white muscadine disease, named after the layer of white mold that covers the insect after infection. The lingering mold allows for spores to be released into the host's environment, potentially infecting nearby insects.

Sexually dimorphic responses to fungal infection have been observed in *D. melanogaster* where males tend to outlive females when infected (Farnoudi et al., 2017). Previous studies show significant levels of sexual dimorphism after 118 wild-derived lines of fruit flies were infected with the fungal pathogen *Metarrhizium anisopliae* (*M. anisopliae*), indicating that males were more resistant than females (Wang et al., 2017).

These differences indicates variation in *D. melanogaster* immunity defense among the sexes requiring closer observation using genetic and molecular insights.

Quantitative trait locus (QTL) mapping maps phenotypes to chromosomal regions within an organism's genome (Miles et al. 2008). The *Drosophila* Synthetic Population Resource (DSPR) is a collection of more than 1600 recombinant inbred lines generated from eight founder lines and has been a useful tool in studying traits of interest in *D. melanogaster* (King et al., 2012). It is an excellent instrument for identifying loci related to complex traits, such as effects of different chemotherapies and alcohol dehydrogenase (ADH) enzyme activity (Long et al., 2014; King et al., 2012). In this study, we used the DSPR in a QTL mapping study to identify novel loci related to immune defense against fungal infection with *B. bassiana*. We identified candidate genes involved in *D. melanogaster* immune response.

### III. MATERIALS & METHODS

The *Drosophila* Synthetic Population Resource was created from 2 synthetic populations, labeled pA and pB. Each of these populations was created from 8 inbred founder populations that were put through round-robin cross mating (Figure 1). The pA populations were derived from A1-A7 and the pB populations were derived from B1-B7; both populations include AB8. After the synthetic populations were created and separated into subpopulations (pA1, pA2, pB1, pB2), the flies were allowed to freely mate for 50 generations, and then underwent full-sib mating for 25 generations, to create several hundred recombinant inbred lines from each population (RILs). The genomic segments of the RILs average to 3 cM, which provides a high mapping resolution when examined using QTL, compared to traditional QTL mapping (King, 2012).

297 RILs from the A1 population were obtained from the laboratory of Anthony Long at the University of California, Irvine. These were maintained on Cornell Biotech Glucose media (per liter of deionized water: 82 g glucose, 82b Brewer's yeast, 10g agar, 10 mL acid mix

composed of 4.15% phosphoric acid by volume), at 25 °C on a 12 hour light/dark cycle. Before experimentation, 100 male and 100 female flies per line were anesthetized with carbon dioxide and placed in small fly cages with a Petri dish of fly media and yeast. The flies were allowed to lay eggs for 24 hours. Then, the eggs were separated into vials at densities of approximately 60-80 eggs/vial. The flies were inoculated with *B. bassiana* at approximately 17 days from egg, as described below.

#### Preparation of *B. bassiana*:

*D. melanogaster* were infected with *B. bassiana* ARSEF 8246, a shore-fly isolate from the United States Department of Agriculture on the Cornell campus. A spore that grew on one *D. melanogaster* was removed and cultured on Petri plates of fungus growing medium (per 1 L of deionized water: 10 g glucose, 2.5 g autolyzed yeast extract, 2.5 g bactopeptone, and 15 g agar). This new *B. bassiana* strain was stored at -20 °C as "ARSEF 12460 Shahrestani & Vandenberg."

#### Inoculation of flies with *B. bassiana*:

Adult flies that were 5-7 days old post-eclosion were briefly anesthetized with carbon dioxide (CO<sub>2</sub>) and measured in a centrifuge tube to 0.5 mL, which corresponds to approximately 100 flies or 50 flies/sex. The measured flies were then spread out on a small Petri plate lid placed on ice to continue to anesthetize the flies. Flies were sprayed with 5 mL of a fungal suspension (0.034 g spores/25 mL of 0.05% Silwet), which introduced approximately 103 spores/mm<sup>2</sup> of *B. bassiana* to the fly surfaces. These inoculated flies were placed into cages and kept at 25° C and 100% humidity for 24 hours. After 24 hours, the cages were maintained at 25° C at 60-70% humidity with a 12/12 hour-light/dark cycle. Mortality was counted daily and recorded for ten days, distinguishing the number of males and females that were dead or lost due to handling. After ten days, the surviving flies were terminated and counted in order to determine the exact number of flies that were in each cage for the experiment.

### Fungal Viability Check and Spore Count:

To confirm spore viability, a 2 mL Silwet suspension of a very small amount of spores was sprayed onto a small Petri plate containing fungal growth media per inoculation session. The plate was then incubated at 25 °C. After 24 hours, the plate was examined for even distribution of spores. After 72-96 hours, the plate was checked for a lawn of fungus growth.

In order to verify dosage sprayed onto the flies, a microscope cover slip was sprayed alongside the flies in each inoculation. The coverslip was then placed in a 50 mL microfuge tube with about 15 small glass beads and covered with 5 mL of 0.03% Silwet. A vortex shaker was used to remove spores from the coverslip and into the suspension. The spore suspension was then added to another coverslip over a counting area. Using a disposable pipette, a drop of the suspension was placed onto each of the two grids of two hemacytometers. Using a light microscope, the spores in the four corner squares and center square were counted in a consistent way, as to obtain the best estimation of spores per mm<sup>2</sup>.

### Data Analysis:

Fly lines were divided into groups based on when the flies were reared and sets based on the date of inoculation. We used the programming language R version 3.3.2. We installed RStudio, an integrated development environment (IDE) compatible with R. We downloaded and installed the DSPRqtl and DSPRqtlDataA packages provided by <http://wfitch.bio.uci.edu/~dspr/Tools/index.html>. The DSPRqtl package contains functions useful for mapping the regions of interest of the *D. melanogaster* genome. The DSPRqtlDataA package contains data tables with probabilities for fly lines from the ancestral pA population. To analyze the data, we loaded the libraries for these packages and our data set into R. We ordered our data set by fly line and renamed the rows to reflect this reordering. We tested for independence of groups and sets using ANOVA (Analysis of Variance), and then

displayed the results (Table 1). We made a table where each row contained the number of a fly line and the number of replicates for that fly line, and converted the table to a different format called a data frame. We used this data table to calculate the mean values for survival, male survival, female survival, and sexual dimorphism of survival for each fly line. We stored these values in a new data frame, where the first column was called patRIL to match the conventions of the DSPRscan function called later. The other columns were named according to the values they represented. We used the DSPRscan function from the DSPRqtl package to perform the QTL mapping for each of the means of interest. We used the DSPRplot function from the DSPRqtl package to plot the loci of significance against the chromosomes of the *D. melanogaster* genome. We used the DSPRpeaks function from the DSPRqtl package to output the significant locations of the genome, in cM and bp. Then, we used the genomic database FlyBase to cross-reference the identified genomic regions with previously identified *Drosophila* genes.

#### IV. FIGURES

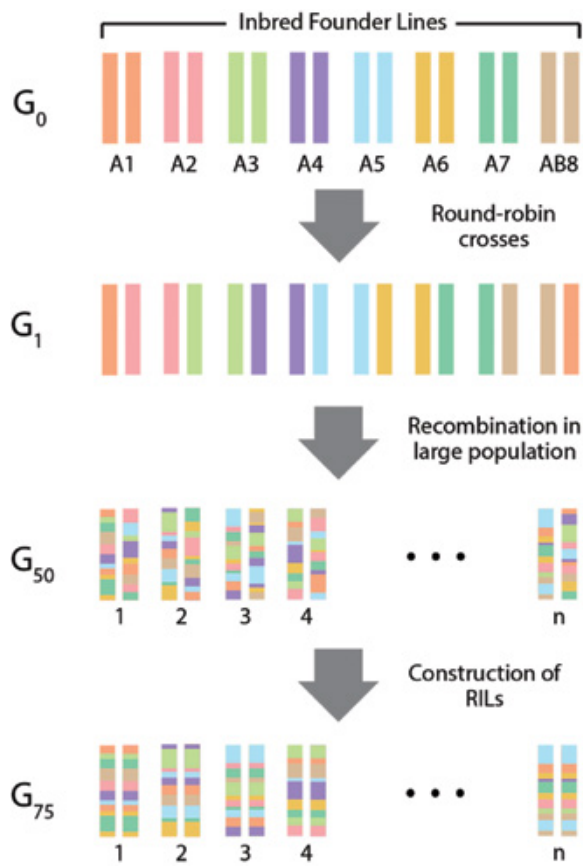


**Figure 1.** The *Drosophila* Synthetic Population Resource contains 750 recombinant inbred lines derived from 8 founder lines. Our experiment analyzed genomic data from 297 of these fly lines, all from the pA panel.

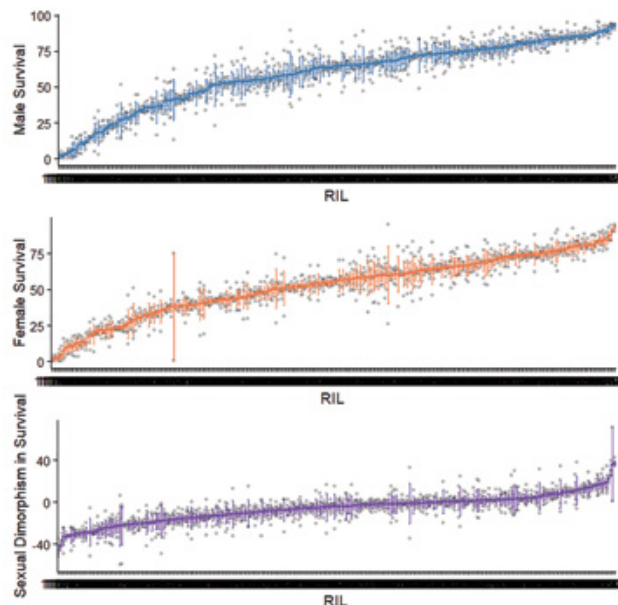


**Figure 2.** For both males and females, RILs were ordered by increasing average survival and then plotted with standard error bars. The order of the RILs differs between males and females because they are plotted by increasing survival.

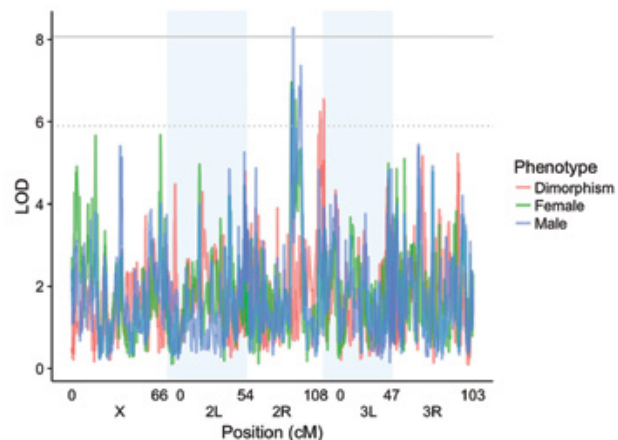


**Figure 3.** Chromosome mapping of all tested flies (males, females and difference between them). This chromosome mapping returns 4 loci of interest over the threshold (shown by a solid line), all for males.

**Table 1.** ANOVA results of flies based on rearing time (group) and inoculation time (set). As expected, there was no significant difference between flies with different rearing times or inoculation times, nor was there a significant interaction between rearing and inoculation time.

	Degrees of Freedom	Sum Sq	Mean Sq	F value	Pr(>F)
Group	1	542	542.5	1.235	0.267
Set	1	17	16.7	0.038	0.845
Group : Set	1	1131	1130.8	2.575	0.109
Residuals	874	383805	439.1		

**Table 2.** ANOVA results of flies based on sex. As expected, there was a significant difference between male and female survivability.

	Degrees of Freedom	Sum Sq	Mean Sq	F value	Pr(>F)
Sex	1	18672	18672	37.65	1.04e-09
Residuals	1754	869791	496		

**Table 3.** QTL identification of candidate genes related to *D. melanogaster* immune regulation.

Gene Symbol	Gene Name	Sequence Location	Known Functions	Associated Papers
Fak	Focal adhesion protein	2R:19,430,659..19,437,259 [-]	Innate immune response	Gaudet et al., 2010
DptA	Diptericin A	2R:18,865,765..18,866,260 [+]	Antibacterial humoral response; Defense response to Gram-negative bacterium; Positive regulation of innate immune response	Cronin et al., 2009; Kwiatkowski et al., 2005
DptB	Diptericin B	2R:18,867,391..18,867,895 [+]	Humoral response to Gram-positive bacterium	Verleyen et al., 2006
Imd	Immune deficiency	2R:18,409,796..18,4	Defense response to	Corbo and Levine et

Gene Symbol	Gene Name	Sequence Location	Known Functions	Associated Papers
		13,599 [-]	Gram-negative bacterium and virus; Positive regulation of innate immune response	al., 1996; Bernal and Kimbrell et al., 2000; Goto et al., 2008; Kwiatkowski et al., 2005
IM23	Immune induced molecule 23	2R:18,382,704..18,383,235 [-]	Antibacterial hormonal response; Defense response to Gram-positive bacterium	Apidianakis et al. 2005; Telonis-Scott et al., 2009; Kwon et al., 2008; Ellis and Carney et al., 2009
IM1	Immune induced molecule 1	2R:18,383,949..18,384,378 [+]	Defense response to bacterium	Levy et al., 2004; Uttenweiler-Joseph et al., 1998
IM2	Immune induced molecule 2	2R:18,386,602..18,387,030 [+]	Defense response to bacterium	Levy et al., 2004; Uttenweiler-Joseph et al., 1998
IM3	Immune induced molecule 3	2R:18,387,895..18,388,734 [+]	Antibacterial humoral response; Toll signaling pathway	Levy et al., 2004; Uttenweiler-Joseph et al., 1998
Dmel\E(bx)	Enhancer of bithorax	3L:233,926..246,912 [-]	Negative regulation of innate immune response	Badenhorst et al., 2005; Kwon et al., 2009; Bai et al., 2007; Badenhorst et al., 2002; Parrish et al., 2006; Mummery-Widmer et al., 2009; Xiao et al., 2001; Hamiche et al., 1999; Li et al., 2010; Mizuguchi et al., 2001
Dmel\EbpIII	Ejaculatory bulb protein III	2R:24,026,172..24,027,518 [+]	Immune response against viral infection	Zheng et. al. 2011
Dmel\IM18	Immune induced molecule 18	2R:23,600,914..23,601,773 [-]	Defense response to bacterium	Levy et. al., 2004
Dmel\RYBP	Ring and YY1 Binding Protein	2R:22,670,587..22,673,212 [+]	Negative regulation of immune response	Aparicio et al., 2013
Dmel\Swim	Secreted Wg-interacting molecule	2R:22,189,817..22,202,671 [-]	General immune response	Mulligan et. al., 2012

Gene Symbol	Gene Name	Sequence Location	Known Functions	Associated Papers
Dmel\pirk	poor Imd response upon knock-in	2R:21,660,967..21,662,995 [-]	Negative regulation of innate immune response	Lhocine et al., 2008
Dmel\Tim10	Translocase of inner membrane 10	2R:21,690,215..21,691,139 [-]	Defense response to Gram-negative bacterium	Cronin et al., 2009
IM4	Immune induced molecule 4	2R:20,868,496..20,869,321 [-]	Humoral immune response to bacterium	Verleyen et al., 2006; Levy et al., 2004
IM14	Immune induced molecule 14	2R:20,870,392..20,870,678 [+]	Defense response to bacterium	Uttenweiler-Joseph et al., 1998; Levy et al., 2004
DMAP1	DNA methyltransferase 1 associated protein 1	2R:20,644,036..20,645,865 [+]	Positive regulation of antimicrobial peptide production; Positive regulation of innate immune response	Goto et al., 2014
18w	18 wheeler	2R:20,111,511..20,116,932 [+]	Antimicrobial humoral response	Williams et al., 1997; Ligoxygakis et al., 2002

## V. RESULTS

### Verifying Rearing and Spraying Effects

ANOVA (Analysis of Variance) tests examining the relationships between group, set, and mortality found that no grouping significantly impacted the mortality of the inoculated flies ( $p>0.05$ ) (Table 1). In other words, there is no significant relationship between *group* and survival, *set* and survival, or *group* and *set* with survival. This is expected since groups and sets were chosen randomly, and we do not expect the time of rearing or the time of spraying to affect survival rates significantly.

### Sexual Dimorphism

To determine the sexual dimorphism in regards to survivability following inoculation with *B. bassiana*, data from male and female flies were graphed separately. In both cases, percent survivability by line was graphed

by increasing survival (Figure 2). In congruence with previous studies, our results show a sexually dimorphic response to fungal infection. An ANOVA test determined that sex had a significant effect on survivability ( $p<0.05$ ) (Table 2). According to our data, male flies have higher survivability than females when inoculated with *B. bassiana*.

### Identifying Significant Loci

QTL analysis shows the results for the females, males, and sexual dimorphism (Figure 3). We identified a total of four statistically significant QTL, all from the male genome. The female and sexual dimorphism results did not generate any significant loci. All four loci of interest overlap on the right arm of chromosome 2, across 1.415-1.638 Mb. 382 genes are located in this region, but of these, only a handful could provide useful resistance mechanisms. We chose to examine those genes that dealt

with signal pathways, AMPs, chitin and its properties or other defense mechanisms. A summary of all genes found in the 4 peaks can be found in the Supplemental material. These gene segments include the significant peaks found for males, females, and the difference between the two. The threshold was only reached by the male peaks, which are the same as seen in Figure 3.

## VI. DISCUSSION

Recombinant inbred lines are made up of genetically (almost) identical individuals. By using RILs in our study, we were able to observe flies that were nearly identical within fly line, but genotypically different across fly lines. Therefore we were able to observe considerable variation in phenotypic characters associated with survivability related to immune defense after infecting the flies with *B. bassiana*. By sorting RILs in order of increasing survivability, the genomic role in activating an immune response was clear, given that fly handling during experimentation was not statistically significant. Several of the RILs displayed very little survivability after fungal infection while others were able to withstand the pathogen over twice the rate of other populations. Therefore, the large magnitude of variation must be related to the genomic background of the flies such that those that were not able to fight the infection had a genetic makeup hindering their immune defense, greatly contrasting the genetic variants present in other RILs that surpassed the survivability of their counterparts. RILs were also aligned by the level of sexual dimorphism upon fighting fungal infection. The difference between male and female survivorship showed an increasing trend indicating that, in addition to survivability, there is a genetic contribution to sexual dimorphism. For nearly two decades, experiments involving *D. melanogaster* and pathogens have shown that males are overall less susceptible to infection than their female counterparts (Fellowes et al., 1999). Our experiment suggests that males are more efficient than females in fighting pathogenic infection as a result of differential gene expression since the genome was the only manipulated

variable of the fruit fly populations. However, it is necessary to investigate alternative reasons as to why males outlive their female counterparts. One postulation is that males are better at tolerating the same level of infection, or fungal load, than females. Another suggestion is that females are less efficient at ridding their body cavities of the infection than males from the same population. In addition to our current genomic work, our lab plans to explore both physiological theories of infection regulation.

Within the loci of interest identified by the QTL analysis, there were 19 candidate genes determined to be related to immune response in the DSPR populations. Though these findings explain a small fraction of heritable variation and present a starting point for future research, they have promising value for obtaining insight into the complexities behind the *D. melanogaster* immune system.

Toll pathway immune signaling is reported to be initiated after fruit flies are infected with Gram-positive bacteria, yeast, or fungi, while Imd signaling is responsive to Gram-negative bacteria. Interestingly, both the Toll and Imd immune pathway genes were identified to be upregulated after QTL analysis was performed (Table 3). Immune induced molecule 23, 1, 2, and 3 (IM23, IM1, IM2, and IM3) were determined to have contributory roles after infection with a fungal pathogen. IM3 is part of the humoral response under the Toll signaling pathway, confirming activation of a signaling cascade known to be involved in fighting fungal infection. However, the gene coding for Imd was identified to also be involved as a part of the fungal immune response contradicting its role of positively regulating the Imd immune system which is traditionally activated upon Gram-negative bacterial infections. The synergistic relationship between the Toll and Imd pathways has been recently reevaluated after multiple accounts of cross activation. In a previous experiment under the Shahrestani laboratory, several mutant fly lines lacking genes in the Toll and Imd immune pathways were created. After fungal infection, a fly

line lacking the *relish* gene, previously thought to be insignificant in fighting fungal infections, turned out to be directly involved in regulating the dimorphic response to a fungal pathogen. Prior to that, however, bacterial infections demonstrated how regulatory pathways of fruit fly immunity engage in synergistic activation of AMP genes after infection with *E. coli* (Taji et al., 2007). Spätzle is a ligand that responds to the Toll pathway while Gram-negative peptidoglycan (the PGRP-LC ligand) contributes to the Imd pathway. AMPs from both signaling cascades were upregulated after bacterial infection including Drosomycin, Diptericin, and AttacinA. In relation to our experiment, we saw upregulation in Diperticin B and Dmel/Tim10 as a response to fungal infection contradicting what is traditionally known about their commitment to the Imd pathway (Table 3).

These list of candidate genes related to immune defense are not only giving greater insight into the dynamics of *D. melanogaster* immune regulatory systems, but signify the genomic contribution behind fighting pathogenic infections in a fly population. Their role in enhancing RIL survivability post infection require future experiments to elucidate the mechanistic interactions potentially pointing to immune defense synergism.

## VII. CONCLUSION

The dynamics of immune defense in *D. melanogaster* were evaluated using DSPR fly lines with genomic variability between each population and analyzing survivability and sexual dimorphism post-infection with fungal pathogen *B. bassiana*. Both phenotypes were positively correlated to their genetic makeup suggesting a meaningful role of the genome during regulation of the immune response. QTL analysis revealed 19 immune-related genes that were involved in fighting fungal infection, including genes coding for AMPs in both the Toll and Imd pathways. These findings discover how important the genome is for fighting infection while also providing greater insight into the synergistic interaction

between two immune pathways traditionally thought to be distinct from one another.

## VIII. ACKNOWLEDGEMENTS

This work was conducted under the guidance of Dr. Parvin Shahrestani and contributing members of the Shahrestani laboratory at California State University, Fullerton.

## IX. LITERATURE CITED

- Alarco, A., Marcil, A., Chen, J., Suter, B., Thomas, D., Whiteway, M. Immune-Deficient *Drosophila melanogaster*: A Model for the Innate Immune Response to Human Fungal Pathogens. *The Journal of Immunology* May 1, 2004, 172 (9) 5622-5628; DOI: 10.4049/jimmunol.172.9.5622
- Buchon, N., Silverman, N., Cherry, S. Immunity in *Drosophila melanogaster*--from microbial recognition to whole-organism physiology. *Nat Rev Immunol.* 2014 Dec;14(12):796-810. doi: 10.1038/nri3763.
- Farnoudi, N., Hunt, B., Sadoughi, S. Battle of the Sexes: A Sexually Dimorphic Response to Fungal Infection in *Drosophila melanogaster*. *Dimensions: The Journal of Undergraduate Research in Natural Sciences and Mathematics.* 2017; 19: 10-17.
- Fellowes, M.D.E., Kraaijeveld, A.R., and Godfray, H.C.J., 1999. The relative fitness of *Drosophila melanogaster* (Diptera, Drosophilidae) that have successfully defended themselves against the parasitoid *Asobara tabida* (Hymenoptera, Braconidae). *Journal of Evolutionary Biology*, 12, 123–128.
- King EG, Merkes CM, McNeil CL, et al. Genetic dissection of a model complex trait using the *Drosophila* Synthetic Population Resource. *Genome Research.* 2012;22(8):1558-1566. doi:10.1101/gr.134031.111.
- Lemaitre B, Reichhart J-M, Hoffmann JA. *Drosophila* host defense: Differential induction of antimicrobial peptide genes after infection by various classes of microorganisms. *Proceedings of the National Academy of Sciences of the United States of America.* 1997;94(26):14614-14619.
- Long AD, Macdonald SJ, King EG. Dissecting Complex Traits Using the *Drosophila* Synthetic Population Resource. *Trends in genetics : TIG.* 2014;30(11):488-495. doi:10.1016/j.tig.2014.07.009.
- Miles, C. & Wayne, M. (2008) Quantitative trait locus (QTL) analysis. *Nature Education* 1(1):208

Pandey UB, Nichols CD. Human Disease Models in *Drosophila melanogaster* and the Role of the Fly in Therapeutic Drug Discovery. Barker EL, ed. *Pharmacological Reviews*. 2011;63(2):411-436. doi:10.1124/pr.110.003293.

Paparazzo F, Tellier A, Stephan W, Hutter S. Survival Rate and Transcriptional Response upon Infection with the Generalist Parasite *Beauveria bassiana* in a World-Wide Sample of *Drosophila melanogaster*. Missirlis F, ed. PLoS ONE. 2015;10(7):e0132129. doi:10.1371/journal.pone.0132129.

Reiter LT, Potocki L, Chien S, Grbskov M, Bier E. A Systematic Analysis of Human Disease-Associated Gene Sequences In *Drosophila melanogaster*. *Genome Research*. 2001;11(6):1114-1125. doi:10.1101/gr.169101.

Tanji T, Hu X, Weber ANR, Ip YT. Toll and IMD Pathways Synergistically Activate an Innate Immune Response in *Drosophila melanogaster*. *Molecular and Cellular Biology*. 2007;27(12):4578-4588. doi:10.1128/MCB.01814-06.

Wang JB, Lu H-L, St. Leger RJ. The genetic basis for variation in resistance to infection in the *Drosophila melanogaster* genetic reference panel. Andrianopoulos A, ed. PLoS Pathogens. 2017;13(3):e1006260. doi:10.1371/journal.ppat.1006260.

Zhang, L., & Gallo, R. (2016). Antimicrobial peptides. *Current Biology*, 26(1), R14-R19. 0960-9822.

# **Relaxed Selection of Experimentally-Evolved *Drosophila* Shows Transient Evolutionary Trade-Offs**

**Neeka Farnoudi, Cristina Narvosa, Melissa Riddle, Silvia Orozco, and Stephen Gonzalez**

**Advisor: <sup>1</sup>Parvin Shahrestani, Ph.D., and <sup>2</sup>Sam Behseta, Ph.D.**

<sup>1</sup>Department of Biological Science, California State University, Fullerton, <sup>2</sup>Department of Mathematics, California State University, Fullerton

## **I. ABSTRACT**

The genetic makeup of a population can change over time and these changes are manifested in the DNA of individuals, thus also in their physiology and physical characteristics. Populations of *Drosophila melanogaster*, the common fruit fly, were experimentally-evolved for increased resistance against infection from the fungus *Beauveria bassiana* and tested for longevity against their control populations. Resistant flies lived shorter lives during the initial selection period of 19 generations. This suggests that increased immune defense against *B. bassiana* comes at a cost to longevity. But after nearly 75 generations of undergoing relaxed selection, the resistant populations exhibited longer lifespans than their controls. The disappearance of this trade-off signifies other contributory factors that impact immune defense and organismal lifespan including resource allocation and environmental stress factors.

## **II. INTRODUCTION**

Population genomics reveals how environmental factors influence the genetic makeup of a group of individuals from the same species through natural selection. *Drosophila melanogaster* (*D. melanogaster*), or the common fruit fly, is a widely studied model organism, useful for its short generation time, ability to produce high numbers of progeny, relatively easy maintenance, and fully sequenced genome containing many genes homologous to human diseases (Hales et al., 2015). These genes have been linked to diabetes, cardiovascular dysfunction, and cancer (Pandey & Nichols, 2011). Although the innate immune systems of *D. melanogaster* are less complex than the immune defenses in humans,

their genetic similarities to humans pose a reason to study them for the expansion of research on immune function (Buchon, Silverman, & Cherry, 2014). The fruit fly holds important applications in uncovering more about humans and other invertebrates such as crop pests and disease-carrying mosquitoes that spread illnesses including malaria and dengue. The entomopathogenic fungus *Beauveria bassiana* (*B. bassiana*), which is found to be harmless to plants, birds, and mammals, is also recognized for its potential to act as a potent and selective natural biological control agent against insects, including harmful mosquito populations of *Aedes aegypti* and *Anopheles stephensi* (Ragavendran, Dubey, & Natarajan, 2017). This agent was also shown to have the potential to decrease mosquito contact with humans and lower their propensity for blood-feeding (Darbro et al., 2012).

*D. melanogaster* possess an innate immune system, or a nonspecific immune response activated by the presence of any material that the system regards as being foreign from the body. There are various physical and molecular characteristics that defend against bacteria, fungi, and viruses. Components of this immune system consist of epithelial barriers such as the cuticle and gut, while the humoral response produces antimicrobial peptides (AMPs), hemocyte-dependent microbe phagocytosis, and larger pathogen encapsulation (Govind, 2008). Their cuticle, along with grooming behavior, provides outer protection against harmful agents. When pathogens cross through this initial cuticle barrier and enter the body, the activation of internal innate immune responses occur. The humoral response activates the Toll and Imd

pathways which regulate the release of various AMPs that differ in their structures, and consequently, their functions (Zhang & Gallo, 2016). In cases where there is expression of unsuitable levels of AMPs, autoimmune disorders from inflammation have been found to occur (Zhang & Gallo, 2016).

Previously we found that fruit fly populations experimentally-evolved for increased resistance to fungal infection from *B. bassiana* live shorter lives when they are uninfected, compared to control populations that do not possess strengthened immunity against fungal infection (Nguyen et al. 2017). Fungal-resistant populations had less longevity compared to controls when uninfected, suggesting that there is a trade-off between immune defense and lifespan, and that investments towards immune defense come at a cost to longevity (Nguyen et al. 2017). It is known that cellular activity and metabolic processes require a continuous supply of energy and materials. Therefore, because the upregulation of the immune system comes at a large expenditure, activating it may be beneficial only when it improves survivability and fitness. Additionally, previous research shows immune regulated gene expression to increase during adult mid-life, and that under starvation, activation of the immune system shortens longevity (DeVeale, Brummel, & Seroude, 2004). Upregulation of the immune system can also lead to chronic inflammation (DeVeale, Brummel, & Seroude, 2004). We saw that uninfected *D. melanogaster* survival started to plummet shortly after mid-life (Nugyen et al. 2017).

To further investigate this trade-off phenomenon, we tested the immune function and lifespan of the fly populations of Nguyen et al. 2017, but after ~75 generations of relaxed selection. Because it has been found that population phenotype and genetic variation is most substantially impacted by the most recent selection regime imposed on populations, (Graves et al., 2017; Burke et al., 2016), after relaxed selection, we expected to see convergence on both immune defense and longevity between the formerly resistant populations and their controls. Instead, we found that the formerly resistant

populations have retained their better immunity against the fungus. But surprisingly, the immune-defense trade-off with longevity has disappeared, such that the resistant populations no longer have a decrease in longevity, and even have a slight increase in longevity compared to their controls. In other words, after ~75 generations of relaxed selection, heightened immune defense was maintained but longevity increased compared to controls. This promotes the idea that many factors can influence the immune system including a redistribution of physiological resources or environmental stressors, and that trade-offs between immune defense and longevity are not obligatory.

### **III. MATERIALS & METHODS**

#### **Fly Populations:**

We used an outbred fly population that contained flies originating from 5 locations worldwide, including New York, Zimbabwe, Netherlands, Beijing, and Tasmania, by conducting round-robin crossing of isofemale lines to allow for increased genetic diversity. The flies were maintained on discrete 14-day generations in a 12:12 light/dark incubator. The outbred population was then divided into eight populations, each with 10,000 individuals. Four of these eight populations were selected for increased resistance to fungal infection (S) while the other four were held as controls (C).

#### **Fungal Selection:**

To select for fungal resistance, 10,000 flies from the four S populations were sprayed with 7.5 ml of 0.34 g fungal pathogen *B. bassiana* (ARSEF 12460) suspended in 25 ml 0.03% Silwet using a spray tower. Those flies were divided into five cages at densities of 2,000 flies per cage. Inoculated flies were placed inside population cages and kept at 100% humidity for 24 hours in the dark to allow the fungus to germinate. Dead flies were removed daily and fresh food was provided to surviving flies daily. After 80% of the individual flies died from infection, the remaining 20% individuals produced offspring to contribute to the next generation. Surviving flies across all cages were combined to form one 2,000 fly cage.

This process was continued for nineteen generations alongside the four C populations which were handled in a similar manner yet only 0.03% Silwet was used during the spray, and of remaining 20% from the 5 cages, flies were randomly selected to contribute to the next generation.

Egg collections were performed by keeping 100 vials of ~60-80 eggs/vial for each population to provide over 10,000 eggs for the next round of selection. A hemocytometer determined that we introduced 104 spores/mm<sup>2</sup> of fly cuticle by counting spores that landed on microscope slides placed adjacent to flies during each spray.

#### **Relaxed Selection:**

After 19 generations of selection, the S and C populations were then kept on the same exact regimen for the following ~75 generations. In these ~75 generations, none of the populations were selected for immune defense, instead all eight populations were maintained under identical conditions – we call this “relaxed selection.”

#### **Genomics and Data Analysis:**

During fungal selection, adult female fly samples were obtained at generation 0 and generation 19 and kept frozen in a -80° C freezer. Nine genomic libraries were constructed and sequenced on Illumina Hi-Seq platforms at the Cornell sequencing core facility. The Conchran-Mantel-Haenzel test determined non-random differences regarding allele frequency changes among loci on each chromosome arm. Regions that were differentiated among the populations showed to be inconsistent with neutral genetic drift and indicative of a response to selection.

We used the programming language R, version 3.4.2. We installed RStudio, an integrated development environment (IDE) compatible with R. Mortality rates were compared between populations at generation 19 and at generation 94, after 19 generations of forward selection plus 75 generations of relaxed selection. For each generation (19 and 94), infected and uninfected flies were analyzed separately using Cox proportional hazards models in R. Each model considered survivability as a

function of population replicate, treatment replicate, population, and interaction between treatment replicate and population.

## **IV. RESULTS**

### **Analyzing Generation 19 Data**

In uninfected flies of generation 19, population S had decreased survivability compared to population C ( $p < 0.001$ ). Population replicates 1 and 3 were statistically similar, while replicates 2 and 4 had decreased survivability ( $p < 0.5$ ). Treatment replicate and the interaction between treatment replicate and population were not significant. In infected flies of generation 19, population S had increased survivability compared to population C ( $p < 0.001$ ). Population replicate, treatment replicate, and the interaction between treatment replicate and population were not significant.

### **Applying Model to Generation 94 Data**

In uninfected flies of generation 94, population S had increased survivability compared to population C ( $p < 0.05$ ). Population replicates 1 and 2 were statistically similar, while replicates 3 and 4 had increased survivability ( $p < 0.01$ ). Treatment replicate 3 had increased survivability compared to replicates 1 and 2 ( $p < 0.01$ ). There was also a significant interaction between population S and treatment replicate 3 resulting in decreased survivability ( $p < 0.05$ ). In infected flies, population S had increased survivability compared to population C ( $p < 0.01$ ). Population replicates 1 and 4 were statistically similar, replicate 2 had increased survivability, and replicate 3 had decreased survivability ( $p < 0.01$ ). Treatment replicate and the interaction between treatment replicate and population were not significant.

## **V. DISCUSSION**

Eight fly populations derived from the same outbred ancestor were bred either as controls or for increased resistance to fungal infection. Selection for improved immune defense resulted in a loss to longevity, however, the trade-off between immune defense and longevity

disappeared after roughly 75 generations of relaxed selection. This transient observation of a trade-off that then disappeared, brings up the important question of what actually causes and maintains evolutionary trade-offs.

The initial trade-off between immunity and longevity during fungal resistance selection has been known to affect organisms paradoxically. The enhanced immune response is often associated with a shorter lifespan, perhaps due to the enormous expenditure of energy in developing resistance to a given pathogen (Alonso-Fernández & De la Fuente, 2011). A recent study tested the effects of fungal infection using *B. bassiana* and *M. anisopliae* on two cross-hybrid populations of *D. nasuta* nasuta and *D. nasuta* albomicans, Cytorace- 3 (short-lived) and Cytorace- 9 (long-lived) (Sinam et al., 2016). Cytorace-3 displayed greater resistance and higher tolerance to both fungal species than Cytorace-9, where males had a steeper decline in survivability than females. Additionally, flies from Cytorace-9 were able to tolerate greater levels of oxidative stress than their counterparts, indicating that shorter-lived populations are not able to handle stress as efficiently as longer-lived populations.

The disappearance of the initial trade-off in our research could signify a number of possibilities regarding evolved immune defense in organisms. The initial trade-off from evolving resistance to pathogenic infection could be a result of allocating more resources and energy into immune defense rather than longevity. However, after undergoing relaxed selection, those organisms may not have needed to reallocate as much energy into immune defense as before since they were not actively fighting infection for as many generations as the initial selection period. Therefore, the evolved immune defense is still present without a cost to longevity.

Using diet to curtail the reallocation of resources during the fungal resistance selection period might be one way to address this hypothesis. Supplementing a nutrient-rich diet to populations with evolved immune defenses during infection may redistribute the energy used in immune defense back to longevity. However, other studies have shown that dietary restriction (DR) can extend lifespan of females while limiting their

reproductive output, yet no such changes in longevity were observed in males (Tatar et al., 2011). Those populations, on the other hand, had not been subject to external selection pressures, therefore laboratory selection may alter these findings in future studies. Another possibility is that prior to relaxed selection, stress levels were elevated in the flies due to consistent exposure to pathogenic infection. Therefore, strong selection pressures may have upregulated stress-related genes as a response to infection, leading to reduced life span of the S population. By removing the flies from an ongoing stressful situation during the relaxed selection period, they were able to extend their longevity while maintaining their evolved immune defense. Testing levels of oxidative stress and levels of specific antimicrobial peptides (AMPs) released during the two selection periods is a direct method of answering this possibility in future experiments.

Additionally, even though longevity was no longer a trade-off after relaxed selection, that is not to say there was not a trade-off in other traits such as reproduction, fecundity, stress tolerance, or other immune responses that have not been investigated. Potential trade-offs between larval development and immunity might be areas worth investigating in the S and C populations in the next round of experimentation. Studies outside of our laboratory have shown that trade-offs between longevity and immunity were not apparent after generations of relaxed selection (Gupta et al., 2016). Though the pathogen used in their experiment was not a fungus, infection did not compromise any effect on other traits, similar to our research. We are currently experimenting with populations that have been bred for accelerated development (ACO) and their counterparts (CO) to further investigate the relationship between longevity and immune defense.

Future genomic analyses of these populations will be performed to help answer why the trade-off disappeared to provide greater insight into the role of immune defense in population genomics. These findings could impact what is known in the field of evolution and immunology regarding the impact infection resistance has on behavioral changes and survival in *D. melanogaster*.

## VI. FIGURES AND TABLES

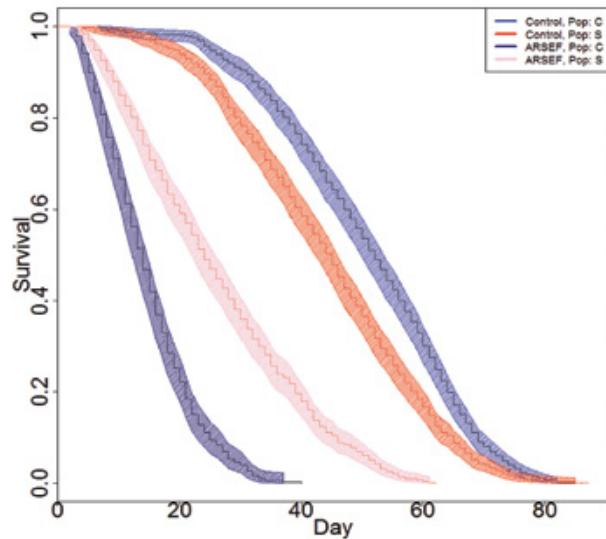


**Figure 1.** Average survivability for infected C population (dark blue), infected S population (pink), uninfected S population (red), and uninfected C population (light blue) in Generation 19. The mean for each group is represented by the central line, and the shaded area represents the 95% confidence interval.

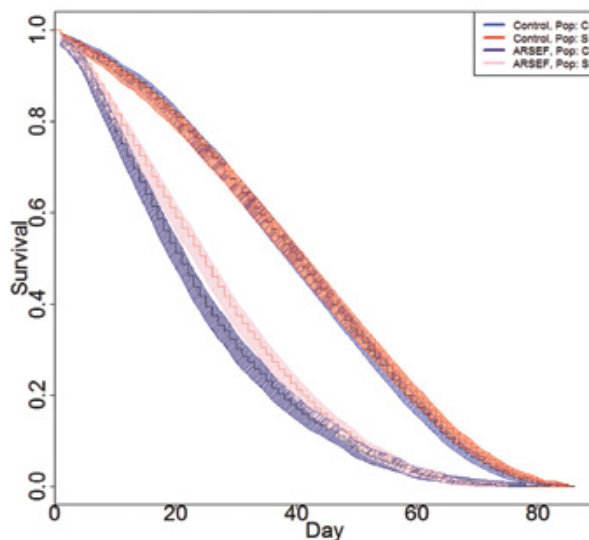


**Figure 2.** Average survivability for infected C population (dark blue), infected S population (pink), uninfected S population (red), and uninfected C population (light blue) in Generation 94. The mean for each group is represented by the central line, and the shaded area represents the 95% confidence interval.

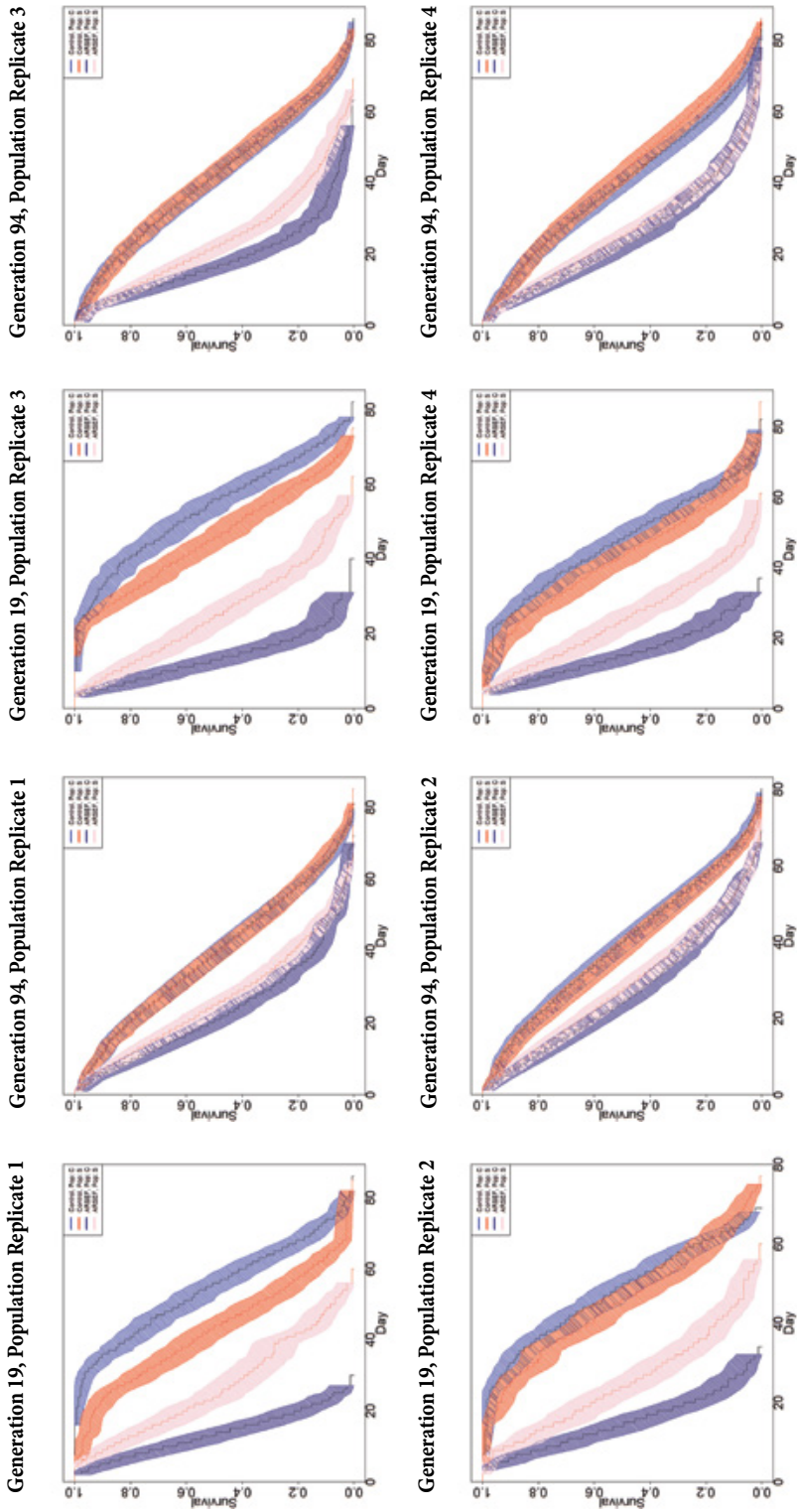


**Figure 3.** Average survivability for infected C population (dark blue), uninfected S population (red), infected C population (pink), and uninfected S population (light blue). Data is shown for the four replicate sets of populations in Generations 19 and 94. The mean for each group is represented by the central line, and the shaded area represents the 95% confidence interval.

## VII. REFERENCES

- Alonso-Fernández, P. & De la Fuente, M. (2011). Role of the immune system in aging and longevity. *Current Aging Science*, 4(2), 78-100.
- Buchon, N., Silverman, N., & Cherry, S. (2014). Immunity in *Drosophila melanogaster* — from microbial recognition to whole-organism physiology. *Nature Reviews Immunology*, 14(12), 796-810.
- Burke, M. K., Barter, T. T., Cabral, L. G., Kezos, J. N., Phillips, M. A., Rutledge, G. A., Phung, K. H., Chen, R. H., Nguyen, H. D., Mueller, L. D. & Rose, M. R. (2016). Rapid divergence and convergence of life-history in experimentally evolved *Drosophila melanogaster*. *Evolution*, 70 (9), 2085–2098.
- Darbro, J. M., Johnson, P. H., Thomas, M. B., Ritchie, S. A., Kay, B. H., & Ryan, P. A. (2012). Effects of *Beauveria bassiana* on Survival, Blood-Feeding Success, and Fecundity of *Aedes aegypti* in Laboratory and Semi-Field Conditions. *The American Journal of Tropical Medicine and Hygiene*, 86(4), 656–664.
- DeVeale, B., Brummel, T., & Seroude, L. (2004). Immunity and aging: the enemy within? *Aging Cell*, 3(4), 195–208.
- Govind, S. (2008). Innate immunity in *Drosophila*: Pathogens and pathways. *Insect Science*, 15(1), 29–43.
- Graves, J.L., Hertweck K. L., Phillips M. A., Han M. V., Cabral L.G., Barter T. T., Greer L.F., Burke M. K., Mueller L.D., & Rose M. R. (2017). Genomics of Parallel Experimental Evolution in *Drosophila*. *Molecular Biology and Evolution*, 34(4), 831–842.
- Gupta, V., Venkatesan, S., Chatterjee, M., Syed, Z. A., Nivsarkar, V., & Prasad, N.G. (2016). No apparent cost of evolved immune response in *Drosophila melanogaster*. *Evolution*, 70(4), 934-943.
- Huang, D.H., Chang, Y.L., Yang, C.C., Pan, I.C., & King, B. (2002). pipsqueak encodes a factor essential for sequence-specific targeting of a polycomb group protein complex. *Molecular and Cellular Biology*, 22(17), 6261-6271.
- Nguyen, J., Thornburg, M., Khanbijian, S., Wood, R., Ramezan, R., & Shahrestani, P. (2017). Evolved immune response of *Drosophila melanogaster* to entomopathogenic fungus *Beauveria bassiana*. *Dimensions* 19, 26-33.
- Pandey U. B. & Nichols C.D. (2011). Human disease models in *Drosophila melanogaster* and the role of the fly in therapeutic drug discovery. *Pharmacological Reviews*, 63(2), 411–436.
- Sinam, Y., Chatterjee, A., Ranjini, M., Poojari, A., Nagarajan, A., Ramachandra, N., & Nongthombam, U. (2016). A newly evolved *Drosophila* Cytorace-9 shows trade-off between longevity and immune response. *Infection, Genetics and Evolution*, (44), 1-7.
- Ragavendran, C., Dubey, N., & Natarajan, D. (2017). *Beauveria bassiana* (Clavicipitaceae): a potent fungal agent for controlling mosquito vectors of *Anopheles stephensi*, *Culex quinquefasciatus* and *Aedes aegypti* (Diptera: Culicidae). *RSC Advances*, 7(7), 3838-3851.
- Tatar M. (2011). The plate half-full: Status of research on the mechanisms of dietary restriction in *Drosophila melanogaster*. *Experimental gerontology*, 46(5), 363-368.
- Wiberg R.A.W., Gaggiotti O.E., Morrissey M.B., & Ritchie M.G. (2017). Identifying consistent allele frequency differences in studies of stratified populations. *Methods in Ecology and Evolution*, 8(12), 1899–1909.
- Zhang, L., & Gallo, R. (2016). Antimicrobial peptides. *Current Biology*, 26(1), R14-R19.

# Gonadal Development of the Black-belly Dragonfish (*Stomias atriventer*)

Sean Zulueta and Kristy Forsgren, Ph.D.

Advisor: Kristy Forsgren, Ph.D.

Department of Biological Science, California State University, Fullerton

## ABSTRACT

The black-belly dragonfish (*Stomias atriventer*) is a mesopelagic species that has a geographic range in the eastern Pacific Ocean. Aspects of dragonfish life history have been described including general morphology and behavior, biomechanics, and larval development. However, little is known about the reproductive biology of this infrequently observed mesopelagic fish. In the current study, we sampled gonadal tissues from black-belly dragonfish to describe gamete development. Museum specimens were examined, and fish were caught via mid-water trawls onboard the R/V Yellowfin. The ovaries and testes were dissected, preserved in Bouin's fixative, and histologically processed using paraffin wax. We determined the volume of ovarian follicles of various stages of development: primary ovarian follicles were  $0.1193 \pm 0.008 \text{ mm}^3$ , secondary ovarian follicles were  $1.06 \pm 0.083 \text{ mm}^3$ , and tertiary ovarian follicles were  $5.93 \pm 0.35 \text{ mm}^3$ . The ovary consisted of  $62.8 \pm 5.40\%$  primary ovarian follicles,  $26.3 \pm 2.47\%$  secondary ovarian follicles, and  $10.9 \pm 4.55\%$  tertiary ovarian follicles. The testes contained primary and secondary spermatocytes that were  $21.7 \pm 2.80 \mu\text{m}^3$ , spermatids were  $3.49 \pm 0.45 \mu\text{m}^3$ , and spermatozoa were  $3.57 \pm 0.46 \mu\text{m}^3$ . Most of the testes were composed of spermatids ( $76.9 \pm 4.31\%$ ), but also contained spermatocytes ( $13.5 \pm 2.95\%$ ), and mature sperm ( $9.65 \pm 2.48\%$ ). Ovarian follicle development resembled other teleost fish reproduction. The presence of multiple stages of ovarian follicles and sperm development indicates the black-belly dragonfish are batch spawning fish and have an asynchronous ovarian development pattern. Supplemental fish and seasonal data are needed to understand the gonadal development of mesopelagic fish.

## INTRODUCTION

The black-belly dragonfish (*Stomias atriventer*; Order Stomiiformes) is an infrequently studied mesopelagic fish. The ray-finned fish has unique teeth configurations, hexagonal scales, photophore across the body, and extended light barbel below the jaw that make the dragonfish a distinctive animal (Gibbs 1969). Other research on the biomechanics of the jaw has shown information about the morphology and efficiency of consuming similar sized fish (Schnell and Johnson 2017). The black-belly dragonfish also has a diel vertical migration pattern and is distributed at depths <100-1500 meters (Gibbs 1969), classifying the animal as a mesopelagic fish. The geographic range of the dragonfish is along the coast of California, USA to Baja California, Mexico and the equator to northern Chile (Moser 1996). The general morphology and some of the unique attributes of the Family Stomiidae have been previously described, however, the reproductive biology of dragonfish has limited information. After fertilization, the smooth egg of the black-belly dragonfish will grow to a diameter of 0.88-0.92 mm and include a diagnostic feature of a segmented yolk (Moser 1996). The slender, elongated larvae hatch at a length of 2-3 mm and are characterized by the elongated straight gut and paired fins that form at transformation (Moser 1996). During the California Cooperative Oceanic Fisheries Investigations (CalCOFI) surveys, the planktonic eggs and larvae were present throughout the year. The peak of the larvae presence occurred in the February and September months (Moser 1996).

Reproductive biology is not highly studied in mesopelagic fish. The information of post-fertilization and development is available for the black-belly

dragonfish. However, there is no information on the gonadal development. We had the opportunity to describe the ovarian and testicular gonadal development of six mesopelagic dragonfish, which leads to a better understanding of the degree of ecological importance.

## MATERIALS AND METHODS

Black-belly dragonfish (*Stomias atriventer*) were collected in southern California. Fish were collected using an Isaac Kidd Midwater Trawl net with wing width of 10 ft and a 1 mm mesh cod end onboard R/V Yellowfin to a depth of 550 meters and was deployed two-thirds of the way across the San Pedro Channel for 1-2 hours in the evening. Fish were euthanized using an overdose of tricaine methanesulfonate (MS-222) of purity at least 98% (1g:5000ml seawater). Standard length (SL) to the nearest mm and weight (g) were recorded. Gonadal tissue was dissected from the body cavity and total gonadal length was determined to the nearest mm and weighed to the nearest 0.0001 mg.

Gonadal tissues were placed in Bouin's fixative for 48 hours, then transferred to 70% ethanol until histological processing. Specimens from the Los Angeles County Museum of Natural History were dissected, and a small portion of the gonadal tissue was removed for histological analysis. Fixed gonadal fragments (from the middle portion of the gonad) were dehydrated in a series of graded ethanols, cleared with xylene, and infiltrated and embedded in paraffin wax. Gonadal tissues were sectioned using a rotary microtome to a thickness of 5  $\mu\text{m}$  and mounted on glass microscope slides. Tissue sections were stained with hematoxylin and eosin stains. Tissues were examined using a bright-field microscopy (Olympus BX60) and photographed using a digital camera (QICAM QImaging Fast 1394, QImaging) mounted to the microscope and imaging software (Q-Capture Pro 7, QImaging 2010).

The diameter ( $\mu\text{m}$ ) of gametes was measured using ImageJ software (version 1.51j8, National Institutes of Health). Only ovarian follicles and sperm cells that appeared to be sectioned through the approximate

center of the nucleus were measured. Three diameter measurements were recorded. The mean of the diameter measurements was used to calculate the volume [ $V = (4/3) \pi r^3$ ]. The reproductive phases of female and male dragonfish were determined based on the developmental stage of the gonad as previously established for fish (Brown-Peterson et al. 2011).

### Ovarian Follicle Morphology

Ovarian follicles were staged based on morphological characteristics previously established for teleost oogenesis (Wallace and Selman 1981, Nagahama and Yamashita 1983, Guraya 1986, Wallace and Selman 1990). The following developmental characteristics used to categorize ovarian follicles: (1) primary ovarian follicle characterized by the numerous nucleoli; (2) secondary ovarian follicle identified by the presence of cortical alveoli present throughout the ooplasm; (3) tertiary ovarian follicle characterized by the presence of vitellogenin and egg yolk proteins. The diameters of the ovarian follicles were measured to the nearest 0.001  $\mu\text{m}$ ; three measurements for each ovarian follicle were obtained, and the mean of the measurements was recorded. At least 15 ovarian follicles of each developmental stage were determined by classifying, counting, and calculating the percentage of all follicles in 2-3 tissue sections per female representing tissue collected from the middle portion of the ovary.

### Sperm Cell Morphology

Sperm cells were staged based on morphological characteristics previously established for teleost spermatogenesis (Grier 1981, Schulz et al. 2010, Uribe et al. 2014). Sperm cells were categorized based on size and developmental characters as follows: (1) spermatocytes characterized by relatively larger size; (2) spermatids stained all purple and of smaller size; (3) spermatozoa identified by smaller size and presence of a flagella. The diameters of the sperm cells were measured to the nearest 0.001  $\mu\text{m}$ ; three measurements for each sperm cell were obtained and the mean of the measurements

was recorded. 30 sperm cells of each developmental stage was determined by classifying, counting, and calculating the percentage of area within the micrograph of each stage of sperm development divided by the total area of the micrograph.

## STATISTICAL ANALYSIS

A single experimenter determined stages and measured gametes in an effort to maintain consistency of classification. A second observer confirmed stages and measurements. To determine statistical differences between gamete diameters and percent composition, a one-way analysis of variance (ANOVA) followed by a Tukey's post hoc multiple means comparison test was performed (Prism 7 version 7.03, GraphPad Software, Inc. 2017). The level of significance was determined at  $p<0.05$ .

## RESULTS

### Ovarian Morphology

One dragonfish was caught in October 2016 ( $n=1$ ) was 212 mm SL and weighed 24.4 g. The ovaries were 163 mm TL and weighed 0.857 g with a GSI of 3.51%. Dragonfish from the Los Angeles County Museum of Natural History ( $n=4$ ) were  $187.4 \pm 20.7$  mm SL (mean  $\pm$  standard deviation) and weighed  $16.7 \pm 6.9$  g. In order to preserve the integrity of the animal as much as possible a portion of the ovary was removed for histological analysis; therefore, an ovarian weight was not obtained.

The diameters of ovarian follicles of dragonfish at the primary, secondary, and tertiary stages were significantly different ( $p<0.0001$ ). Primary ovarian follicles were  $51.34 \pm 1.06$   $\mu\text{m}$  (mean  $\pm$  SEM; size range 11.62-135.25  $\mu\text{m}$ ), secondary ovarian follicles were  $113.22 \pm 2.15$   $\mu\text{m}$  (size range 42.58-292.40  $\mu\text{m}$ ), and tertiary ovarian follicles were  $214.08 \pm 4.51$   $\mu\text{m}$  (size range 97.95-311.05  $\mu\text{m}$ ) in diameter. The volume of the primary ovarian follicles were  $0.1193 \pm 0.008$   $\text{mm}^3$  (mean  $\pm$  SEM), secondary ovarian follicles were 1.06

$\pm 0.083$   $\text{mm}^3$ , and tertiary ovarian follicles were  $5.93 \pm 0.35$   $\text{mm}^3$  (Fig. 2). The volumes of ovarian follicles at the primary, secondary, and tertiary stages were significantly different ( $p<0.0001$ ).

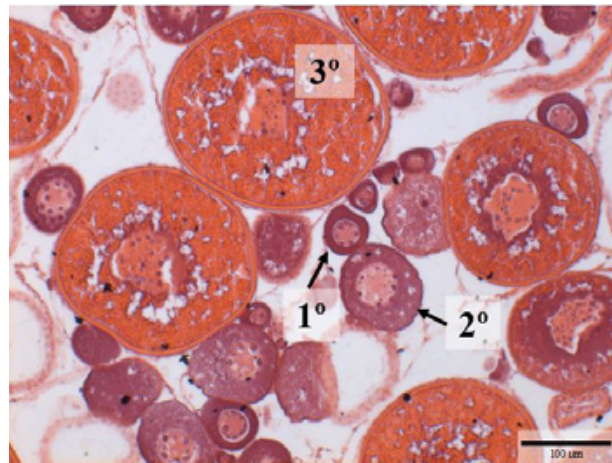


**Figure 1.** Cross section of black-belly dragonfish (*Stomias atriventer*) ovarian tissue; 10x magnification. (A) Primary ovarian follicle stage; (B) secondary ovarian follicle stage; (C) tertiary ovarian follicle stage.

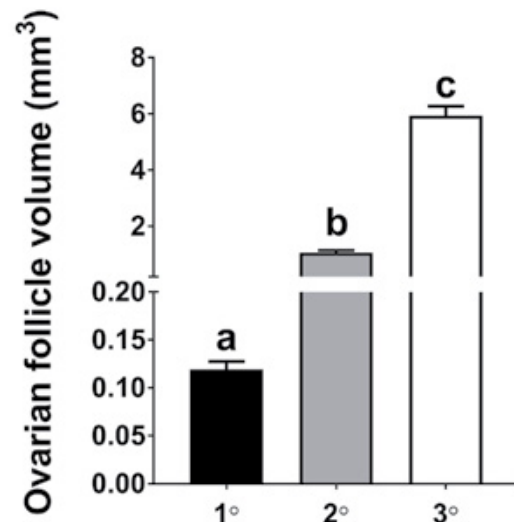


**Figure 2.** Black-belly dragonfish ovarian follicle volumes ( $n=790$  ovarian follicles measurements from five individuals;  $p<0.0001$ ). Different letters indicate significant differences between ovarian follicle stages. Data represented as mean  $\pm$  standard error of the mean.

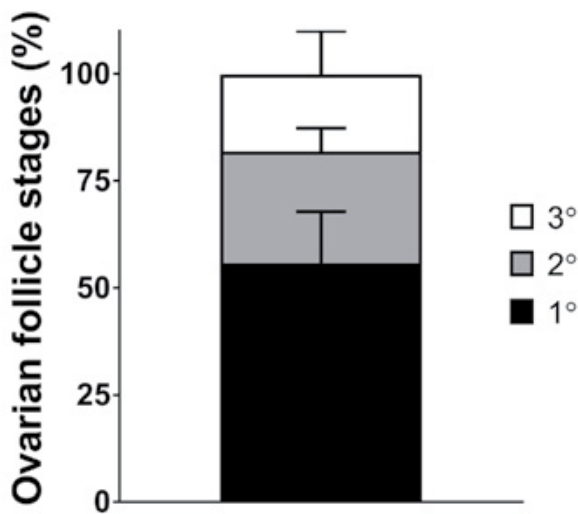


**Figure 3.** Percent composition of each stage of ovarian development of black-belly dragonfish ( $n=5$ ). Error bars represent the standard deviation.

The percent composition of ovarian follicles at the primary, secondary, and tertiary stages were significantly different ( $p<0.0001$ ). Dragonfish ovaries consisted of  $62.8 \pm 5.40\%$  primary ovarian follicles,  $26.3 \pm 2.47\%$  secondary ovarian follicles, and  $10.9 \pm 4.55\%$  tertiary ovarian follicles ( $n=5$ ; Fig. 3).

Three of the dragonfish were determined to be in the developing stage of reproduction ( $n=1$  freshly caught,  $n=2$  museum specimens). Two dragonfish were in the immature stage of reproduction ( $n=2$  museum specimens).

#### Sperm Cell Morphology

One dragonfish was caught in October 2016 ( $n=1$ ) was 126.0 mm SL and weighed 4.7 g. The testes were 97.0 mm TL and weighed 0.1111 g with a GSI of 2.36%. The diameters of spermatocytes and spermatids, and spermatocytes and spermatozoa of dragonfish were significantly different ( $p<0.0001$ ). The diameters of spermatids and spermatozoa of dragonfish were not significantly different ( $p=0.8452$ ). The spermatocytes were  $3.41 \pm 0.06 \mu\text{m}$  (mean  $\pm$  SEM; size range 2.45–4.61  $\mu\text{m}$ ), spermatids were  $1.86 \pm 0.03 \mu\text{m}$  (size range

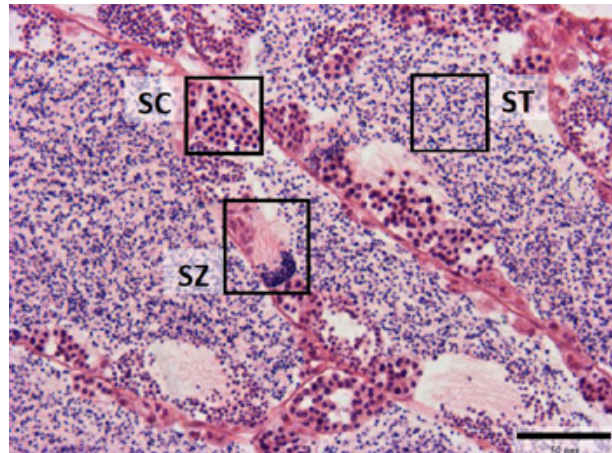


**Figure 4.** Cross section of black-belly dragonfish (*Stomias atriventer*) testicular tissue; 20x magnification. Abbreviations: SC, spermatocyte; ST, spermatid; SZ, spermatozoa.

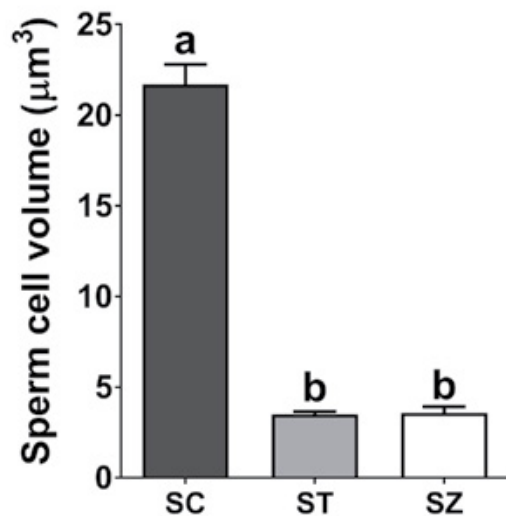


**Figure 5.** Black-belly dragonfish sperm volumes ( $n=180$  sperm cells measurements from one individual;  $p<0.0001$ ). Different letters indicate significant differences between ovarian follicle stages. Data represented as mean  $\pm$  standard error of the mean.

1.41–2.46  $\mu\text{m}$ ), and spermatozoa were  $1.82 \pm 0.05 \mu\text{m}$  (size range 1.30–3.25  $\mu\text{m}$ ) in diameter. The volume of the spermatocytes were  $21.7 \pm 1.10 \mu\text{m}^3$  (mean  $\pm$  SEM), spermatids were  $3.48 \pm 0.17 \mu\text{m}^3$ , and spermatozoa were  $3.57 \pm 0.34 \mu\text{m}^3$  (Fig. 5). The volume of sperm cells at the

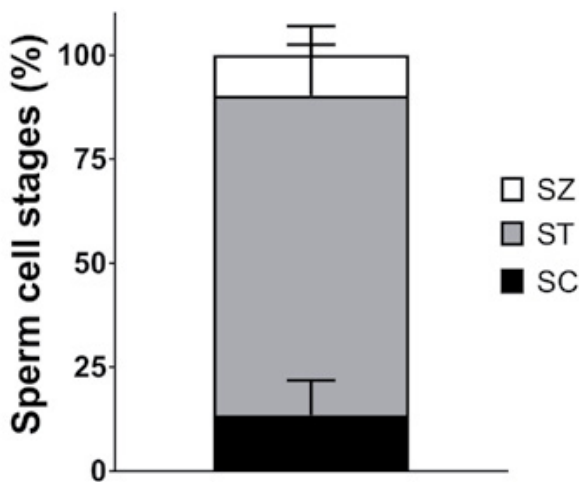


**Figure 6.** Percent composition of each stage of sperm development of black-belly dragonfish ( $n=1$ ). Error bars represent the standard deviation.

spermatocyte and spermatids, and spermatocytes and spermatozoa of dragonfish were significantly different ( $p<0.0001$ ). The volume of spermatids and spermatozoa of dragonfish were not significantly different ( $p=0.996$ ).

The percent composition of sperm at the spermatocyte and spermatid, and at the spermatid and spermatozoa were significantly different ( $p<0.0001$ ). The percent composition of sperm at the spermatocyte and the spermatozoa stage of sperm development was not significantly different ( $p=0.7002$ ). Dragonfish testes consisted of  $13.48 \pm 2.95\%$  (mean  $\pm$  SEM) spermatocytes,  $76.88 \pm 4.31\%$  spermatids, and  $9.65 \pm 2.49\%$  spermatozoa ( $n=1$ ; Fig. 6). One dragonfish was determined to be in the developing stage of reproduction ( $n=1$ ).

## DISCUSSION

This study is the first to describe black-belly dragonfish (*Stomias atriventer*) ovarian follicle and sperm development. In the fish examined, three distinctive stages of ovarian follicle development were described. Ovarian development appears to be similar to previously described teleost fish (Wallace and Selman 1981, Nagahama and Yamashita 1983).

Ovarian development in one other mesopelagic species, the oceanic lightfish (*Vinciguerria nimbaria*), has been examined (Stequet 2003). Compared to the black-belly dragonfish, the lightfish is smaller in length (4.2 cm SL). However, the lightfish and dragonfish exhibited similar sized ovarian follicles (i.e., primary, secondary, and tertiary development). The dragonfish and lightfish have similar ovary composition that consisted of multiple ovarian follicle stages (i.e., primary, secondary, and tertiary) in each mature individual. Diameters of dragonfish ovarian follicles encompass the type 2-3c (120-320  $\mu\text{m}$  in diameter) stages of ovarian development examined in lightfish (Stequet 2003).

Reproductive development has been examined in an epimesopelagic species, the oarfish (*Regalecus russellii*; Forsgren et al. 2017). Like the dragonfish, the oarfish has an elongated, eel-like body but has a maximum standard length of 8 m. The dragonfish and oarfish have similar stages in ovarian follicle development (i.e., primary, secondary, and tertiary development; Forsgren et al. 2017). The diameters of ovarian follicles in the dragonfish are larger relative to the oarfish (41-153  $\mu\text{m}$  in diameter; Forsgren et al. 2017). However, the dragonfish ovarian follicle diameters have a wider range that overlaps into multiple ovarian follicle stages of reproductive development in the oarfish. Diameters of dragonfish ovarian follicles encompass the perinuclear and cortical alveoli stage of ovarian development examined in oarfish (Forsgren et al. 2017).

Reproductive maturity was characterized based on the ovarian follicle advancement to tertiary ovarian follicles. Two dragonfish were reproductively immature based on the absence of tertiary ovarian follicles. Three dragonfish were reproductively mature because the ovaries consisted of all stages of ovarian follicle development (i.e., primary, secondary, and tertiary). The size of the dragonfish showed a pattern of sexual maturity. The immature dragonfish ( $n=2$ ) were smaller in length ( $166.0 \pm 4.24$  mm; mean  $\pm$  standard deviation) compared to the sexually mature dragonfish ( $n=3$ ;  $201.7 \pm 9.07$  mm).

Male dragonfish are likely rare to collect. We can infer that sperm development is similar across individuals. The sperm cell morphology showed similar developmental characteristics of other teleost fish (Uribe et al. 1981). The sperm cell diameter ( $p<0.0001$ ) and volume significantly ( $p<0.0001$ ) decreased in size from meiotic division during the transition from spermatocytes to spermatids. The continuing of spermatogenesis of the spermatids to spermatozoa were not significantly different in sperm diameter ( $p=0.845$ ) and sperm volume ( $p=0.996$ ). The main morphological difference between spermatids and spermatozoa was the development of flagella in the spermatozoa. The one male dragonfish had three stages of sperm development, including spermatocytes, spermatids, and spermatozoa. The male dragonfish was sexually mature and in the spawning phase of spermatogenesis based on the presence of secondary spermatocytes, spermatids, and spermatozoa (Brown-Peterson 2011).

The mature dragonfish caught in August, May, and October provided some insight on seasonality of mid-water reproductive development. The ovaries of dragonfish consisted of mostly of primary ovarian follicles followed by secondary and tertiary ovarian follicles, respectively. The multiple stages of ovarian follicle development support the hypothesis that the black-belly dragonfish is a batch spawning species. Unlike total spawners, ovarian follicle composition in batch spawning is determined based on how quickly the gamete develops and goes through vitellogenesis (Brown-Peterson 2011).

The lightfish (Stequert 2003) and oarfish (Forsgren et al. 2017) are hypothesized to be batch spawning species, and the dragonfish resembles similar gonadal development patterns. Like the lightfish and the oarfish, the dragonfish exhibited multiple stages of ovarian follicle and sperm development in each mature individual. Previous studies have collected dragonfish (Moser 1996) and lightfish larvae (Stequert 2003) throughout the year in multiple mid-water trawls. Evidence of dragonfish and light fish larvae in year-

round trawls supports the hypothesis that dragonfish are batch spawning species and show asynchronous development.

We had the rare opportunity to investigate the reproduction of mesopelagic a fish. The vertical distribution and environment at which dragonfish are collected make studying mesopelagic fish difficult to further investigate. Based on the six dragonfish examined, we have determined that black-belly dragonfish exhibit asynchronous patterns of gonadal development and are batch spawning fish. Additional dragonfish specimens and seasonal data are needed to make further conclusions on the seasonal reproductive biology.

## ACKNOWLEDGEMENTS

We thank the Southern California Ecosystems Research Program (SCERP) for funding our research under the National Science Foundation (URM-DBI 1041203) and the CSUF Department of Biological Science, especially Steve Karl and Drs. Misty Paig-Tran and Ryan Walter. We would also like to thank the Southern California Marine Institute and the R/V Yellowfin staff, Rick Feeney and the Los Angeles Museum of Natural History, Dr. Kimo Morris from Santa Ana College, the CSU Council on Ocean Affairs, Science and Technology. We also thank Homam Jamal, Evelyn Bond, Justin Stuart, Jacob Javier, Alison Cover, Holly Suther, and Griselda Lezo for their assistance and support in the lab.

## REFERENCES

- Brown-Peterson, N.J., Wyanski, D.M., Saborido-Rey, F., Macewicz, B.J., Bowerre-Barbieri, S.K. (2011). A standardized terminology for describing reproductive development in fishes. *Marine and Coastal Fisheries*, 3(1), 52-70.
- Forsgren, K. L., Jamal, H., Barrios, A., and Paig-Tran, E.W. M. (2017). Reproductive Morphology of Oarfish (*Regalecus russellii*). *The Anatomical Record*, 300, 1695–1704.
- Gibbs, R., and Smithsonian Institution. (1969). Taxonomy, sexual dimorphism, vertical distribution, and evolutionary zoogeography of the bathypelagic fish genus *Stomias* (Stomiidae). *Smithsonian Contributions to Zoology*, 31, 1-25.

- Grier, H. J. (1981). Cellular organization of the testis and spermatogenesis in fishes. *American zoologist*, 21(2), 345-357.
- Guraya, S.S. (1986). The cellular and molecular biology of fish oogenesis. *Monographs in developmental biology*, 18, 1-223.
- Moser, H.G. (1996). Stomiidae: Scaly dragonfish. In: *The early stages of fishes in the California current region*, 301-303.
- Nagahama, Y., and Yamashita, M. (2008). Regulation of oocyte maturation in fish. *Development, Growth and Differentiation*, 50, S195-S219.
- Schnell, N.K., and Johnson, G.D. (2017). Evolution of a Functional Head Joint in Deep-Sea Fishes (Stomiidae). *PLoS ONE*, 12(2), e0170224.
- Schulz, R. W., Renato de Franca, F., Lareyre, J., LeGac, F., Chiarini-Garcia, H., Nobrega, R. H., Miura, T. (2010). Spermatogenesis in fish. General and Comparative Endocrinology, 165, 390-411.
- Stequet, B., Mernard, F., and Marchal, E. (2003). Reproductive biology of *Vinciguerria nimbaria* in the equatorial waters of the eastern Atlantic Ocean. *Journal of Fish Biology*, 62(5), 1116-1136.
- Sutton, T., and Hopkins, L. (1996). Trophic ecology of the stomiid (Pisces: Stomiidae) fish assemblage of the eastern Gulf of Mexico: Strategies, selectivity and impact of a top mesopelagic predator group. *Marine Biology*, 127(2), 179-192.
- Uribe, M. C., Grier, H. J., and Mejia-Roa, V. (2014). Comparative testicular structure and spermatogenesis in bony fish. *Spermatogenesis*, 4(3).
- Wallace, R., and Selman, K. (1981). Oocyte Growth and Recruitment in Teleosts. *BioScience*, 31(4), 323-324.
- Wallace, R., and Selman, K. (1990). Ultrastructural Aspects of Oogenesis and Oocyte Growth in Fish and Amphibians. *Journal of Electron Microscope Technique*, 16, 175-201.

# **No Apparent Effect of Elevated Atmospheric CO<sub>2</sub> On Growth Response or Competition Between Native and Non-Native California Grasses in a Growth Chamber Study**

**Tilly M. Duong, Kyle L. Gunther, Jillian J. Stephens, Darren R. Sandquist, Ph.D., and Joel K. Abraham, Ph.D.  
Advisor: Joel K. Abraham, Ph.D.**

*Department of Biological Science, California State University, Fullerton*

## **ABSTRACT**

Global levels of atmospheric carbon dioxide (CO<sub>2</sub>) have increased, and are predicted to continue increasing, due to human activities. Although many studies have evaluated species-specific responses to atmospheric CO<sub>2</sub>, not enough is known about how specific plant species interactions are projected to change, especially in the context of plant invasions. Certain traits of non-native plants, such as fast growth and preemption of resources, may lead to greater competitive advantages over existing native plants. Alternatively, increased atmospheric CO<sub>2</sub> may minimize impacts of competition. In this study, we performed a growth chamber experiment to test the hypothesis that elevated atmospheric CO<sub>2</sub> conditions increase the competitive ability of non-native California grasses. We grew two California native grasses, *Stipa pulchra* (purple needlegrass) and *Festuca californica* (California fescue), and two non-native grasses, *Festuca arundinacea* (tall fescue) and *Lolium multiflorum* (Italian rye grass) in monoculture or in competition with all other grasses, across two CO<sub>2</sub> concentrations (ambient [~361 ppm] and elevated [~476 ppm]) in environmental growth chambers. We measured plant height weekly and final shoot dry biomass. At the concentrations used in the study, our preliminary results indicate elevated CO<sub>2</sub> levels did not increase the average biomass or plant height of Italian rye grass, but may increase shoot height in tall fescue under interspecific competition. Relative to the monoculture treatment, all species of grasses showed decreased plant height and dry biomass when under interspecific competition. Analysis of the data is ongoing, and complementary projects to measure temperature and precipitation effects on native and non-native grass competition are underway. It is our hope that this suite of studies may help better predict impacts of climate change on California grassland systems.

# **Intestinal Barrier Dysfunction as a Possible Predictor of Death in *Drosophila melanogaster***

**Yasamin Hajy Heydary and Sabeeeca Vadakkan**

**Advisor: Parvin Shahrestani, Ph.D.**

*Department of Biological Science, California State University, Fullerton*

## **ABSTRACT**

The life history of *Drosophila melanogaster* populations and physiological processes that occur across it have long been an area of high interest to researchers. As aging occurs, many physiological processes and phenotypic characteristics begin to degrade. However, researchers have recently identified another phase of life, in which the degradation of characteristics, such as fecundity and virility, increases rapidly, regardless of chronological age, with the occurrence of death right afterward. This stage, called the death spiral, can have various implications in future studies to help researchers understand what causes death and what physiological changes occur when individuals are near death. In this experiment, we explore intestinal barrier dysfunction as a possible predictor of death approaching, with the ultimate goal to evaluate the gut microbiota of dying flies and same-aged flies that are not dying. One rationale behind intestinal barrier dysfunction as a sign of death spiral considers the point that intestinal microbiota can leak into the rest of the body, with deleterious effects to its immune and digestive systems. Previous studies have implemented a technique called Smurfing, in which flies are fed a blue dye and observed for dye bleeding, to identify when gut barrier degradation is taking place. We hypothesized that Smurfing would be a possible technique to identify when death spiral would occur, since flies were previously reported to die within one day of dye bleeding from the gut. In coordination with the Mueller Lab at UC Irvine, two populations of flies were treated with six different blue dyes added to banana-molasses food (SPS Alfachem Blue, Sigma Aldrich, Spectrum Blue, Flavors & Color Blue, Chemistry Connection, Electric Blue, Regular Food) and a control group was given regular banana-molasses food. The mortality of flies treated with blue dyes along with the mortality of their controls were checked daily. Based on graphs, it was found that flies that were fed any of the six blue dyes died at a faster rate than the controls, and that not all the flies Smurfed before dying. Furthermore, by analyzing the data on the effect of each dye on each population, it was established that the dye that results in the most Smurfing in the ACO population (SPS Alfachem Blue) does not work effectively on the CO population. Our results are not necessarily indicative of gut barrier degradation being independent of death spiral, because there is a possibility that the Smurfing technique could have been flawed and is not reliable for identifying gut barrier degradation. Nevertheless, we demonstrated that the Smurf assay is not an effective assay for identifying flies that are in the death spiral. Therefore, the Smurf assay cannot be used to reliably separate flies that are in the death spiral from same-aged flies that are not in the death spiral. Several previous studies have successfully used a measure of female reproduction, fecundity, to identify flies that are in the death spiral. Therefore, our future research will use fecundity as an indicator of death spiral to compare the gut microbiota composition of flies that have entered the death spiral to the gut microbiota composition of same-aged flies that have not entered the death spiral.

## **Probing Rare Earth Concentration Quenching in Doubly Ordered Double Perovskites**

**Aida Dadashzadeh**

**Advisor: Allyson M. Fry-Petit, Ph.D.**

*Department of Chemistry and Biochemistry, California State University, Fullerton*

### **ABSTRACT**

This research project involves the synthesis of rare earth cation doped doubly ordered double perovskites,  $\text{NaLaMnWO}_6$  and  $\text{NaNdMnWO}_6$ , for potential use in luminescent materials. This project works to understand the correlation between crystal structure and concentration quenching that is present in luminescence materials. This will allow for the optimization of efficient white light production in light emitting diodes (LEDs). Solid-state methods including, heating under reducing atmospheres, are being used to synthesize these compounds. To ensure that the correct compounds are being made, X-ray Diffractions (XRD) patterns are run after each heating. Results show that the compounds have been synthesized—this has been evidenced through XRD patterns and Ultraviolet-Visible (UV-Vis) Diffuse Reflectance analysis. Future work includes the analysis of varying ratios of cerium and europium in conjunction to the lanthanum and neodymium to analyze the effect of rare earth concentration on the luminescence. The initial reaction conducted was for the formation of  $\text{NaLa}_{0.97}\text{Ce}_{0.03}\text{MnWO}_6$ ,  $\text{NaNd}_{0.97}\text{Ce}_{0.03}\text{MnWO}_6$ , and  $\text{NaLa}_{0.97}\text{Ce}_{0.03}\text{MnWO}_6$ ,  $\text{NaNd}_{0.97}\text{Ce}_{0.03}\text{MnWO}_6$  that have been tested and proven plausible. This means that lanthanides such as cerium and europium can be used in place of the lanthanum and neodymium A sites without greatly altering the crystal structure.

# **Understanding How Two Similar Rna Binding Domains Of Paralogous Proteins Mediate Different Protein-Protein Interactions**

**Collin M. Marshall and Jeffrey Pina**

**Advisor: Niroshika M. Keppetipola, Ph.D.**

*Department of Chemistry & Biochemistry, California State University, Fullerton*

## **ABSTRACT**

Polypyrimidine Tract Binding Protein (PTBP) is an RNA binding protein that has a high affinity for pyrimidine rich regions of RNA sequences. Studies have shown that it acts primarily as a negative regulator of alternative pre-mRNA splicing events (ASEs); however, it has been shown in some cases to enhance ASEs. Improper regulation of ASEs is linked to neurodegenerative diseases and cancer. Two well studied paralogs of PTBP are PTBP1 and PTBP2. The two proteins share 74% amino acid sequence identity and share a similar domain arrangement consisting of four RNA recognition motifs (RRMs) connected by three linker sequences and an N-terminal region. Nevertheless, the paralogs are localized in distinct tissue types and exert different splicing outcomes on certain regulated exons in which PTBP1 acts as a more potent repressor of alternative splicing than PTBP2. This difference in splicing activity coupled with their expression patterns plays a critical role in neuronal development and maturation. Neuronal progenitors express PTBP1, however during differentiation the expression of PTBP1 decreases and the expression of PTBP2 is induced. This results in a change in the neuronal splicing program in which exons repressed by PTBP1 are now included in the mRNA transcripts. A second shift in the splicing program occurs during neuronal maturation in which the level of PTBP2 is decreased. Collectively, these changes in protein concentration result in modulated regulation of alternative splicing programs critical for neuronal differentiation and maturation. How these two related proteins exert different splicing outcomes is not well understood. Recent studies generating chimeras of the two proteins demonstrated that multiple regions of PTBP1 can confer splicing repression activity when integrated in the PTBP2 backbone. These studies also highlighted that despite the high amino acid sequence identity, the RRM 2 region of the two proteins demonstrate different affinities for a partner protein, Raver 1. The PTBP1-Raver1 interaction motif has been identified, and within their respective Raver1 interaction motifs, PTBP1 and PTBP2 share 87% amino acid sequence identity. These results suggest that additional factors such as post-translational modifications (PTMs) might influence protein-protein interactions, and in turn, splicing repression activity. To test this, we assayed PTBP1 RRM2 for PTMs via immunoprecipitation followed by mass spectrometry and have identified several ubiquitin modifications. Our current goal is to determine the type of ubiquitination that is found to occur by western blot analysis. In addition, we have detected differences in phosphorylation in the linker regions adjacent to the RRM2 domain between the two paralogs by mass spectrometry and plan to test the importance of these differences in contributing to partner protein interactions by mutagenesis analysis.

*Keywords: RNA binding proteins, protein interactions and binding, protein modifications*

*This work was supported by a Maximizing Access to Research Careers grant to CSUF from the National Institutes of Health [5T34GM008612-21]*

# Adsorption Potential Energy of Ascorbic Acid Enantiomers on Pd (111)

Jacqueline Estrada

Advisor: Michael Groves, Ph.D.

Department of Chemistry and Biochemistry, California State University, Fullerton

## ABSTRACT

Ascorbic Acid (AA), commonly known as vitamin C, can be used as an alternative fuel for direct oxidation of fuel cells. AA oxidation has been shown to be effective on Pd electrocatalysts in acidic fuel conditions; however, recent studies have demonstrated that it is a more efficient fuel in alkali media. In AA, there are two chiral centers occurring at two adjacent carbon atoms resulting in four stereoisomers. In this study, the stereoisomers of AA were computationally simulated on Pd (111) at different atomic positions to understand the intermolecular interactions between the molecules and the catalyst, Pd. Density functional theory (DFT) was used to determine the adsorption potential energy and stability of AA stereoisomers on Pd (111). D-Ascorbic acid (S, R) had the highest adsorption potential energy (APE) of -1.76 eV followed by isoascorbic acid (S, S), L- ascorbic acid (R, S) and finally erythorbic acid (R, R) with the lowest APE of -1.38. eV. AA molecules were most stable when specific OH species bonded to the Pd surface on top of a Pd atom. The orientation of the OH species on AA molecules was dependent on chirality and consequently affected the adsorption potential energy on Pd (111). Chirality is an important factor to consider not only in AA acid but also in the next generation of fuels.

## INTRODUCTION

A fuel cell is like a battery; however, unlike a battery, it must be supplied with a continuous fuel and oxygen to maintain ongoing electrochemical reactions (Nice and Strickland, 2000). Some fuel cells use hydrogen or a hydrogen rich molecule as fuel. Many different types of fuel cells have been designed and like all electrochemical systems, they all comprise of an electrolyte, an anode,

and a cathode as shown in Figure 1. The fuel is supplied to the anode and oxygen to the cathode. A catalyst is present at the anode which oxidizes the fuel into protons and electrons. The electrons flow through a circuit, generating an electrical current (Nice and Strickland, 2000). Fuel cells have the capacity to power small electronic devices and even utility power stations (Nice and Strickland 2000).

Fuel cells are characterized by the type of fuel they require, the type of electrolyte, types of catalysts and other conditions such as pH and temperature (Cui et al., 2009) Many fuel cells are operated with hydrogen as fuel;

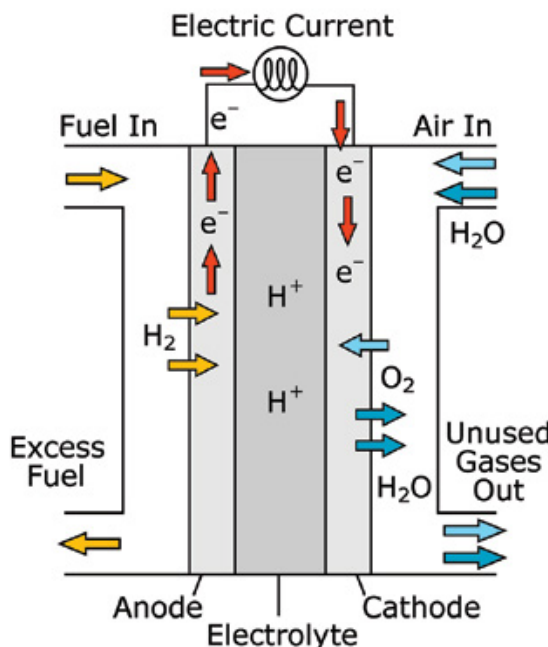


Figure 1. Schematic of a fuel cell. Diagram of a proton conducting solid oxide fuel cell, by Sakurambo, 2007. [https://en.wikipedia.org/wiki/File:Solid\\_oxide\\_fuel\\_cell.svg](https://en.wikipedia.org/wiki/File:Solid_oxide_fuel_cell.svg). Public domain.

however, some can be powered with ethanol, methanol, and polyalcohols (Haan et al., 2016) The ability to oxidize these fuels effectively depends on the catalyst. Commonly used catalysts are made of platinum (Pt). Platinum catalysts are the most expensive part of the fuel cell; therefore, scientists have turned their attention to palladium (Pd), an abundant resource, as the platinum catalyst alternative (Cui et al., 2009).

Cui et al., (2009) studied ethanol oxidation on Pd electrocatalysts and demonstrated that Pd-based electrocatalysts are affected by the pH of the ethanol aqueous solutions. Cui et al., (2009) used density functional theory (DFT) calculations to demonstrate that there is a continuous ethanol electrooxidation when ethanol adsorbs to Pd in alkaline media compared to acidic media. The media refers to the type of electrolyte used, alkaline or acidic. Cui et al., (2009) computationally created a Pd (111) surface (reflective to their lab work) consisting of five atoms in the first layer and four atoms on the second layer. In their study, ethanol,  $\text{H}_3\text{O}^+$ , and  $\text{OH}^-$  ions adsorbed on the top site of the central Pd atom. In acidic solution, the strongest interactions occurred between  $\text{H}_3\text{O}^+$  and the Pd surface (Cui et al., 2009). The oxidation of ethanol was not possible due to a lack of adsorbed  $\text{OH}^-$  species. In contrast, in alkaline conditions, the hydroxyl groups were interacted with Pd surface and oxidation of ethanol occurred (Cui et al., 2009).

Similarly, Haan et al., (2016) studied the catalytic activity of Pd with the addition of Cu, Pd/Cu/C. Different carbon supported Cu:Pd ratios ( $\text{Pd}_{63}\text{Cu}_{37}/\text{C}$ ,  $\text{Pd}_{46}\text{Cu}_{54}/\text{C}$ ,  $\text{Pd}_{28}\text{Cu}_{72}/\text{C}$  and  $\text{Pd}_{11}\text{Cu}_{89}/\text{C}$ ) were used to compare oxidation rates between Pd/C and Pd/C/Cu catalysts. These catalysts, in alkaline media, are more effective compared to acidic media in the electrooxidation of polyalcohols: ethylene glycol (EG), propylene (PG), and glycerol (G) (Han et al., 2016). These polyalcohols can be sourced renewably and are more bio friendly compared to the production of ethanol. Due to electronic effects, oxidation rate of polyalcohols (EG, PG and G) was improved 3 to 14

times when the Cu concentration was increased (Han et al., 2016). The addition of copper to the Pd surface promoted the adsorption of hydroxyl in polyalcohols at lower potentials and thus increasing the oxidation rate (Han et al., 2016).

Another study by Zeng et al., (2007) examined another alternative fuel for direct oxidation of fuel cells such as AA, commonly known as vitamin C. A mathematical model was developed to describe direct ascorbic acid fuel cells. It concluded that the cathode and concentration of AA was affecting fuel cell performance. They proposed that an increase in AA concentration may increase oxidation rates; however; more research needs to be conducted (Zeng et al., 2007).

Recent studies by Haan et al., (2017) demonstrated that AA is a much more powerful fuel on PdCu alloys in alkaline media compared to acidic media. A fuel cell was built with the addition of L-ascorbic acid in the presence of KOH (basic media). A significant increase in catalytic activity utilizing L-ascorbic acid was recorded in direct liquid fuel cells (DLFCs) compared to alkaline DLFCs fueled by alcohols (Han et al., 2017).

Chirality plays an important role in the way AA oxidizes on Pd. There is an important feature that makes a molecule chiral such as when four different atomic groups attach to a central carbon; these atoms can be arranged in either clockwise or anticlockwise resulting in a pair of enantiomers (Libretexts, 2017). These enantiomers have the same atomic composition and cannot be superposed on their mirror images (Libretexts, 2017). Chirality is applicable in the food, fragrance and pharmaceutical industry; however, it has not been examined in the fuel cell industry. Chiral molecules with different isomeric forms have different properties (Libretexts, 2017). The geometry of chiral molecules should be examined properly in the synthesis of molecules.

For example, in AA, there are two chiral centers occurring at two adjacent carbons. Therefore, there are two sets of enantiomers resulting in four stereoisomers: D-ascorbic acid (S, R), L-ascorbic acid (R, S), isoascorbic

acid (S, S) and erythorbic acid (R, R) as shown in Figure 2. Each differs in the arrangement in three-dimensional space about two tetrahedral, sp<sup>3</sup> hybridized carbons (National Center for Biotechnology Information, n.d.). Each stereoisomer is made up of a five-membered ring (cyclopentene) including an ether. Each carbon in the ring is attached to a functional group including an ester, two hydroxyl groups between a double bond and an ethyl group containing two more hydroxyl groups (National Center for Biotechnology Information, n.d.). L-ascorbic acid, most commonly referred as vitamin C, is bio-friendly and an inexpensive compound that was used in direct oxidation of fuel cells (Han et al., 2017). Computationally, this study considers all AA acid stereoisomers and observes how chirality may affect oxidation in fuel cells.

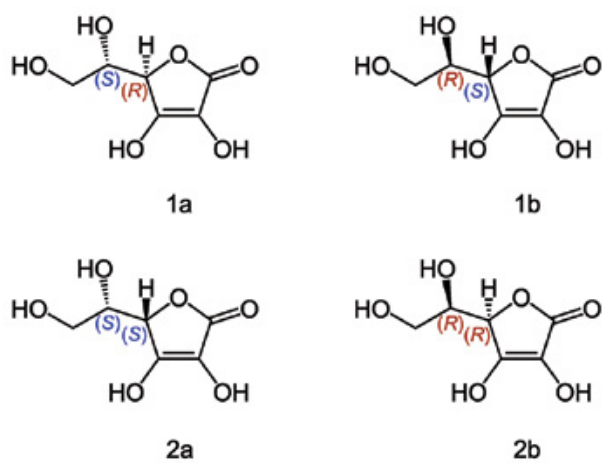


Figure 2. Ascorbic acid isomers, by Yikrazuul, 2009. [https://commons.wikimedia.org/wiki/File:Ascorbic\\_acid\\_isomers.svg](https://commons.wikimedia.org/wiki/File:Ascorbic_acid_isomers.svg). Public domain. AA has two chiral centers resulting in four stereoisomers: (1a) D-ascorbic acid (S, R), (1b) L-ascorbic acid (R, S), (2a) isoascorbic acid (S, S) and (2b) erythorbic acid (R, R).

The objective of this research is to understand the interactions AA enantiomers are having with the catalyst and ultimately, provide a computational model of how they adsorb onto Pd. This model may be used as a basis for creating PdCu alloys in the same ratio used in the

experiments by Haan et al. (2017), and directly compare how each AA stereoisomers interacts with the catalyst. Finally, researchers may be able to use these structures as a starting point to calculate catalytic pathways in future experiments.

## METHODS

A computational quantum mechanical model known as Density Functional Theory (DFT) was used to calculate adsorptions potential energies (APE). DFT can be described as a method for calculating an approximate solution to the Schrodinger equation from the electron density of many body-systems (Cuevas, n.d.). It can predict different molecular properties such as molecular structures, adsorption energies, atomization energies, magnetic properties and many other molecular properties (Cuevas, n.d.).

DFT calculations were performed using GPAW (projector augmented wave) supported by Atomic Simulation Environment (ASE) (Larsen et al., 2017 and Mortensen, Hensen, Jacobsen, 2017). PBE-vdW<sup>Surf</sup> exchange correlation-functionals were employed to account for the van der Waals interactions to the adsorption energy of AA on Pd (111) (Ruiz et al., 2012). A 4 x 4 double layer (Pd 111) slab was created using 32 Pd atoms with the bottom layer fixed. Calculations were evaluated using a 2 x 2 x 1 k-point mesh and the forces relaxed until  $F_{\max} = 0.05 \text{ eV}/\text{\AA}$ . The PBE-vdW<sup>Surf</sup> optimized lattice parameter of 3.85 Å determined the initial Pd-Pd spacing giving a grid box spacing of 0.176 Å.

Stereoisomers of AA were simulated on a Pd (111) surface to determine adsorption potential energies. Initially, there was 2 - 3 Å distance between atoms closest to the Pd slab and molecules were optimized until stable. Each AA stereoisomers was designed to have two footprints. The first footprint is shown when the ether functional group in the cyclopentene is pointing down over the x-axis in a three-dimensional plane consisting of x, y, z axes. The second footprint is visible when the ether in the cyclopentene is pointing up as

shown in Figure 4. A total of eight configurations were examined and rotated at the point around the center of rotation indicated with a hexagon on top of a carbon atom as shown in Figure 3. The molecules were rotated at different angles of rotation ( $0^\circ$ ,  $15^\circ$ ,  $30^\circ$ ,  $45^\circ$ ) and then placed on the Pd slab at different atomic positions FCC, HCP, bridge; and on top to account for all adsorption sites. Configurations were optimized to determine the most stable configurations of AA. The APE of each molecule was recorded. Adsorption potential energies were determined by:

$$E_{APE} = E_{molecule + slab} - E_{slab} - E_{molecule}.$$

The more negative the energy (exothermic reaction), the greater the attraction force between the molecules to the surface.

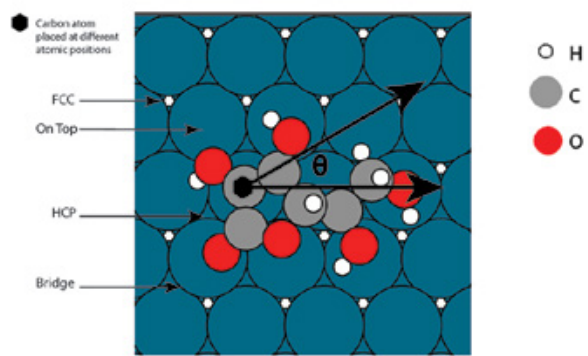


**Figure 3.** AA configurations were simulated on a Pd surface at different atomic positions: FCC, HCP Bridge and on top. Configurations were rotated at different angles where  $\theta = 0^\circ$   $15^\circ$   $30^\circ$   $45^\circ$ .

## RESULTS

DFT calculations demonstrated that the molecular structure and adsorption potential energy of AA is dependent on chirality. A summary of the molecules with the highest APE is shown in Table 1. There is a direct relationship between the APE and the distance ( $\text{Å}$ ) between specific hydroxyl groups atoms in AA to the Pd surface. As the distance between the OH species

and the Pd surface decreases, the APE increases. A distance responsible for adsorption (between oxygen atoms and the Pd to the surface) is defined as not greater than  $3.40 \text{ Å}^\circ$  (Table 2). Distances above  $3.40 \text{ Å}^\circ$  were considered too away from the surface and were not major interactions. The lowest possible distance to the Pd surface was  $2.44 \text{ Å}^\circ$  and thus yielded the highest adsorption potential energy: D-Ascorbic acid (S, R), pointing down, with an APE of  $-1.76 \text{ eV}$ . The hydroxyl group attached to the ethyl group and farthest away from the ring, stabilized when it was  $2.44 \text{ Å}^\circ$  away from the Pd surface. The hydroxyl group attached to the ring

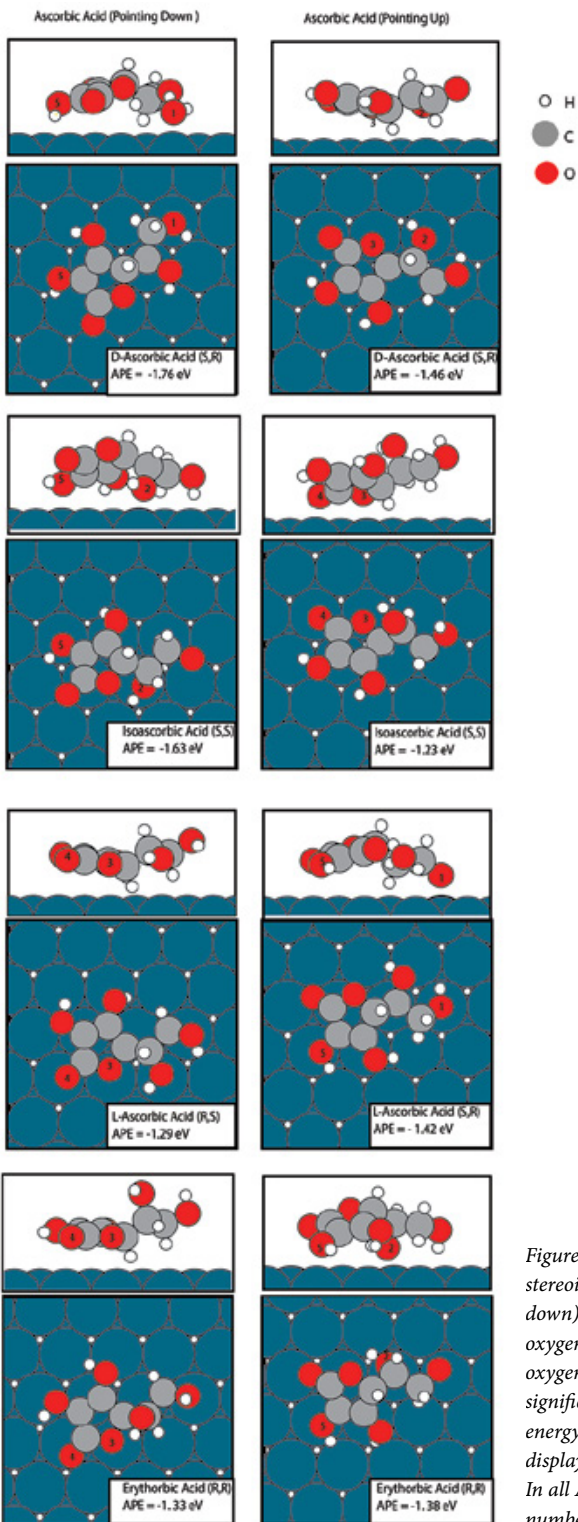
Highest APE	
AA	APE (eV)
D-ascorbic acid (S,R)	-1.76
Isoascorbic acid (S,S)	-1.63
L-ascorbic acid (R,S)	-1.42
Erythorbic acid (R,R)	-1.33

**Table 1.** Highest APE of AA stereoisomers.

### Distance between oxygen atoms to Pd (111)

AA	Oxygen attached to the ethyl group labeled (1)	Oxygen attached to ethyl group labeled (2)	Oxygen attached to the alkene labeled (5)
D-ascorbic acid (S,R)	<b><math>2.44 \text{ Å}^\circ</math></b>	not sig	$3.15 \text{ Å}^\circ$
L-ascorbic acid (R,S)	<b><math>2.45 \text{ Å}^\circ</math></b>	not sig	$3.01 \text{ Å}^\circ$
Isoascorbic acid (S,S)	not sig	<b><math>2.47 \text{ Å}^\circ</math></b>	<b><math>2.73 \text{ Å}^\circ</math></b>
Erythorbic acid (R,R)	not sig	<b><math>2.85 \text{ Å}^\circ</math></b>	<b><math>2.95 \text{ Å}^\circ</math></b>

**Table 2.** Distance between oxygen atoms to the Pd surface of all AA stereoisomers with the highest APE. Distances  $>3.40 \text{ Å}^\circ$  were too far away from the surface and not considered significant (not sig). Enantiomers (S, R) and (R, S) displayed the highest APE when oxygen atoms labeled 1, 5 were closest to the Pd surface. Enantiomers (S, S) and (R, R) displayed the highest APE when oxygen atoms labeled 2, 5 were closest to the Pd surface. Oxygen atom labeled as 5 was present in all stereoisomers indicating a key player in the adsorption potential of AA to the Pd surface.



and closest to the ester group stabilized at 3.15 Å away from the surface. The next most stable molecule was isoascorbic acid (S, S) with an APE of -1.63 eV. The hydroxyl group in the ethyl closest to the ring optimized when it was 2.47 Å away from the surface. The hydroxyl closest to the ester group stabilized when it was 2.73 Å away from the surface. L- ascorbic acid (R, S) had an APE of -1.42 eV. The OH species more associated with adsorption were the same as in D-ascorbic acid (S, R); the distances away from the surface were almost the same: 2.45 Å and 3.01 Å respectively. Finally, erythorbic acid (R, R) with an APE of -1.38 eV shared the same adsorption characteristics noted in isoascorbic acid (S, S). The distance of the oxygen atoms to the surface were 2.85 Å and 2.95 Å respectively. A summary of the distances between oxygen atoms with the strongest interactions to the Pd surface is shown Table 2.

## DISCUSSION

Figure 4 shows two trajectories (one pointing up and pointing down) of each AA stereoisomer with the highest APE. D-ascorbic acid (S, R), compared to all other stereoisomers, displayed the highest potential energy due to the interactions that specific oxygen atoms (labeled as 1 and 5 in Figure 4) were having with the surface. The oxygen atom attached to the ethyl group, 1, had the largest distance (3.15 Å) to the Pd surface. The slightly larger distance observed may be a result of the free rotation occurring around the single bonds in the ethyl group. Carbon atoms with single bonds rotate freely because of the orbitals that form sigma bonds

*Figure 4. Highest adsorption potential energies for AA stereoisomers. Each stereoisomer has two footprints: Down (when the oxygen in the ring is pointing down) and up (when the oxygen in the ring is pointing up). Numbers represent oxygens that have a strong adsorption to the Pd surface. The distance between an oxygen to the palladium surface is between 2.00 Å to 3.40 Å (to be considered a significant adsorption). Enantiomers, (SR) and (R, S) display the highest potential energy when oxygens 1, 5 are closest the Pd surface. Enantiomers (S, S) and (R, R) display the highest potential energy when oxygens 2, 5 are closest to the Pd surface. In all AA stereoisomers shown above, the highest binding oxygens (indicated with numbers) were most stable on top of a Pd atom.*

(Calmes et al., n.d.). The electron density concentrates equally along the bond axis allowing free rotation while remaining unaffected (Calmes et al., n.d.). Thus, the distance between the oxygen atom to the surface may be ideal for the free rotation of the ethyl group. The OH, labeled 5, is attached to the ring that forms a double bond with a neighboring carbon atom containing another hydroxyl group. The distance between the surface and oxygen atom was  $2.44\text{ \AA}^\circ$ ; this was the closest distance recorded from an oxygen atom to the Pd surface. The stronger attraction to the Pd surface may be attributed to the alkene in the ring. The two carbon atoms creating the double bond are  $\text{sp}^2$  hybridized and have bond angles of  $120^\circ$  (Calmes et al., n.d.). Unlike a single bond, a double bond is made of a sigma and a pi bond which puts restrictions on rotation. A double bond is more stable when it is planar (Calmes et al., n.d.). As a result, the double bond in the ring of AA may be causing one of the hydroxyl groups to have a closer contact to the surface to reach optimal stability. It is unknown as to why the other OH group on the alkene does not stabilize closer to the Pd surface.

It is important to note that the oxygen atom (indicated with number 5) attached to the double bond is present in all of AA configurations as a major adsorption site due to the proximity to the Pd surface as shown in Table 2.

L-ascorbic acid (S, R) had an APE of  $1.42\text{ eV}$  when it was pointing up compared to when it was pointing down,  $1.29\text{ eV}$ . The major contributors to the adsorption potential energy were the same atoms indicated in D-ascorbic acid as shown in Figure 5. The results proved to be logical. The only difference between (S, R) and (R, S) enantiomers is that in one molecule, the H and the OH species point to the back, and in the other enantiomer, the H and OH species point towards the front. When the (R, S) configuration was pointing down, the APE decreased to  $1.29\text{ eV}$ . However, when the (R, S) configuration was pointing up (opposite of the (S, R) configuration), the APE went up to  $1.42\text{ eV}$ , resulting in the third most stable AA stereoisomer. It is important to

note that changing a molecules position from pointing down to pointing up (rotating along the x-axis  $180^\circ$ ) does not alter the chirality. It just helps us understand and provide more evidence on the intermolecular interactions happening between specific atoms and the surface.

For enantiomers (S, S) and (R, R), the two OH species directly associated with the adsorption potential energy were the hydroxyl group attached to the ethyl group connected to the chiral center farthest away from the ring, and once again, the OH group closest to the ester group (labeled 5). Isoascorbic acid (S, S) had a higher APE of  $-1.63\text{ eV}$  compared to erythorbic acid (R, R) with the lowest APE of  $1.38\text{ eV}$ . What distinguishes isoascorbic acid (S, S) the most is the close proximity to the Pd surface,  $2.47\text{ \AA}^\circ$ , which can be attributed to the single bond in the ethyl group allowing the hydroxyl to be rotated towards the z-direction and thus creating a closer proximity to the surface as shown in Figure 5. Oxygen atom, labeled 5, had a similar interaction to the Pd surface in both set of enantiomers. Erythorbic acid

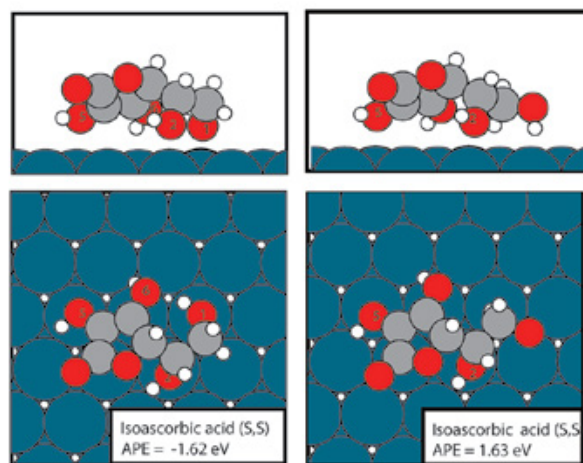


**Figure 5.** a) All OH species with a number label on the oxygen atoms were oriented closer to the Pd surface with a Pd to oxygen distance between  $2-3\text{ \AA}^\circ$ . The APE ( $-1.62\text{ eV}$ ) in isoascorbic acid did not have a significant change when all OH species were brought closer to the surface. b) The oxygens labeled with numbers in isoascorbic acid ( $\text{APE} = 1.63\text{ eV}$ ) are responsible for the high APE in isoascorbic acid. Orienting all OH species close to the surface does not increase the APE.

displayed the lowest APE, -1.38 eV simply because what differentiates this enantiomer from (S, S) is the fact the OH group on the chiral center must point towards the front to become (R, R). As a result, there was no visible contact between the OH group to the surface. Even when erythorbic acid (R, R) was pointing up, as opposed to pointing down, the APE did not change significantly, -1.33 eV. Based on these results, we can conclude that APE of AA is highly dependent of chirality.

It is important to note that the OH species directly associated with adsorption to the Pd surface stabilized on top of a Pd atom with a distance not greater than 3.15 Å. OH species with the largest distance to the surface were optimized on the atomic positions such as the bridge, HCP and FCC. Atoms positioned on these atomic positions did not have a major impact on adsorption to the Pd surface.

In figure 5, the OH towards the end of the ethyl group (labeled 1) in isoascorbic acid (S, S) was not close to the surface nor on top of the Pd atom. Computationally, the OH was brought closer to the surface and placed on top of a Pd atom to examine changes in intermolecular interactions. It was predicted that the binding energy would increase when all OH species were brought closer to the surface and positioned on top of a Pd atom as shown in Figure 5b. However, the binding energy almost remained the same. Isoascorbic acid (S, S) pointing down had an APE of 1.63 eV when hydroxyl groups labeled 2 and 5 were on top of a Pd atom as shown in figure 6b. The ethyl group with the OH groups attached was rotated about 120° around the x-axis causing the OH group farthest from ring to point directly to the surface as shown in Figure 6a. The resulting APE was 1.62 eV indicating adsorption potential of AA is dependent to the binding of specific hydroxide species at different configurations determined by chirality. Rotating the molecule to bring all OH groups closer to the surface did not increased or decreased the APE.

Figure 6 shows, the configuration with the lowest APE: erythorbic acid (R,R) placed on the FCC site on the

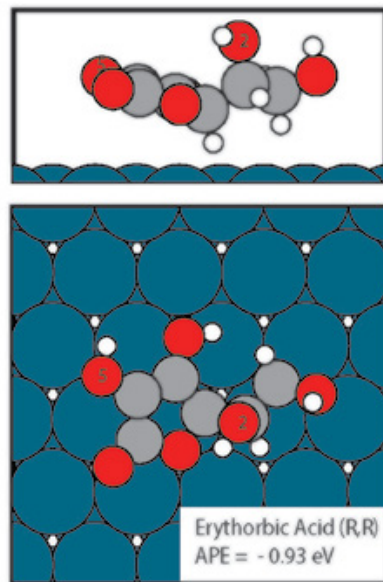


**Figure 6.** AA configuration with the lowest binding energy.

Pd surface (-0.93 eV). For AA enantiomers, (R,R) and (S,S), there are two oxygens that interact the most with the Pd surface: the oxygen attached to the ethyl group (labeled as 2 ) and the oxygen attached to the alkene (labeled 5). In the figure 6, oxygen atoms ( 2 and 5) are oriented away from surface resulting in a larger distance relative to the Pd surface (over 4.0 Å). A larger distance between these oxygen atoms is directly proportional to a low adsorption potential energy.

Another important feature of AA that was not examined in detail in this study is the resonance occurring between the ester group in the ring and the double bond between the two hydroxyl groups in the ring. Resonance stabilizes a molecule by the delocalization of electrons that spread out equally between two oxygen atoms (Calmes et al., n.d.). Therefore, resonance structures of AA may affect the binding energies to the metal surface. Future experiments may examine how the deprotonation of the most acidic protons in AA result in different resonance structures. Additional studies may also examine how AA adsorbs to the surface when each OH group is deprotonated independently.

The oxygen in the ether group contained in the ring appeared to be interacting with the Pd surface when the enantiomers (S, R) and (S, S) are pointing up and when enantiomers (R, S) and (R, R) are pointing down. When the enantiomers (R, S) and (R, R) were flipped (from their original configuration), the ether group optimized away from the surface and the APE increased. In contrast, when the ether group interacted with the surface, the APE decreased as shown in Figure 4. When enantiomers S, R) and (S, S) were flipped from their original configuration, the ether group optimized closer to the surface however; it did not increase the APE, instead the binding energy decreased. The main role of the ether group in the cyclopentene is ambiguous. More research needs to be conducted to understand the interactions the ether group is having with the Pd surface.

## CONCLUSION

DFT calculations demonstrated that molecular structure and adsorption potential energy of AA is dependent on chirality. Chirality is an important factor to consider; especially when molecules have more than one chiral center as in the case of AA. In fuel cells, L-ascorbic acid (R,S) is currently used as an alternative fuel for direct oxidation of fuel cells. This research showed that out of all AA stereoisomers, L-ascorbic acid has the third highest binding energy compared to all three AA conformations. D-ascorbic acid was shown to have the highest APE due to the strongest interaction between specific OH species to the Pd surface. Thanks to the finding from this study, scientists are now studying how D-ascorbic acid operates in direct oxidation of fuel cells compared to L-ascorbic acid. Perhaps D-ascorbic may yield a higher catalytic activity or it may yield a lower catalytic activity which can help us understand how adsorption to the Pd surface affects oxidation of AA. The findings from this study may guide future studies in the development of more stable fuel cells. The next

goal of this study is to calculate catalytic pathways of Pd electrocatalysts and AA using DFT calculations.

## REFERENCES

- Larsen, A.H., Jens J.M., Blomqvist, J., Castelli, I.E., Rune, C., Dulak, M., Friis, J., Groves, N.M. ... Wedel, K.J. The Atomic Simulation Environment—A Python library for working with atoms *J. Phys. Condens. Matter* Vol. 29 273002, 2017. (accessed January 23, 2017).
- Cui, G., Song, S., Shen, P. K., Kowal, A., & Bianchini, C. (2009). First-Principles Considerations on Catalytic Activity of Pd toward Ethanol Oxidation. *The Journal of Physical Chemistry C*, 113(35), 15639-15642. doi:10.1021/jp900924s. (accessed January 24, 2017).
- Cuevas, C. J. (n.d.). Introduction to Density Functional Theory. (accessed: December 12, 2017) [https://www.uam.es/personal\\_pdi/ciencias/jcuevas/Talks/JC-Cuevas-DFT.pdf](https://www.uam.es/personal_pdi/ciencias/jcuevas/Talks/JC-Cuevas-DFT.pdf)
- Calmes, J., Dash, S., Ner, R. "Sigma and Pi bonds". <https://brilliant.org/wiki/sigma-and-pi-bonds>. (accessed February 2, 2018).
- Fuel cells. (n.d.). Retrieved from <http://americanhistory.si.edu/fuelcells/sources.htm> (accessed Feb 2, 2017).
- Fujiwara, N., Yamazaki, S., Siroma, Z., Ioroi, T., & Yasuda, K. (2007). L-Ascorbic acid as an alternative fuel for direct oxidation fuel cells. *Journal of Power Sources*, 167(1), 32-38. doi: 10.1016/j.jpowsour.2007.02.023. (accessed January 30, 2017).
- Haan, J.L., Muneeb, O., Estrada, J., Tran, L., Nguyen, K., Flores, J., Hu, S. (2016). Electrochemical Oxidation of Polyalcohols in Alkaline Media on Palladium Catalysts Promoted by the Addition of Copper. *Electrochimica Acta*, 218, 133-139 doi: 10.1016/j.electacta.2016.09.105. (accessed January 30, 2017).
- Haan, J. L., Muneeb, O., Do E., Tran, T., Boyd, D., Huynh, M., Ghosn, G. (2017). A direct ascorbate fuel cell with an anion exchange membrane. *Journal of Power Sources*, 351, 74-78 (accessed January 30, 2017).
- J. J. Mortensen, L. B. Hansen , and K. W. Jacobsen. Real-space grid implementation of the projector augmented wave method. *Physical Review B*, Vol. 71, 035109, 2005. (accessed January 23, 2017).
- J. Enkovaara, C. Rostgaard, J. J. Mortensen et al. Electronic structure calculations with GPAW: a real-space implementation of the projector augmented-wave method *J. Phys.: Condens. Matter* 22, 253202 (2010) (accessed January 23, 2017).
- Libretexts. 2017, 25.7: Chirality in Organic Chemistry: [https://chem.libretexts.org/LibreTexts/University\\_of\\_Missouri/MU%3A\\_\\_1330H\\_\(Keller\)/25%3A\\_Chemistry\\_of\\_Life%3A\\_Organic\\_and\\_Biological\\_Chemistry/25.07%3A\\_Chirality\\_in\\_Organic\\_Chemistry](https://chem.libretexts.org/LibreTexts/University_of_Missouri/MU%3A__1330H_(Keller)/25%3A_Chemistry_of_Life%3A_Organic_and_Biological_Chemistry/25.07%3A_Chirality_in_Organic_Chemistry) (accessed January 10, 2018).

M. Walter, H. Häkkinen, L. Lehtovaara, M. Puska, J. Enkovaara, C. Rostgaard and J. J. Mortensen Time-dependent density-functional theory in the projector augmented-wave method *Journal of Chemical Physics*, Vol. 128, 244101, 2008. (accessed January 23,2017).

National Center for Biotechnology Information. PubChem Compound Database; CID=54670067, <https://pubchem.ncbi.nlm.nih.gov/compound/54670067> (accessed Feb. 2, 2018).

Nice, Karim & Strickland, Jonathan. "How Fuel Cells Work" 18 September 2000. (accessed Feb 2, 2017).

HowStuffWorks.com. <<https://auto.howstuffworks.com/fuel-efficiency/alternative-fuels/fuel-cell.htm>> (accessed 31 January 2017).

Ruiz, V.G., Liu, W., Scheffler, M., and Tkatchenko, A. "Density-Functional Theory with Screened van der Waals Interactions for the Modeling of Hybrid Inorganic-Organic Systems." *APS Physics* , April 06, 2012. Rev. Lett. 108, 146103 (January 23, 2017).

S. R. Bahn and K. W. JacobsenAn object-oriented scripting interface to a legacy electronic structure code Comput. Sci. Eng., Vol. 4, 56-66, 2002 (accessed January 23, 2017).

Sakurambo. (2007) *Solid oxide fuel cell* [Digital Image]. Image accessed January, 31, 2017.Retrieved from Wikipedia website: [https://en.wikipedia.org/wiki/File:Solid\\_oxide\\_fuel\\_cell.svg](https://en.wikipedia.org/wiki/File:Solid_oxide_fuel_cell.svg)

Yikrazuul. (2009). *Ascorbic acid isomers* [Digital Image]. Image accessed January 31, 2017. Retrieved from Wikipedia Commons website: [https://commons.wikimedia.org/wiki/File:Ascorbic\\_acid\\_isomers.svg](https://commons.wikimedia.org/wiki/File:Ascorbic_acid_isomers.svg)

Zeng, Y., Fujiwara, N., Yamazaki, S., Tanimoto, K., & Wu, P. (2008). Modelling and analysis of a direct ascorbic acid fuel cell. *Journal of Power Sources*, 185(1), 95-103. doi: 10.1016/j.jpowsour.2008.06.062. (accessed January 30, 2017).

A special thanks to Dr. Groves for his guidance and advice on this research project.

## **Synthesis of Proposed System of Ionic-Conducting Materials**

**XAgTa<sub>4-y</sub>Mo<sub>y</sub>O<sub>11</sub> (X: Na, K, Rb, Cs)**

**Karen Tom**

**Advisor: Allyson M. Fry-Petit, Ph.D.**

*Department of Chemistry and Biochemistry, California State University, Fullerton*

### **ABSTRACT**

A system of AgTa<sub>4</sub>O<sub>11</sub> compounds have exhibited promise for the materials development of batteries, an advancement in the search for alternative batteries. XAgTa<sub>4-y</sub>Mo<sub>y</sub>O<sub>11</sub> (X: Na, K, Cs, Rb) consists of a crystal structure paralleling the known P2<sub>1</sub>/n monoclinic compound, NaAgNb<sub>4</sub>O<sub>11</sub>. The published structure contains distinctive channels that hold the sodium and silver ions, further suggesting the potential ionic conducting properties of NaAgNb<sub>4</sub>O<sub>11</sub> and its derivatives, including the proposed XAgTa<sub>4-y</sub>Mo<sub>y</sub>O<sub>11</sub> (X: Na, K, Cs, Rb) system. X-ray powder diffraction and Rietveld refinement were used to determine whether the NaAgNb<sub>4</sub>O<sub>11</sub> structure was attained following the synthesis of XAgTa<sub>4</sub>O<sub>11</sub> (X: Na, K, Cs, Rb). Standard ceramic and flux growth methods were used to successfully synthesize the system of compounds. While the compounds had ideal channel-like structures of battery materials, the lack of d orbital electrons and an absence in color suggested minimal conductive capabilities. To compensate, molybdenum, in the form of MoCl<sub>5</sub> and MoO<sub>3</sub>, was doped into the Na analog to increase the electrochemical potential of the compounds. X-ray powder diffraction analyses on the NaAgTa<sub>4-y</sub>Mo<sub>y</sub>O<sub>11</sub> compounds revealed a structure comparable with NaAgTa<sub>4</sub>O<sub>11</sub> as well as a color change, a promising sign for increased ion conducting properties. Moreover, analysis of UV-Vis Spectroscopy data collected on NaAgTa<sub>4-y</sub>Mo<sub>y</sub>O<sub>11</sub>, synthesized with MoCl<sub>5</sub>, suggested the incorporation of chlorine into the crystal structure. Thus, an oxy-chloride material has emerged amongst the proposed system of AgTa<sub>4</sub>O<sub>11</sub> compounds, specifically NaAgTa<sub>4-y</sub>Mo<sub>y</sub>O<sub>11</sub>, having the ideal structure and conductive properties needed for a practical battery material.

# **The Effect of Synthesis Conditions on the Formation and Crystal Structure of Perovskite Oxygen Transport Membranes**

**Liz Hitch**

**Advisor: Allyson M. Fry-Petit, Ph.D.**

*Department of Chemistry and Biochemistry, California State University, Fullerton*

## **ABSTRACT**

Oxygen transport membranes (OTM) are a promising technology that improves current oxygen separation methods by lowering costs and increasing efficiency. OTMs are composed of metal oxides which transport both oxygen ions and electrons across a membrane. Perovskite materials have been proposed as OTMs. This project focuses on synthesizing three perovskites related to  $\text{SrFeO}_3$  with varying composition, including the addition of lanthanum and cobalt to alter the electronic properties, using three different synthesis techniques. The compounds have been synthesized using a solid-state ceramic method and two different sol-gel method that involve the use of citrate/EDTA and citrate/ethylene glycol to understand the effect of synthesis technique on the underlying structure. The structure of all compounds has been investigated using powder X-ray diffraction. We shown that all three compounds can be successfully synthesized via all three synthesis routes and the details of the crystal structure analysis is ongoing. Furthermore, we have shown that the material is flexible enough to accommodate altering the oxygen content.

## **Fitting of Perovskite Structure Using PDFgui & Determination of Structure Transition of $\text{Sr}_{3-n}\text{Pb}_n\text{WO}_6$ ( $n=0, 1, 1.5, 2, 3$ )**

**Luis Gamez**

**Advisor: Allyson M. Fry-Petit, Ph.D.**

*Department of Chemistry and Biochemistry, California State University, Fullerton*

### **ABSTRACT**

The perovskite structure is important in the field of inorganic chemistry, as compounds with this structure show useful properties. This study included the study of two different families of perovskites. One project uses software (PDFgui) to refine a structural model to a Paired Distribution Function (PDF) neutron total scattering data.

Two compounds were investigated using this method,  $\text{Ba}_2\text{ZnTeO}_6$  and  $\text{Sr}_2\text{ZnTeO}_6$ . Previous refinements of long range structure from diffraction data indicated that the local and long range structure differed. However, PDFgui refinements in this study could not determine for certain how the structures differ, due to technological limitations. The other project deals with determining the composition at which a structural change happens in the solid solution  $\text{Sr}_{3-n}\text{Pb}_n\text{WO}_6$  ( $n=0, 1, 1.5, 2, 3$ ).  $\text{Sr}_3\text{WO}_6$  is known to have a non-cooperative octahedral tilting (NCOT) perovskite structure and  $\text{Pb}_3\text{WO}_6$  is known to have an edge sharing perovskite structure. The solid state binary synthesis of  $\text{Sr}_2\text{PbWO}_6$ ,  $\text{Sr}_{1.5}\text{Pb}_{1.5}\text{WO}_6$ , and  $\text{SrPb}_2\text{WO}_6$  were attempted. The three compounds were analyzed via X-ray diffraction and compared to known compounds. The three compounds were determined to not yet be pure and are stuck in thermodynamically favorable phases that are not the target compositions. Using a precursor method instead of a binary method of synthesizing the compounds may result in the synthesis of the intended compounds.

# **Improvement of the Evolutionary Algorithm on the Atomic Simulation Environment Through Intelligent Starting Population Creation and Clustering**

**Nicholas Kellas**

**Advisor: Michael Groves, Ph.D.**

*Department of Chemistry and Biochemistry, California State University, Fullerton*

## **ABSTRACT**

The Evolutionary algorithm (EA), on the Atomic Simulation Environment (ASE), provides a means to find the lowest energy conformation molecule of a given stoichiometry. By augmenting the way in which the EA creates its starting population, the efficiency with which it locates the most stable molecular configuration can be improved. For this purpose, the starting population generator was altered to generate molecules using standard hybridized orbital geometries to determine bond angle and bond length. An agglomerative clustering program was also implemented in which molecules were analyzed for similarity and divided into groups, or clusters. By selecting molecules from different clusters a population with more diverse structures is formed, leading to more consistent success. C<sub>9</sub>H<sub>7</sub>N was used for testing purposes as the molecular stoichiometry because the global minimum (GM) is known (quinoline), the potential energy surface is well explored, and because the presence of a double ring structure in the GM makes it challenging to find. Through testing of EA runs with and without clustering and intelligent population creation, a significant increase in success rate was found. Results showed the following success rates; no intelligence and no clustering, 31%, no intelligence with clustering, 29%, with intelligence but without clustering, 50%, with intelligence and clustering, 55%.

# The Decomposition of Ethylamine on Pt(111)

**Waseefa Ahmed**

**Advisor: Michael Groves, Ph.D.**

*Department of Chemistry and Biochemistry, California State University, Fullerton*

## ABSTRACT

Chirality is important in pharmaceuticals as enantiomers can produce different effects *in vivo*. Naphthylethylamine (NEA) is a chiral modifier that transfers chirality to non-chiral molecules when adsorbed to an achiral metal surface. To understand the mechanism of chirality transfer from NEA to a non-chiral substrate, we want to determine the stability of the intact modifier. To this end, we studied the decomposition of the major functional group, ethylamine ( $\text{CH}_3\text{CH}_2\text{NH}_2$ ), on Pt(111) using density functional theory (DFT). Ethylamine was placed onto a Pt surface on different adsorption sites. It was determined that ethylamine is most stable when nitrogen is bonded to the surface with a binding energy of -1.01 eV. Ethylamine undergoes dehydrogenation resulting in two intermediates being formed,  $\text{CH}_2\text{CH}_2\text{NH}_2$  or  $\text{CH}_3\text{CHNH}_2$  with binding energies -0.800 eV and -0.821 eV, respectively. Based on these results, it is plausible to take into consideration the decomposition of NEA in chiral transfer mechanisms.

## INTRODUCTION

Chiral molecules are non-superimposable mirror images whose form and function dictate how they interact with biological systems [1]. These enantiomer pairs are identical except in the spatial arrangement of their atoms [2]. For example, the chemical compound carvone produces two odors depending on its form. These odors are produced from the interactions between olfactory receptors and odor molecules. As shown in Figure 1, The R configuration produces a spearmint smell while the S configuration produces a caraway smell.

Stereoisomers can have different effects on the body. These effects may be therapeutic, toxic, or have no

effect at all. In pharmaceuticals, the therapeutic kind is necessary when administering drugs. Therefore, being very specific with the synthesis is critical.

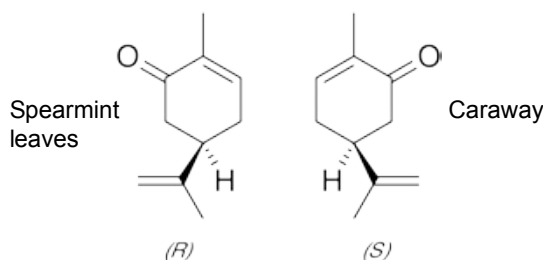


**Figure 1.** R and S enantiomers of the chemical compound carvone.

Improving enantioselectivity, or the selection of one enantiomer over the other, has been emphasized in biochemistry through catalysis [2]. The presence of a catalyst facilitates a chemical reaction by lowering the energy barrier for the reaction to be complete.

During heterogeneous catalysis, the catalyst and reactants are in different phases. Enantioselective heterogeneous catalysis generally happens in one of three ways. Achiral surfaces can be used to transfer chirality to molecules with the presence of a chiral modifier. Molecules of liquid or gas forms can then be adsorbed to the surface [3-4]. Another method involves molecules that are achiral adsorbing to achiral surfaces in chiral ways. Lastly, chirality can be transferred using naturally chiral surfaces. Chiral surfaces contain chiral atomic structures, allowing interactions between the surface and the chiral adsorbate to be enantioselective [2]. When a chiral modifier is adsorbed onto a catalytic surface and a non-chiral substrate is introduced, chirality is transferred to the substrate through the modifier.

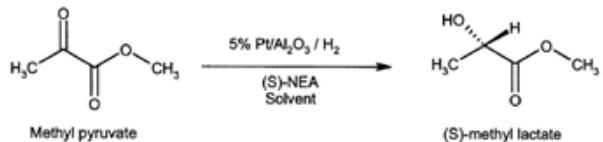


**Figure 2.** Reaction of (S)-NEA producing (S)-methyl lactate through chirality transfer.

First observed in 1979, a chiral modifying agent identified as cinchonidine was treated on a platinum catalyst, resulting in enantioselective  $\alpha$ -ketoester hydrogenation [5-6]. This reaction was investigated along with a simpler synthetic modifier known as NEA.

pathway in how ethylamine decomposes on a platinum surface.

We calculated adsorption potential energies (APE) using density functional theory (DFT). DFT is a computational quantum mechanical method that uses electron density to perform calculations. The Hohenberg-Kohn theorem states that the ground-state properties of a system is determined by the density. Therefore, the total energy of the system can be calculated if the electron density functional is known. Modern DFT also relies on the Kohn-Sham formalism, where the electrons operate in a noninteracting potential [9].

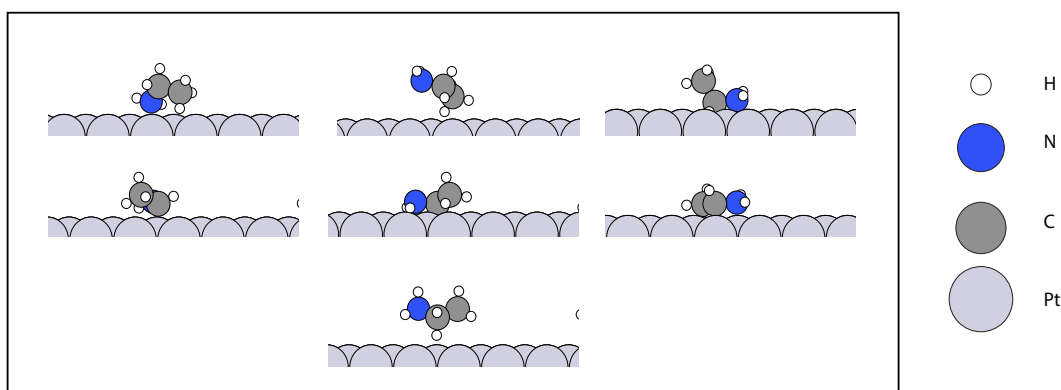


**Figure 3.** Configurations of ethylamine with  $\text{CH}_3$ ,  $\text{CH}_2$ , and  $\text{NH}_2$  placed onto the surface.

A study has been done with NEA on the geometries of pro-chiral substrates 2,2,2-trifluoroacetophenone (TFAP) and 3,3,3-methyltrifluoropyruvate (MTFP) [7]. Depicted in Figure 2, another study has shown that the chiral modifier (S)-NEA allows an achiral metal surface to enantioselectively hydrogenate a prochiral reactant (methyl pyruvate) to (S)-methyl lactate [8].

It is known from these previous studies that the intermolecular interaction between the modifier and substrate play a key role in enantioselection. In order to fully understand the role of the modifier, we must confirm its structure. The aim of our study was to simplify the problem by studying the modifier's major functional group, ethylamine. We then mapped out a

Reactions involving hydrogenation and dehydrogenation of surface C-N bonds have been studied on transition-metal surfaces [10]. For example, the hydrogenation of CN or decomposition of azomethane ( $\text{CH}_3\text{N}=\text{NCH}_3$ ) and methylamine ( $\text{CH}_3\text{NH}_2$ ) can form  $\text{CNH}_2$  on Pt(111) [11-13]. When methyl isocyanide ( $\text{CH}_3\text{NC}$ ) is hydrogenated or dimethylamine ( $(\text{CH}_3)_2\text{NH}$ ) is partially dehydrogenated, methylaminocarbyne ( $\text{CNHCH}_3$ ) is formed on Pt(111) [14-16]. To enhance our understanding of the mechanism of chirality transfer for NEA, the decomposition of the major functional group ethylamine is studied. Ethylamine is an aminocarbyne, a class of stable surface intermediates with the general formula

CNRR' that have been found to form on Pt(111) through reflection absorption infrared spectroscopy (RAIRS). The dehydrogenation of ethylamine can also serve as a model for the formation of nitriles or imines [10].

## MATERIAL AND METHODS

DFT calculations were performed using GPAW software v1.1.0 (projector-augmented wave) supported by the Atomic Simulation Environment (ASE) v3.13.0 [17-19]. A double layer of 36 Pt atoms was created for a Pt(111) slab. The bottom layer was constrained. The maximum force was relaxed to 0.05 Å/eV. The exchange-correlation functional used was PBE and the grid box spacing was 0.175 Å.

Search parameters included placing different configurations of ethylamine on the surface as shown in Figure 3. There was a distance of 2 Å between the atom closest to the Pt and the slab. Unoptimized ethylamine molecules were rotated and placed onto the Pt surface. Shown in Figure 3, different orientations of ethylamine molecules with CH<sub>3</sub>, CH<sub>2</sub>, and NH<sub>2</sub> facing the surface were optimized to determine the most stable intermediates. These configurations were created to assess all the possibilities of how ethylamine may adsorb onto the surface. Each intact molecule of ethylamine was also placed onto four adsorption sites on the Pt surface, as shown in Figure 4.

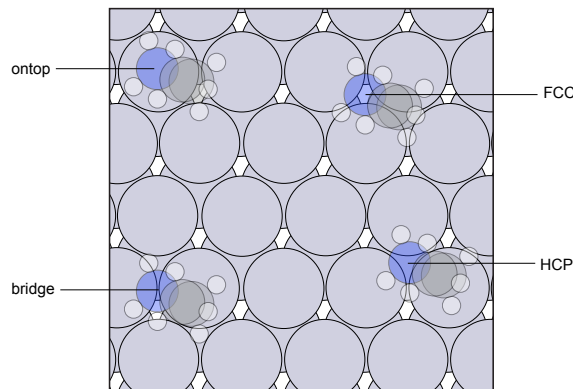


**Figure 4.** Configuration of ethylamine in which nitrogen is bonded to the surface and placed onto four adsorption sites (ontop, FCC, bridge, and HCP).

Four unique adsorption sites exist on the Pt slab (Figure 4). Each configuration was placed onto the ontop, FCC, HCP, and bridge positions in order to compare any noticeable differences in APE.

For dehydrogenation, a hydrogen atom was removed from each carbon and nitrogen atom individually, and the H atom was placed onto the FCC site. This method was done to each orientation of ethylamine, shown in the illustrated orientations in Figure 3. Each time a H atom was removed, the molecule was placed on the four adsorption sites (Figure 4) again. Therefore, the number of configurations multiply as each hydrogen is taken off an atom.

## RESULTS

Adsorption potential energies are calculated by the following equation:

$$E_{APE} = E_{molecule+slab} - (E_{slab} + E_{molecule}) \quad (1)$$

The APE is the energy difference between the molecule adsorbed to the surface and the molecule very far from the surface. This energy represents how strongly the molecule binds to the surface.

The most stable configuration for the intact molecule of ethylamine is when nitrogen is bonded to the surface with a binding energy of -1.01 eV, as shown

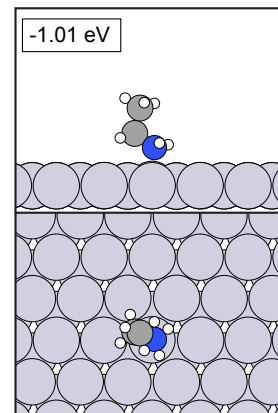


**Figure 5.** NH<sub>2</sub> adsorbed onto the platinum surface with the highest binding energy of -1.01 eV.

in Figure 5. When compared to the molecule shown in Figure 5, the binding energies of the other configurations from Figure 3 were significantly lower (-0.09 ~ -0.35 eV). Certain instances occurred when this was the most stable geometry, with the nitrogen bonded to the surface. Many of the initial configurations illustrated in Figure 3 relaxed and adopted a similar configuration as shown in Figure 5.

The first step in the dehydrogenation of ethylamine resulted in removing a single hydrogen atom from the molecule. After completing the search outlined from before, two dehydrogenated candidates have emerged as potential decomposition intermediates. These are illustrated in Figure 6. The binding energy calculated when the hydrogen was removed from the CH<sub>2</sub> group was -0.821 eV, as shown in Figure 6A. Figure 6B represents a hydrogen removed from the CH<sub>3</sub> group

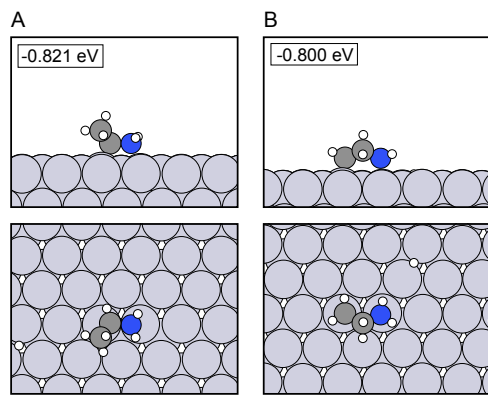


**Figure 6.** Two most stable configurations of ethylamine where A and B represents the removal of a H atom from CH<sub>2</sub> and CH<sub>3</sub>, respectively.

with a binding energy of -0.800 eV.

## DISCUSSION

The strongest binding energy indicates the strongest attraction between the molecule and Pt surface. As previously shown in Figure 5, the APE is -1.01 eV when nitrogen is bonded to the surface through its lone pair. Ethylamine exhibits nucleophilic properties with the ability of donating its electrons from nitrogen to the Pt atom. Therefore, the Pt surface acts as an electrophile.

Four sites of the Pt slab were tested to compare any differences in adsorption energies depending on location. The ontop position yielded the highest binding energies with about a -0.1 eV difference compared to the other sites. The ontop position was the preferred binding site due to the instance of the nitrogen lone pair interacting directly with a Pt atom.

The most favorable mode of adsorption for the intact molecule is through the nitrogen lone pair. A study reported that methylamine and ethylamine on Ni(111) [20] as well as methylamine, dimethylamine, and trimethylamine on Pt(111) have also adsorbed nitrogen to the metal surface [21-23]. Reflection absorption infrared spectroscopy, temperature-programmed desorption, and DFT also showed ethylamine to adsorb through nitrogen's lone pair [4]. Radicals in the gas phase also tend to be more stable when observed on surfaces. Considering the radical formed, CH<sub>3</sub>CHNH<sub>2</sub> (Figure 7), the metal surface interacts with the single electron on the carbon atom by filling a Pt empty orbital.

The APE for the two possible pathways are -0.821 eV and -0.800 eV when hydrogen is removed from CH<sub>2</sub> and CH<sub>3</sub>, respectively. There is an energy difference of -0.189 eV between the intact molecule and the adsorbed molecule from Figure 6A. The energy difference between the intact and dehydrogenated molecule in Figure 6B is -0.210 eV. Systems tend to populate states that are low in energy. If dehydrogenation takes place, these are the two likely candidates that would be observed.

## CONCLUSION

The proposed mechanism of the initial steps in ethylamine decomposition on Pt(111) is shown in Figure 7. Intact ethylamine is adsorbed to the surface through nitrogen's lone pair. When CH<sub>2</sub>CH<sub>2</sub>NH<sub>2</sub> is formed, the molecule adsorbs through the lone pairs on CH<sub>2</sub> and NH<sub>2</sub>. When CH<sub>3</sub>CHNH<sub>2</sub> is formed, the molecule adsorbs through the lone pair on NH<sub>2</sub>. An association is also formed between the lone electron on C and the surface, stabilizing the species.

Chiral modification is important in the synthesis

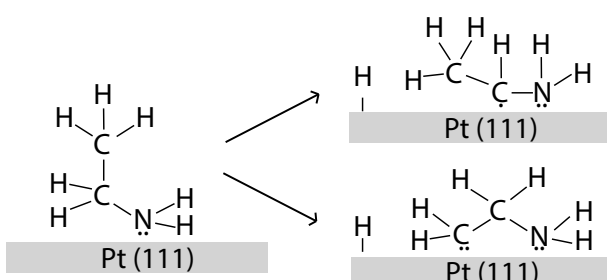


**Figure 7.** Proposed scheme of ethylamine adsorbed onto the Pt(111) surface.

of enantiomer compounds. Due to different effects enantiomers produce in vivo, it is critical to choose the correct form. Chiral modifying agents such as cinchonidine or naphthylethylamine offer the advantage of facilitating this process. Through DFT, we calculated adsorption potential energies to compare the most stable conformations.

Examining the decomposition of ethylamine on Pt(111) will allow us to further study the chiral modifier NEA. Future studies on NEA can confirm if chirality is successfully transferred to other non-chiral substrates when adsorbed to a catalytic surface. The mechanism behind chirality transfer can also be examined.

## ACKNOWLEDGEMENTS

I would like to show my gratitude to Dr. Groves for his support and guidance on this research project.

## REFERENCES

- [1] Chong, D., Mooney, J. Chirality and Stereoisomers. [https://chem.libretexts.org/Core/Organic\\_Chemistry/Chirality/Chirality\\_and\\_Stereoisomers](https://chem.libretexts.org/Core/Organic_Chemistry/Chirality/Chirality_and_Stereoisomers) (Accessed January 2018).
- [2] Gellman, A. J., Tysoe, W. T., Zaera, F. Surface Chemistry for Enantioselective Catalysis. *Catal Lett.* 2015, 145, 220–232.
- [3] Davis, M. E., & Davis, R. J. (2012). *Fundamentals of Chemical Reaction Engineering*. McGraw-Hill Higher Education, New York, NY.
- [4] Chieh, C. Heterogeneous Catalysts. <http://www.science.uwaterloo.ca/~cchieh/cact/applychem/heterocat.html> (Accessed January 2018).
- [5] Orito, Y., Imai, S., Niway, S., Hung, N. G. *J. Synth. Org. Chem. Jpn.* 1979, 37, 173.
- [6] Niwa, S., Imai, S., Orito, Y. *J. Chem. Soc. Jpn.* 1982, 137.
- [7] Groves, M.N., Goubert, G., Rasmussen, A.M.H., Dong, Y., Lemay, J.-C., Carpentier, V.D., McBreen, P.H., Hammer, B. Structure determination of chemisorbed chirality transfer complexes: Accelerated STM analysis and exchange -correlation functional sensitivity. *Surface Science*. 2014, 629, 48-56.
- [8] Bonello, J.M., Williams, F.J., Lambert, R.M. Aspects of Enantioselective Heterogeneous Catalysis: Structure and Reactivity of (S)-(-)-1-(Naphthyl)ethylamine on Pt{111}. *J. AM. CHEM. SOC.* 2003, 125, 2723-2729.
- [9] Kohn, W. Electronic Structure of Matter - Wave Functions and Density Functionals. *Nobel Lecture*. 1999, 213-237.
- [10] Waluyo, I., Krooswyk, J. D., Yin J., Ren Y., Trenary, M. Spectroscopic Identification of Surface Intermediates in the Dehydrogenation of Ethylamine on Pt(111). *J. Phys. Chem. C*. 2013, 117, 4666-4679.
- [11] Jentz, D.; Celio, H.; Mills, P.; Trenary, M. Formation of Aminomethylidyne from Hydrogen Cyanide on Pt(111). *Surf. Sci.* 1995, 341, 1-8.
- [12] Jentz, D.; Trenary, M.; Peng, X. D.; Stair, P. The Thermal Decomposition of Azomethane on Pt(111). *Surf. Sci.* 1995, 341, 282-294.
- [13] Jentz, D.; Mills, P.; Celio, H.; Trenary, M. The Surface Chemistry of CN and H on Pt(111). *Surf. Sci.* 1996, 368, 354–360.
- [14] Kang, D. H.; Trenary, M. Methylaminomethylidyne: A Stable Intermediate Formed on the Pt(111) Surface from the N-Protonation of Methyl Isocyanide. *J. Am. Chem. Soc.* 2001, 123, 8432–8433.
- [15] Kang, D. H.; Trenary, M. Formation of Methylaminocarbyne from Methyl Isocyanide on the Pt(111) Surface. *J. Phys. Chem. B* 2002, 106, 5710–5718.
- [16] Kang, D. H.; Trenary, M. Surface Chemistry of Dimethylamine on Pt(111): Formation of Methylaminocarbyne and Its Decomposition Products. *Surf. Sci.* 2002, 519, 40–56.
- [17] J. J. Mortensen, L. B. Hansen , and K. W. Jacobsen. Real-space grid implementation of the projector augmented wave method, *Physical Review B*, Vol. 71, 035109, 2005.
- [18] J. Enkovaara, C. Rostgaard, J. J. Mortensen et al., Electronic structure calculations with GPAW: a real-space implementation of the projector augmented-wave method, *J. Phys.: Condens. Matter* 22, 253202, 2010.

- [19] Larsen, A., Mortensen, J., Blomqvist, J., Castelli, I., Christensen, R., Dulak, M., Friis, J., Groves, M., Hammer, B., Hargus, C., Hermes, E., Jennings, P., Jensen, P., Kermode, J., Kitchin, J., Kolsbjerg, E., Kubal, J., Kaasbjerg, K., Lysgaard, S., Maronsson, J., Maxson, T., Olsen, T., Pastewka, L., Peterson, A., Rostgaard, C., SchiÅÿtz, J., Schütt, O., Strange, M., Thygesen, K., Vegge, T., Vilhelmsen, L., Walter, M., Zeng, Z., Jacobsen, K.W. *J. Phys.: Condens. Matter* 2017, 29, 273002.
- [20] Gardin, D. E.; Somorjai, G. A. Vibrational Spectra and Thermal Decomposition of Methylamine and Ethylamine on Ni(111). *J. Phys. Chem.* 1992, 96, 9424–9431.
- [21] Jentz, D.; Trenary, M.; Peng, X. D.; Stair, P. The Thermal Decomposition of Azomethane on Pt(111). *Surf. Sci.* 1995, 341, 282–294.
- [22] Kang, D. H.; Trenary, M. Surface Chemistry of Dimethylamine on Pt(111): Formation of Methylaminocarbyne and Its DecompositionProducts. *Surf. Sci.* 2002, 519, 40–56.
- [23] Kang, D. H.; Chatterjee, B.; Herceg, E.; Trenary, M. Adsorption and Decomposition of Trimethylamine on Pt(111): Formation of Dimethylaminocarbyne ( $\text{CN}(\text{CH}_3)_2$ ). *Surf. Sci.* 2003, 540, 23–38.

# **Ground Source Heat Pump Potential Characterization for California State University Fullerton**

**Adrian Escobar**

**Advisor: Richard Laton, Ph.D.**

*Department of Geological Sciences, California State University, Fullerton*

## **ABSTRACT**

The reality of anthropogenic climate change is well understood within the scientific community and steps for mitigation are imperative for all to take if there is to be any change in the current greenhouse gas emission trends (Council, 2001; Oreskes, 2004; Change, 2015). The solution for climate change will likely be a myriad of approaches on the local and national scale which stands in stark contrast to the current system in place that was to build upon a single fuel category. Currently within solutions like wind, photovoltaics, hydro-electric and geothermal, there lies lesser known technologies in each of the over-arching categories of wind, solar, hydro, and geothermal. One of the lesser known technologies is ground source heat pumps (GSHP). GSHPs have been in use for over 50 years in the United States (US) and around the world. The technology has seen greater implementation in Scandinavian countries than in the US but has proven its ability to reduce carbon emissions as well as economic viability over its lifetime in both regions of the world (O'Connell and Cassidy, 2003). Within the US several institutions have taken the initiative to implement GSHPs to heat and cool portions of their campuses. Ball State University in Indiana has switched to have its entire campus moved over to GSHPs and stands to be one of the largest projects of its kind in the nation (Muncie, 1979). CSUF has several; Leadership in Energy and Environmental Design (LEED) and University of California/California State University Energy Efficiency Partnership Program recognized and awarded projects, showing that sustainability is a priority of the institution. Steps towards increasing environmental sustainability

are encouraged on campus by several groups that also work alongside the community and local business to improve conditions within the Orange County area. With multiple large-scale buildings the CSUF campus is an ideal candidate for the study of implementing GSHP to alleviate its energy needs.

GSHP systems work by using the constant subsurface temperature as a medium by which to deposit or withdraw heat. The factors affecting the performance of these systems are: demand, the medium for exchange, the available surface area for exchange, the climate of the region, and construction materials. One of the leading factors in the performance of a system is the medium in which heat is exchanged. Thermal properties of subsurface materials can vary drastically, for example, the thermal conductivity of a dry soil can be as low as  $0.20 \text{ Btu}/(\text{h}^*\text{ft}^*\text{°F})$  while different petrologic groups can measure up to and exceed  $4.00 \text{ Btu}/(\text{h}^*\text{ft}^*\text{°F})$  (Association, 2008). Furthermore, groundwater flow can work to improve or retard the performance of the ground heat exchanger and must be assessed as thoroughly as all other aspects (Busby et al., 2009; Funabiki and Oguma, 2017). GSHPs are designed in multiple ways by which exchange of heat with the subsurface is the most common, and exchange of heat with a body of water, e.g. a pond, is the alternative method. Subsurface temperatures beyond a few meters stabilize and do not have the same seasonal fluctuations as the temperatures near the surface and are assumed to remain constant annually for all depths up to 60 meters (m) (200 feet (ft)) (Association, 2008). Due to space constraints on the CSUF campus, a vertical system

stands to maximize available space for implementation of a GSHP system due to utilization of potentially extensive subsurface space. GSHP systems are divided into vertical or horizontal systems, and open or closed systems. Open vertical GSHP systems use groundwater as the main medium to exchange heat with the subsurface, whereas contrast a closed system uses a pipe filled with solution to dissipate the heat with the surrounding subsurface – maintaining no exchange of fluids with the subsurface in its entirety.

The Ground Loop Design software (GLD) by Thermal Dynamics Inc. is a software suite specifically intended for ground heat exchangers system design. GLD enables designers to take heating and cooling loads from buildings and design site specific GSHP systems. The software permits users to design a system to the highest degree of accuracy for commercial use utilizing leading industry technology. GLD allows for the comparison of vertical, horizontal, pond, and hybrid systems to make the best decisions for varying geologic, regional, and economic conditions. The GLD software suite is the most sophisticated GSHP design software available, allowing for the greatest flexibility and accuracy when designing a GSHP system. The versatility of GLD makes it ideal for the investigation of GSHP implementation at CSUF.

The La Habra 7.5 minute geologic quadrangle shows that the university is situated on top of alluvial gravel, sand, and silt of valleys and floodplains (Dibblee, 2001). There are approximately 70 buildings on the 0.76 km<sup>2</sup> CSUF campus and, of this area, there is approximately 19%, 0.15 km<sup>2</sup>, of open space to potentially install ground heat exchangers. The available space is made up of a mix of sidewalks, parking lots, landscaping, engineered structures, and athletics fields. The largest open spaces are athletic fields situated on the north end of the university, while smaller corridors of space occupy the southern half of the campus, the majority of which are located between buildings, mostly sidewalks and landscaping.

Dolmat, identified aquifer zones between 36 m (120

ft) and 140 m (460 ft) beneath CSUF and are confirmed to be relatively shallow by both Masters (2015) and the Orange County Water District (OCWD) (District, 2004). The rule of thumb for vertical GSHP installation is approximately 50 m (165ft)/ton of cooling, meaning that large commercial loads will routinely exceed 30 m (100 ft) and potentially cross into groundwater. This aspect of drilling is well matured and has allowed for the drilling of boreholes to cross both shallow and deep aquifers while maintaining their integrity (Company, 1964). None the less, strict regulations and protection of groundwater resources within Orange County will require thorough evaluation of a GSHP system if it is to be implemented. Available space on the CSUF campus was assessed via Google EarthTM and ArcMapTM for a site adequate to host a vertical or horizontal field effectively sized for potential building loads. Sites were considered if they met the following criteria: relative proximity to building of interest, presence of landscaping and engineered features and overall area. Proximity to building is important because effectiveness of systems diminishes with increased distance between borehole fields and building being serviced. The removal of landscape and engineered features for installation of heat sink serves to greatly increase cost of the project. Trees pose multiple challenges with GSHP installation because of potential economic cost for removal and replacement as well as being physical barriers for drilling rigs for vertical installation. The final criterion is that the space be of an appropriate size to service the loads from buildings. Without sufficient space, demand from heating and/or cooling systems cannot be met and will render projects infeasible.

McCarthy Hall and Pollak Library were identified to have the largest heating and cooling demands of all buildings for which data has been acquired. Both buildings are directly adjacent to areas that may potentially host a borehole field of sufficient size for building demands. Preliminary work on system design for McCarthy Hall, the greatest demanding building, has shown that the heating of buildings may be unachievable

using GSHPs. However, cooling demand in southern California is significantly greater than that of heating, and results within GLD have shown that cooling demands for McCarthy Hall can be met using GSHPs. Simulations ran in GLD showed that cooling demands may be achieved with a single borehole field at depths of greater than or equal to 182 m (600 ft). Further work into system design will be investigating options for multiple borehole fields and hybrid vertical and horizontal systems to reduce the depth of boreholes in order to decrease cost, avoid groundwater interactions, and improve overall project likelihood.

## REFERENCES

- Association, I. G. S. H. P., 2008, Accredited GeoExchange Installer Training; Designing the Ground Heat Exchanger, IGSHPA, p. 47.
- Busby, J., Lewis, M., Reeves, H., and Lawley, R., 2009, Initial geological considerations before installing ground source heat pump systems: Quarterly Journal of Engineering Geology and Hydrogeology, v. 42, no. 3, p. 295-306.
- Change, I. P. o. C., 2015, Climate change 2014: mitigation of climate change, Cambridge University Press.
- Company, J. P. R., 1964, Borehole Casing, in Office, U. S. P., ed., Volume US3126959A: United States of America.
- Council, N. R., 2001, Climate change science: An analysis of some key questions, National Academies Press.
- Dibblee, T. W., 2001, Geologic Map of the Whittier and La Habra Quadrangles (western Puente Hills) Los Angeles and Orange Counties, California, Dibblee Geological Foundation.
- District, O. C. W., 2004, Groundwater management plan: See: [www.ocwd.com](http://www.ocwd.com).
- Funabiki, A., and Oguma, M., 2017, Effects of Groundwater Flow on a Ground Source Heat Pump System: Journal of Thermal Science and Engineering Applications, v. 9, no. 2, p. 021008.
- Muncie, I., 1979, Ball State University: Department of Urban Planning.
- O'Connell, S., and Cassidy, S. F., Recent large scale ground-source heat pump installations in Ireland, in Proceedings Proc. International Geothermal Conference2003, Citeseer.
- Oreskes, N., 2004, The scientific consensus on climate change: Science, v. 306, no. 5702, p. 1686-1686.

## **Testing Relations Between Volcanic and Plutonic Rocks on the Kern Plateau, Sierra Nevada**

**Brian Magumcia**

**Advisor: Diane Clemens-Knott, Ph.D.**

*Department of Geological Sciences, California State University, Fullerton*

### **ABSTRACT**

The Sierra Nevada was once a continental arc similar to the chain of volcanoes in Chile. Mesozoic in age, hundreds of magma bodies, or plutons, were emplaced along the western coast of the North American plate. Understanding products of arc magmatism by studying the exposed plutons in the Kern Plateau will contribute to improving our understanding of the overall history of the Southern Sierra Nevada, as well as our understanding magmatism at continental margins during the Mesozoic.

For this project three igneous rocks--a granite, a hypabyssal granite, and a dacite--will be explored by comparing their composition, petrography, and numerical ages. Cogenetic plutonic and volcanic rocks are uncommon in the Sierra Nevada; however, according to the reconnaissance geologic map by Donald Ross, all of the rocks are mapped as Cretaceous. One possible relationship the rocks might share is that these plutonic and volcanic rocks originated from the same magma chamber (i.e., "comagmatic"). Another hypothesis is that the hypabyssal granite and the granite are related to each other but not to the overlying volcanic ash. Petrological observations, such as documenting common mineral assemblages, will establish a baseline to whether the rocks are related or not. Geochemical analysis utilizing XRF will hopefully support conclusions regarding relationships derived from the mineral assemblages. Lastly, uranium-lead dating of zircons separated from the rocks will provide a final test of the possible relationship between the plutonic and volcanic rocks of the southern Kern Plateau.

### **REFERENCE**

Ross, D.C , 1995 Reconnaissance geologic map of the southern Sierra Nevada, Kern, Tulare, and Inyo counties, California: U.S Geological Survey, scale 1:125,000

# **Geochemical and Petrographic Analysis of Salt Dome Associated Calcite Phases in Gulf Coast Cap Rocks: Implications for Carbon Sources and Paragenetic Evolution**

**Connor Frederickson**

**Advisor: Sean Loyd, Ph.D.**

*Department of Geological Sciences, California State University, Fullerton*

## **ABSTRACT**

Salt dome-associated calcites of the Gulf of Mexico region exhibit multiple phases with varying physical properties. These phases are thought to form through microbially mediated chemical reactions that involve hydrocarbons, which locally accumulate around salt domes. Cap rock calcites from six salt domes in the Gulf of Mexico region were analyzed for this study. Petrographic analysis was used to identify different calcite phases within each sample and document their crystallographic and spatial characteristics, to assess their relative order of precipitation (i.e. paragenetic evolution). Samples were then drilled from each identified phase and subjected to carbon isotope analysis. Measurements of isotope composition allowed for comparison to known values of Gulf Coast hydrocarbons (e.g., methane and petroleum) and could be used to identify the carbon source(s) for each phase. It was hypothesized that observed petrographic differences between phases was a result of differences in carbon sources.

A total of six distinct crystallographic phases were observed among the samples, with most samples containing at least two phases. Measured  $\delta^{13}\text{C}_{\text{carb}}$  values for these phases range from  $-52.42$  to  $-20.23\text{\textperthousand}$  (VPDB). The majority of values (27 of 38) fall between  $-25$  and  $-35\text{\textperthousand}$ . These values are consistent with those of regional methane and petroleum. The range of values suggest that phases incorporated carbon from a mixture of the two sources. Petroleum and methane fractions for each sample were calculated and range from 0.019 to 0.969 for methane and from 0.031 to 0.981 for petroleum. The data collected does not show a direct relationship between the carbon sourcing and petrographic characteristics of calcite phases. Despite a lack of correlation between calcite phase morphology and isotope composition, the results of this study indicate that salt dome environments represent significant sinks for subsurface hydrocarbons.

## **Using a Virtual Field Trip to Teach the Plutonic History of Yosemite**

**Isabel A. Guinto**

**Advisor: Natalie Bursztyn, Ph.D.**

*Department of Geological Sciences, California State University, Fullerton*

### **ABSTRACT**

As a way to compensate for lack of economic support and convenience of real world field trips, educational virtual field trips (VFT) can be incorporated into teaching strategies to provide experience based learning to a broader audience. The incoming college students are from Generation Y, a group that grew up with the familiarity of technology, view repetition as mundane, and want to be guided through tasks, not enforced. VFTs provide an immersive that allows students to experience learning in a dramatically different way than the typical classroom scenario. Students can work independently at their own pace using their own smartphones and tablets. When used as a pre and post method for enhancing and reviewing real field trips or lectures, virtual field trip technology and interactive experiences have been proven to increase student motivation.

Through a roadside field trip guide application for smartphones and tablets, our proposed VFT of Yosemite National Park informs users about the volcanic geologic history of the area. Users are guided to observe outcrops that tell the plutonic story of how Yosemite's rocks formed from magma millions of years ago. The users are intended to be entry level geology students and public tourists who visit the park. The story line for this virtual field trip will follow interpreting the formation of Yosemite through geologic evidence found along the two main driving routes through the park of the park. The first route is through Yosemite Valley and the second, along Tioga Pass Road (Figure 1). To explain the geologic processes along a particular route, the app will activate a narration of each field trip stop based on the user's GPS location. The VFT app may also be used in classroom without GPS triggers. This interactive virtual field trip of Yosemite National Park will provide an example of a geologic history that can intrigue the general public and educate college students about geology applied in a spectacular real-world setting.

# Stratigraphic Variability in Response to Environmental Changes Across Short and Long Time Scales Along the Southern Monterey Bay Continental Shelf

Jamie Hayward

Advisor: Joe Carlin, Ph.D.

Department of Geological Sciences, California State University, Fullerton

## DISCUSSION

Modern continental shelf stratigraphy preserves a high-resolution record of complex natural and anthropogenic processes that operate on a variety of timescales. Long-term scales, from centuries to millennia, can record sea level and/or climatic changes, whereas short-term scales, from days to years, may record events such as storms and floods. Mid-shelf mud deposits offer the ideal location to study how strata form from these variable

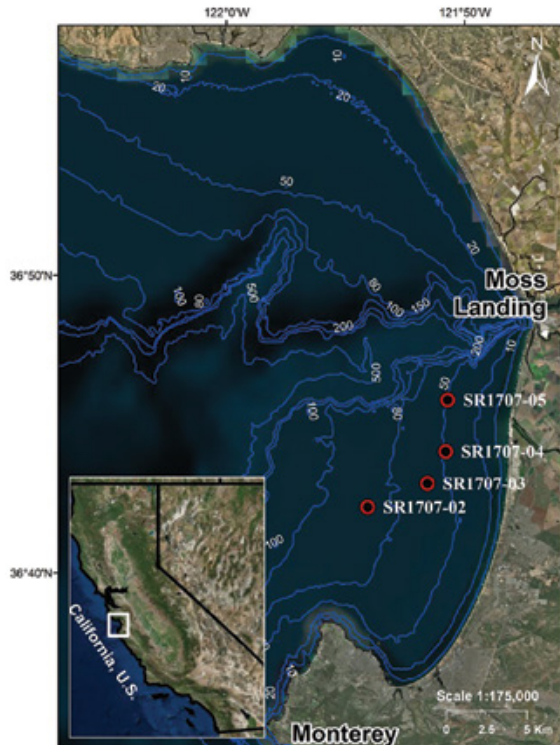


**Figure 1.** Map of the study area in Monterey Bay, CA. Coring locations are shown by the red and black dots. Blue contour lines indicate sea floor depth in meters.

processes and timescales. These features are common to continental shelves across a variety of climate and tectonic settings (high and low latitude shelves and along active and passive margins), and ultimately provide a significant contribution to continental margin sediment budgets during interglacial periods. One such mid shelf mud deposit, the Salinas River Mudbelt (SRM) located along the central California coast within Monterey Bay, is a dynamic system over modern times (past ~200 years) as it responds to both short-term event-driven processes and longer-term climatic cycles. Over shorter terms, the SRM is the sink for the Salinas River, which has produced some of the most substantial event-driven sediment fluxes in the conterminous U.S. While over longer terms, the SRM is heavily influenced by climatic cycles such as the Pacific Decadal Oscillation (PDO). Therefore, the SRM may offer insight into how both event-scale and decadal-scale processes collectively influence strata formation along continental margins.

To address this, we collected short sediment cores, ~30 cm long, from four locations throughout the SRM (Figure 1). Using a multi-corer, four subcores were collected at each location, with one subcore from each location dedicated to core imaging and properties scanning, one subcore dedicated to physical properties analyses, one subcore dedicated to geochronology, and one subcore preserved as an archive. The physical properties subcores were subsampled into 1cm intervals for sediment texture and composition analyses, and the geochronology subcore was subsampled into 1-2 cm intervals for short-lived radioisotope analyses.

Sediment texture was determined by grain size analysis where each sample was pretreated to remove organic

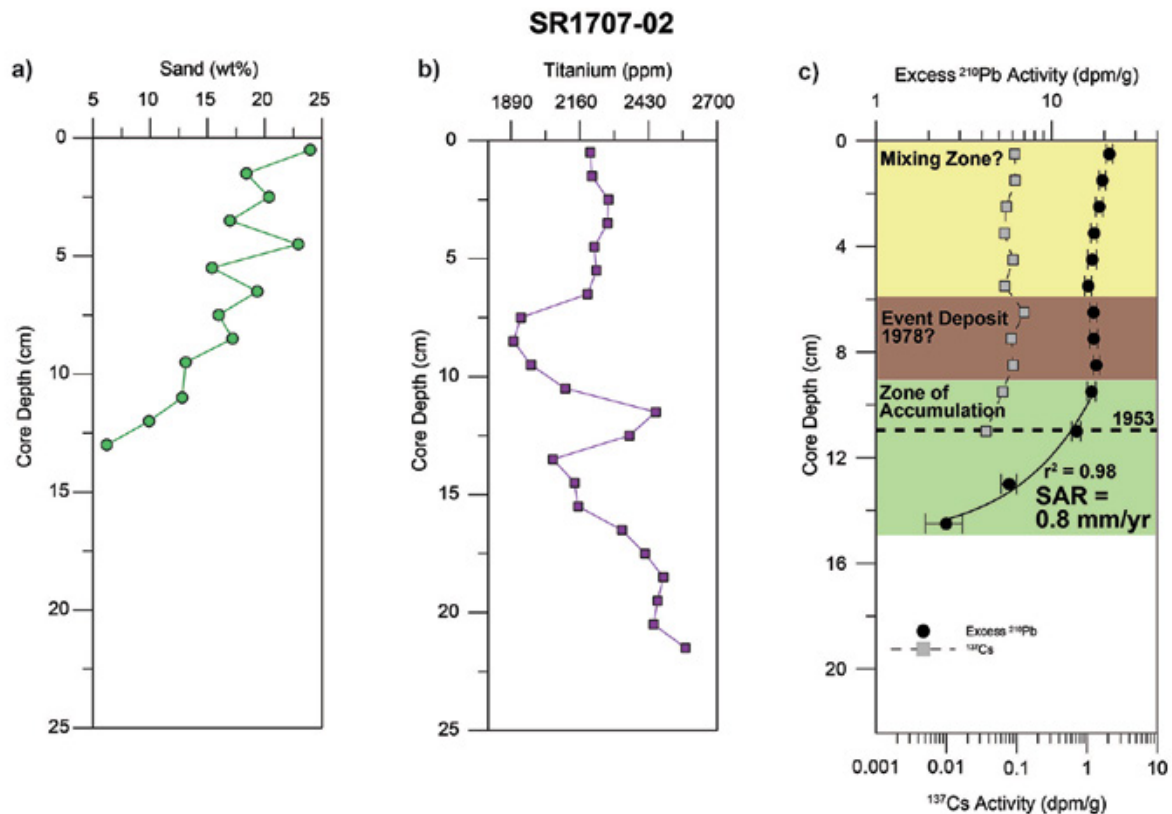


**Figure 2.** Sediment texture, composition, and geochronological results for site SR1707-02. a) Plot of the sand content down core. b) Plot of titanium concentration in parts per million down core as measured from the XRF analysis. c) Plot of excess  $^{210}\text{Pb}$  activities (black circles) and  $^{137}\text{Cs}$  activities (grey squares) down core. From the  $^{210}\text{Pb}$  we have identified 3 zones within the core: a possible surface mixed layer (yellow) with near uniform activity with depth, an event deposit (brown) with relatively elevated and uniform activities we have dated to  $\sim 1978$ , and the zone of accumulation (green) where activities decrease exponentially with depth. From the zone of accumulation, we have estimated a sedimentation rate of  $\sim 0.8 \text{ mm/yr}$ . From the  $^{137}\text{Cs}$  data we have identified the 1953 horizon (dashed black line).

matter, carbonates, and biogenic silica prior to being measured using laser diffraction to determine particle size distributions. Additionally, sediment composition was determined for each core through x-ray fluorescence (XRF) using a Thermo Niton Portable XRF. For XRF analyses, the cores were measured at a 1 cm sampling frequency with four energy filters at 30 seconds per filter to obtain elemental concentrations in parts per million (ppm). For these analyses, we focused on the abundance of titanium in the core as a proxy for terrestrial sediment. Sediment accumulation rates and age estimates were determined by measuring down-core activities of short-lived radionuclides  $^{210}\text{Pb}$  and  $^{137}\text{Cs}$  using high purity, broad energy, germanium gamma spectrometer.

Grain size results from site SR1707-02 show an upward coarsening sequence, increasing consistently from 5% to 25% sand content over a 15 cm depth (Figure 2a). The titanium concentrations downcore for SR1707-02 are shown in Figure 2b, with titanium concentrations generally decreasing up core. Geochronology results from site SR1707-02 are shown in Figure 2c for both  $^{210}\text{Pb}$  and  $^{137}\text{Cs}$  activities. The  $^{137}\text{Cs}$  had a maximum penetration of 11 cm, a depth which we can assign the date of 1953AD. From the  $^{210}\text{Pb}$  activities, we observed three distinct layers. The upper layer, from the surface down to a depth of 6 cm, showed relatively uniform activities with depth, thus we classify this as the surface

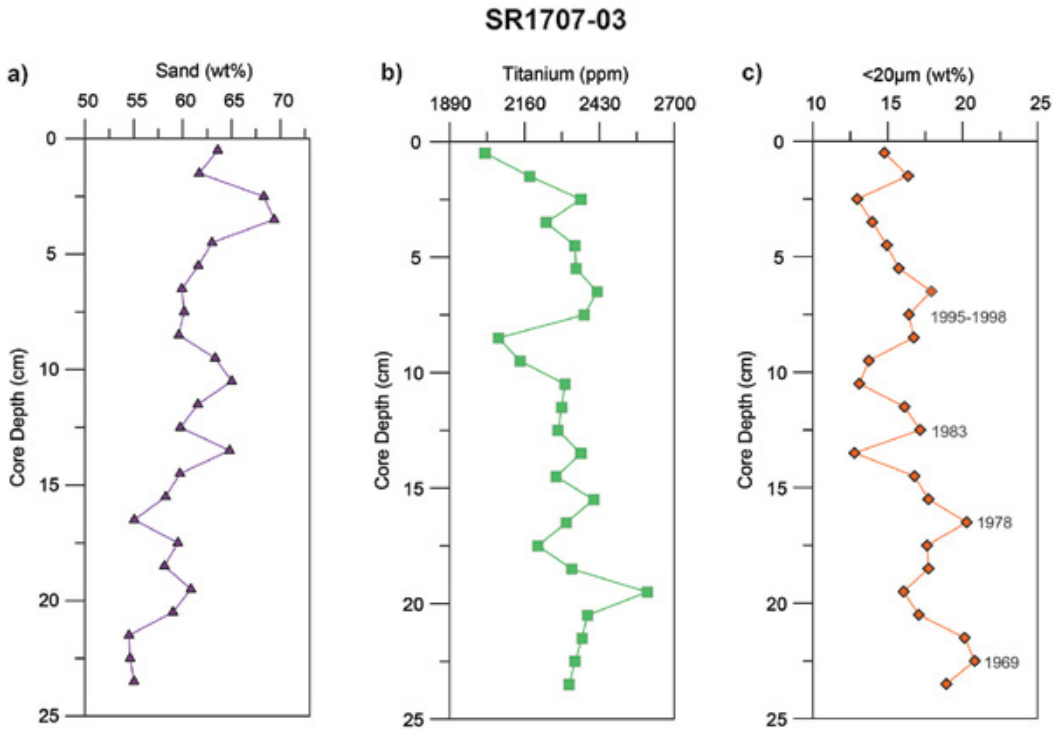


**Figure 3.** Sediment texture and composition result for site SR1707-03 down core. a) Plot of sand content. b) Plot of titanium concentration in parts per million as measured from the XRF analysis. c) Plot of fine sediment fraction (< 20 µm), with peaks attributed to specific flood years.

mixed layer. The second layer, from 6-9 cm, also shows relatively uniform activity with depth, but slightly elevated activities from the surface mixed layer, thus we interpret this as a possible event deposit. The bottom layer, below 9cm, activities decrease exponentially with depth, thus reflecting steady-state accumulation. From this bottom part of the core, we can estimate a ~ 0.8 mm/yr accumulation rate.

Grain size results for site SR1707-03 reveal a similar coarsening upward sequence like site SR1707-02. Notably, this core has a much higher sand content than site SR1707-02, with increases from ~55% to a maximum of ~70% sand (Figure 3a). While this core was generally sand-dominated with the coarsening upward trend, we also observed four distinct peaks in fine-grained sediment (< 20 um) at depths of 7-9cm, 13cm, 17 cm, and 23cm (Figure 3c). The titanium concentrations from site SR1707-03 show a similar decreasing up

core trend as was observed at SR1707-02 (Figure 3b). Geochronology from site SR1707-03 was inconclusive, however, <sup>137</sup>Cs was detected throughout the core, indicating that all the sediment was deposited after 1953 AD.

Using geochronology results from site SR1707-02, we reconstructed mass accumulation rates (MAR) over time (Figure 4a). Prior to the 1950s, the MAR averaged 0.05 g/cm<sup>2</sup>/yr. During the mid-1950s to late 1960s, the MAR increased, reaching a maximum of 0.3 g/cm<sup>2</sup>/yr at the event deposit identified from the <sup>210</sup>Pb data, which we attribute to the combined effect of major floods in 1969 and 1978. Post flooding events from 1969-1978, we see a decrease in MAR. However, it maintains a higher average rate (0.14 g/cm<sup>2</sup>/yr), than before 1969.

These results indicate that the combined event deposits in 1969 and 1978 (we are unable to separate given the data) may have served as the tipping point, initiating a more systemic change in the sedimentary

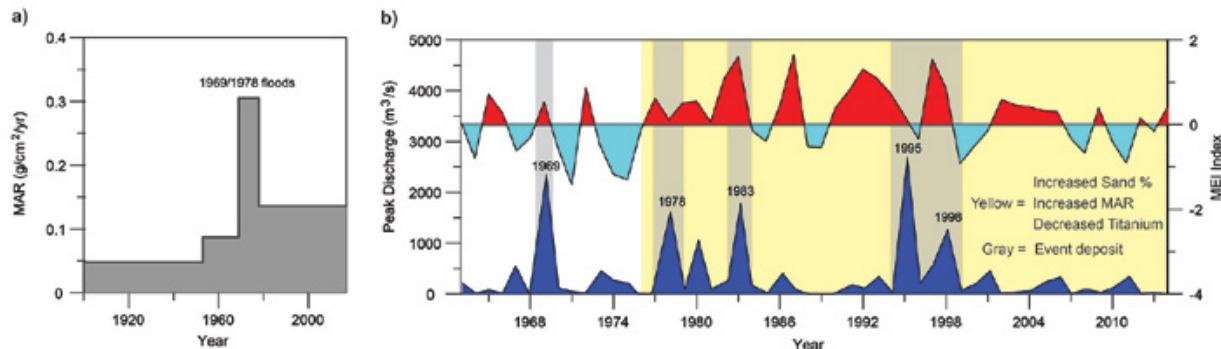


**Figure 4.** Plots of sedimentation, climatic, and hydrologic variability over time. a) Plot of mass accumulation rates (MAR) versus time, reconstructed from geochronology results in Figure 2c. The peak is attributed to the 1969–1978 floods. b) Plot of El Niño and peak discharge on the Salinas River. The upper plot shows the Multivariate El Niño Index (MEI) where El Niño years are shown in red and La Niña years in blue. In the lower plot the dark blue peaks represent the peak discharge of the Salinas River from 1963–2014 as measured from the lowermost gage station at Spreckles, CA. The gray shaded areas labeled with years represent event deposits that are also labeled in the < 20 µm graph in Figure 3c. The yellow shaded area marks the change in Pacific Decadal Oscillation (PDO) where El Niño events are more frequent and intense, and when we begin seeing increasing sand, MARs, and decreasing titanium in the sediment cores.

system which increased the total amount of sediment delivered to the shelf. Similarly, in the same time period, we observed trends of increasing sand and decreasing titanium content at both sites. As titanium is strongly aligned with terrestrial sediment sources, a decreasing terrestrial signal coupled with increasing sand content implies that the increased sediment delivery is coarser but is progressively being sourced from non-terrestrial environments. We interpret these changes to reflect increasing sediment delivery from an oceanographic source, likely the result of remobilization and transport of inner shelf sands due to increased wave activity. This period of increased oceanographic sediment transport corresponds to a climatic shift, specifically changes in El Niño Southern Oscillation (ENSO) events and Pacific Decadal Oscillation (PDO) cycles. In Figure 4b the PDO change can be seen as more frequent, intense, and prolonged ENSO events starting in the late 1970s. This climate shift is reflected in the cores as the increased MAR, increased sand, and decreased titanium as oceanic storms during these ENSO events remobilize sand from the shelf and transport it across-shelf to the SRM.

Superimposed on this decadal climate signal, we also observe event-scale layers preserved in the cores. At site SR1707-02 we see this event layer in the  $^{210}\text{Pb}$  data, which we attribute to floods in 1969 and 1978. Additionally, at site SR1707-03 we observe event signals as peaks in the < 20 µm grain size fraction, a proxy for fluvial flood deposits on continental shelves. We attribute the four peaks in the < 20 µm grain size fraction as the four largest floods on the Salinas River in terms of peak discharge since 1953 (Figure 4b). The lowermost peak we attribute to the 1969 flood, with 1978 and 1983 above that, and the uppermost double peak likely a combination of floods in 1995 and 1998.

Collectively these results indicate the stratigraphy of the SRM reflects decadal-scale shifts in climate with the shift in the PDO driving a change in sedimentation dominated by fluvial delivery to oceanic delivery. Yet, super-imposed on this overall trend are signals from individual events such as the floods in 1969, 1978, 1983, and 1995/1998. Over a broader context, this study reveals that decadal-scale ocean-climate forcing's, like PDO, and episodic event deposits from storms can be preserved in the sedimentary record on a continental shelf.

# **Investigating The Causes Of Compositional Variation In The Half Dome Granodiorite, Tuolumne Intrusive Complex, Yosemite National Park, Ca: Big Or Small Magma Chambers?**

**John Ayers**

**Advisor: Valbone Memeti, Ph.D.**

*Department of Geological Sciences, California State University, Fullerton*

## **ABSTRACT**

The understanding of the growth and behavior of magmas in deep magma reservoirs (now preserved as plutons) provides knowledge on volcanic eruptions and improves the ability to predict future volcanic events. Scientists agree that magma reservoirs at depth feeding such eruptions grow incrementally over time, however, the size magma reservoirs reach when they grow at the emplacement level and which process is responsible for the compositional variations found in these plutonic bodies is not very well understood.

Coleman et al. (2012) suggested that the formation of the Half Dome Granodiorite unit in the western lobe (and by inference the entire Tuolumne Intrusive complex) occurred through a stacked series of km scale repeating magmatic ‘cycles’ (i.e. sills or laccoliths). These moderately outward dipping sheet-like bodies display a sharp eastern contact of more mafic composition granodiorite that gradationally becomes more felsic towards the west due to local fractional crystallization. This stacked sill-model contrasts with previous models of large magma mush bodies (e.g. Memeti et al., 2014; Paterson et al., 2016), which suggest that pulses of magma amalgamate to form large magma chambers whose compositional variation is derived from magma chamber processes, such as wide-scale fractionation and mixing of magmas.

Research in Lyell Canyon of Yosemite National Park tested the Coleman et al. (2012) and Memeti et al. (2014) models in the Half Dome granodiorite unit on the east side of the Tuolumne intrusion where compositional variations are observed. If the Coleman

et al. (2012) model is correct, the stack of sills should be observed on the west side as well. Field mapping at the transition of the southeastern Kuna Crest lobe to the main Tuolumne intrusive complex determined gradational transitions between units. The equigranular Half Dome granodiorite unit exhibits localized, meter-wide scale aplite dike intrusions with sharp contacts and varied orientations. Locally, equigranular Half Dome granodiorite is more leucocratic, i.e. containing less mafic minerals. Leucocratic equigranular Half Dome predominately displays gradational transitions within the equigranular Half Dome unit occasionally accompanied by localized intermingling regions expressing a sharp contact. XRF whole rock geochemical analysis was conducted on nine samples to determine the type of magmatic process(es) and the length scale that are responsible for the changes in composition. Geochemical analysis for example shows a decrease in mg # and Sr with increasing SiO<sub>2</sub> with the equigranular Half Dome Granodiorite plotting at lower SiO<sub>2</sub> and high mg #, while the leucocratic equigranular Half Dome and aplite dike samples plot at increased SiO<sub>2</sub>.

The findings suggest that the sheet-model interpretation by Coleman et al. (2012) developed for the west side of the Tuolumne cannot be verified for the east side. The gradational variations between different Half Dome compositions and local aplite dikes, cross cutting relationships, petrography and geochemistry are more in accord with wide-scale fractionation, better agreeing with a larger, interconnected magma mush model.

# **Manageable Molecular Mineralogy: Developing a User-Friendly Interactive Mineralogy Game for Mobile Devices**

**Leah Wiitableke**

**Advisor: Natalie Bursztyn, Ph.D.**

*Department of Geological Sciences, California State University, Fullerton*

## **ABSTRACT**

In this digital age, pedagogy falls short with methods of teaching mineralogy being stuck in the past. This project aims to address the problem documented in the chemistry community and anecdotal in the geology community: students cannot visualize crystal structure. In the geoscience community, there have been papers published on students having difficulty with the visualization of structural geology and ways to solve this problem. However, with respect to mineralogy, the struggle students have with the material has not been documented. Nonetheless, anecdotally, there is teacher dissatisfaction with the poor retention of material from mineralogy classes.

Research has found that information relayed through images is retained better than information relayed through text. In fact, three-dimensional (3D) models and visuals have been shown to be the most effective methods for teaching and have results of greatest student retention of material. Due to the great leap in technology in the last decade, reports on the use and effectiveness of virtual reality and games in education has taken off.

Here we describe the design of an interactive game to teach crystal structure to undergraduates. Game-like elements engage the user, while touch-manipulated 3D models allow students to play with the structure of a mineral at the molecular level. Starting from an outcrop and zooming into minerals, then to individual atoms, students will be able to build different silicate minerals by rearranging silicon tetrahedra to see how different structures affect the outward appearance of the crystal. We believe this game will improve student learning of minerals and their structure and will help bridge the technology gap between the outdated ball and stick models and today's digital native undergraduates. By using up-to-date technology we can combine text, audio, video, and user-manipulated 3D models to better help students understand the molecular world with a game for mobile smart devices.

# **Are the “Cretaceous” High-Silica Granites Associated with the Low-silica Summit Gabbro Actually Late Jurassic age?**

**Rodrigo Aviles**

**Advisor: Diane Clemens-Knott, Ph.D.**

*Department of Geological Sciences, California State University, Fullerton*

## **ABSTRACT**

The Summit gabbro is a very low silica magmatic intrusion that crops out in the southern Sierra Nevada Mountains. Outcrops of the Summit gabbro are aligned along two NW-oriented trends along with very high silica rocks called aplites. This aplite unit (Ka) is significant because it has high concentrations of tungsten (W) and molybdenum (Mo). Previous geochronologic work by CSUF students have demonstrated that the Summit Gabbro is Late Jurassic in age, while previous mappers assumed that the aplite was Cretaceous in age, or younger than the gabbro. In this study, I will date the aplite rock, along with nearby high-silica granites (e.g., Krr, Kcd) to assess whether these rocks may all actually be Late Jurassic in age. Dating, coupled with petrographic descriptions and whole-rock geochemical analysis, will be directed at evaluating whether the low-silica Summit gabbro and the high-silica aplite might together form the plutonic equivalents of the 148-million-year-old Independence dike swarm. If the low-silica Summit gabbro and the high-silica aplite correspond to the Independence dike swarm, then the ages of both rocks will be confirmed to being Late Cretaceous.

Samples collected (3) in eastern Sierra Nevada will be tested by petrography, geochemical analysis, and Zr dating. Want to determine if these cretaceous high-silica granites (Ka), and other granitic plutons (Krr, Kcd) are associated with the low silica-gabbro rocks. If high-silica granites are same age as low-silica Summit gabbro, can these high-silica granites be associated with the Independence Dike Swarm (~148 m.y.).

# **Investigating Volcanic and Plutonic Connections at Iron Mountain Pendant, Sierra National Forest, CA**

**Sabrina Green**

**Advisor: Valbone Memeti, Ph.D.**

*Department of Geological Sciences, California State University, Fullerton*

## **ABSTRACT**

Volcanic eruptions and associated secondary hazards pose a threat to society on a daily basis, yet the causes of eruption and what occurs in the magma chamber before and during an eruption is poorly understood. Volcanoes are connected to deeper plutonic systems of a vertically extensive magma plumbing; both volcanic and plutonic rocks record magmatic histories that help unravel the magma processes at depth. The focus research area is the Iron Mountain pendant in the Sierra Nevada batholith, located northeast of Oakhurst, CA, which exposes both Cretaceous volcanic and plutonic rocks of what we hypothesize to be coeval in age and thus part of the same plumbing system. The purpose of this research is to ascertain the rocks are contemporary and to understand the chemical connection between the volcanic and plutonic rocks in order to help predict volcanic eruptions in the future.

The goals are to firstly determine the age of the volcanic and plutonic rock units in the area to make sure the rocks all formed contemporaneously and therefore could have belonged to the same magma plumbing. If this can be established, the geochemical analyses of volcanic and plutonic rocks will test if the rocks are compositionally equivalent or complementary to one another. If these different units are complementary in composition, we will conclude that fractional crystallization of the magma chamber took place. If they are equivalent, then we can deduce that part of a homogeneous magma chamber was evacuated.

To determine the age of the volcanic and plutonic rocks, zircon separations will be obtained from the rock samples and used for U-Pb zircon geochronology using the LA-ICPMS technique at the University of Arizona Laserchron lab. Using a polarizing light microscope, minerals present in the different rocks will be determined by studying thin sections to investigate if the mineralogy between volcanic and plutonic rocks is similar or different. Disequilibrium mineral textures will point to magma mixing before the eruption. Lastly, to also test this hypothesis through geochemical compositions, one-inch homogeneous glass beads will be made from powders of the rock samples and analyzed with the XRF machine at Pomona College, which will determine major oxides and trace elements present in both rock types. Petrography and whole rock geochemistry will help determine whether the system is equivalent or complementary in composition and test if magmas were fractionated or mixed in the magma chamber before the volcanic rocks erupted.

# **Basalt Correlation in the Sylvania Mountains, California, by X-ray Fluorescence Spectroscopy (XRF)**

**Shayna Avila**

**Advisor: Jeffrey R. Knott, Ph. D.**

*Department of Geological Sciences, California State University, Fullerton*

## **ABSTRACT**

I collected four rock samples from Willow Wash in Fish Lake Valley, California, and two rock samples from Horse Thief hills, California. I analyzed these samples with X-Ray Fluorescence (XRF) and obtained the geochemical signature for all six samples. The Willow Wash samples are classified as basalt (47-52% SiO<sub>2</sub>). The Horse Thief hills samples are classified as andesite-trachyandesite (56-60% SiO<sub>2</sub>). The four samples from Willow Wash are dated at 11.5 Ma (by others) and using Zr/Ba and Ce/Y ratios I correlated these basalts with basalts in the White Mountains, atop the Horse Thief hills, Fish Lake Valley, and Deep Springs Valley. This correlation shows that the 11.5 Ma basalt flowed over 40 km and predates the formation of Fish Lake Valley. The 6.2 Ma andesitic rocks are unique and interbedded with sedimentary rocks, thus representing a remnant Miocene basin now uplifted and exposed on the south side of the Horse Thief hills. These data constrain the formation of Fish Lake Valley and the Fish Lake Valley Fault zone to after 11.5 Ma.

## **INTRODUCTION**

### **Location**

The Sylvania Mountains are located in Inyo County, California, and Esmeralda County, Nevada, 50 km (30 miles) east of Bishop, California between Death Valley, to the south, and Fish Lake Valley, to the north (Figure 1). The Sylvania Mountains are a subrange of the Last Chance Range separated by Cucomungo Canyon. The Horse Thief hills are another Last Chance subrange that was informally named by Reheis and Sawyer (1997). The

Horse Thief hills are a NW-SE trending ridge connecting the Last Chance Range and the White/Inyo Mountains that forms the topographic divide between Fish Lake Valley and Eureka Valley just west of the Sylvania Mountains.

McKee and Nelson (1967) mapped three groups of basalt outcrops in the Sylvania Mountains and Horse Thief hills. The first group is in Willow Wash of the Sylvania Mountains and are part of the Tertiary Esmeralda Formation (Tb on Figure 2). The second basalt group is also Tertiary basalt (Tb on Figure 2); however, these outcrops are on the south flank of the Horse Thief hills. The third group is Quaternary-

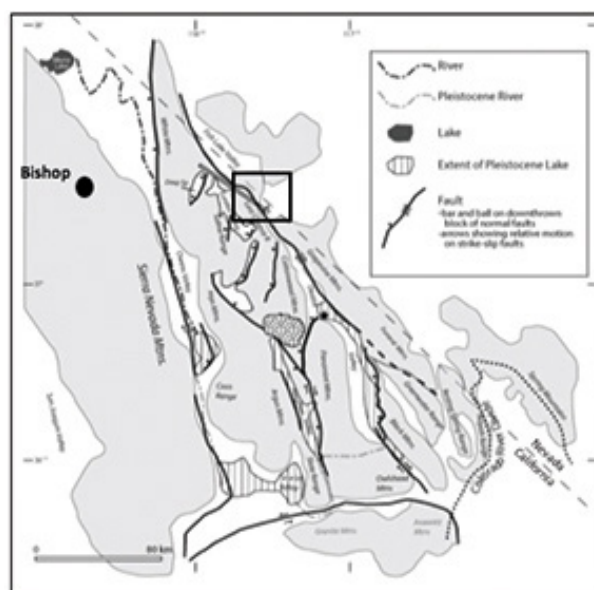


**Figure 1.** Geographic map of mountains and valleys of the western Basin and Range, showing major faults. The box is the area of research in the Sylvania Mountains.



**Figure 2.** A portion of the Geologic Map of the Soldier Pass Quadrangle, California and Nevada (McKee and Nelson, 1967). The circles indicate sample locations from the Tertiary Esmeralda Formation basalt and Tertiary basalt. The squares are the locations of QTb basalt samples collected by Kato (2015) and J. Knott.

Tertiary basalt (Qtb on Figure 2), which are presumably younger than the Teb and Tb. Reheis and Sawyer (1997) combined all three of these basaltic rocks into one map unit described as Miocene basalt and rhyolite (Tv).

## OBJECTIVES

The objectives of this study are to examine the geochemistry of the basalts found in the Willow Wash and Horse Thief hills, in order to determine if these three groups of basalts mapped by McKee and Nelson (1967) are the same flow or from the same magmatic source. Correlating these basalts may have implications for the timing of Basin and Range extension and reconstruction of Fish Lake Valley and the Fish Lake Valley fault zone.

## BACKGROUND

### Basalt Geochemistry

Ormerod et al. (1988) studied the late Cenozoic basalts

in the Western Great Basin of California and Nevada. They compared Zr/Ba ratios to  $^{87}\text{Sr}/^{86}\text{Sr}$  ratios in order to determine trace element patterns that indicate magmatic source and assimilation. They found that these basalts are “from two distinct mantle source regions”; mantle lithospheric dominated, and asthenospheric upper mantle dominated. Zr/Ba values  $<0.20$  indicate older lithospheric dominated basalts with a “subduction related geochemistry”, and Zr/Ba values  $>0.20$  indicate younger asthenospheric dominated basalts “after slab subduction ceased”.

Kempton et al. (1991) explained that basalt volcanism is associated with extensional tectonics in the Southwestern United States. They stated that Basin and Range basalts “have an asthenospheric source,” and “have not been significantly contaminated by lithospheric mantle or crustal material” (Kempton et al., 1991). Kempton et al. found that various ratios of elements and oxides might establish regional trends. They classified the Sylvania Mountains area as western

Great Basin (WGB). Basalts in the WGB were enriched in Ba and depleted in Nb concentrations. Plots of Zr/Ba versus Ce/Y showed, like Ormerod et al. (1988), that the majority of WGB basalts had Zr/Ba ratios  $<0.5$  and Ce/Y ratios ranging from  $\sim 2\text{--}7$ .

In the Pliocene Coso volcanic field, 150 km south of the Sylvania Mountains, Pluhar et al. (2005) used geochemical composition determined by x-ray fluorescence (XRF) to separate basalts that are not visually distinct into distinct volcanic units. They showed, like Ormerod et al. (1988) and Kempton et al. (1991), that using ratios of large ion lithophile elements (e.g., Ba, Rb) and high field strength elements (e.g., Zr, Nb) are useful in discriminating among different volcanic rocks.

### Basalt Geochronology

Dalyrymple (1963) dated by K/Ar a basalt flow in Deep Springs Valley at  $10.8\pm1.0$  Ma (whole rock) with an underlying rhyolite tuff at  $10.9\pm0.2$  Ma (whole rock). He named these samples the Deep Springs basalt and Deep Springs tuff and traced the basalt flow west into the White Mountains.

Reheis and Sawyer (1988) studied the basalts of the White Mountains, Fish Lake Valley and Deep Springs Valley as well. They stated, “Major oxide and trace element analyses indicate that the basalts are from the same sequence of flows or at least share a common parentage” (Reheis and Sawyer 1997, p. 284), but did not present the geochemical data. They published a K/Ar

age determination of  $6.7\pm0.2$  Ma (KA-43) for the Tb of McKee and Nelson (1967) on the south side of the Horse Thief hills along with  $11.0\pm0.3$  Ma and  $11.5\pm0.4$  Ma ages for the Tev basalt of McKee and Nelson (1967). Based on these age determinations, Reheis and Sawyer (1988) re-designated the Tb, QTb and Tev of McKee and Nelson as Miocene basalt (Tb).

Several outcrops of the Tb of Reheis and Sawyer were dated using the  $^{40}\text{Ar}/^{39}\text{Ar}$  method by N. Mueller. This includes the basalt at Willow Wash and atop the Horse Thief hills. These analyses yielded similar ages of 11.5 Ma (N. Mueller, personal communication).

### Tectonics

According to Reheis and Sawyer (1997), the basalt flows in Willow Wash are 11.9–10.7 Ma, and the rhyolite of Horse Thief hills is 8.2 Ma. “Thus motion on the Fish Lake Valley Fault zone began after 11.9–8.2 Ma” (Reheis and Sawyer, 1997, pg. 287).

McQuarrie and Wernicke (2005, pg.7) made a similar statement that: “recognition and correlation of the dismembered early extensional basin, in conjunction with stratigraphic constraints from other Tertiary deposits in the region indicates that fragmentation occurred mainly 12–2 Ma”.

### METHODS

I collected six basalt samples from the Sylvania Mountains (Figure 3) and recorded the locations with a GPS (Table 1).

**Table 1.** Sample Names, latitude and longitude of samples collected.

Sample Name	Latitude	Longitude
STA-WW-060216-1	37.37134	-117.78992
STA-WW-060216-2	37.36977	-117.79115
STA-WW-060216-3	37.36741	-117.78120
STA-WW-060216-4	37.36592	-117.79092
STA-HTH-060216-5	37.34595	-117.83612
STA-HTH-060216-5A	37.34595	-117.83612



**Figure 3.** Photograph of sample STA-WW-060216-1 in Willow Wash. The sampled basalt outcrop is the upper dark rock with a light-colored rhyolite below.



**Figure 4 (Upper left).** Cooled graphite crucibles that contain fused glass beads.

**Figure 5. (Upper right).** Heating of graphite crucibles in oven in order to make glass bead for XRF.

These samples were crushed and powdered at CSU Fullerton. The powdered samples were transported to Pomona College where 3.5 g of sample were mixed with 7.0 g of dilithium tetraborate (2:1 ratio; Lackey et al., 2012). These materials were then placed in graphite crucibles and heated to 1000°C to form glass beads (Figures 4 and 5). These glass beads were then powdered a second time, refused again, and then polished on a

diamond lap for analysis by x-ray fluorescence (XRF; Lackey et al 2012).

The XRF data from Pomona College provided the major and trace element whole-rock composition of each of the basalts (Lackey et al 2012). The trace elements were Ba, Ce, Cr, Cu, Ga, La, Nb, Ni, Pb, Rb, Sc, Sr, Th, U, V, Y, Zn, and Zr.

An XRF instrument bombards the sample with emissions of fluorescent x-rays (Wikipedia: [https://en.wikipedia.org/wiki/X-ray\\_fluorescence](https://en.wikipedia.org/wiki/X-ray_fluorescence); accessed March 2016). XRF provides a chemical analysis of the sediment, rock, mineral, or fluid with no destruction of the sample (Wirth and Barth, 2016; Wikipedia: [https://en.wikipedia.org/wiki/X-ray\\_fluorescence](https://en.wikipedia.org/wiki/X-ray_fluorescence); accessed March 2016).

XRF illuminates a sample with an incident beam of x-rays or gamma rays (Wirth and Barth, 2016). The sample becomes excited by the short-wavelength, high-energy radiation. The sample becomes ionized and ejects electrons. These ejected electrons are replaced by electrons from a higher energy orbital. When this occurs, energy is released in the form of radiation (photons or light) (Wirth and Barth 2016). The wavelength and amount of energy released provides both the type and amount of a particular atom (Wirth and Barth 2016).

In order to correlate sample results, I plotted the results on Total Alkali versus SiO<sub>2</sub>, Harker and spider diagrams. This information will provide correlation if the basalts are from the same or a different source.

## RESULTS AND DISCUSSION

Table 2 provides a description of each sample collected. The age of samples STA-WW-060216-1 through 4 is 11.5 Ma (N. Mueller, personal communication, 2016). The color of each of STA-WW-060216-1-4 are all shades of medium to dark gray on the Munsell Rock-Color Chart. Samples STA-WW-060216-1-4 all contain olivine phenocryst ghosts. Geochemically, these samples are basalt with 49.3-51.5 weight percent SiO<sub>2</sub> (Table 3 and Figure 7).

The AJC and EV samples (Figure 7) used in

**Table 2.** Sample Name and description of samples collected

Sample Name	Age (Ma)	Description
STA-WW-060216-1	11.5	Dark gray (N3) Vesicular (<1mm) basalt with olivine phenocryst ghosts; vesicles are symmetrical
STA-WW-060216-2	11.5	Med. Dark gray (N4) vesicular (<1mm) basalt with olivine phenocryst ghosts; vesicles are symmetrical
STA-WW-060216-3	11.5	Dark gray (N3) slightly vesicular (<1mm) basalt with olivine phenocryst ghosts; vesicles are symmetrical
STA-WW-060216-4	11.5	Med. dark gray (N4) slightly vesicular (<1mm) basalt with olivine phenocrysts; vesicles are symmetrical
STA-HTH-060216-5	6.3	Med. Light gray (N6) vesicular (<1mm) basaltic agglomerate volcanic breccia matrix; vesicles are a mix of symmetrical and asymmetrical; less dense
STA-HTH-060216-5A	6.3	Blackish red (5R2/2) highly vesicular (up to 6mm) basaltic agglomerate volcanic breccia clast; vesicles are a mix of symmetrical and asymmetrical shapes; dense

comparison are <50 weight percent  $\text{SiO}_2$  and plot in the basalt and tephrite basanite fields. These rocks are found to the west of Willow Wash in Deep Springs Valley and in the Horse Thief hills, respectively. These rocks are the same age and geochemically similar to the Willow Wash basalts.

The age of samples STA-HTH-060216-5 and 5A is 6.3 Ma (Reheis and Sawyer, 1997). Sample STA-HTH-060216-5 is medium light gray (N6) whereas sample STA-HTH-060216-5A (Figure 6) is a blackish red (5R2/2). Clearly, the volcanic breccia clast sample (STA-HTH-060216-5A) is much darker. Geochemically, sample STA-HTH-060216-5, which makes up the matrix of the volcanic breccia, is andesite with 60.4 weight percent  $\text{SiO}_2$  (Table 3 and Figure 7). STA-HTH-060216-5 is also less dense than STA-HTH-060216-5A. Geochemically, STA-HTH-060216-5A is a trachyandesite (Table 3 and Figure 7).

Based on the petrography, age and geochemical compositions the rocks in the Horse Thief hills and Willow Wash are different. The Willow Wash basalts are a flow with the likely source to the west where the flows



**Figure 6.** Photograph of the volcanic breccia (Samples STA-HTH-060216-5 & 5A) from Horse Thief hills. Sample STA-HTH-060216-5A is the darker clasts of trachyandesite and STA-HTH-060216-5 is the lighter matrix of andesite.

are thicker. In contrast, the Horse Thief hills andesite is a volcanic breccia produced by a more explosive eruption from an unknown source. From a map perspective in

**Table 3.** X-Ray Fluorescence data with concentrations ppm and when labeled weight %.

Sample	STA-WW-060216-1	STA-WW-060216-2	STA-WW-060216-3	STA-WW-060216-4	STA-HTH-060216-5	STA-HTH-060216-5A
SiO <sub>2</sub> (%)	51.5	49.8	49.5	49.3	60.4	56.3
Al <sub>2</sub> O <sub>3</sub> (%)	16.5	15.7	15.3	15.5	16.8	17.4
Fe <sub>2</sub> O <sub>3</sub> (%)	7.4	8.2	8.5	8.8	6.1	6.7
MgO (%)	6.8	8.2	9.5	10.4	2.2	2.2
MnO (%)	0.1	0.2	0.2	0.2	0.1	
CaO (%)	10.5	11.5	11.0	10.1	5.9	8.4
Na <sub>2</sub> O (%)	2.9	2.4	2.2	2.0	3.2	3.3
Ba	1256	1101.3	979	942	3787.3	1425
Na+K	4.7	4.2	3.8	3.5	6.3	6.6
Rb	51	42	36.7	33.3	92.3	99.6
K <sub>2</sub> O (%)	2.1	1.8	1.6	1.5	3.1	3.3
Nb	12.3	12.3	11.3	11.3	28.3	21.7
La	42.8	42.4	45.7	37.8	70.3	77
Ce	96	102	89.3	90	159.3	150
Sr	1079.7	1039.3	950	903.3	763.3	945.3
Nd	52	54.3	55.7	42.3	262.7	56.7
P <sub>2</sub> O <sub>5</sub> (%)	0.6	0.6	0.5	0.5	0.5	0.5
TiO <sub>2</sub> (%)	1.3	1.3	1.3	1.3	1.1	1.3
Sm						
Zr	168	163	155	156.3	0.5	0.5
Hf	10	13	12.3	11	10.3	12
Y	21.3	20.3	21.3	23	33	31
Zn	94.7	94	98.3	91	103.7	94.3
V	248.3	241	230.3	230.7	117.7	155.7
U	5	5.3	5.7	5	3.3	6
Th	8	8	7.3	6.7	11.3	19.3
Ta						
Sc	29	29	28	28	12.3	12
Pr	10.3	11.7	9	9.7	16.7	17
Pb	14	13.3	10.3	9.7	26.7	25.3
Ni	151.3	186.7	596	193.3	3.3	3
Ga						
Cu						
Cr	486.7	476.7	540	480.7	10.3	11.3

may be useful to use the symbol Tvb for the Willow Wash basalts and Tva for the Horse Thief hills andesitic rocks.

The spider diagram of trace elements confirms the differences between the Willow Wash basalts and the Horse Thief hills andesitic rocks (Figures 8 and 9). The trace elements are arranged left to right with incompatibility decreasing to the right and similar

to Figure 3 of Kempton et al. (1991). According to Kempton et Al. (1991), “basin and range basalts have smooth downward trace element patterns that peak at Nb”, and WGB basalts have patterns with “generally lower trace element abundances and peak at Ba rather than Nb.” Willow Wash samples (STA-WW-060216-1-4) and Horse Thief hills samples (STA-HTH-060216-5-5A) all have patterns that peak at Ba rather than Nb (Figure

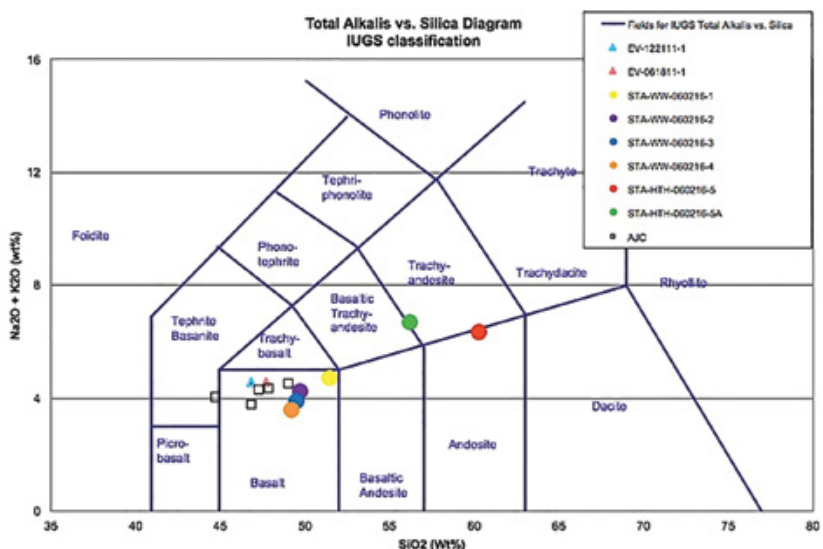


**Figure 7.** Total Alkalies vs Silica diagram used to determine volcanic rock type by plotting  $\text{SiO}_2$  (weight percent) against  $\text{Na}_2\text{O}$  and  $\text{K}_2\text{O}$  (weight percent). All of the Willow Wash samples are basalt. The Horse Thief hills samples are andesite and trachyandesite. EV samples are unpublished results from J. Knott. AJC samples are from Case (2014).

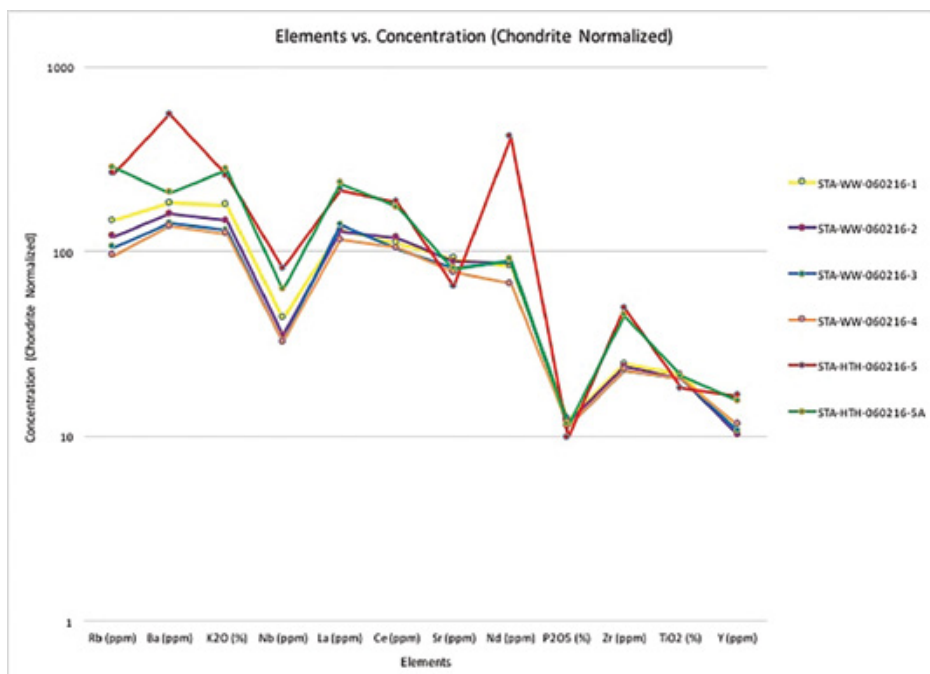


**Figure 8.** Trace element spider diagram patterns for Willow Wash, and Horse Thief hills.

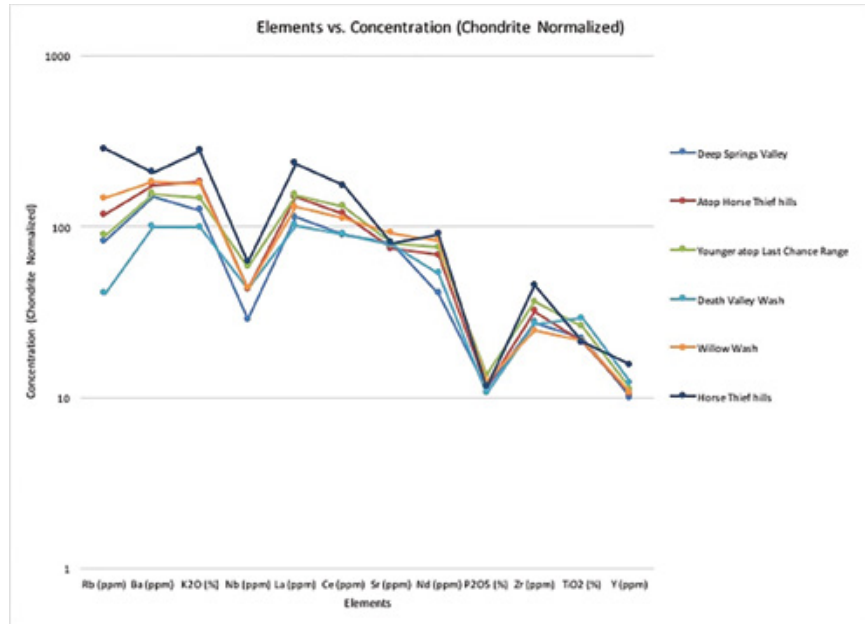


**Figure 9.** Trace element spider diagram patterns for Willow Wash, Horse Thief hills and surrounding area: Deep Springs Valley (Case, 2014), Atop Horse Thief hills (Kato, 2015), younger atop Last Chance Range (J.Knott, unpublished), Death Valley Wash (Kennis, 2017).

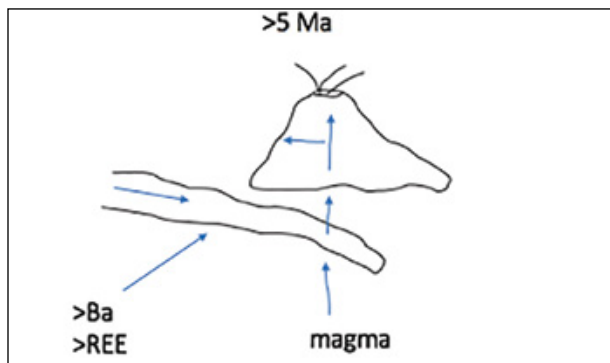


**Figure 10.** Older than 5 Ma, magmas generated in the mantle passed through a subducting slab, in which Ba and rare earth elements (REE) were scavenged out.

8). At Nb, there is a generally concave upward pattern for all samples taken (Figures 8 and 9). This would imply that samples (STA-WW-060216-1-4) and (STA-HTH-060216-5 &5A) are classified as WGB provenance. The higher concentration of rare earth elements (La & Ce) and incompatible elements (Rb & Ba) in the Horse Thief hills andesite/trachyandesite suggest lithospheric

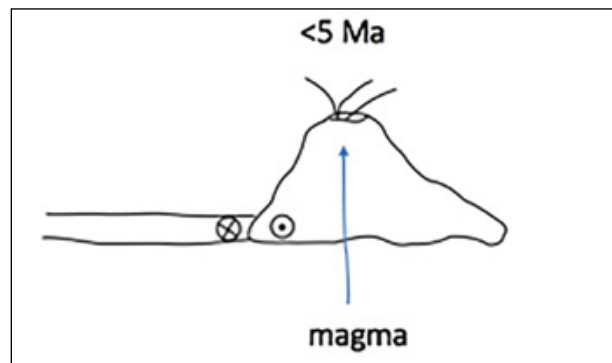


**Figure 11.** Younger than 5 Ma, a transform boundary moved in and magmas show no increase in REE, so they are geochemically different from those prior to 5 Ma.

contamination of these younger rocks (Figures 10 & 11).

The Zr values are much greater in the Willow Wash basalts compared to the Horse Thief hills andesite/trachyandesite. Ba and Ce values are greater in Horse Thief hills, and Ce values are about the same in both localities. Based on the clustering of Zr/Ba vs. Ce/Y (Figure 12) and the fact that they are all the same age,

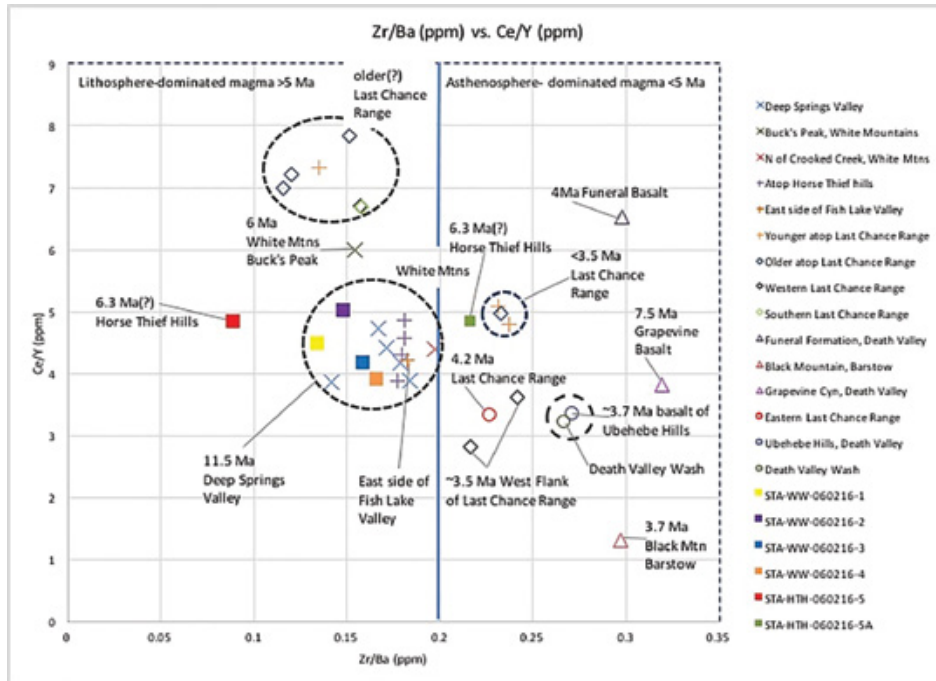


**Figure 12.** Plotting Zr/Ba vs. Ce/Y (after Kempton et al., 1991) shows that the 11.5 Ma basalts have Zr/Ba ratios of <0.2 which corresponds with Ormerod et al. (1988) that values <0.2 indicate older lithospheric dominated basalts with a “subduction related geochemistry.” Additional data from Case (2014), Kato (2015), Kennis (2017) and J. Knott (unpublished data).

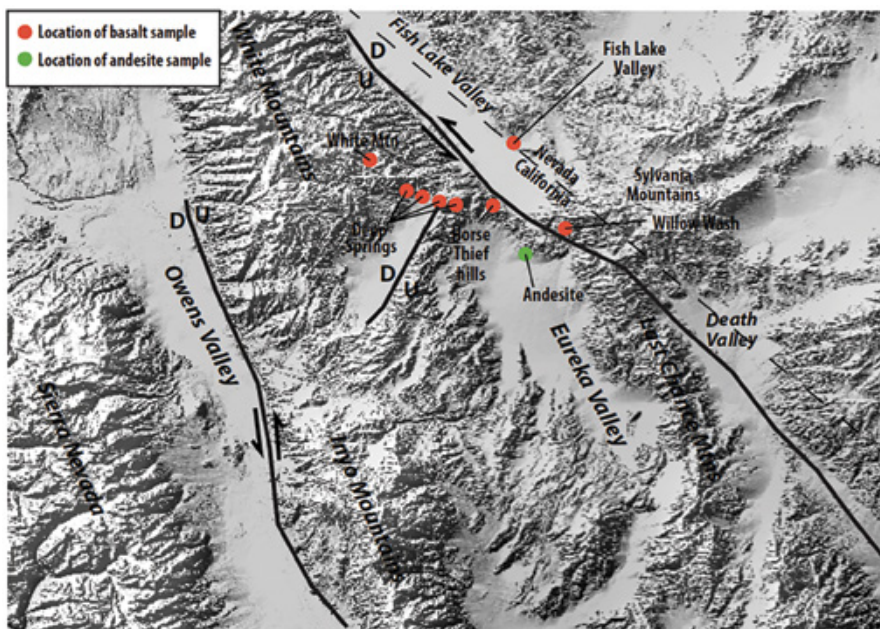


**Figure 13.** Digital Elevation Model showing locations of samples, major faults, and valleys. These basalts were analyzed for trace elements and found to have similar geomorphic position and age.

as stated by others previously (e.g., McKee and Nelson, 1967), I interpret that the samples from Willow Wash (STA-WW-060216-1-4) are the same flow. The Willow Wash basalts have a pattern similar to other 11.5 Ma basalts from Deep Springs Valley and Fish Lake Valley. I interpret these data to indicate that these are all the same basalt flow.

Basalts of Willow Wash are geochemically similar to other 11.5 Ma basalts of the White Mountains, atop Horse Thief hills, Fish Lake Valley, and Deep Springs Valley (Figure 13). Basalts in Willow Wash are buried by younger sediment whereas other outcrops are exposed on ridges, therefore Willow Wash must be on a down dropping block. This also shows that Basin and Range extension in this area began after 11.5 Ma.

The 6.2 Ma andesite-trachyandesite rock on the south flank of the Horse Thief hills interbedded with sediments must have been a depositional basin 6.2 Ma. This basin was subsequently uplifted and tilted. If the uplift and tilting of these deposits is related to Basin and Range extension, it might be interpreted that extension is post-6.2 Ma.

## **CONCLUSIONS AND FUTURE WORK**

Whole-rock composition shows that the 11.5 Ma basalts of Willow Wash are the same as the 11.5 Ma basalts of the White Mountains, atop Horse Thief hills, and Fish Lake Valley. A source in the White Mountains is reasonable and indicates that the Sylvania Mountains were a topographic low 11.5 Ma and Fish Lake Valley did not exist. Future work might include sampling and geochemical analysis of remnant basalt from Coyote Flat in the Sierra Nevada, west of Willow Wash, as well as samples east south east through Death Valley.

## **REFERENCES**

- Case, A.J., 2014, Geochemical correlation of basalts in northern Deep Springs Valley, California, by X-ray Fluorescence Spectroscopy, (XRF) ; Undergraduate Thesis, California State University, Fullerton, 16 pp.
- Dalrymple, G. Brent, 1963, Potassium-Argon Dates of Some Cenozoic Volcanic Rocks of the Sierra Nevada, California : Geological Society of America Bulletin, v., 74(4), p. 379.
- Kato, J.Y, 2015, Geochemical analysis of basalts from White Mountains and Horse Thief hills, California, by X-ray fluorescence Spectroscopy (XRF) : Undergraduate Thesis, California State University, Fullerton, 15 pp.
- Kempton, P. D., Fitton, J.G., Hawkesworth, C.J., Ormerod, D.S., 1991, Isotopic and Trace Element Constraints on the Composition and Evolution of the Lithosphere Beneath the Southwestern United States: Journal of Geophysical Research, v., 96, p. 13713-13735.
- Lackey, Jade Star, Cecil M. Robinson, Windham, Cameronn J., Frazer, Ryan E., Bindeman, Ilya N., Gehrels, George E. 2012, The Fine Gold Intrusive Suite : The roles of basement terranes and magma source development in the Early Cretaceous Sierra Nevada batholith : Geosphere.
- McKee, E.H. and Nelson, C.A., 1967, Geologic map of the Soldier Pass quadrangle, California and Nevada: U.S. Geological Survey, Geologic Quadrangle Map GQ-654, scale 1:62,500.
- Mcquarrie, Nadine and Wernicke, Brian P., 2005, An Animated Tectonic Reconstruction of Southwestern North America since 36 Ma.
- Ormerod, David S., Christopher J. Hawkesworth, Rogers, Nicholas M., Leeman, William P., Menzies, Martin A., 1988. Tectonic and magmatic transitions in the Western Great Basin: Nature, no. 333.
- Pluhar, Christopher J., Coe, Robert S., Sampson, Daniel. E., Glen, J.M., Monastero, F.C., Tanner, S.B., 2005, Lava fingerprinting using paleomagnetism and innovative X-ray fluorescence spectroscopy: A case study from the Coso volcanic field, California, v. 6, n. 4.
- Reheis, M. C. Sawyer., 1997. T.L. Late Cenozoic history and slip rates of the Fish Lake Valley, Emigrant Peak, and Deep Springs fault zones, Nevada and California. Geological Society of America (GSA): Boulder, CO, United States v. 109, n. 3, p. 280-299.
- Wirth, K. and Barth, A., 2016, X-Ray Fluorescence (XRF): [http://serc.carleton.edu/research\\_education/geochemsheets/techniques/XRF.html.pdf](http://serc.carleton.edu/research_education/geochemsheets/techniques/XRF.html.pdf) (accessed March 2, 2016).
- Wikipedia, 2016. X-ray fluorescence: [https://en.wikipedia.org/wiki/X-ray\\_fluorescence](https://en.wikipedia.org/wiki/X-ray_fluorescence). (accessed March 2016).

## **ACKNOWLEDGEMENTS**

Support for this study comes from a grant from the National Science Foundation Integrated Earth Sciences Program to J. Knott (Award# 1516593).

## **13 Year Analysis of Water Pressure and Chemical Changes from Well CSF-1, Fullerton, CA**

**Terrinda Alonzo**

**Advisor: Richard Laton, Ph.D.**

*Department of Geological Sciences, California State University, Fullerton*

### **ABSTRACT**

To better understand the hydrogeology in Northern Orange County, a deep multiport monitoring well, CSF-1, was installed in the northwest corner of California State University, Fullerton (CSUF) in 2003. Since the installation of the well, Orange County Water District (OCWD) has been collecting monthly water pressure profiles; in addition, the water chemistry is analyzed annually. In order to understand the groundwater conditions under CSUF, a detailed review of the data from the past 13 years has been proposed. Patterns in the assembled data show correlations between tracer chemicals (i.e. nitrate and perchlorate) that can be traced to a potential source of recharge. These correlations are found at lower than expected depths. Out of six defined aquifers, there are abnormally high concentrations of nitrate and perchlorate in aquifers 2 and 5 with lower, but still significant levels in aquifers 3, 4, and 6. The key finding is that even though the lower aquifers showed abnormally high amounts of these chemicals, they showed low to no traces of the tracer chemicals in the upper unconfined aquifer. Based upon this finding, it was determined that the tracer chemicals, nitrate and perchlorate, do not originate from local runoff or recharge. In fact, the recharge of the lower aquifers must originate further away, most likely the OCWD recharge area east of the City of Placentia.

# Interpreting Recent Stratigraphic Changes for the Northern Monterey Bay Continental Shelf

**Victoria Severin**

**Advisor: Joe Carlin, Ph.D.**

*Department of Geological Sciences, California State University, Fullerton*

## DISCUSSION

Continental shelves are dynamic environments that are influenced by marine, terrestrial, and climatic process. As such, shelf environments can be important recorders of global change, however there is a lack of understanding about how strata form in continental shelf mud deposits over the past century as human activities have had an increasing impact on geologic processes. To address this problem we investigated the Monterey Bay shelf located in central California. Monterey Bay is an ideal study area because it is dominated by variable,

but high sediment loads from small mountainous rivers, impacted by high-energy wave events from the North Pacific Ocean, and lies at the northern extent of the influence of El Niño. Further, over the past century the region has experienced significant increases in human perturbations including agriculture, urbanization, and hydrologic modifications. To this point, preliminary data suggests that modern sedimentation in the bay has changed over recent decades with a net increase in sediment accumulation and an overall coarsening trend

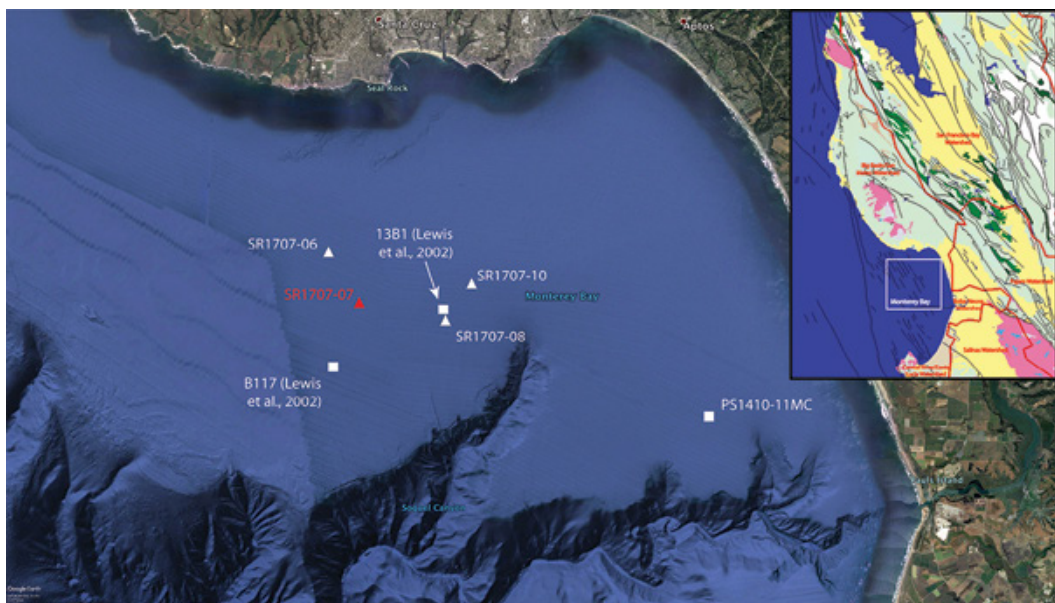


**Figure 1.** Study area map for northern Monterey Bay. Triangles depict core locations from this study, with the red triangle designating the location of SR1707-07 where geochronological data is available. Locations depicted by squares are cores from other studies referenced herein. Inset map shows a regional view of the study area with the local geology depicted by the different colors. Notable geologic units in the area include Quaternary alluvium and marine deposits in yellow, Miocene marine rocks in light green, Mesozoic granitic rocks in dark pink, Mesozoic gabbroic rocks in light pink, and Quaternary sand deposits in light tan. The red lines represent the boundaries of the regional watersheds. Both maps and imagery were generated using Google Earth. Geological data and watershed data on the locator map are from the USGS.

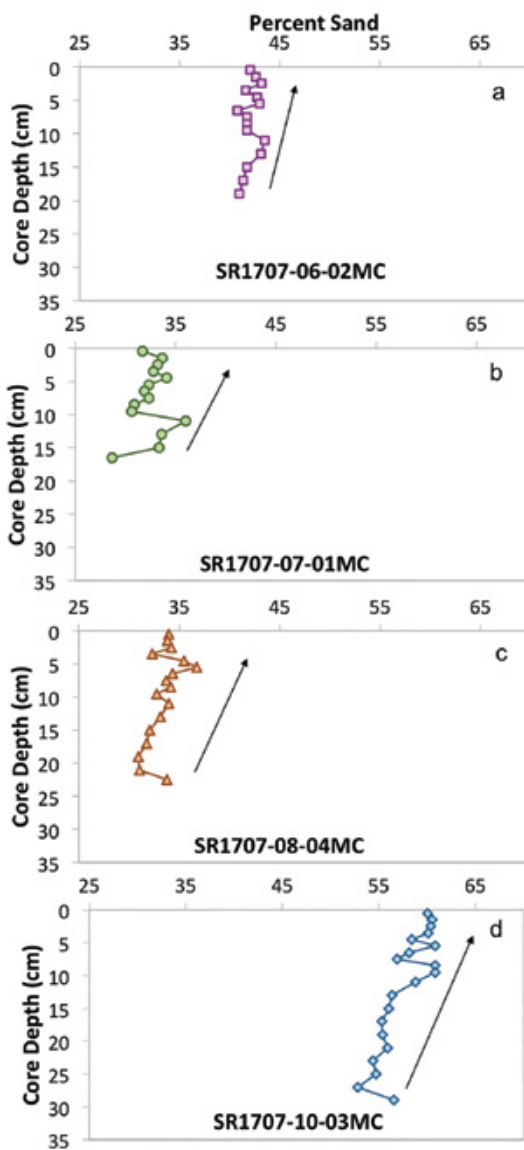


**Figure 2.** Down core grain size results for sites a) SR1707-06, b) SR1707-07, c) SR1707-08, and d) SR1707-10. Arrows on each graph show the general increasing trend in sand upcore in each core from the study area.

through time, however these results do not encompass areas proximal to Santa Cruz, the largest coastal population center in the bay. The goal of the project is to determine the impact of humans on sedimentation throughout Northern Monterey Bay through a focused investigation of shelf areas proximal to Santa Cruz.

To accomplish this, we collected cores from four locations on the shelf (Figure 1), and analyzed the cores in 1 cm intervals to determine modern sedimentation rates, as well as sedimentological characteristics. Sedimentation rates were determined from the short-lived radionuclides  $^{210}\text{Pb}$  and  $^{137}\text{Cs}$ . Lead-210 is a naturally occurring isotope with ~22 year half-life, while  $^{137}\text{Cs}$  is an anthropogenic isotope that was introduced to the environment in the 1950s from nuclear weapons testing. Cesium-137 provides an independent chronometer to  $^{210}\text{Pb}$  by establishing two time horizons at 1953 and 1963. The sedimentological characteristics analyzed in the cores include sediment texture via grain size analysis. Grain size analysis was performed on all cores at a 1 cm sampling frequency, with samples pretreated to remove organic matter, carbonates, and biogenic silica prior to being analyzed by laser diffraction using a Malvern Mastersizer 2000.

Grain size data from all four cores show a general trend of increasing sand up core (Figure 2). The most consistent changes were observed in cores SR1707-08-04MC, SR1707-07-01MC, SR1707-10-03MC where the sand content increased from 31 to 36 percent, 29 to 34 percent, and 52 to 61 percent respectively. Radioisotope data for core SR1707-07-01MC is shown in Figure 3. From the  $^{210}\text{Pb}$  data we have identified two layers, an upper layer from 0 to 7 cm with uniform activity with depth that we interpret as the surface mixed layer, while below 7 cm activities decrease exponentially with depth. This lower layer suggest steady-state accumulation, where we can estimate a sedimentation rate of 4.4 mm/yr. Cesium-137 was detected down to the base of this core suggesting all sediment was deposited after 1953. For core SR1707-10-03MC the  $^{210}\text{Pb}$  data was inconclusive, but  $^{137}\text{Cs}$  was also detected down to the base, thus we can estimate a minimum sedimentation of 4.7 mm/yr for this core.

The increases in sand over time is consistent with other cores collected in the region. The cores that exhibited the strongest trends in sand increases with depth were SR1707-07-01MC, SR1707-08-04MC, and

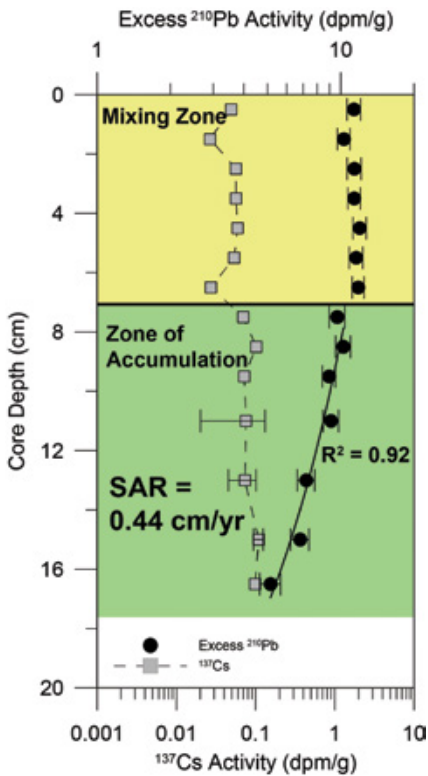


**Figure 3.** Geochronological results from SR1707-07-01MC. The plot shows down core activities of  $^{210}\text{Pb}$  (black circles) and  $^{137}\text{Cs}$  (grey squares). From the  $^{210}\text{Pb}$  data we have identified two zones within the core: the mixed zone (yellow) characterized by uniform activities with depth, and the zone of accumulation (green) where activities decrease exponentially with depth. From the zone of accumulation we are able to determine a the average sedimentation rate. Cesium-137 was detected throughout the core suggesting these sediments were all deposited post-1953.

SR1707-10-03MC, all cores that were collected directly seaward of urbanization in and around Santa Cruz. Core SR1707-06-02MC was located seaward of the western edge of Santa Cruz and demonstrated a weaker relationship between sand content and core depth. This suggests that urbanization and/or modification to the San Lorenzo River, which flows through the city, may have increased the delivery of coarse material to proximal shelf areas.

The most notable changes to sedimentation in the region over time can be seen in the sedimentation rates. Figure 4 shows sedimentation rates averaged over specific time intervals from cores collected from throughout the region. From this data we see that when rates are averaged just over the late 19th and the first half of the 20th century the rates are lower ( $\sim 1 \text{ mm/yr}$ ) and approximate the long-term Holocene average rate that approximates sea level rise. Rates that included the latter half of the 20th century are double this rate, and rates exclusive to the past several decades are 4-times the Holocene/pre-1950s rate. The data consistently demonstrates that rates throughout the bay have increased 2 to  $>4$ -fold in the later half of the 20th century and first part of the 21st century.

Looking at these most recent rates spatially, we also see that core PS1410-11MC, a core collected during a previous study, demonstrated an accumulation rate of  $\sim 2 \text{ mm/yr}$  over the past several decades, while the

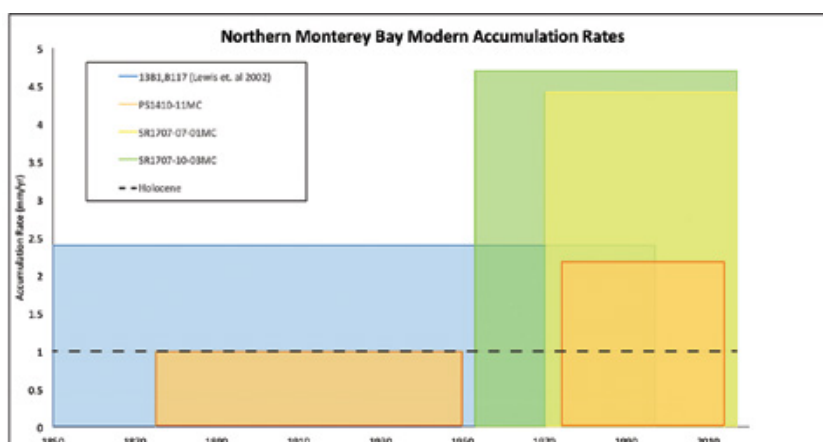


**Figure 4.** Plot of average sediment accumulation rates over time from multiple cores throughout the study area (core locations shown in Figure 1). The difference in rates at each site is partly a function of the time period over which the rates were averaged. The plot shows that rates averaged over the most recent decades are faster than those that include periods in the early 20th and late 19th century, and the long-term Holocene average (black dashed line). This plot suggests that sedimentation rates have been increasing significantly in the area over the past several decades.

cores analyzed from this study had rates > 4 mm/yr. The PS1410-11MC was collected to the east of Santa Cruz proximal to the Pajaro River mouth in an area dominated by agriculture, while the cores from this study were located proximal to the urbanized areas including Santa Cruz. These data collectively with the grain size data suggest that not only are the urbanized areas delivering more sand to the shelf, they may also be delivering more sediment total. Thus the human modifications to the San Lorenzo River may have had a more significant impact than those modifications to the Pajaro River in terms of sediment delivery to the shelf.

Overall, the results from this study demonstrate that previous observations of increased total sediment delivery and increased sand delivery are consistent throughout northern Monterey Bay. Further, the most significant increases in these sedimentation characteristics appear to be located proximal to the more urbanized areas near Santa Cruz. Therefore, this study has demonstrated the impacts that humans, in particular urbanization and modifications to hydrologic processes in urban environments can have on the delivery of terrestrial material to the coastal ocean.

## **REFERENCES**

- Lewis, R.C., Coale, K.H., Edwards, B.D., Marot, M., Douglas, J.N. Burton, E.J., 2002. Accumulation rate and mixing of shelf sediments in the Monterey Bay National Marine Sanctuary. *Marine Geology* 181, 157-169.

## **Shapes of Giant Soap Bubbles**

**Angelica Arredondo and Breanna McBean**

**Advisor: Nicholas Brubaker, Ph.D.**

*Department of Mathematics, California State University, Fullerton*

### **ABSTRACT**

The behavior of bubbles has intrigued both physicists and mathematicians for over a hundred years. Much of the intrigue comes from the inherent ability of a soap-bubble to solve the well-posed mathematical problem: Given a bounded volume, what is the shape of the boundary surface with minimal area? In this classical problem, which was first formulated by nineteenth-century physicist Joseph Plateau, the weight of the soap film is neglected. However, as the size of the bubble grows, macro-scale effects such as gravity, become more important and the shape of the surface can change significantly. We seek to characterize these qualitative changes via the following modified problem that captures the behavior of both small and large soap bubbles: Find the surface that minimizes the sum of surface and gravitational energy and encloses a specified volume. Additionally, this question is intimately related to the construction of heavy surface and provides practical insights into shapes of energetically-optimal domes.

# Alternating Hamiltonian Cycles

**Christian Do and James Shade**

**Advisors: Adam Glesser, Ph.D., and Matt Rathbun, Ph.D.**

*Department of Mathematics, California State University, Fullerton*

## ABSTRACT

A variation on the 1969 Lovász Conjecture states that all finite connected Cayley graphs contain a Hamiltonian cycle [1]. A consistent and algorithmically simple method of traversing an entire group from a small subset of its elements would improve running time and storage requirements for computer programs that work with groups. We examine the case of generating 2-generator groups by repeatedly multiplying two group elements in alternating order, especially as it applies to dihedral, semidihedral, and generalized quaternion groups.

## INTRODUCTION

Symmetry is broadly useful in various fields, from art to architecture to chemistry. A common mathematical tool for studying symmetry is a group. Groups are algebraic structures that can informally be thought of as collections of symmetries. For instance, consider the set of symmetries of a square (see Fig. 1). We can leave the square unaffected, we can rotate a square in increments of  $90^\circ$ , we can flip the square across an axis, and we can perform any number of these transformations in a row and the result will be an identical square. This set of transformations forms a group under composition.

Generating sets are an important property of a group, as well. A generating set of a group is a subset of the group such that every group element can be written as a product of powers of elements of the subset. This is useful when working with groups via computer since it means the memory requirement for even very complicated groups can be quite small. However, this can also prove to be complicated, as there is not always a clear, algorithmically simple way to generate all the elements of the group.

Another useful structure is a graph, which emphasizes connections between different objects while downplaying any internal structure on these objects. A graph consists of a set of vertices and a set of edges connecting them. Notably, a Cayley graph is a graph where each vertex represents a group element and each edge represents multiplication by an element of the generating set. The structure of the Cayley graph then depends on the choice of generating set. A 1969 conjecture by Lovász states that all Cayley graphs have a Hamiltonian cycle; that is, starting from some vertex, we can traverse the edges of the graph to reach each vertex exactly once and return to the starting vertex. We examine here a related problem: we aim to identify which generating sets, when multiplying the elements in alternating order, yield a Hamiltonian cycle in the corresponding Cayley graph.

In this paper, we identify a method of generating a 2-generator group by alternately multiplying two elements, and we determine all pairs of elements that can generate a group in such a way for dihedral, semidihedral, and generalized quaternion groups. This method gives us a simple, straightforward method of generating these groups, which has applications in coding theory and computer science.

## BACKGROUND

We provide here the definition of a group, and other relevant classical definitions.

**Definition 1.** A group  $(G, \star)$  is a set  $G$  with an associative binary operation  $\star$  that satisfies the following properties:

1. For all  $a, b \in G$ ,  $a \star b \in G$ .

## Elements of $D_8$

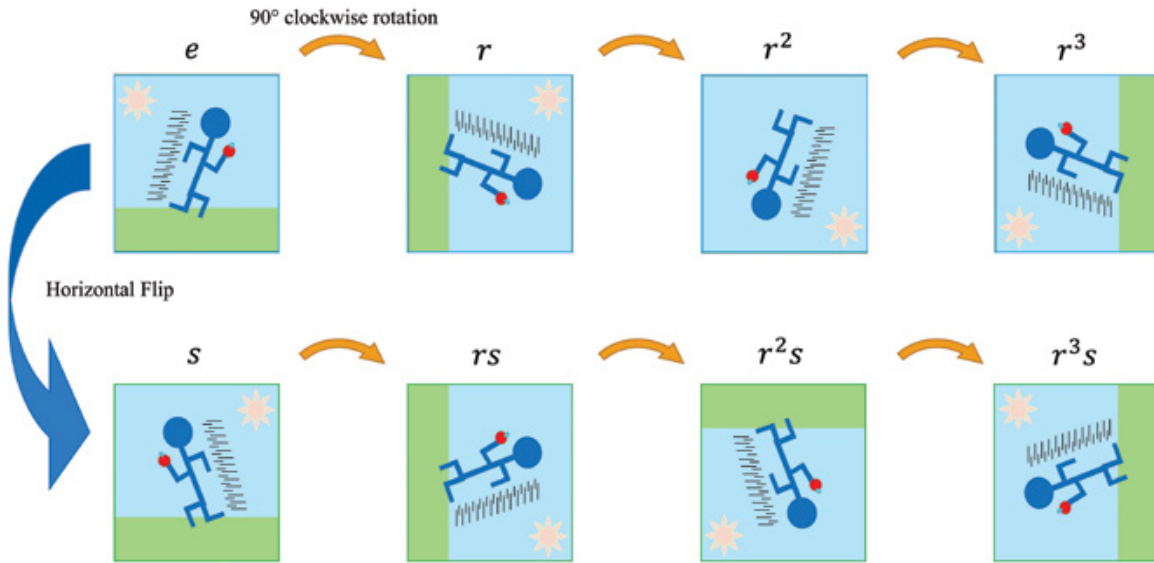


**Figure 1.** The set of symmetries of a square, also known as the dihedral group of order 8,  $D_8$ .

2. There exists  $e \in G$  such that  $e * a = a * e = a$  for all  $a \in G$ .
3. For each  $a \in G$ , there exists  $a^{-1} \in G$  such that  $a * a^{-1} = a^{-1} * a = e$ .

Groups can be either finite or infinite. A simple example of an infinite group is  $(\mathbb{Z}, +)$ , while a simple example of a finite group is  $(\{0\}, +)$ .

**Definition 2.** Let  $(G, \star)$  be a group. We denote  $|G|$  be the order of the group, or the number of elements in the group.

**Definition 3.** Let  $(G, \star)$  be a group, and let  $A \subseteq G$ . We call  $A$  a subgroup of  $G$  if  $(A, \star)$  also forms a group.

**Definition 4.** Let  $G$  be a group, let  $a \in G$ , and let  $H$  be a subgroup of  $G$ . The left coset of  $H$  in  $G$  with respect to  $a$  is given by  $aH = \{ah : h \in H\}$ .

**Definition 5.** A subset  $A$  of a group  $G$  is a generating set for  $G$  if every element in  $G$  can be represented as a product of finitely many powers of elements of  $A$ . We say that the elements of  $A$  generate  $G$ .

As an example, the set  $\{r, s\}$  is a generating set of  $D_8$ , pictured in Fig. 1, since every element can be created by some combination of flipping and rotating.

**Definition 6.** A cyclic group  $G$  is a group that can be generated by a single element  $a \in G$ , and is denoted  $\langle a \rangle$ .

It is important to note that every element  $a$  of a group  $G$  yields a cyclic subgroup  $\langle a \rangle$ . An important theorem identifies generators of a cyclic group.

**Theorem 1 ([2]).** Let  $\langle a \rangle$  be a finite cyclic group. We have that  $\langle a^k \rangle = \langle a \rangle$  if and only if  $\gcd(k, |\langle a \rangle|) = 1$ .

$$P(r^2, s)$$

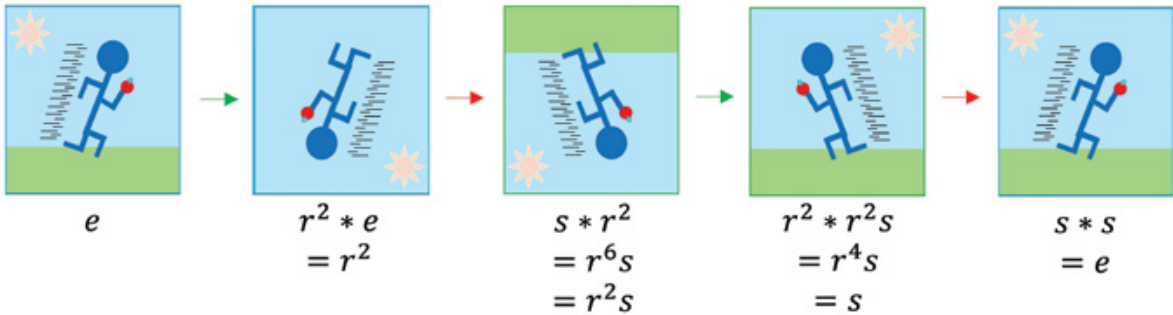


**Figure 1.** The set of symmetries of a square, also known as the dihedral group of order 8,  $D_8$ .

### PATHS AND COMPLETENESS

Our goal is to identify all pairs of elements in a given group that, when multiplied in alternating order, will generate the whole group without repeating any elements. To this end, we introduce the concept of the path of two elements over a group. For all definitions in this section, let  $(G, \star)$  be a finite group and let  $a, b \in G$ .

**Definition 7.** We define  $S(a, b)$  to be the sequence generated by the following relation:

$$\begin{aligned} S(a, b)_0 &= e \\ S(a, b)_{2k+1} &= a \star S(a, b)_{2k}, \text{ for } k \geq 0 \\ S(a, b)_{2k} &= b \star S(a, b)_{2k-1}, \text{ for } k \geq 1. \end{aligned}$$

**Definition 8.** The path of  $a$  and  $b$  over  $G$ , denoted  $P(a, b)$ , is the subsequence of  $S(a, b)$  such that each  $P(a, b)_k = S(a, b)_k$ , and that terminates at the first repeated element.

For an example of a path in  $D_8$ , see Fig. 2.

**Definition 9.** The length of  $P(a, b)$ , denoted  $L(a, b)$ , is the number of distinct elements that appear in the path.

**Definition 10.** We say  $P(a, b)$  is a complete path if every element of  $G$  appears in  $P(a, b)$ .

Note that  $L(a, b) = |G|$  if and only if  $P(a, b)$  is complete.

With these definitions, we can see that our goal is to find all pairs in a given group which form a complete path over that group.

### DIHEDRAL GROUPS

The dihedral group of order  $2n$ ,  $n \geq 4$ , is given by

$$D_{2n} = \langle r, s \mid r^n = s^2 = e, sr = r^{n-1}s \rangle.$$

The complete classification of complete paths in  $D_{2n}$  is given by the following theorem.

**Theorem 2.** For any dihedral group  $D_{2n}$  containing elements  $a, b$ , the path,  $P(a, b)$ , is complete if and only if  $a = r^l s$  and  $b = r^m s$  such that  $l - m$  is relatively prime to  $n$ .

Proof. First, we show that any path not of the form  $P(r^l s, r^m s)$  is not complete.

If  $a, b$  lie in the same cyclic subgroup, then  $P(a, b)$  cannot be complete, as  $D_{2n}$  is a 2-generator group and thus cannot be generated by a cyclic subgroup. To show that a path of the form  $P(r^l, r^m s)$  is not complete, it suffices to show that  $L(r^l, r^m s) \leq 4$ . Consider  $S(r^l, r^m s)_4$ . We have

$$\begin{aligned} r^m s r^l r^m s r^l &= (r^{m-l-m+l}) \\ &= e. \end{aligned}$$

This implies that  $L(r^l, r^m s) \leq 4$ . Thus,  $S(r^l, r^m s)$  is not complete.

Similarly, consider  $S(r^m s, r^l)_4$ . We have

$$\begin{aligned} r^l r^m s r^l r^m s &= (r^{l+m-l-m}) \\ &= e. \end{aligned}$$

Thus,  $L(r^m s, r^l) \leq 4$ . It follows that  $P(r^m s, r^l)$  is not complete. Hence, if a path is complete, then it must be of the form  $P(r^l s, r^m s)$ .

Now, we show that  $P(r^l s, r^m s)$  is complete if and only if  $l - m$  is relatively prime to  $n$ . Consider the sequence  $S(r^l s, r^m s)$ :

$$S(r^l s, r^m s) = e, r^l s, r^{m-l}, r^{2l-m} s, r^{2m-2l}, r^{3l-2m} s, \dots$$

Note that every odd element within the sequence takes the form  $r^k$  and every even element takes the form  $r^k s$ . This sequence will form a complete path if and only if every element of  $\langle r \rangle$  appears as an odd element of the sequence and every element of  $\langle r \rangle s$  appears as an even element of the sequence. Thus, this is a complete path if and only if  $\langle r^{m-l} \rangle = \langle r \rangle$  and  $r^l \langle r^{l-m} \rangle = \langle r \rangle$ .

We have  $\langle r^{m-l} \rangle = \langle r \rangle$  if and only if  $m - l$  is relatively prime to  $n$ , which is true if and only if  $l - m$  is relatively prime to  $n$ .

Similarly, we have  $r^l \langle r^{l-m} \rangle = \langle r \rangle$  if and only if  $\langle r^{l-m} \rangle = \langle r \rangle$ . So,  $\gcd(l - m, n) = 1$ .

Therefore,  $P(r^l s, r^m s)$  is complete if and only if  $l - m$  is relatively prime to  $n$ .  $\square$

## SEMDIHEDRAL GROUPS

The semidihedral group of order  $2^n$  is given by

$$SD_{2^n} = \langle r, s | r^{2^n} = s^2 = e, sr = r^{2^{n-1}-1}s \rangle.$$

These groups are a natural alternative to the dihedral groups, inspired by the presentations of those groups. The complete classification of elements that generate a complete path in  $SD_{2^n}$ ,  $n \geq 4$ , is given by the following theorem.

**Theorem 3.** For any semidihedral group  $SD_{2^n}$  containing elements  $a, b$ , the path,  $P(a, b)$ , is complete if and only if  $a = r^l s$  and  $b = r^m s$  such that  $l - m$  is odd.

Proof. First, we show that any path not of the form  $P(r^l s, r^m s)$  is not complete.

If  $a, b$  lie in the same cyclic subgroup, then  $P(a, b)$  cannot be complete, as  $SD_{2^n}$  is a 2-generator group and thus cannot be generated by a cyclic subgroup. To show that a path of the form  $P(r^l, r^m s)$  is not complete, it suffices to show that  $L(r^l, r^m s) \leq 8$ . Consider  $S(r^l, r^m s)_8$ . We have

$$\begin{aligned}
r^m sr^l r^m sr^l r^m sr^l r^m sr^l &= (r^{m+l(2^{n-2}-1)} sr^{m+l(2^{n-2}-1)} s)^2 \\
&= (r^{m+2^{n-2}l-l+(2^{n-2}-1)(m+2^{n-2}l-l)})^2 \\
&= (r^{2^{n-2}(m-l)})^2 \\
&= e.
\end{aligned}$$

This implies that  $L(r^l, r^m s) \leq 8$ . Thus,  $P(r^l, r^m s)$  is not complete.  
Similarly, consider  $S(r^m s, r^l)_8$ . We have

$$\begin{aligned}
r^l r^m sr^l r^m sr^l r^m sr^l r^m s &= (r^{l+m} sr^{l+m} s)^2 \\
&= (r^{l+m+(2^{n-2}-1)(l+m)})^2 \\
&= (r^{l+m+2^{n-2}l+2^{n-2}m-l-m})^2 \\
&= e.
\end{aligned}$$

Thus,  $L(r^m s, r^l) \leq 8$ . It follows that  $P(r^m s, r^l)$  is not complete. Hence, if a path is complete, then it must be of the form  $P(r^l s, r^m s)$ .

Now, we show that  $P(r^l s, r^m s)$  is complete if and only if  $l - m$  is odd. Let  $k = 2^{n-2} - 1$ . Consider the sequence  $S(r^l s, r^m s)$ :

$$S(r^l s, r^m s) = e, r^l s, r^{m+kl}, r^{2l+km} s, r^{2m+2kl}, r^{3l+2km} s, \dots$$

This sequence will form a complete path if and only if  $\langle r^{m+kl} \rangle = \langle r \rangle$  and  $r^l \langle r^{l+km} \rangle = \langle r \rangle$ .

We have  $\langle r^{m+kl} \rangle = \langle r \rangle$  if and only if  $\gcd(m + kl, 2^{n-1}) = \gcd(m + (2^{n-2} - 1)l, 2^{n-1}) = \gcd(m - l + 2^{n-2}l, 2^{n-1}) = 1$ , which is true if and only if  $l - m$  is odd.

Similarly, we have  $r^l \langle r^{l+km} \rangle = \langle r \rangle$  if and only if  $\gcd(l + (2^{n-2} - 1)m, 2^{n-1}) = \gcd(l - m + 2^{n-2}m, 2^{n-1}) = 1$ , which is true if and only if  $l - m$  is odd.

Hence,  $P(r^l s, r^m s)$  is complete if and only if  $l - m$  is odd. □

## GENERALIZED QUATERNION GROUPS

The generalized quaternion group of order  $2^n$ ,  $n \geq 4$ , is given by

$$Q_{2^n} = \langle x, y | x^{2^n} = e, x^{2^{n-1}} = y^2, yx = x^{-1}y \rangle.$$

The complete classification of pairs of elements in  $Q_{2^n}$  is given by the following theorem.

**Theorem 4.** For any quaternion group  $Q_{2^n}$  containing elements  $a, b$ , the path,  $P(a, b)$ , is complete if and only if  $a = x^l y$  and  $b = x^m y$  such that  $l - m$  is odd.

Proof. First, we show that any path not of the form  $P(x^l y, x^m y)$  is not complete.

If  $a, b$  lie in the same cyclic subgroup, then  $P(a, b)$  cannot be complete, as  $Q_{2^n}$  is a 2-generator group and thus cannot be generated by a cyclic subgroup. To show that a path of the form  $P(x^l, x^m y)$  is not complete, it suffices to show that  $L(x^l, x^m y) \leq 8$ . Consider  $S(x^l, x^m y)_8$ . We have

$$\begin{aligned}
x^m y x^l x^m y x^l x^m y x^l x^m y x^l &= (x^{m-l-m+l} y^2)(x^{m-l-m+l} y^2) \\
&= y^4 \\
&= e.
\end{aligned}$$

$$\begin{aligned}
r^m sr^l r^m sr^l r^m sr^l r^m sr^l &= (r^{m+l(2^{n-2}-1)} sr^{m+l(2^{n-2}-1)} s)^2 \\
&= (r^{m+2^{n-2}l-l+(2^{n-2}-1)(m+2^{n-2}l-l)})^2 \\
&= (r^{2^{n-2}(m-l)})^2 \\
&= e.
\end{aligned}$$

This implies that  $L(r^l, r^m s) \leq 8$ . Thus,  $P(r^l, r^m s)$  is not complete.  
Similarly, consider  $S(r^m s, r^l)_8$ . We have

$$\begin{aligned}
r^l r^m sr^l r^m sr^l r^m sr^l r^m s &= (r^{l+m} sr^{l+m} s)^2 \\
&= (r^{l+m+(2^{n-2}-1)(l+m)})^2 \\
&= (r^{l+m+2^{n-2}l+2^{n-2}m-l-m})^2 \\
&= e.
\end{aligned}$$

Thus,  $L(r^m s, r^l) \leq 8$ . It follows that  $P(r^m s, r^l)$  is not complete. Hence, if a path is complete, then it must be of the form  $P(r^l s, r^m s)$ .

Now, we show that  $P(r^l s, r^m s)$  is complete if and only if  $l - m$  is odd. Let  $k = 2^{n-2} - 1$ . Consider the sequence  $S(r^l s, r^m s)$ :

$$S(r^l s, r^m s) = e, r^l s, r^{m+kl}, r^{2l+km} s, r^{2m+2kl}, r^{3l+2km} s, \dots$$

This sequence will form a complete path if and only if  $\langle r^{m+kl} \rangle = \langle r \rangle$  and  $r^l \langle r^{l+km} \rangle = \langle r \rangle$ .

We have  $\langle r^{m+kl} \rangle = \langle r \rangle$  if and only if  $\gcd(m + kl, 2^{n-1}) = \gcd(m + (2^{n-2} - 1)l, 2^{n-1}) = \gcd(m - l + 2^{n-2}l, 2^{n-1}) = 1$ , which is true if and only if  $l - m$  is odd.

Similarly, we have  $r^l \langle r^{l+km} \rangle = \langle r \rangle$  if and only if  $\gcd(l + (2^{n-2} - 1)m, 2^{n-1}) = \gcd(l - m + 2^{n-2}m, 2^{n-1}) = 1$ , which is true if and only if  $l - m$  is odd.

Hence,  $P(r^l s, r^m s)$  is complete if and only if  $l - m$  is odd. □

## GENERALIZED QUATERNION GROUPS

The generalized quaternion group of order  $2^n$ ,  $n \geq 4$ , is given by

$$Q_{2^n} = \langle x, y | x^{2^n} = e, x^{2^{n-1}} = y^2, yx = x^{-1}y \rangle.$$

The complete classification of pairs of elements in  $Q_{2^n}$  is given by the following theorem.

**Theorem 4.** For any quaternion group  $Q_{2^n}$  containing elements  $a, b$ , the path,  $P(a, b)$ , is complete if and only if  $a = x^l y$  and  $b = x^m y$  such that  $l - m$  is odd.

Proof. First, we show that any path not of the form  $P(x^l y, x^m y)$  is not complete.

If  $a, b$  lie in the same cyclic subgroup, then  $P(a, b)$  cannot be complete, as  $Q_{2^n}$  is a 2-generator group and thus cannot be generated by a cyclic subgroup. To show that a path of the form  $P(x^l, x^m y)$  is not complete, it suffices to show that  $L(x^l, x^m y) \leq 8$ . Consider  $S(x^l, x^m y)_8$ . We have

$$\begin{aligned}
x^m y x^l x^m y x^l x^m y x^l x^m y x^l &= (x^{m-l-m+l} y^2)(x^{m-l-m+l} y^2) \\
&= y^4 \\
&= e.
\end{aligned}$$

This implies that  $L(x^l, x^m y) \leq 8$ . Thus,  $P(x^l, x^m y)$  is not complete. Similarly, consider  $S(x^m y, x^l)_8$ . We have

$$\begin{aligned} x^l x^m y x^l x^m y x^l x^m y x^l x^m y &= (x^{l+m-l-m} y^2)(x^{l+m-l-m} y^2) \\ &= y^4 \\ &= e. \end{aligned}$$

Thus,  $L(x^m y, x^l) \leq 8$ . It follows that  $P(x^m y, x^l)$  is not complete. Hence, if a path is complete, then it must be of the form  $P(x^l y, x^m y)$ .

Now, we show that  $P(x^l y, x^m y)$  is complete if and only if  $l - m$  is odd. Let  $k = 2^{n-2}$ . Consider the sequence  $S(x^l y, x^m y)$ :

$$\begin{aligned} S(x^l y, x^m y) = e, x^l y, x^{m-l+k}, x^{l+(l-m-k)} y, x^{2(m-l+k)}, \\ x^{l+2(l-m-k)} y, x^{3(m-l+k)}, x^{l+3(l-m-k)} y, \dots \end{aligned}$$

This sequence will form a complete path if and only if  $\langle x^{m-l+k} \rangle = \langle x \rangle$  and  $x^l \langle x^{l-m-k} \rangle = \langle x \rangle$ .

We have  $\langle x^{m-l+k} \rangle = \langle x \rangle$  if and only if  $\gcd(m - l + k, 2^{n-1}) = \gcd(m - l + 2^{n-2}l, 2^{n-1}) = 1$ , which is true if and only if  $l - m$  is odd.

Similarly, we have  $x^l \langle x^{l-m-k} \rangle = \langle x \rangle$  if and only if  $\gcd(l - m - k, 2^{n-1}) = \gcd(l - m - 2^{n-2}, 2^{n-1}) = 1$ , which is true if and only if  $l - m$  is odd.

Hence,  $P(x^l y, x^m y)$  is complete if and only if  $l - m$  is odd.  $\square$

## CONCLUSIONS AND FUTURE RESEARCH

All three of these groups belong to a classification called **metacyclic 2-groups**, and the similarity suggests that there may be a more general pattern at play. Our next step is to solve this problem for the metacyclic 2-groups in general. For more information on metacyclic 2-groups, see [3].

## REFERENCES

- Pak I., Radoičić R., 1996, "Hamiltonian paths in Cayley graphs", *Discrete Mathematics*, 309, 17, 5501-5508.
- Hungerford, T. W., 2012, *Abstract Algebra: An Introduction*, 3rd Edition, Brooks Cole, 595 pp.
- Liedahl, S., 1996, "Enumeration of Metacyclic p-Groups", *J. Algebra*, 186, 2, 436-446.

# Linearizing the Repressilator Model

Killian Wood

Advisor: Anael Verdugo, Ph.D.

Department of Mathematics, California State University, Fullerton

## ABSTRACT

The functionality of a cell is comprised of thousands of interconnected parts. It is the relationship between some grouping of these numerous parts that constitute an intracellular network. Prior to the work of Elowitz and Leibler [1], such systems were not well understood; though not by lack of effort as previous efforts took the form of quantitative analysis. Elowitz and Leibler proposed an alternative approach in which a synthetic network with an anticipated function was constructed and implemented within an *E. Coli* cell. The model that describes this network was called *the repressilator* and is comprised of a system of six non-linear first order ordinary differential equations. Such systems cannot be solved analytically and are thus studied via numerical methods. In this work, we aim to understand the dynamic behavior of the model by computing the steady state solutions of the system. We employ Newton's method for nonlinear systems and a graphical approach as verification for our analysis. Our conclusions include a verification of the long-term biological behavior of the system. Numerical concentrations of messenger RNA and protein levels are compared with the experimental results and good agreement was found. Finally, linear stability analysis was used to confirm the system is robust to perturbations.

## BACKGROUND

The repressilator consists of a network of three transcriptional repressor systems. The primary components of the plasmid in Figure 2 are three genes for repressor proteins whereby each protein represses production of another protein in the sequence. The main process which we are concerned with is transcription. This is the process by which genetic information, which is coded in the DNA strand, is copied onto a strand called mRNA, or messenger RNA. After the mRNA has been constructed, it is used as the blueprint to construct a protein by a machine-like protein structure called a ribosome. This process is represented in Figure 1.

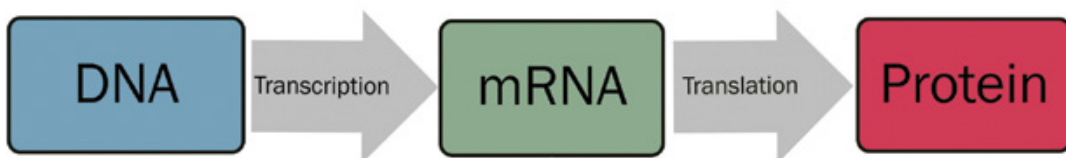


**Figure 1.** Central dogma of molecular biology. Progression of genetic information in the cell follows a two-step process: transcription and translation.

In Figure 2, we provide the network diagram from the original work in Elowitz and Leibler [1]. The network is represented as a biological system in the form of a plasmid where the first protein, LacI, inhibits transcription of the second gene, *tetR*. In turn, TetR protein inhibits transcription of the third gene,  $\lambda$ -*cI*. Finally,  $\lambda$ -*cI* protein inhibits the transcription of the *lacI* gene, thus making a complete cycle.

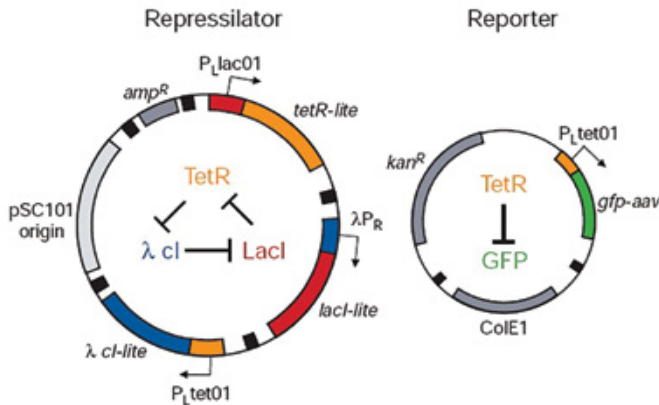


**Figure 2.** The repressilator in the form of indicator plasmids.

The reporter plasmid, displayed next to the repressilator in Figure 2, demonstrates that the indicator protein GFP is produced in the absence of TetR protein. Since TetR is not consumed after binding to the *gfp* promoter, the behavior of reporter system is independent of the repressilator and thus is excluded from the model.

### THE REPRESSILATOR MODEL

The construction of the mathematical model begins with the assignment of variables with subindices to the three different genes. We let the gene *lacI* be represented by the index 1, *tetR* with 2, and *cl* with 3. From our description, the messenger RNA and corresponding protein product have the a cyclic relationship. In the figure that follows, we demonstrate this relationship graphically where arrows denote a promotive relationship and the lines with horizontal bars denote an inhibitive relationship.

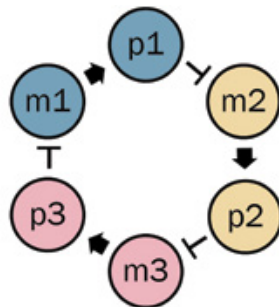


**Figure 3.** The relationship between variables in the repressilator Model. Inhibition is represented by a perpendicular symbol ( $\perp$ ) and activation by an arrow ( $\uparrow$ ).

The dynamic relationship between each of the components in the network is given by Figure 3. Here each of the concentrations is changing over time and the cyclic nature of their relationship implies that each variable depends on the “previous” variable as seen in the diagram. From the diagram alone, we see that the qualitative behavior of protein present at any given time depends on the messenger. Similarly, we would see that each messenger RNA is negatively effected by the presence of protein. That is, we expect for large values of protein, the next link in this sequence would be produced minimally. The following system of equations describes this relationship.

$$\dot{m}_{lacI} = -m_{lacI} + \frac{\alpha}{1 + p_{cI}^n} + \alpha_0 \quad (1)$$

$$\dot{p}_{lacI} = -\beta(p_{lacI} - m_{lacI}) \quad (2)$$

$$\dot{m}_{tetR} = -m_{tetR} + \frac{\alpha}{1 + p_{lacI}^n} + \alpha_0 \quad (3)$$

$$\dot{p}_{tetR} = -\beta(p_{tetR} - m_{tetR}) \quad (4)$$

$$\dot{m}_{cI} = -m_{cI} + \frac{\alpha}{1 + p_{tetR}^n} + \alpha_0 \quad (5)$$

$$\dot{p}_{cI} = -\beta(p_{cI} - m_{cI}) \quad (6)$$

Here  $\beta$  denotes the ratio of protein lifetime to messenger lifetime;  $n$  represents the affinity that the repressor protein has for the promoter site;  $\alpha_0$  is the quantity of protein produced during saturation of depressor; and  $\alpha + \alpha_0$  is the number of protein copies per cell in the absence of repressor. Thus,  $\alpha_0$  represents the efficiency with which repressor protein inhibits transcription. In this work we consider the case when  $\alpha_0 = 0$ , which is the biological scenario when no messenger is produced for saturating concentrations of repressor protein. For the sake of clarity, we switch to a familiar notation that makes use of the index convention discussed above. Specifically, we make the following substitutions

$$m_{lacI} = x_1 \quad (7)$$

$$p_{lacI} = y_1 \quad (8)$$

$$m_{tetR} = x_2 \quad (9)$$

$$p_{tetR} = y_2 \quad (10)$$

$$m_{cI} = x_3 \quad (11)$$

$$p_{cI} = y_3, \quad (12)$$

and rewrite the repressilator model as follows:

$$\dot{x}_1 = -x_1 + \frac{\alpha}{1 + y_3^n} \quad (13)$$

$$\dot{y}_1 = -\beta(y_1 - x_1) \quad (14)$$

$$\dot{x}_2 = -x_2 + \frac{\alpha}{1 + y_1^n} \quad (15)$$

$$\dot{y}_2 = -\beta(y_2 - x_2) \quad (16)$$

$$\dot{x}_3 = -x_3 + \frac{\alpha}{1 + y_2^n} \quad (17)$$

$$\dot{y}_3 = -\beta(y_3 - x_3). \quad (18)$$

By using compact notation we may further reduce the system to the following six coupled ordinary differential equations

$$\dot{x}_i = -x_i + \frac{\alpha}{1 + y_j^n} \quad (19)$$

$$\dot{y}_i = \beta x_i - \beta y_i, \quad (20)$$

where  $i = 1, 2, 3$  corresponds to  $j = 3, 1, 2$ . Closed form analytical solutions of Equations (19) and (20) are mathematically intractable to obtain due to the highly nonlinear terms give by Hill term

$$h(y_j) = \frac{1}{1 + y_j^n} \quad (21)$$

which prevents us from solving these with conventional techniques in linear differential equation theory. We thus resort to nonlinear dynamical systems theory to analyze the equilibrium solutions and their associated stability.

## STEADY STATES

We begin by linearizing Equations (19) and (20), which will provide us with a first glance of the system's dynamic behavior. By setting  $\dot{x}_i = \dot{y}_i = 0$  we can find the solutions for which the concentration of messenger and protein are not changing. This will allow us to determine how the system behaves once it has reached an equilibrium state. Setting  $\dot{x}_i = 0 = \dot{y}_i$  we obtain

$$-x_i^* + \frac{\alpha}{1 + (y_j^*)^n} = 0 \quad (22)$$

$$\beta x_i^* - \beta y_i^* = 0. \quad (23)$$

Equation (23) implies that  $\dot{y}_i = 0$  if and only if

$$x_i^* = y_i^*. \quad (24)$$

Since we want both  $\dot{y}_i$  and  $\dot{x}_i$  to be zero, we can substitute (23) into (21) to obtain

$$-x_i^* + \frac{\alpha}{1 + (x_j^*)^n} = 0, \quad (25)$$

or equivalently

$$x_i^*(1 + (x_j^*)^n) = \alpha. \quad (26)$$

This generates a system of 3 nonlinear algebraic equations whose solution correspond to the steady state solution for the messenger Equation (19). That is, we have the system

$$x_1^*(1 + x_3^{*n}) = \alpha \quad (27)$$

$$x_2^*(1 + x_1^{*n}) = \alpha \quad (28)$$

$$x_3^*(1 + x_2^{*n}) = \alpha. \quad (29)$$

From here, we have several options to compute a solution. The first is to use numerical analysis to compute the roots of the vector valued function

$$f(x_1, x_2, x_3) = \begin{pmatrix} x_1(1 + x_3^n) - \alpha \\ x_2(1 + x_1^n) - \alpha \\ x_3(1 + x_2^n) - \alpha \end{pmatrix}. \quad (30)$$

In the case of systems of equations, Newton's method takes the form:

$$x^{k+1} = x^k - J_f^{-1}(x^k) \cdot f(x^k)$$

where  $x^k$  corresponds to the  $k^{th}$  iteration;  $f$  is the vector valued function represented by the system of algebraic equations; and  $J_f^{-1}$  is the inverse of the Jacobian matrix of  $f$ . In computing the Jacobian associated with  $f$ , we receive

$$J_f(x_1, x_2, x_3) = \begin{pmatrix} 1 + x_3^n & 0 & x_1(1 + nx_3^{n-1}) \\ x_2(1 + nx_1^{n-1}) & 1 + x_1^n & 0 \\ 0 & x_3(1 + nx_2^{n-1}) & 1 + x_2^n \end{pmatrix}. \quad (31)$$

Then, we invert the matrix as a separate step within our algorithm. Here we must make a choice of parameters to in order to execute the algorithm. Our initial choice of  $\alpha$  and  $n$  were informed by [1]. Namely, the Hill coefficient  $n$  was taken to be within a neighborhood of 2 and we chose  $\alpha = 1000$ . The result is given by

$$\begin{pmatrix} x_1 \\ x_2 \\ x_3 \end{pmatrix} = \begin{pmatrix} 9.9667 \\ 9.9667 \\ 9.9667 \end{pmatrix}, \quad (32)$$

or that  $x_1^* = x_2^* = x_3^*$ . In fact, running numerous simulations for varying  $\alpha$  and  $n$ , we received  $x_1^* = x_2^* = x_3^*$  at steady state. So our steady state solution has the form

$$x_i^* = y_j^* \quad (33)$$

for  $i, j \in \{1, 2, 3\}$ . A necessary and sufficient condition for steady state is the all protein and messenger are at equal concentrations. We assume the existence of other steady solutions. Since Newton's method as applied above only returns this steady state solution, we require a different method.

Using substitution on the system in (26) to (28), we are able to obtain the equation

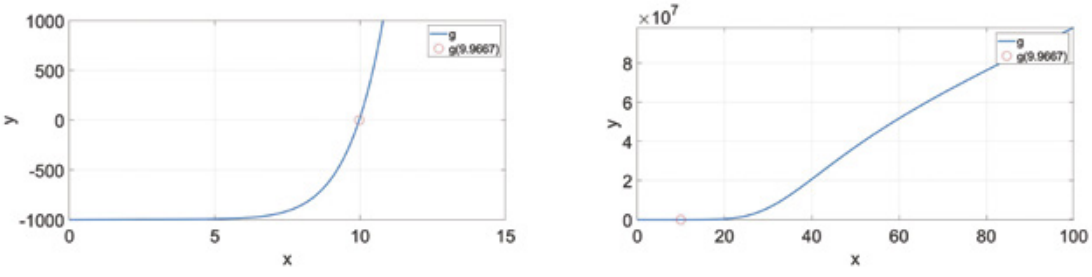
$$x_i^* \left( 1 + \left( \frac{\alpha}{1 + \left( \frac{\alpha}{1+x_i^{*n}} \right)^n} \right)^n \right) = \alpha \quad (34)$$

for  $i = 1, 2, 3$ . It is our ability to organize the system of equations into an equation of one variable independent of index that implies  $x_1^* = x_2^* = x_3^*$ . In order to ensure consistency however, we supply verification via Netwon's method. Again choosing  $n = 2$  and  $\alpha = 1000$ , we found  $x^* = 9.9667$  as the root of the equation.

As a means of additional verification, we graph the function

$$g(x) = x \left( 1 + \left( \frac{\alpha}{1 + \left( \frac{\alpha}{1+x^n} \right)^n} \right)^n \right) - \alpha \quad (35)$$

to observe all possible fixed points. That is, if (32) is the only steady state solution as our first check suggests, then  $g$  will only have one root.



(a) We display  $g$  for small time scale.      (b) We show that we can expect  $g$  to be globally increasing.

**Figure 4.** We graph  $g$  for varying time scales to analyze its behavior.

In Figure 4a, we see that  $g$  is increasing and  $g(9.9667) = 0$ . In Figure 4b,  $g$  is found to be increasing for large values of  $x$ . Note that we exclude any values corresponding to  $x < 0$  as it is meaningless to have negative concentration of

messenger.

For our final means of verification, we graph the system of equations. We apply Runge-Kutta order four for systems to the function

$$F(x_1, y_1, x_2, y_2, x_3, y_3) = \begin{pmatrix} -x_1 + \frac{\alpha}{1+y_3^n} + \alpha_0 \\ \beta x_1 - \beta y_1 \\ -x_2 + \frac{\alpha}{1+y_1^n} + \alpha_0 \\ \beta x_2 - \beta y_2 \\ -x_3 + \frac{\alpha}{1+y_2^n} + \alpha_0 \\ \beta x_3 - \beta y_3 \end{pmatrix} \quad (36)$$

for an initial condition that assumes all concentrations are zero at  $t = 0$ .

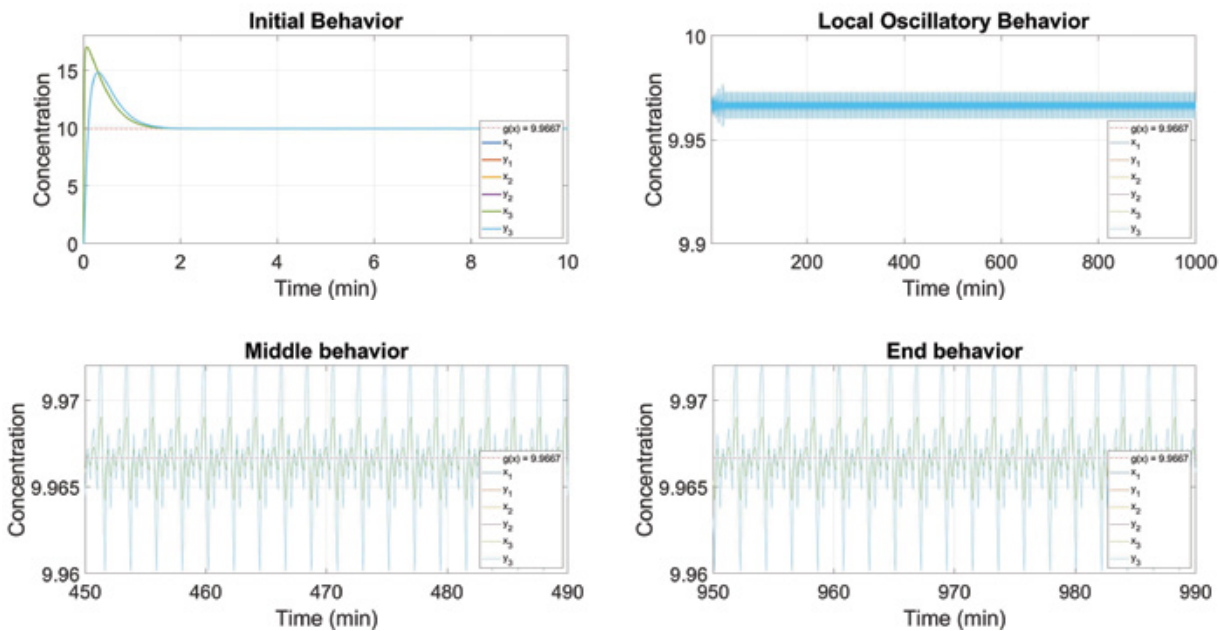


**Figure 5.** We graph the system of equations and zoom for varying time scales

In the first figure, we see that all six curves are variant for small time scale. As  $t$  increases, each curve asymptotically approaches the steady state solution. Namely, this figure suggests not only that our calculated steady state solution is the only solution, but also that the steady state is stable. Were it unstable, we would expect all curves to diverge away from the steady state. This, however, is not possible within the context of our biological system, provided that all initial conditions are zero.

The adjacent figure shows the oscillatory behavior of the system about the steady state solution.

In the bottom right, we have a closer look at the oscillatory behavior. Again the red dotted line represents our steady state solution. We notice that this graph, as well as the one adjacent are identical. This suggests that the system, under the given initial condition, is expected to oscillate about the steady state for large time, or indefinitely. This runs contrary to what we might expect in a biological system; rather, we expect that over time, the system will stabilize—not oscillate.

We have provided now four means of verification for the unique steady state solution represented in Equation (33). Going forward, we make the assumption that at steady state all concentrations are equal.

## LINEARIZATION

In order to carry our the linearization procedure, we organize Equations (13) through (18) into a vector equation. We assign messenger related functions to  $f_i$  and protein related functions are  $g_i$ . This has the form

$$\begin{pmatrix} \dot{x}_1 \\ \dot{y}_1 \\ \dot{x}_2 \\ \dot{y}_2 \\ \dot{x}_3 \\ \dot{y}_3 \end{pmatrix} = \begin{pmatrix} f_1(x_1, y_1, x_2, y_2, x_3, y_3) \\ g_1(x_1, y_1, x_2, y_2, x_3, y_3) \\ f_2(x_1, y_1, x_2, y_2, x_3, y_3) \\ g_2(x_1, y_1, x_2, y_2, x_3, y_3) \\ f_3(x_1, y_1, x_2, y_2, x_3, y_3) \\ g_3(x_1, y_1, x_2, y_2, x_3, y_3) \end{pmatrix} = \begin{pmatrix} -x_1 + \frac{\alpha}{1+y_3^n} + \alpha_0 \\ \beta x_1 - \beta y_1 \\ -x_2 + \frac{\alpha}{1+y_1^n} + \alpha_0 \\ \beta x_2 - \beta y_2 \\ -x_3 + \frac{\alpha}{1+y_2^n} + \alpha_0 \\ \beta x_3 - \beta y_3 \end{pmatrix}. \quad (37)$$

Letting  $z = (x_1, y_1, x_2, y_2, x_3, y_3)^T$ , it follows that the system can be simplified to the vector equation  $\dot{z} = F(z)$ .

For our analysis, we let  $\eta_i$  represent a perturbation in messenger concentration and we let  $\xi_i$  be perturbation in protein concentration. Now, we suppose that

$$x_i = x_i^* + \eta_i \quad (38)$$

$$y_i = y_i^* + \xi_i, \quad (39)$$

or that  $x_i$  and  $y_i$  are small perturbations about the steady state solutions. Rearranging these terms yields

$$\eta_i = x_i - x_i^* \quad (40)$$

$$\xi_i = y_i - y_i^*, \quad (41)$$

and in differentiating, we obtain

$$\dot{\eta}_i = \dot{x}_i \quad (42)$$

$$\dot{\xi}_i = \dot{y}_i. \quad (43)$$

Recall that the steady state solution implies all fixed points are equal. For this reason, we proceed by suppressing the indices on steady state values and replace all fixed point terms with  $x^*$ .

Let  $z^* = (x^*, x^*, x^*, x^*, x^*, x^*)^T$  and  $\theta = (\eta_1, \xi_1, \eta_2, \xi_2, \eta_3, \xi_3)^T$ . Then  $z$  is a vector-valued function dependent on time,  $z^*$  is a constant vector with the steady state in each coordinate and  $\theta$  is a perturbation vector. and From (42) and (43) we conclude that

$$\dot{\eta}_i = \dot{x}_i = f_i(z) = f_i(z^* + \theta) \quad (44)$$

$$\dot{\xi}_i = \dot{y}_i = g_i(z) = g_i(z^* + \theta), \quad (45)$$

hence

$$\dot{\theta} = \dot{z} = F(z) = F(z^* + \theta). \quad (46)$$

In applying the multi-variable Taylor expansion into the functions  $f_i$  and  $g_i$  about steady states we receive

$$f_i(z^* + \theta) = f_i(z^*) + \theta \cdot \nabla f_i(z^*) + h.o.t \quad (47)$$

$$g_i(z^* + \theta) = g_i(z^*) + \theta \cdot \nabla g_i(z^*) + h.o.t \quad (48)$$

where

$$\theta \cdot \nabla f_i(z^*) = \sum_{k=1}^3 \frac{\partial f_i}{\partial x_k}(x^*) \eta_k + \sum_{k=1}^3 \frac{\partial f_i}{\partial y_k}(x^*) \xi_k \quad (49)$$

$$\theta \cdot \nabla g_i(z^*) = \sum_{k=1}^3 \frac{\partial g_i}{\partial x_k}(x^*) \eta_k + \sum_{k=1}^3 \frac{\partial g_i}{\partial y_k}(x^*) \xi_k. \quad (50)$$

Since  $x^*$  is a fixed point,  $f_i(x^*) = 0 = g_i(x^*)$ . Also, the higher order terms (represented by h.o.t.) are negligible provided that  $f'_i(z^*)$  and  $g'_i(z^*)$  are different from zero. Thus,  $\dot{\eta}_i \approx \theta_i \cdot \nabla f_i(z^*)$  and  $\dot{\xi}_i \approx \theta \cdot \nabla g_i(z^*)$ . Thus the linearization for the system of six equations has the form

$$\dot{\theta} = F'(z^*)\theta, \quad (51)$$

which can be expanded to the matrix equation

$$\begin{pmatrix} \dot{\eta}_1 \\ \dot{\xi}_1 \\ \dot{\eta}_2 \\ \dot{\xi}_2 \\ \dot{\eta}_3 \\ \dot{\xi}_3 \end{pmatrix} = \begin{pmatrix} \frac{\partial f_1}{\partial x_1} & \frac{\partial f_1}{\partial y_1} & \cdots & \frac{\partial f_1}{\partial x_3} & \frac{\partial f_1}{\partial y_3} \\ \frac{\partial g_1}{\partial x_1} & \frac{\partial g_1}{\partial y_1} & \cdots & \frac{\partial g_1}{\partial x_3} & \frac{\partial g_1}{\partial y_3} \\ \vdots & \vdots & \ddots & \vdots & \vdots \\ \frac{\partial f_3}{\partial x_1} & \frac{\partial f_3}{\partial y_1} & \cdots & \frac{\partial f_3}{\partial x_3} & \frac{\partial f_3}{\partial y_3} \\ \frac{\partial g_3}{\partial x_1} & \frac{\partial g_3}{\partial y_1} & \cdots & \frac{\partial g_3}{\partial x_3} & \frac{\partial g_3}{\partial y_3} \end{pmatrix} \begin{pmatrix} \eta_1 \\ \xi_1 \\ \eta_2 \\ \xi_2 \\ \eta_3 \\ \xi_3 \end{pmatrix}. \quad (52)$$

Here each partial derivative is evaluated at the steady state  $z^*$  which suggests that the Jacobian matrix is merely a matrix of numbers. Substituting our information into Equation (52) yields the linear system of differential equations

$$\begin{pmatrix} \dot{\eta}_1 \\ \dot{\xi}_1 \\ \dot{\eta}_2 \\ \dot{\xi}_2 \\ \dot{\eta}_3 \\ \dot{\xi}_3 \end{pmatrix} = \begin{pmatrix} -1 & 0 & 0 & 0 & 0 & \alpha \frac{n(x^*)^{n-1}}{(1+(x^*)^n)^2} \\ \beta & -\beta & 0 & 0 & 0 & 0 \\ 0 & \alpha \frac{n(x^*)^{n-1}}{(1+(x^*)^n)^2} & -1 & 0 & 0 & 0 \\ 0 & 0 & \beta & -\beta & 0 & 0 \\ 0 & 0 & 0 & \alpha \frac{n(x^*)^{n-1}}{(1+(x^*)^n)^2} & -1 & 0 \\ 0 & 0 & 0 & 0 & \beta & -\beta \end{pmatrix} \begin{pmatrix} \eta_1 \\ \xi_1 \\ \eta_2 \\ \xi_2 \\ \eta_3 \\ \xi_3 \end{pmatrix} \quad (53)$$

which can be further reduced to the following linear system of first order equations

$$\dot{\eta}_1 = -\eta_1 + \alpha \frac{n(x^*)^{n-1}}{(1+(x^*)^n)^2} \xi_3 \quad (54)$$

$$\dot{\xi}_1 = \beta \eta_1 - \beta \xi_1 \quad (55)$$

$$\dot{\eta}_2 = -\eta_2 + \alpha \frac{n(x^*)^{n-1}}{(1+(x^*)^n)^2} \xi_1 \quad (56)$$

$$\dot{\xi}_2 = \beta \eta_2 - \beta \xi_2 \quad (57)$$

$$\dot{\eta}_3 = -\eta_3 + \alpha \frac{n(x^*)^{n-1}}{(1+(x^*)^n)^2} \xi_2 \quad (58)$$

$$\dot{\xi}_3 = \beta \eta_3 - \beta \xi_3. \quad (59)$$

We revert back to compact notation to develop a means of comparison to Equations (19) and (20). Specifically, letting  $i = 1, 2, 3$  and  $j = 3, 1, 2$  the system becomes

$$\dot{\eta}_i = -\eta_i + \alpha \frac{n(x^*)^{n-1}}{(1 + (x^*)^n)^2} \xi_j \quad (60)$$

$$\dot{\xi}_i = \beta \eta_i - \beta \xi_i. \quad (61)$$

Thus we have a system of six linear first order homogeneous ordinary differential equations that can be solved for any given parameters  $\alpha, \beta$  and  $n$ .

## CONCLUSION

In this work we have provided a complete linear analysis of the repressilator model. The resulting system of linear equations provides an exact solution for our model in a neighborhood about the steady state. Further analysis of the equilibrium solution shows that the steady state is stable, which confirms the biological requirement that cells adapt to small external perturbations. Additionally, computing the steady state solution in terms of the system parameters,  $\alpha$  and  $n$ , provides a better understanding into the overall dynamic behavior of the repressilator. For example, an interesting result from our parameter study was the existence of oscillations. In Figure 5 we show that the full nonlinear system exhibits oscillations for some parameter values. However, since these cannot be adequately studied with our linear approach, we decided to confirm them via numerical techniques on the full nonlinear system. Future research to study these oscillations analytically would entail analyzing the nonlinear higher order terms, which would provide a nonlinear bifurcation analysis of the system.

## REFERENCES

- Elowitz, M. & Leibler, S. A Synthetic Oscillatory Network of Transcriptional Regulators. *Nature* 403, 335-338 (2000)

# **Don't Walk and Text!: An Investigation of Cell Phone Usage by Pedestrians on CSUF's Campus**

**Crystal Rodela, Kimberly M. Zavala, and Natalie Lincoln**

**Advisor: Alison S. Marzocchi, Ph.D.**

*Department of Mathematics, California State University, Fullerton*

## **ABSTRACT**

Our research observation study was centered around the motivating question, *How many Cal State Fullerton pedestrians are engaged in their phones while walking through campus?* Based on our own experience walking through campus and noticing what seemed to be a large number of people on their phones, we conjectured that the majority of the students we observed would be on their cellphones while walking to class. To conduct this study, we sat in the Quad on campus, a busy area in the center of California State University, Fullerton (CSUF), to observe students passing by on their way to classes. The results that we gathered were able to show how many pedestrians were or were not on their phones while walking through this space. This is important to investigate because of the potential dangers people face while walking and looking down at their phones, including tripping or bumping into someone or something. Despite our initial conjecture, our results indicated that there were more students off their phones than on them.

## **INTRODUCTION**

The motivation of our study was to determine the amount of CSUF faculty and students that use their phone while walking through campus. We initially chose this topic because we were curious as to whether individuals were able to maneuver around trees, buildings, and other people properly while using their phones as well as to observe how many individuals preferred the company of others or the enjoyment of their surroundings over the use of their cellular device. To fully understand the question posed, the reader

should be informed that the CSUF campus is very large, with roughly 40,000 students, and has the largest student population throughout all of the Cal State Schools. As is likely the case with many universities, cellular phone use appears to be increasingly popular. Our findings help to quantify how common cell phone usage is amongst pedestrians.

## **METHOD**

To collect our data, the research team met on a Thursday in Spring 2017 from 10-11:15 a.m. in a common campus location called the Quad. The Quad is an area in between several important classroom buildings and the library so we were confident that it would receive a good amount of foot traffic. The population of our study are people who walk on CSUF's campus, and the sample set of our study are the individuals walking in the quad during the time that we observed. We assumed that most people on campus would have a phone on them somewhere, and we were curious as to whether it would be located hidden away in their backpacks, pockets, or in use. To conduct this survey, we situated ourselves in the Quad facing different directions to ensure that pedestrians coming from different pathways would all be equally counted. This experiment did not require any interaction between the observers and the participants. To stay out of the way of those passing by, we sat on a bench in the center of the Quad. Each researcher made use of a tally sheet which had two columns, YES and NO. Since we observed for an hour and fifteen minutes, we divided up the time into five sections, each representing a time frame of 15 minutes. See the Appendix for a sample tally sheet.

There are several potential limitations present in our study. One limitation would be the risk of counting the same person twice. To prevent this, we faced different pathways and only counted the person if they walked towards us. Another potential limitation was our location. Although we feel we chose a spot located at the center of many common areas, we still only witnessed a small number of individuals on campus as compared to the entire campus body. Additionally, the accuracy of our findings may be impacted by the minimal amount of observational research that was conducted. There are roughly 40,000 students on campus at some point, Monday through Saturday, from 7 a.m. to 10 p.m., but we only observed pedestrians on one Thursday for an hour and fifteen minutes. Obviously, to have more accurate results there would need to be more people observed over more varying times and days, in different areas on campus. Our study captured a small sample. Lastly, our study sought to make claims about student cell phone usage; however, we soon realized that it would be challenging to discern between students and faculty or staff walking on campus. For this reason, we chose to include all pedestrians. Perhaps if we had a way to isolate students, the results would have indicated more cell phone usage, as students are likely from a younger generation with more cell phone dependency.

## VISUAL RESULTS

Our findings are captured in the pie graph in Figure 1. We chose this graph to show the overall results of our motivating question: *How many CSUF pedestrians are engaged on their phones while walking around campus?* We felt that a pie graph would display our results accurately and effectively for our study. Clearly shown in the graph below is the majority of pedestrians not on their phones. Sixty percent were not on their phone while forty percent were. The limitations to the pie graph include not being able to split the time intervals, which demonstrates at what time there was a large influx of pedestrians on their phones. The pie graph only allows us to look at the end results. We tried to avoid creating a misleading

graph by adding the information at the bottom of the graph, which explains that the sample of the study was 546 pedestrians, not the whole population of CSUF. This graph would be beneficial to use in promoting staying off phones while walking around and shows that there is a good amount of people disengaged from their surroundings.

Our findings are also displayed in the bar graph in

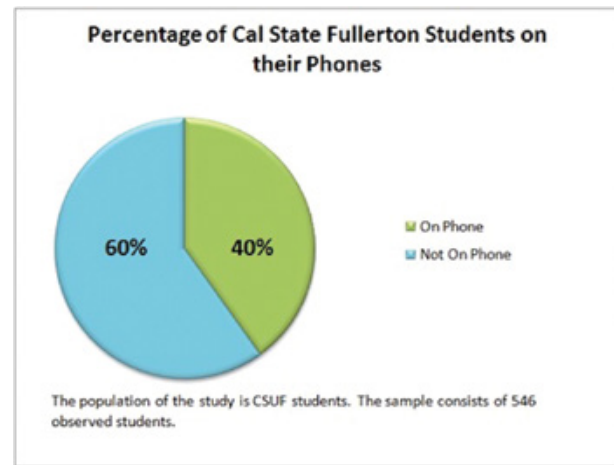
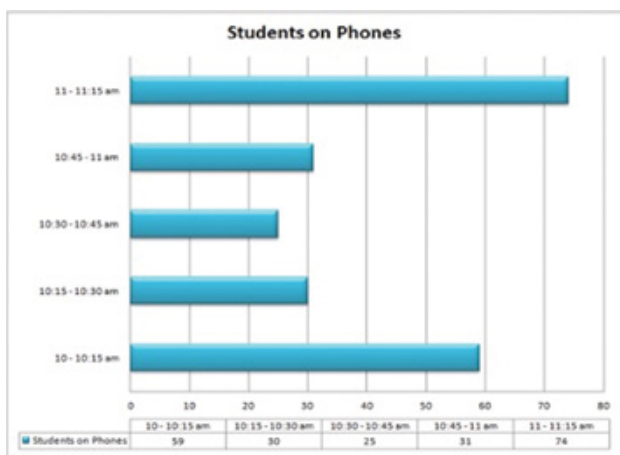


Figure 1. Pie Graph Chart

Figure 2, showing our results and the time increments that we took while we observed pedestrians. We felt that it was important to separate the time intervals and show how the amount of pedestrians changed, depending on the time, due to getting there, leaving or just walking around campus. The most popular times for pedestrians walking through the quad was between 10:00-10:15 a.m. and 11:00-11:15 a.m. We conjecture this to be the case because students and faculty are either on their way to class or just leaving the classroom. By using this graph, we were able to show the exact amount of pedestrians on their phones at the specific time intervals very clearly. This graph, however, doesn't allow us to easily see the end results of the entire study. Nor does it allow us to see the results of the people who weren't on their phones. This would be a good graph to use to communicate to people that being on the phone is a problem and urge everyone to refrain from using their phones.

while walking to fix the problem. The graph is easily understood and could serve as a good 'heads up' for students passing through the quad, at these specifically busy times, to be aware that as they pass their peers they need to be attentive due to the increase in cellular phone use.



**Figure 2.** Bar Graph showing time intervals of when people were on their phones while walking

## WRITTEN RESULTS

Our results are best understood through probability calculations. Our motivation was to observe the frequency of CSUF pedestrians on their phones while walking to calculate the amount of people who are inattentive to their surroundings or fellow peers while walking through campus. This motivating question arose from the desire to find the probabilities of people being on their phones at different times.

### #1: Probability:

(Pedestrians on their phone while walking through the Quad from 10-11:15)

( Total number of pedestrians observed in the Quad from 10-11:15 )

To calculate the probability of a pedestrian being on their phone while walking through the Quad on a Thursday between 10-11:15 a.m., we took the total

number of pedestrians on their phones from 10-11:15 a.m. (**219**) and divided that by the total number of pedestrians observed between 10-11:15 a.m. (**546**). The probability of a pedestrian being on his or her phone on a Thursday between 10-11:15 a.m. is (**219/546**) about a 40 percent chance.

### #2: Probability:

(Pedestrians not on phone while walking through the Quad from 10-11:15 )

( Total number of pedestrians observed in the Quad from 10-11:15 )

To calculate the probability of a pedestrian not being on their phone while walking through the Quad on a Thursday between 10-11:15 a.m., we took the total number of pedestrians not on their phones from 10-11:15 a.m. (**327**) and divided that by the total number of pedestrians observed between 10-11:15 a.m. (**546**). The probability of a pedestrian not being on their phone while walking through the Quad on a Thursday between 10-11:15 a.m. (**327/546**) is about a 60 percent chance. Probability #1 (40%) and Probability #2 (60%) sum to be 100% because each pedestrian we observed was recorded as either being on their phone or not being on their phone.

### #3: Probability:

(A pedestrian is on their phone while walking through Quad from 11-11:15 )

( Total number of pedestrians observed in the Quad from 11-11:15 )

To calculate the probability of a pedestrian being on their phone while walking through the Quad after class gets out at 11 a.m., we took the number of pedestrians who were on their phones from 11-11:15 a.m. (**74**) and divided that by the total number of pedestrians observed in the Quad between 11-11:15 a.m. (**177**). The probability of a pedestrian being on his or her phone while walking through the Quad on a Thursday between 11-11:15 a.m. is (**74/177=37/88.5=.42**) about a 42 percent chance. We isolated this particular time interval because it was the interval during which we observed

the greatest number of pedestrians, so we were curious whether the increased traffic would relate to increased or decreased cell phone usage while walking.

By answering these questions of the probability of people being on or off their phones at the specified times, students can benefit. The benefit is having a rough idea of what the Quad will be like if they decided to pass through on a Thursday, between the times that we studied. This can be helpful to plan out which route one might take when on their way to class in order to avoid inattentive walkers. This study also provides a snapshot of general pedestrian phone usage around campus.

Additionally, these questions are insightful to the common student. As a group CSUF students, we found our results to be different than what our personal experiences here on campus had made us believe. There is still much to investigate about this phenomenon due to the fact that our personal experiences on campus had led us to assume a different conclusion than we actually reached with our observations. Rather than a majority of pedestrians being on their phones like we had predicted, our data demonstrated that the majority of pedestrians during this time actually had their phones put away.

## SUMMARY

The motivation of this study was to determine the amount of California State University, Fullerton pedestrians that were on their phone while walking through the Quad on campus. Before conducting this observation, we posed a prediction of there being more students on their phones than not. To our surprise, there was a different outcome with a greater amount of individuals not on their phones. After looking over our data, we noticed that there was a significant amount of walkers between 10:00-10:15 a.m. and 11:00-11:15 a.m. compared to the rest of the time slots. Our best explanation for the increase of traffic flow during these two fifteen-minute intervals is due to students running late to class or leaving their classrooms. The middle time slots are more than likely the least popular due to the larger number of students being in class.

The contribution of our study is telling CSUF students the least popular times to walk through the

Quad on a regular school day or to at least avoid certain times where people may not be paying attention.

Another contribution would be to perhaps inform the student body of our results so they can better understand how often phones are used on campus; particularly in common areas. Additionally, our study captured the fact that people are engaged with their phones while walking, which means for an increment of time, they are not paying attention to their surroundings. This is a problem if the number of students on the phone is not zero. One of the authors is a biking student and she has seen many dangerous situations due to people not paying attention. She has even encountered physical harm due to people passing by not paying attention, because of cellular distraction. This is one reason why we felt this was an important study to investigate.

We originally intended to study *student* cell phone use specifically however, during data collection, we found that it was difficult to distinguish whether a given pedestrian was a student, faculty or staff member, or visitor. For this reason, we expanded our sample to include any pedestrians we observed. This could account for the lower percentage of cellphone users than conjectured. This is because students are likely from a younger generation that may suffer from greater cell phone dependency than older individuals. Had we been able to isolate student pedestrians, we may have seen a higher percentage of cellphone users.

To modify this study for more accurate results, we would branch out to different areas of campus, at different times, to try and capture a more campus-wide study. We hypothesize that our results might begin to change if the study included more time, to observe more people, in more areas. Due to the minimal study subjects **546** out of roughly **40,000** students, the accuracy of our study could be greatly improved with more subjects observed.

In the end, 40% of pedestrians using cellphones while walking is still a considerably high number. Though it is lower than we had conjectured, we still think that “four out of ten people” or “two out of five people” walking while using their phones is alarming. This could cause a hazard to yourself or those around you. Future research could investigate whether this is a growing problem.

## APPENDIX

*Sample raw data tally sheet.*

Time	# of students on their phone	# of students not on their phone
10-10:15am		
1:15-10:30am		
10:30-10:45am		
10:45-11am		
11-11:15am		

# **Mathematical Model to Noninvasively Detect Dry-eye Diseases**

**Trini Nguyen<sup>1</sup>**

**Advisors: Charles Lee, Ph.D.<sup>1</sup>, Mr. Stanley Huth<sup>2</sup>, and Nattapol Ploymaklam, Ph.D.<sup>3</sup>**

<sup>1</sup>*Department of Mathematics, California State University, Fullerton,*<sup>2</sup> *Abbott Medical Optics Inc., Santa Ana, CA (Retired),*<sup>3</sup> *Department of Mathematics, Chiang Mai University, Thailand*

## **ABSTRACT**

Noninvasive interferometry is a diagnostic technique for dry-eye diseases. The process requires shining light on the eye while measuring its reflectance at multiple wavelengths. After this measurement, the tear film layers can then be extracted implicitly. In a 2013 patent from Abbott Medical Optics, Inc., a mathematical model for the reflectance measurement was presented; however, it did not characterize well all data sets because it did not take into account the nonlinear scattered light at the corneal surface. In this work, several models that describe the eye reflectance are derived and compared to find one that characterizes all datasets. The models take into account electromagnetic properties, angles of the incident light, and the tear thicknesses, which are to be solved. The exponential parts of these models that consider the scattered light are all of higher order, which contrast the model in the 2013 patent. With a higher order, we observe higher accuracy in the models. In addition, a computer program based on these models has been written. A similar program in the patent was quite complicated because its scheme took up over ten pages of code and 45 minutes to produce the thicknesses. Our scheme runs within a few minutes, making it practical for clinical dry-eye disease diagnoses.

## **INTRODUCTION**

Dry-eye diseases are among the most frequent diagnoses in ophthalmology. Approximately five million Americans who are 50 years of age and older have been diagnosed with these diseases, but younger people, especially contact lens wearers and those that stare at computer screens for long amounts of time, are susceptible to them as well [15]. Dry eye occurs

when the tear film, which consists of all the tear layers on the eye, becomes too thin, either because the eye is unable to produce the adequate amount of tears (aqueous-deficient dry-eye) or because the tears are evaporating too quickly (lipid-deficient dry-eye) [29]. Numerous factors affect a person's chance of developing the disease, including age (older adults are more prone to autoimmune diseases that can lead to dry-eye diseases), gender (women are more likely than men to have dry eyes), certain medications that can decrease tear production, medical and environmental conditions such as vitamin deficiency, dry weather or strong winds, and long-term use of contact lenses [2]. For example, women undergoing menopause are more likely to have dry eyes, since the imbalance of hormones during this period can upset the lacrimal gland, which secretes tears onto the eye [32]. Although some view dry-eye disease as only a mere irritation, the symptoms can be serious, such as extreme pain and eye redness (Figure 1), and are experienced constantly by those with the disease, so everyday activities such as reading or using a computer can be impacted [29]. If left untreated, dry-eye diseases can lead to permanent eye damage and thus impair one's vision. Many treatments are available for these diseases, with the purpose of comfort, symptom relief, and further corneal damage prevention [31]. Artificial tears are used by patients who are unable to produce adequate amounts of tears, punctal plugs are inserted into tear ducts of those with moderate to severe dry eyes, and vitamin A and omega 3 fatty acids supplements are recommended to protect the eye from inflammation [29]. However, current diagnostic methods are inaccurate, since the sensitivity of the eye makes exact tear measurements nearly impossible, so prescribing an effective medication is often difficult without a confident diagnosis. Due to the

risk of serious eye damage and the large number of people that are affected by these diseases, there is a dire need for the condition to be accurately diagnosed and treated efficiently [6].

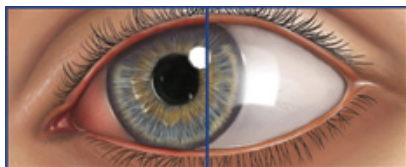


**Figure 1. Dry Eye vs. Normal Eye.** When the eye becomes dry, redness can occur (as seen on the left-hand side), which is a sign of a damaged cornea [25].

### Current Diagnostic Methods

There are three categorical degrees of dry-eye diseases: mild, moderate, and severe [29]. The current diagnostic methods struggle in detecting each level without depending on another technique. Some approaches provide more accuracy than others but are uncomfortable for the patient, while those that are discomfort-free lack accuracy [26]. In addition, several ophthalmic diseases share similar symptoms, so it is often difficult to interpret whether a certain symptom is caused by dry-eye diseases specifically.

Current diagnostic methods include both invasive and noninvasive techniques. While the noninvasive practices have fewer risks of further eye damage compared to the invasive procedures, both approaches still need improvement, as neither provide the accuracy and comfort that is necessary for such a sensitive part of the body.

### Invasive Methods

Invasive methods include fluorescein staining, tear film break-up time (TBUT), the Schirmer test, the Phenol red thread test, and Rose Bengal or lissamine green staining [12]. Fluorescein and Rose Bengal stainings each require a solution to be dropped onto the eye of the patient, although for different purposes. In fluorescein staining, the intensity of the stain is used to detect corneal injuries, since the stains appear in epithelial erosions and degenerating or dead cells [29]. However, dry-eye diseases are not the only causes of corneal damage, and thus fluorescein stain-

ing must be used with other methods to determine actual dry-eye status [32]. The Rose Bengal method also relies on the intensity of the stain, and it indicates whether a specific layer of the tear film is mildly deficient by staining any healthy cells that are not properly covered enough by tears. However, the tear film consists of several layers, so the method lacks information on the other layers [12]. Moreover, this technique is only useful in the absence of other ocular surface diseases and is rendered useless when these diseases are also at play. Finally, Rose Bengal has been found to damage the cornea by swelling the cells [20]. Lissamine green staining is less toxic for the eye, but it still is useless if a patient has several eye diseases. For these reasons, the staining methods do not allow ophthalmologists to move forward with proper diagnostics.

TBUT also requires fluorescein, but on a strip of paper, which is to be placed on the eye rather than applying the solution directly onto the eye [17]. Fluorescein spots on the eye imply dryness, so blue light is then shone on the eye to check for the rate of these spots appearing [29]. The time it takes for the spots to appear is measured, since the tear film breaks up faster in people with dry eyes and can be used as an indication of tear deficiency. However, the fluorescein strip, when placed onto the eye, causes additional tearing on the eye and thus disrupts the time measurements. In addition, the fluorescein also changes the properties of the tears, so TBUT measurements also yield inaccurate results.

The Schirmer test also uses a strip of paper that is placed onto the eye, but with no solution on the paper. A  $35\text{ mm} \times 5\text{ mm}$  filter paper strip is inserted in the lower cul-de-sac of the eye for five minutes to study the amount of tears produced from the patient in a given amount of time [4]. There are standard amounts of tears that normal, healthy eyes can produce in five minutes, so any amount that is less than this standard implies dryness. However, this test is only relevant for those with severe dry-eye disease; it becomes very inaccurate when attempting to detect mild and moderate levels of dry-eye [16]. Also, like the TBUT method, the strip of paper distorts the measurements, this time by promoting more tears, as the main purpose of tears is to remove foreign objects from the eye. Thus, the process is deemed as highly unfavorable by doctors for its invasiveness and inaccuracy.

curacy.

The Phenol red thread test was developed in an attempt to ease the invasiveness of the Schirmer test [12]. However, it is still quite invasive to patients. In this method, a thread impregnated with red dye is placed onto the eye, and the stain will change color upon contact with tears. The color change in the thread is measured after 15 seconds. Darker colors imply a thicker tear film, while lighter colors imply a thinner tear film. While it is slightly less invasive than the Schirmer test, the Phenol red thread method lacks accuracy when detecting mild and moderate levels of dry-eye, similar to the Schirmer test, so an effective treatment is difficult to prescribe. Overall, invasive techniques do not offer enough precision to compensate for its high discomfort to patients.

### **Noninvasive Methods**

To combat the problems of discomfort with invasive methods, researchers and engineers have developed noninvasive techniques, which as the name implies, do not cause discomfort to the patient and are thus more favorable than invasive methods. These methods include symptom assessment, noninvasive tear film break-up time (NITBUT), and conjunctival hyperemia [12]. Symptom assessment is a method in which the overall feature of the eye is assessed visually and the report of the patient's experience with the current state of the eye is taken into account. This assessment may include symptoms, every day activities (reading, driving, staring at a computer screen, etc.) that are limited due to dry eyes, and the surrounding environmental conditions [29]. Despite the depth of the assessment, this method lacks the much-needed information for diagnosis because the detailed analysis of the cornea is overlooked, since problems on the cornea cannot be determined from only observing the ocular surface alone. Also, the patient may be unable to accurately describe the symptoms he/she is experiencing. The NITBUT method also lacks information, as the specific degree of disease and damaged eye feature are unknown from this method, and it yields inaccurate results. With NITBUT, the ophthalmologist studies the eye through a keratometer, which shows the circular tear patterns on the eye. As with the TBUT method, the time it takes for the pattern to move is measured, as this move-

ment implies that the tear film has begun to break, or dry. However, the tear evaporation rate is approximately the only information the ophthalmologist can pull from this method. The degree of dry-eye disease is not clear from observing the tear patterns alone, since abnormal tear breakup time is present in several dry-eye types. Also, the keratometer can produce inconsistent measurements in detecting dry areas.

Lastly, conjunctival hyperemia assessment is a noninvasive method that studies the redness of the cornea [12]. This test studies dry-eye diseases that cause conjunctival hyperemia, which is an excess of blood in the conjunctival vessels. Since corneal redness can be caused by several eye conditions, and not only dry-eye diseases, the method must be used with other diagnostic methods in determining dry-eye disease status. With the current availability of diagnostic methods producing inconclusive results, efforts are continually made to improve on the noninvasive techniques, as their only drawback is their inaccuracy.

### **Structure of the Tear Film**

Most diagnostic methods study the thickness of the tear film layers, since thinning of the tear film directly implies drier eyes. The tear film is made up of three layers, as depicted in Figure 2: the lipid layer, the aqueous layer, and the mucin layer [30]. The lipid layer, which tops the tears and is secreted by the meibomian glands, can be broken down into two further layers: nonpolar and polar [33, 25]. Nonpolar lipids decrease the evaporation rate of the tears, while polar lipids lie underneath the nonpolar lipids, keeping them attached to the rest of the tear film. The complexity of these lipids makes the entire lipid layer as crucial as the aqueous layer, which lies underneath the lipid layer and is secreted by the lacrimal gland. The aqueous layer contains electrolytes and proteins but is mainly composed of water. This aqueous solution allows for the layer to wash out any foreign substances on the ocular surface and provide comfort. Underneath the aqueous layer and above the corneal epithelium is the top surface of the eye: the mucin layer, which is secreted by conjunctival goblet cells and removed after a blink [8]. The stickiness of the mucin layer keeps the aqueous tears from constantly falling onto the face, ensures that the tears are equally spread over the eye surface, and protects

the corneal epithelium from pathogens [22].

The lipid layer and the aqueous layer are essential for the ocular comfort and are also the most vulnerable to the outside environment. This vulnerability makes the risk for thinning of these layers high. If either layer is too thin, there will not be a sufficient amount of tears on the eye, resulting in dry eye. Thus, the types of dry-eye diseases consist of inadequate tear production (thinning of the aqueous layer) and high tear-evaporation rate (thinning of the lipid layer) [29]. If ophthalmologists can determine the thicknesses of each of these layers, they can decide which layer needs to be treated accordingly.

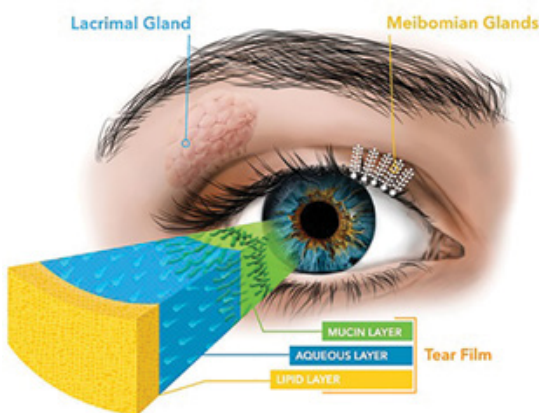


**Figure 2.** Layers of the Tear. The tear film consists of the lipid layer (yellow), the aqueous layer (blue), and the mucin layer (green). If either the lipid or the aqueous layers are too deficient, dry eye will occur [1].

The mucin layer of the tear film is held onto the corneal epithelium by a collection of molecules called the glycocalyx [19]. The glycocalyx helps the mucin layer in preventing foreign bodies and pathogens from entering further than the ocular surface [27]. Damage to this structure results in the rapid loss of tears, even after several blinks, since tears are held onto the eye by the mucin layer, which is attached to the eye by the glycocalyx. Several dry-eye disease patients possess a damaged glycocalyx [22]. Knowledge of the strength of the glycocalyx can thus assist in the diagnosis of dry-eye diseases. To determine the quality of the glycocalyx, researchers can use the corneal

surface refractive index [14]. The refractive index describes the speed of light traveling through a given material [7]. The greater the thickness of the material, the higher the refractive index (assuming the temperature of the material is constant) [21]. Since there are no existing methods that can determine the corneal refractive index noninvasively [14], improvements to dry-eye disease diagnostic tools must include the measurement of this feature.

### Wavelength-Dependent Interferometry

A noninvasive method to calculate the thicknesses of the tear film layers is measuring the reflectance of the eye, or the total light that is reflected from the eye, using wavelength-dependent interferometry. This method has been successfully used in the past to estimate the aqueous layer, but a method to measure the lipid layer thickness and the corneal refractive index is still needed [11]. Total reflected light refers to all of the reflected light that can travel through several layers. The light between each of the layers form oscillations, and these oscillations make up the reflectance of the eye [18]. The reflectance is needed because there is a correlation between the frequency of the light oscillations and the thicknesses of the tear film layers.

In the wavelength-dependent interferometry method, the patient looks through an interferometer, which rapidly shines light onto the patient's eye at different wavelengths. The reflectance of the eye is then measured by wavelength. One only needs the reflectance measurements and a mathematical model that relates the reflectance to layer thickness to determine the thicknesses of the tear film layers. This model must describe the reflectance in terms of the tear film thicknesses so that the tear film thicknesses can be solved, and the dryness of the eye can be established.

A mathematical model that describes the general relationship between the light that is transmitted through the media, and the light that is reflected from this media, already exists [14]. Figure 3 shows the light that is transmitted at each layer and then reflected back. The equation was derived from elec-

<sup>1</sup>The angle between the ray of the light and the normal (perpendicular line to the surface).

<sup>2</sup>A number that describes how light travels through the material. This index is a unitless number and is the ratio of the speed of light in a vacuum to the speed of light through a material [7].

tromagnetic properties of light and layer materials [10, 28]. Utilizing the angle of incidence<sup>1</sup>, the refractive indices<sup>2</sup> of the layers, and the thicknesses of the tear film layers, one can directly calculate the theoretical reflectance of the material being examined [7]. If this predicted reflectance matches the actual reflectance measurements from the interferometer, then the tear thickness and corneal refractive index values used in the model to produce the matching predicted reflectance can be used to interpret the dry-eye disease status of the patient.

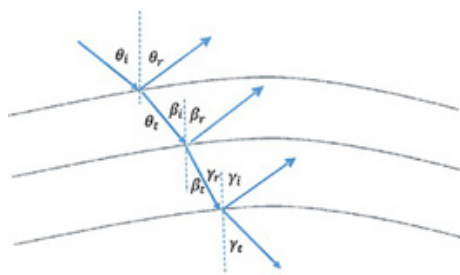


**Figure 3.** Angles of Incidences, Reflectance, and Transmittances. At Boundary I, the angle of incidence ( $i$ ) is equal to the angle of transmittance ( $t$ ) below it. The angles of reflectance ( $r$ ) are calculated using Snell's Law. Boundary I is enacted by  $\theta$ , Boundary II by  $\beta$ , and Boundary III by  $\gamma$  angles.

### Scalar Light Scattering Theory

The general model described can be applied to most substrates. However, the eye is a particular case. The corneal epithelium, mucin, and lipid layers of the eye are all very rough. The light that is reflected from these uneven layers becomes scattered, as is the case for all irregular surfaces [5]. Longer wavelengths will scatter less on a rough surface than shorter wavelengths, which creates different amplitudes [14]. Light traveling through several rough layers will become even more scattered, as each light ray will move differently when hit against different peak lengths [5]. This effect changes the overall spectral reflectance of the eye and is known as the Scalar Light Scattering Theory. A recent patent attempts to mathematically model the reflectance of the eye using this Scalar Light Scattering Theory of the eye [14]. To include the theory, the inventors of the patent had to choose a term that will mathematically reflect

this scattering effect, and they observed that the surface roughness of the corneal epithelium of some eyes possesses a non-Gaussian, or not normal, distribution. Thus, they multiplied a non-Gaussian term to the model that describes the behavior of general thin films. This new mathematical model produced accurate results for some patients while producing inaccurate results for others, since it only considered the Scalar Light Scattering Theory for non-Gaussian distributions in surface roughness and ignored it for Gaussian distributions. Thus, efforts to improve the wavelength-dependent interferometry and produce an accurate and efficient method to diagnose dry-eye diseases remain needed.

### Non-Gaussian Scattering Model

Eye surface roughness can be observed to have either a non-Gaussian or a Gaussian distribution [5]. Huth et al. (2013), the inventors of the recent patent, derived a model that took into consideration only eyes with non-Gaussian distributions. Figure 4 shows the theoretical reflectance that resulted from this model, where the curve and the data do not match at certain wavelengths. An exponential term was derived empirically and used to take into account the non-Gaussian distribution of eye surface roughness.

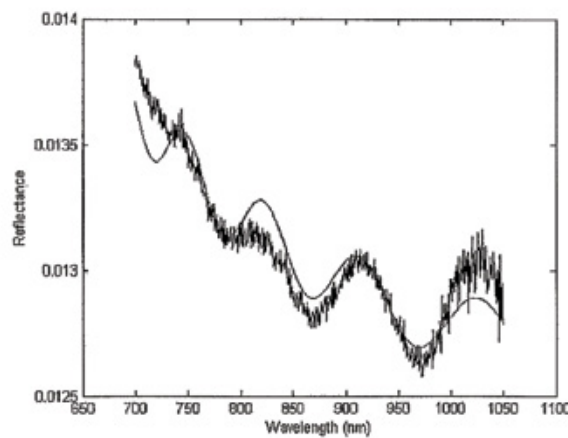


**Figure 4.** Theoretical Reflectance using Huth's Non-Gaussian Model. There are several areas where the theoretical reflectance (curve) do not match the measured reflectance (dots). This mismatch implies that the model used is inaccurate [14].

## Current Study

We have continued the efforts to derive a mathematical model that accurately describes the behavior of light when it is traveling through the rough tear film layers. Our model takes into consideration both types of scattering: non-Gaussian and Gaussian. By developing a model that more accurately describes the tear film, more accurate tear film thickness values will be yielded for better dry-eye disease diagnostics.

## METHODOLOGY

### Data Collection

Data of reflectance measurements from 11 patients were taken from the patents of Abbott Medical Optics Inc.<sup>3</sup> (US 8,602,557 B2 & US 9,456,741 B2), which were retrieved electronically from the United States Patent and Trademark Office. The data are in the form of graphs, and actual numerical data are unavailable to the public since they are the company's proprietary information. Since the graphs contained unwanted information besides the reflectance values, such as grid marks, the figure legend, and the patents' fitted curve, they were manually altered in Microsoft Paint to erase any markings that were not the reflectance values (Figure 6). To extract the numeric data values, the altered figures were then inputted into our Matlab program, which used the pixel levels of the figures to obtain the coordinates of the data and thus the numerical values.

### Model for General Thin Films

Physicist James Clerk Maxwell's model for general thin films was then manipulated to describe the reflectance behavior of the eye [10]:

$$\vec{H} = \sqrt{\frac{\epsilon_0}{\mu_0}} n \hat{k} \times \vec{E}, \quad (1)$$

<sup>3</sup>Company that designs and produces ophthalmology products [14, 13]

<sup>4</sup> $8.854 \times 10^{-12}$  F·m<sup>-1</sup>. Describes the amount of electricity in a vacuum [9]

<sup>5</sup> $4\pi \times 10^{-7}$  N/A<sup>2</sup>. Describes the magnetic field in a vacuum [24]

<sup>6</sup>A vector that points in the direction of a wave's, in this case, the incident light's, propagation [5]

<sup>7</sup>Snell's Law describes the relationship between two opposing angles, which are separated by a medium, and their corresponding refractive indices [14]:

$$n_0 \sin \theta = n_1 \sin \beta$$

where  $H$  denotes the magnetic field,  $\epsilon_0$  is the permittivity<sup>4</sup> (the ability of a material to store energy) of free space,  $\mu_0$  is the permeability<sup>5</sup> (the magnetic strength of a material) of free space,  $n$  is the refractive index of the layer (Figure 5, Table 1),  $\hat{k}$  is the magnitude of the wave vector<sup>6</sup> of the incident light, and  $E$  is the electric field from the incident light [3]. This model describes the relationship between the magnetic and electric fields enacted on a material when light is shone on it [24].

Refractive indices are determined using Snell's Law<sup>7</sup> [14]:

$$\begin{aligned} n_0 &= 1 \\ n_1 &= \sqrt{1 + \frac{(-851.03)\lambda^2}{\lambda^2 - 816.139} + \frac{(420.267)\lambda^2}{\lambda^2 + 706.86} + \frac{(431.856)\lambda^2}{\lambda^2 - 2355.29}} \\ n_2 &= 1.32806 + 0.00306 \left( \frac{1000}{\lambda} \right)^2 \\ n_3 &= 1.338 + 0.00306 \left( \frac{1000}{\lambda} \right)^2, \end{aligned} \quad (2)$$

where  $\lambda$  is the wavelength of light. It is important to note here that the value 1.338 in  $n_3$  is only a starting value used to be optimized later, since the refractive index of the corneal epithelium is unknown. Equation 1 is then separated according to the first two top layers of the tear film, and the resulting system of equations is put into matrix notation:

$$\begin{bmatrix} E_I \\ H_I \end{bmatrix} = M_I \begin{bmatrix} E_{II} \\ H_{II} \end{bmatrix} \quad (3)$$

to describe the relationship between the electromagnetic fields lying on Boundaries I and II (Figure 5), where

$$M_I = \begin{bmatrix} \cos k_0 h & \frac{i \sin k_0 h}{\Omega_1} \\ \Omega_1 i \sin k_0 h & \cos k_0 h \end{bmatrix},$$

$$k = \frac{2\pi}{\lambda},$$

$$h = 2n_1 d \cos \beta_i,$$

$d$  is the layer thickness,

$$\Omega_1 = \sqrt{\frac{\epsilon_0}{\mu_0}} n_1 \cos \beta_i,$$

and  $\beta_i$  is the incidence angle on Boundary II (Figure 3) [10]. It is important to note that  $d$  is the parameter of interest, as it is the thickness value of each tear film layer.

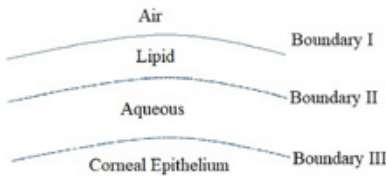


**Figure 5.** Tear Film Layers of a Normal Eye. The air, lipid, and aqueous layers are stacked on top of the corneal epithelium, which is the top surface of the eyeball. Each boundary curve (blue) depicts the ending of one layer and the beginning of the next. The mucin layer is not shown because it is very thin.

**Table 1.** Refractive Indices and their Corresponding Layers. Refractive indices are calculated using Snell's Law and are unitless. For example, the refractive index of air is 1.

$n_0$	Air
$n_1$	Lipid
$n_2$	Aqueous
$n_3$	Corneal Epithelium

To relate Boundaries II and III together, the system of equations is:

$$\begin{bmatrix} E_{II} \\ H_{II} \end{bmatrix} = M_{II} \begin{bmatrix} E_{III} \\ H_{III} \end{bmatrix}. \quad (4)$$

To relate all the layers of the tear film together—since Equations 3 and 4 each describe only two layers of the tear film— $M_I$  is multiplied to both sides of Equation 4:

$$\begin{bmatrix} E_I \\ H_I \end{bmatrix} = M_I M_{II} \begin{bmatrix} E_{III} \\ H_{III} \end{bmatrix} \quad (5)$$

where

$$\begin{aligned} M_I M_{II} &= \begin{bmatrix} \cos k_0 h_1 & \frac{i \sin k_0 h_1}{\Omega_1} \\ \Omega_1 i \sin k_0 h_1 & \cos k_0 h_1 \end{bmatrix} \begin{bmatrix} \cos k_0 h_2 & \frac{i \sin k_0 h_2}{\Omega_2} \\ \Omega_2 i \sin k_0 h_2 & \cos k_0 h_2 \end{bmatrix} \\ &= \begin{bmatrix} m_{11} & m_{12} \\ m_{21} & m_{22} \end{bmatrix}, \end{aligned}$$

$$h_1 = 2n_1 d_{lip} \cos \beta_i,$$

$d_{lip}$  is the thickness of the lipid layer,

$$h_2 = 2n_2 d_{aq} \cos \gamma_t,$$

and  $d_{aq}$  is the thickness of the aqueous layer.  $d_{lip}$  and  $d_{aq}$  are the parameters that we want to solve for in order to determine the thicknesses of the tear film.

Because reflectance is a ratio of the electric field intensities of the reflected light over the total light that is being shone on a medium [14], Equation 5 is manipulated so that theoretical reflectance can be described as:

$$\hat{R} = \frac{\Omega_0 m_{11} + \Omega_0 \Omega_3 m_{12} - m_{21} - \Omega_3 m_{22}}{\Omega_0 m_{11} + \Omega_0 \Omega_3 m_{12} + m_{21} + \Omega_3 m_{22}}, \quad (6)$$

where

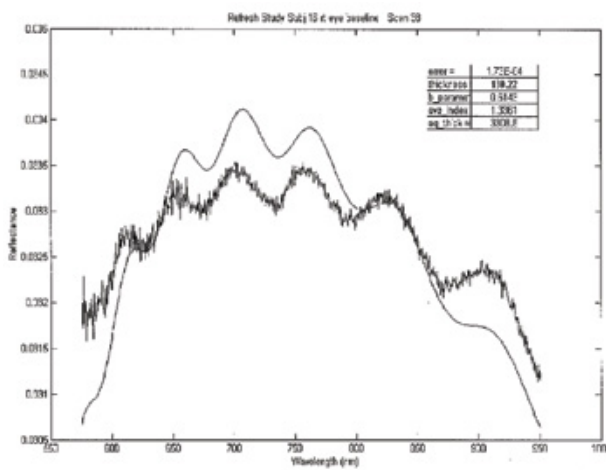
$$\Omega_0 = \sqrt{\frac{\epsilon_0}{\mu_0}} n_0 \cos \theta_i,$$

$$\Omega_3 = \sqrt{\frac{\epsilon_0}{\mu_0}} n_3 \cos \gamma_t,$$

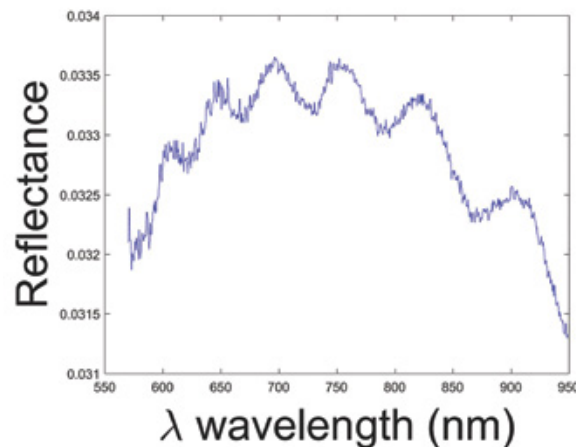
$\theta_i$  is the incident angle of the lipid layer, and  $\gamma_t$  is the transmitted angle under the aqueous layer.  $n_3$  is another parameter of interest, as it is the corneal refractive index, and determining its value will help interpret the integrity of the glycocalyx [14]. Note that  $\Omega_0$  is used to take into account the total light that starts from the air layer, and  $\Omega_3$  is used to take into account all of the layers of the tear film.

## Scattering Models

While light reflected off a smooth surface diffuses, it will scatter for rough surfaces [5]. Though the eye looks smooth, its surface is rough on the microscopic scale. As a result, our models must include a light scattering term.



(a) Embedded graphical data.



(b) Extracted data.

**Figure 6.** Example of Reflectance Data. Reflectance of a patient is graphed over wavelength (dots). The curve is the effort of Abbott Medical Optics Inc. to fit the data to a mathematical model [14]. Since only the dots are needed, the curve, legend, and grid markings were erased before extracting the data (b).

### Non-Gaussian Model

The only known model was given by Huth et al. (2013):

$$R = \hat{R}k_1 \exp \left[ a_1 \frac{1000}{\lambda} \right], \quad (7)$$

where  $\hat{R}$  is from the general model and  $k_1$  and  $a_1$  are constants [14]. While  $k_1$  accounts for the increase in the magnitude of the reflectance due to light scattering, the constant  $a_1$  relates the reflectance with light wavelength.

### Gaussian Model

It is noted that not all eye surfaces have non-Gaussian distributions of surface height [14]. Thus, our next model only includes a Gaussian term to describe the scattered reflected light:

$$R = \hat{R}k_1 \exp \left[ a_2 \left( \frac{1000}{\lambda} \right)^2 \right], \quad (8)$$

where the light scattering term is now replaced by a second-order term to account for Gaussian distributions.

### Bi-scattering Product Model

It is more probable that the scattering takes on both forms of Gaussian and non-Gaussian surface roughness. The Bi-scattering Product model we consider includes both types of surface roughness to check for both simultaneously:

$$R = \hat{R}k_1 \exp \left[ a_1 \left( \frac{1000}{\lambda} \right) + a_2 \left( \frac{1000}{\lambda} \right)^2 \right], \quad (9)$$

where  $k_1$ ,  $a_1$ , and  $a_2$  all are constants to fit the model better.

### Bi-scattering Sum Model

Another form of the Bi-scattering model is considered,

$$R = \hat{R} \left[ k_1 \exp \left( a_1 \left( \frac{1000}{\lambda} \right) \right) + k_2 \exp \left( a_2 \left( \frac{1000}{\lambda} \right)^2 \right) \right]. \quad (10)$$

This model is called the Bi-scattering Sum model, and  $k_1$ ,  $a_1$ ,  $k_2$ , and  $a_2$  are all constants. It is important to note that while the Bi-scattering Product model is the product of two exponential terms, the Bi-scattering Sum model is the sum of two exponential terms.

### Curve-Fitting

From Equation 6, it can be seen that  $R$  is a function dependent on  $\lambda$ ,  $d_{\text{lip}}$ ,  $d_{\text{aq}}$ , and  $n_3$ . Of these parameters, the value of  $\lambda$  is controlled by the interferometer, and  $d_{\text{lip}}$ ,  $d_{\text{aq}}$ , and  $n_3$  are all unknown. To solve for three unknown values with only one equation, a program was written in Matlab to find the optimal values of these parameters. These optimized parameters would compute a theoretical reflectance that should match the measured reflectance. Equation 6 was coded with the value of  $n_3$  as initialized with Equation 2,  $d_{\text{lip}}$  is iteratively changed between 20-140 nm, increasing by 20 nm each time, and  $d_{\text{aq}}$  is iteratively changed between 2000-6000 nm, increasing by 200 nm each time. These chosen values are the observed thicknesses in human eyes that range from extremely dry eyes to very wet eyes [14]. Using these initial starting values, Equation 6 is then optimized to fit the measured reflectance data using Matlab's function nlinfit<sup>8</sup>. The maximum number of functions to be evaluated was set at 2000, and the termination tolerance for  $x$  and the function value was set at  $10^{-10}$  and  $10^{-12}$ , respectively. The error of the determined theoretical reflectance is calculated using the root-mean-squared error:

$$RMSE = \sqrt{\frac{1}{n} \sum_{j=1}^n (t_i - r_i)^2},$$

where  $n$  is the number of data points,  $t$  is the theoretical reflectance,  $i$  is the particular data point, and  $r$  is the actual reflectance. The set of parameters that produces the smallest error is deemed the tear film layer thicknesses. The surface roughness parameters were initialized according to the values in Table 2.

<sup>8</sup>uses the Levenberg-Marquardt algorithm [23]. A starting initial guess will be used to generate a different guess, which is done by using the Jacobian of the function to be optimized.

**Table 2.** Initial Values for the Surface Roughness Parameters. These constants are from Equation 10.  $a_1$  and  $a_2$  are used to fit the different surface roughness distributions better to the data.  $k_1$  and  $k_2$  together form the scalar magnitude term.

$k_1$	$a_1$	$k_2$	$a_2$
1	0	1	0

### Varying Surface Roughness Parameters

After observing a pattern with the surface roughness parameters (Table 3), the parameters are varied according to Table 4 to obtain better accuracy. The value 0.5 was chosen as the absolute value of the parameters seems to hover around 1 and 0.

**Table 3.** Observed Pattern for Magnitude and Surface Roughness Parameters. Each model seems to have a separate parameter pattern.

	$a_0$	$a_1$	$a_2$	$k_1$
No-Scattering	Pos			
Non-Gaussian	Pos	Neg		
Gaussian	Pos		Neg	
Bi-Scattering Product	Pos	Pos	Neg	
Bi-Scattering Sum	Pos	Pos	Neg	Pos

**Table 4.** Initial Surface Roughness Starting Values for All Models. Values were chosen according to observations using the initial values from Table 2.

	$k_1$	$a_1$	$a_2$	$k_2$
No-Scattering	0.5			
Non-Gaussian	0.5	-0.5		
Gaussian	0.5		-0.5	
Bi-Scattering Product	0.5	0.5	-0.5	
Bi-Scattering Sum	0.5	0.5	-0.5	0.5

### Model Assessment

To compare each model's performance to each other, relative difference to the patents' estimates and ability to produce realistic values were studied. The patents' estimates are used for validation because although these estimates are not exact, they are currently the only material we have to validate our estimates. Relative difference is calculated using the equation:

$$\frac{1}{n} \sum_{j=1}^n \left| \frac{m_j - p_j}{p_j} \right|,$$

where  $n$  is the number of datasets,  $m$  is the fitted estimate,  $i$  is the particular parameter (lipid, aqueous, or corneal refractive index), and  $p$  is the patents' estimate. This equation is calculated for each of the five models. This formula was also used to find the relative difference between any value that was outside of the observed thicknesses (20-120 nm for lipid layer, 2000-5000 nm for aqueous layer) [14].

## RESULTS

### Extracted Data

To begin, we needed measured data of reflectance values from human eyes. The data show the reflectance of the patient's eyes, graphed over the wavelength of light that is rapidly shone onto the eye, as seen in Figure 6a. The wavelength typically ranged from 550-1000 nm. Our data contain measured reflectances from 9 subjects. Figure 6b shows the graphical dataset that was extracted from Figure 6a [14]. The coordinates of Figure 6b are then stored, as they are the numerical data points. With this particular dataset, there were 1124 data points total. From these data points, we can now determine the tear film thicknesses.

### Model Results Before Varying Surface Roughness Parameters

#### General Thin Films Model

Although Equation 6 alone only describes general thin films, and the eye has more specific characteristics than these films, the optimization scheme was

still run to confirm that the eye indeed is more complex than general thin films. Figure 7 shows that, when using the model for general thin films, the theoretical curve does not match the measured reflectance. The several mismatches result in an inaccurate tear thickness estimate.

#### *Gaussian-Only Scattering Model*

The Gaussian-Only model still does not result in a perfect fit to the measured data. Figure 8, which uses the same data as Figure 7, shows that the blue curve follows the behavior of the measured data, but it still does not match exactly with the measured data. These areas of mismatch are similar to that of Figure 7 and 4.

#### *Bi-scattering Product Model*

Overall, the Bi-scattering Product model produced very close fits visually. Figure 9 shows that the error obtained is smaller, and the goodness of fit value is greater than the above values. This result was similar with all of the datasets. However, it can be seen that some of the estimates are not biologically realistic. Some of the lipid estimates are too thin ( $< 20$  nm), and some of the aqueous estimates are too thick ( $> 6000$  nm) for the human eye.

#### **Bi-scattering Sum Model**

With the Bi-scattering Sum model, errors and goodness of fit values are similar to those that result from the Bi-scattering Product model (Figure 10). Also, the lipid and aqueous thickness estimates are much more biologically realistic with all of the datasets. However, it can be seen that some of the optimized surface roughness parameters are not realistic, with some that are very much greater than a value of 10 (Table 6).

It can be seen that the magnitude and surface roughness parameters can be negative. Furthermore, there is a pattern with the integer signs of these parameters for each model (Table 3), where some parameters are seen to be mostly positive while others are typically negative.

#### **Bi-scattering Sum Model Results with Varied Surface Roughness Parameters**

While the Bi-scattering Sum model without varied surface roughness initial starting values produced fairly small errors, the surface roughness estimates were unrealistic. When we did vary these initial starting values according to the pattern in Table 3, however, the results had consistently small errors, and the surface roughness estimates were realistic ( $\leq |10|$ ) (Table 5). Biologically realistic tear estimates were still obtained (Figure 11).

#### **Model Assessment**

Relative difference between fitted values and patent estimates and ability to produce realistic estimates are shown in Figures 12 and 13. The non-Gaussian model produces the most similar estimates to patent values, while the Bi-scattering Product model produces the least similar. The general model produces the most unrealistic values.

### **DISCUSSION**

#### **General Thin Films Model**

The mismatch between the theoretical and measured reflectances in Figure 7 implies Equation 6 must be altered. In both examples of Figure 7, the blue curves are simplistic, compared to the more complex measured data, which reflects the simple model used. This simple model only describes the behavior of general thin films, which are smooth [10]. This behavior is not the case for eyes, which have rough surfaces and is superimposed by the tear film, which also has rough mucin and lipid layers [30]. To give the blue curves more intricacies, similar to how the measured data is intricate, a model with more complex terms, such as an exponential one, needs to be used.

#### **Non-Gaussian-Only and Gaussian-Only Scattering Models**

The mismatch between the theoretical and measured reflectances in Figure 8 can be explained by the lack of inclusion of non-Gaussian distributions of surface roughness in Equation 8. Models that only consider

No Scattering, Pat-626, Fig-6, RMSE = 0.00018148, GOF = 95.8%  
 Lip = 23.717nm; Aqu = 2005 nm;  $n_{\text{cornea}} = 1.3329$   
 $k_1 = -0.37205$

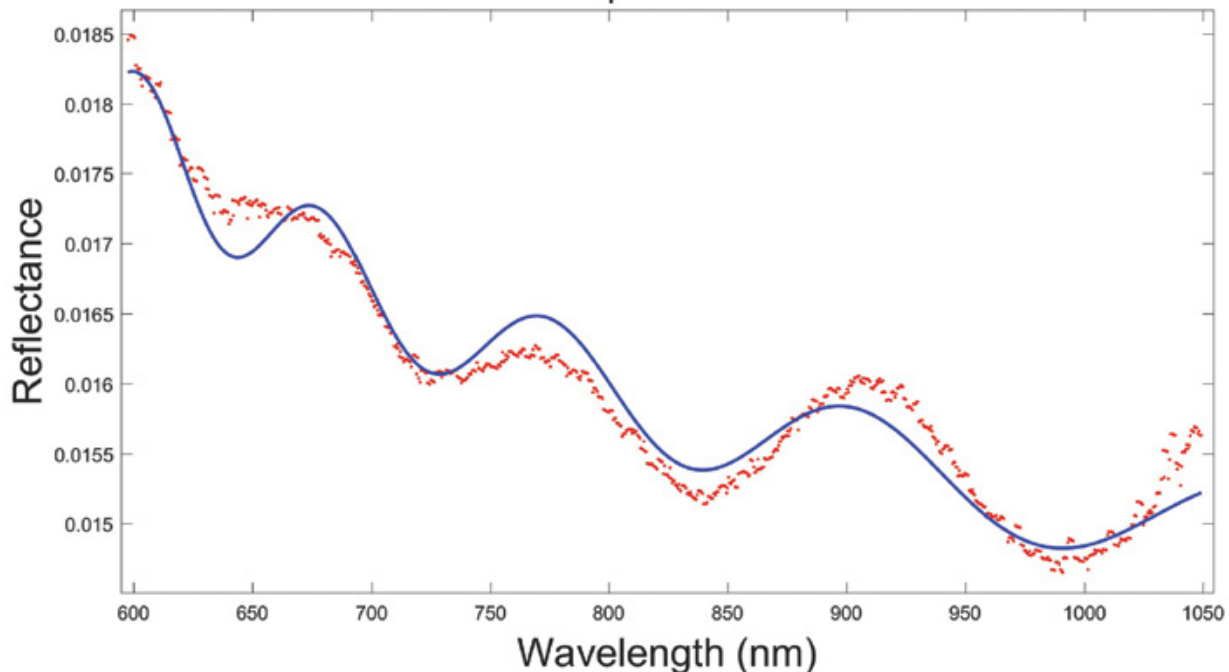


**Figure 7.** Theoretical Reflectance using the General Thin Film Model. The theoretical reflectance using Equation 6 (blue curve) is compared against the measured reflectance data (red dots). Because they do not match, it can be concluded that the eye needs a more complex mathematical model. RMSE is the root-mean-squared error, and GOF is the goodness of fit value. Dataset is from subject sub4#5 of Patent Application 0351626 [13].

one type of eye surface roughness make it difficult to conclude whether a mismatch between theoretical and measured reflectances is due to other reasons besides wrong eye surface roughness type, which is why the non-Gaussian-only model will not suffice either.

### **Bi-scattering Product Model**

This model includes both types of surface roughness and is of higher order, which tends to lead to higher accuracy. This higher accuracy is reflected in the error resulting from this model, which tends to be approximately  $10^{-5}$ . However, small error does not necessarily lead to an actual accurate estimate. The error only accounts for how close the theoretical and measured reflectances are to each other, but there can be more than one combination of lipid and aqueous values that will result in the same reflectance calculation. The difference in estimates can also be explained by the instability of the mathematical model, where a small increase in the algorithm's initial values can result in a completely different estimate. Thus, unrealistic estimates are produced.

### **Bi-scattering Sum Model**

This model still contains a higher order term, as with the Bi-scattering Product model, but has more degrees of freedom. Our optimization program goes through several iterations to test the error of different combinations of layer thickness values. A model that has fewer degrees of freedom will not have many combinations of possible layer thickness estimates, as compared to a model that has more degrees of freedom. Equation 9 only has six parameters that can be changed in each iteration. Since these parameters must produce a number that is very close to the measured reflectance values, there are only so many possible values that these parameters can be. However, Equation 10 has seven parameters, so this model can have more possible combinations of layer thickness estimates. The smallest error possible is more likely to appear with the model that has more combinations of layer thickness estimates, which is the model with more degrees of freedom. Thus,

the Bi-scattering Sum model is better than the Bi-scattering Product model. Also, although this model produces slightly larger errors overall compared to that of the Bi-scattering Product model, it yielded more physically-appropriate tear film thickness values. Hence, it can be concluded that future models to determine tear film layer thicknesses can be constructed similarly to the Bi-scattering Sum model.

While the tear film thickness estimates from this model are realistic, the surface roughness parameters are not when the initial starting values for these parameters were not varied. Varying these parameters resulted in more realistic surface roughness parameters, and accuracy is still attained. Thus, varying the surface roughness parameters in addition to the tear film parameters should be considered.

### **Model Assessment**

Since model performance is dependent upon the patents' estimates, it is expected that the Non-Gaussian and Gaussian-Only models will have the smallest relative difference values, since the patents use the Non-Gaussian model, which is similar to the Gaussian-Only model. The general model can be eliminated in the wavelength-dependent interferometric method, since its biological description does not fit the human eye case, and it performed poorly in comparison to the other models as well. Aside from the general model, the large distance between fitted estimates and observed boundaries seen in the models is due to an abnormally thick aqueous layer in one of the subjects. All the models' estimates for this subject's aqueous layer agree with each other (Figure 11). The Bi-scattering Sum model performed fairly well, and it produces realistic estimates. Although it ranked behind the Non-Gaussian and Gaussian-Only models, it is unknown whether the latter models produce the exact thicknesses; it is only assumed that their estimates are near the actual thicknesses. Thus, the Bi-scattering Sum model can still be considered to be used in the wavelength-dependent interferometry method.

Gaussian Scattering, Pat-626, Fig-6, RMSE = 0.00020982, GOF = 94.4%

Lip = 21.2976nm; Aqu = 2008 nm;  $n_{\text{cornea}} = 1.3328$

$k_1 = -0.37128$ ,  $a_2 = 0.012753$

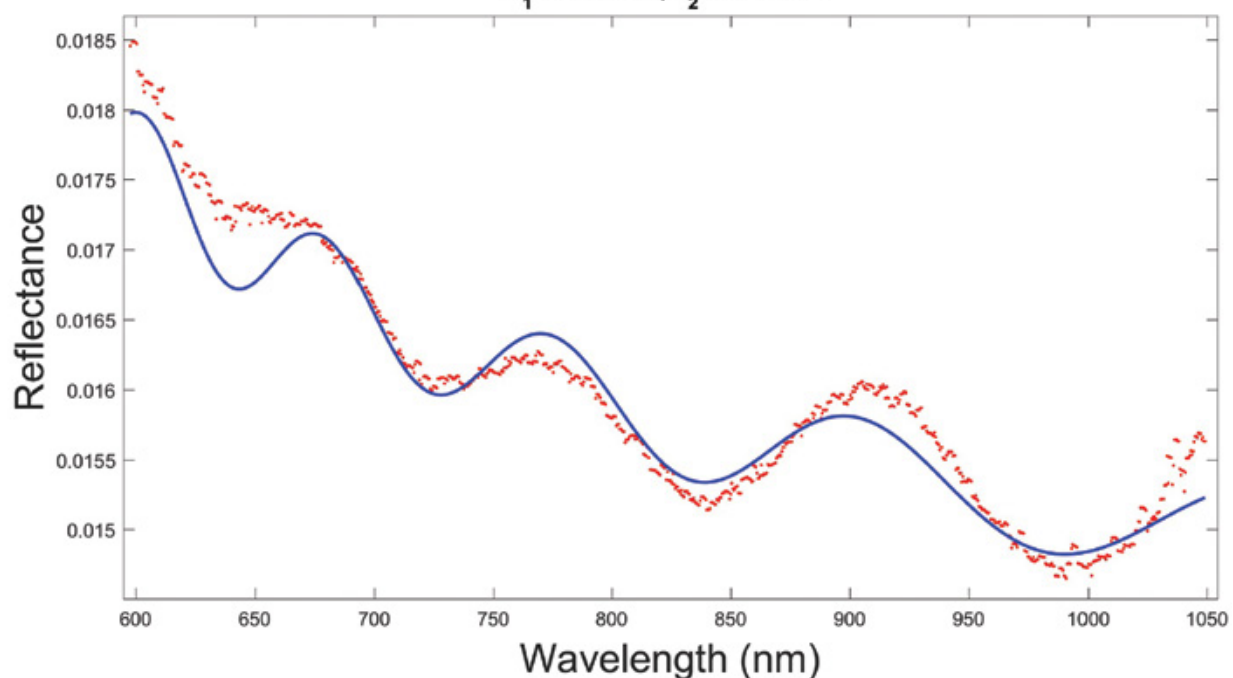


**Figure 8.** Theoretical Reflectance Using Gaussian-Only Scattering Model. There are still areas where the theoretical reflectance does not match up with the measured reflectance data. With this particular dataset, the Gaussian-Only Scattering Model results in a smaller goodness of fit and greater error than that of the general model.

**Bi-Scattering Product, Pat-626, Fig-6, RMSE = 0.00013154, GOF = 97.8%**  
**Lip = 84.4098nm; Aqu = 1936 nm;  $n_{\text{cornea}} = 1.3352$**   
 **$k_1 = 0.38784, a_1 = -1.7837, a_2 = 0.52744$**

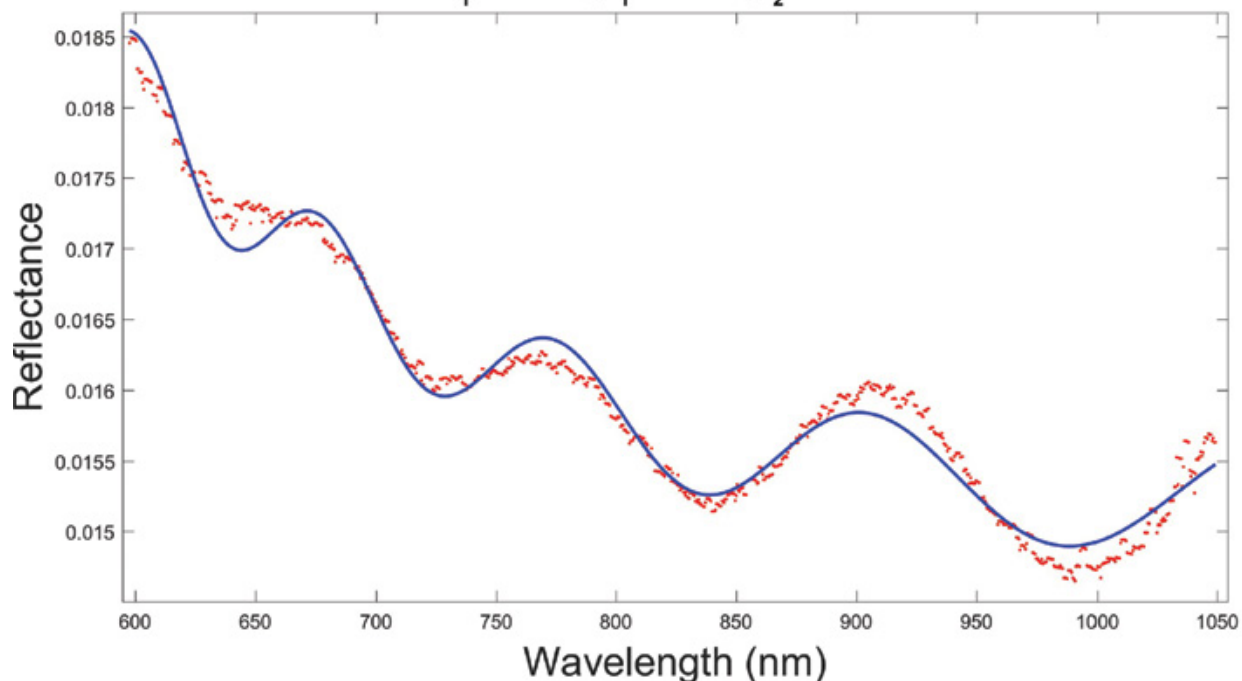


**Figure 9.** Bi-scattering Product Model. Overall fit using this model is better than the previous models, in terms of error and goodness of fit.

**Bi-Scattering Sum, Pat-626, Fig-6, RMSE = 0.00013395, GOF = 97.7%**  
 Lip = 62.4457nm; Aqu = 1959.5 nm;  $n_{\text{cornea}} = 1.3345$   
 $k_1 = 0.82199$ ;  $a_1 = -0.01154$ ;  $a_2 = -0.52573$ ;  $k_2 = -0.51528$

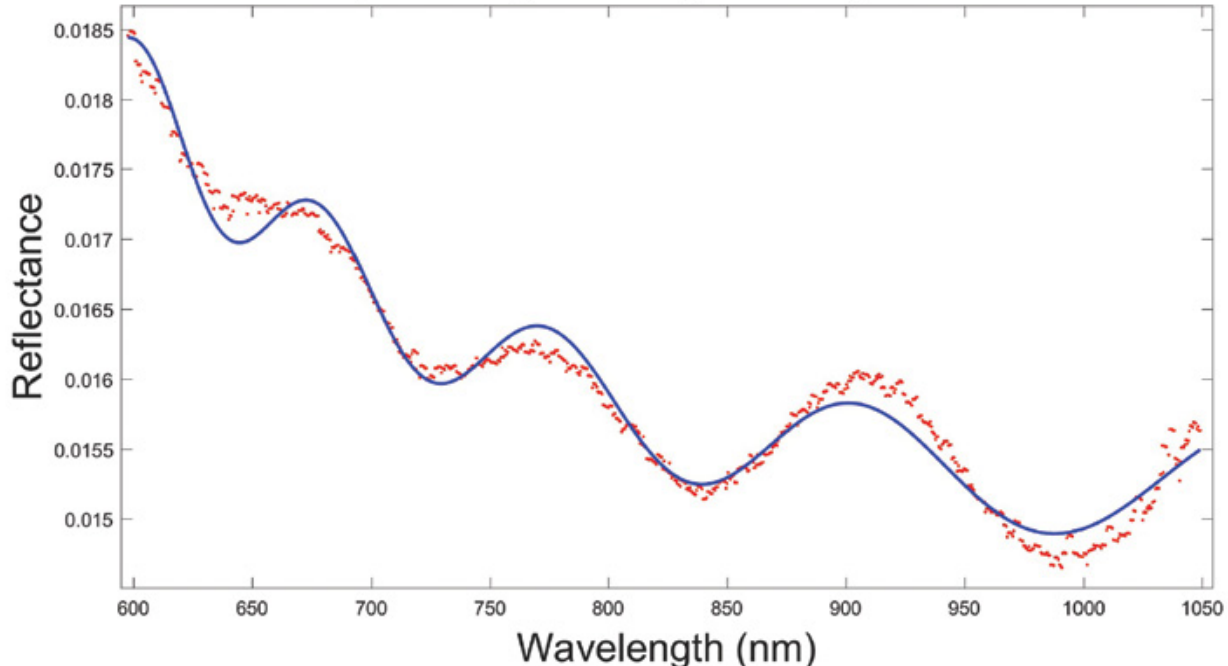


**Figure 10.** Bi-scattering Sum Model. Error and goodness of fit value are very similar to those obtained from the Bi-scattering Product model. However, the lipid and aqueous thickness estimates are different.

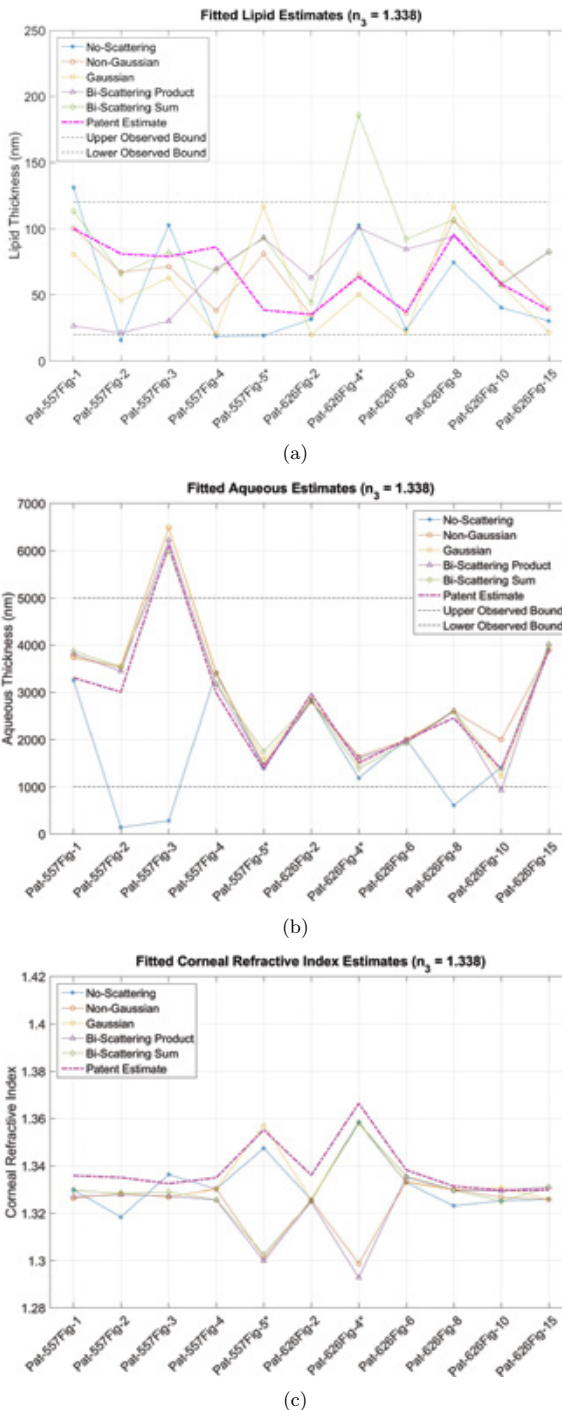


**Figure 11.** Tear Thickness and Corneal Refractive Index Estimates Obtained for All Data Sets. Varying the surface roughness parameters resulted in realistic thickness and corneal refractive index estimates for all tear film parameters. Black dotted lines denote the boundaries for observed human thicknesses [14].

**Table 5.** Optimized Surface Roughness Parameters with Varying Initial Starting Values for these parameters were varied, all of the resulting optimized values were  $\leq |10|$ , which is reasonable for the human eye.

<b>Figure</b>	<b>Surface Roughness Parameters</b>			
	$k_1$	$a_1$	$a_2$	$k_2$
Pat-557 Fig1	0.26446	0.30039	-0.54507	2.2176
Pat-557 Fig2	0.38813	0.049184	-0.44608	2.3789
Pat-557 Fig3	0.23565	0.48797	-0.38969	3.3148
Pat-557 Fig4	0.13763	0.48321	-1.1038	4.0495
Pat-557 Fig5	0.075217	0.34749	0.66543	-0.17348
Pat-626 Fig2	1.7244	-0.75488	-0.51085	-0.45673
Pat-626 Fig4	0.0022707	-0.12198	0.67318	1.7743
Pat-626 Fig6	0.21691	0.2016	-1.3244	2.2557
Pat-626 Fig8	0.47947	0.32549	-0.07982	0.31114
Pat-626 Fig10	0.53405	-0.35611	-0.037326	1.4081
Pat-626 Fig15	0.14875	0.88258	-0.91373	7.2873

**Table 6.** Optimized Surface Roughness Parameters without Varying Initial Starting Values. When the initial starting values for these parameters were not varied, some of the resulting optimized values were extremely large, which does not make sense in the case of the human eye. The Bi-scattering Sum Model was used.

<b>Figure</b>	<b>Surface Roughness Parameters</b>			
	$k_1$	$a_1$	$a_2$	$k_2$
Pat-557 Fig1	0.87978	-0.0011593	-0.79294	-2.6055
Pat-557 Fig2	0.85419	0.25452	-0.7686	-3.1764
Pat-557 Fig3	0.60157	0.3346	1.3058	-0.67874
Pat-557 Fig4	0.21029	0.7101	2387.6922	-25.006
Pat-557 Fig5	0.061229	0.32618	-41.1033	-19.3682
Pat-626 Fig2	2.4996	-1.4621	-1.2983	-1.1938
Pat-626 Fig4	1.576	-4.2556	-0.40714	-3.6304
Pat-626 Fig6	0.82199	-0.01154	-0.51528	-0.52573
Pat-626 Fig8	0.21711	0.7688	0.77105	-0.70203
Pat-626 Fig10	0.89969	0.20583	-611.2555	-22.6829
Pat-626 Fig15	0.62086	0.45097	25808039.8679	-38.2306

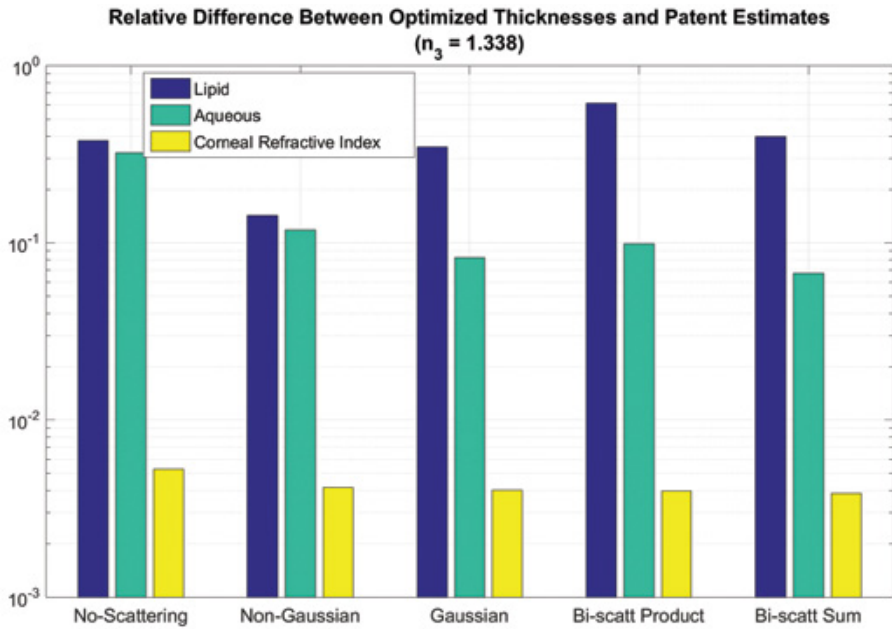


**Figure 12.** Relative Difference Between Fitted Values and Patent Estimates. Relative difference is used to decide a model's performance in comparison to the others. Shorter bars imply better performance.

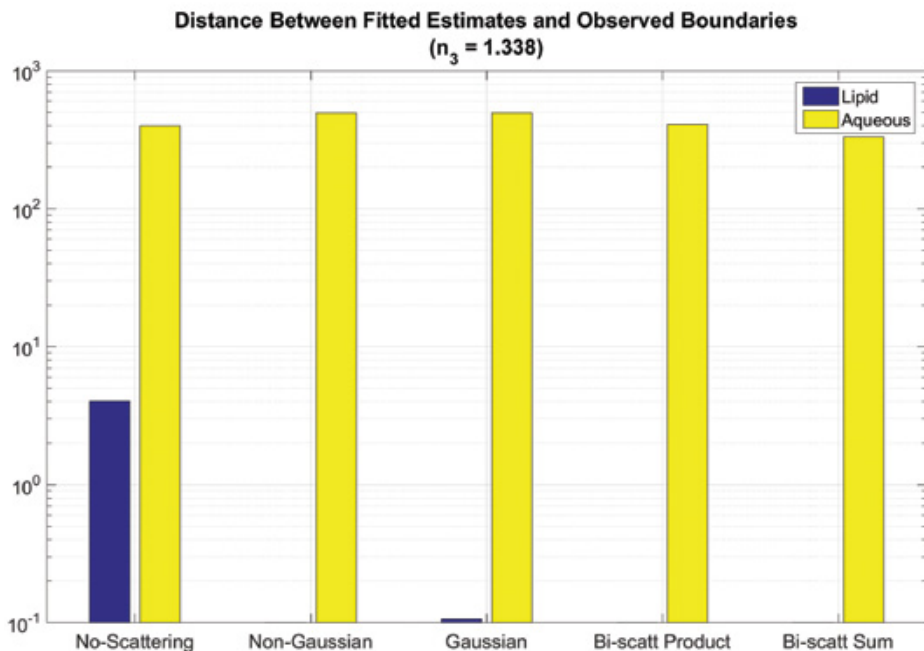


**Figure 13.** Ability to Produce Realistic Estimates. If any values were outside of the observed boundaries for tear thicknesses, the relative difference is calculated between the value and the boundary it crossed.

## REFERENCES

- [1] The leading causes of dry eye disease. <https://dryeyeandmd.com/the-leading-causes-of-dry-eye-disease/>, October 2014.
- [2] American Optometric Association. Dry eye. <http://www.aoa.org/patients-and-public/eye-and-vision-problems/glossary-of-eye-and-vision-conditions/dry-eye?ssot=y>, 2015.
- [3] M. Born and E. Wolf. *Principles of Optics: Electromagnetic Theory of Propagation Interference and Diffraction of Light*. Pergamon Press, Oxford, England, 1980.
- [4] H. Brewitt and F. Sistani. Dry eye disease: The scale of the problem. *Survey of Ophthalmology*, 45:S199--S202, March 2001.
- [5] C. Carniglia. Scalar scattering theory for multilayer optical coatings. *Optical Engineering*, 18(2):104--115, March 1979.
- [6] The Eye Center. Other condition. <http://www.youreyecenter.com/eye-conditions/other/>, 2009.
- [7] Physics Classroom. Light absorption, reflection, and transmission. [http://www.physicsclassroom.com/class/light/ Lesson-2/Light-Absorption,-Reflection,-and-Transmission](http://www.physicsclassroom.com/class/light/Lesson-2/Light-Absorption,-Reflection,-and-Transmission), 2016.
- [8] D. A. Dartt, R. R. Hodges, D. Li, M. A. Shatos, K. Lashkari, and C. N. Serhan. Conjunctival Goblet Cell Secretion Stimulated by Leukotrienes is Reduced by Resolvin D1 and E1 to Promote Resolution of Inflammation. *The Journal of Immunology*, 186(7):4455--4466, 2011.
- [9] W. Eerenstein, N. D. Mathur, and J. F. Scott. Multiferroic and magnetoelectric materials. *Nature*, 442:759--765, August 2006.
- [10] E. Hecht. *Optics*. Addison Wesley, San Francisco, 2002.
- [11] E. Hosaka, T. Kawamorita, Y. Oqasawara, N. Nakayama, H. Uozato, K. Shimizu, M. Dogru, K. Tsubota, and E. Goto. Interferometry in the evaluation of precorneal tear film thickness in dry eye. *American Journal of Ophthalmology*, 151(1):18--23, 2011.
- [12] S. Huth and D. Tran. Methods and devices for measuring tear film and diagnosing tear disorders, May 27 2014. US Patent 8,733,937.
- [13] S. Huth and D. Tran. Method for rapid calculation of tear film lipid and aqueous layer thickness and ocular surface refractive index from interferometry spectra, December 2015. US Patent 9,0351626.
- [14] S. Huth, D. Tran, H. Zhao, and A. Gulses. Method for calculating tear film lipid and aqueous layer thickness and corneal surface refractive index from interferometry data, December 10 2013. US Patent 8,602,557.
- [15] National Eye Institute. Facts about dry eye. <https://nei.nih.gov/health/dryeye/dryeye>, February 2013.
- [16] M.A. Isreb, J.V. Greiner, D.R. Korb, T. Glonek, S.S. Mody, V.M. Finnemore, and C.V. Reddy. Correlation of lipid layer thickness measurements with fluorescein tear film break-up time and schirmer's test. *Eye*, 17(1):79--83, January 2003.
- [17] G. U. Kallarackal, E. A. Ansari, N. Amos, J. C. Martin, C. Lane, and J. P. Camilleri. A comparative study to assess the clinical use of Fluorescein Meniscus Time (FMT) with Tear Break up Time (TBUT) and Schirmer's tests (ST) in the diagnosis of dry eyes. *Eye*, 16:594--600, 2002.
- [18] P.E. King-Smith, B.A. Fink, N. Fogt, K.K. Nichols, R.M. Hill, and G.S. Wilson. The thickness of the human precorneal tear film: Evidence from reflection spectra. *Investigative Ophthalmology & Visual Science*, 41(11):3348--3359, October 2000.
- [19] D. R. Korb, J. Craig, M. Doughty, J. Guillon, G. Smith, and A. Tomlinson. The Tear Film: Structure, Function and Clinical Examination. *The Journal of the British Contact Lens Association*, 2002.
- [20] Y. C. Lee, C. K. Park, M. S. Kim, and J. H. Kim. In vitro study for staining and toxicity of rose bengal on cultured bovine corneal endothelial cells. *Cornea*, 15(4):376--385, 1996.
- [21] H. Liang, H. Miranto, N. Granqvist, J. W. Sadowski, T. Viitala, B. Wang, and M. Yliperttula. Surface plasmon resonance instrument as a refractometer for liquids and ultrathin films. *Sensors and Actuators B: Chemical*, 149(1):212--220, 2010.
- [22] F. Mantelli, J. Mauris, and P. Argueso. The ocular surface epithelial barrier and other mechanisms of mucosal protection: from allergy to infectious diseases. *Current Opinion in Allergy and Clinical Immunology*, 13(5), 2013.
- [23] D. Marquardt. An algorithm for least-squares estimation of nonlinear parameters. *SIAM Journal on Applied Mathematics*, 11(2):431--441, 1963.
- [24] J. C. Maxwell. A dynamical theory of the electromagnetic field. *Philosophical Transactions of the Royal Society*, 155:459--512, January 1865.
- [25] J. P. McCulley and W. Shine. A compositional based model for the tear film lipid layer. *Transactions of the American Ophthalmology Society*, 95, 1997.
- [26] C. McSherry. McBride and mcreesh opticians, helping you to manage dry eye syndrome. <http://www.mcbrideandmcreesh.com/opticians-helping-manage-dry-eye-syndrome/>, December 2014.

- [27] H. Mochizuki, M. Fukui, S. Hatou, M. Yamada, and K. Tsubota. Evaluation of ocular surface glycocalyx using lectin-conjugated fluorescein. *Clinical Ophthalmology*, 4:925–930, 2010.
- [28] G.S. Nikhilesh, N. Jasuja, and P. Sehgal. Electric field vs. magnetic field.
- [29] S. P. Phadatare, M. Momin, N. Premanand, S. Askarkar, and K. Singh. A Comprehensive Review on Dry Eye Disease: Diagnosis, Medical Management, Recent Developments, and Future Challenges. *Advances in Pharmaceutics*, 2015, 2014.
- [30] G. Savini, P. Prabhawasat, T. Kojima, M. Gruterich, E. Espana, and E. Goto. The challenge of dry eye diagnosis. *Clinical Ophthalmology*, 2(1):31–55, March 2008.
- [31] Dara Stevenson, J. Tauber, and B. L. Reis. Efficacy and Safety of Cyclosporine A Ophthalmic Emulsion in the Treatment of Moderate-to-severe Dry Eye Disease. *Ophthalmology*, 107(5):967–974, May 2000.
- [32] C. Underwood. Fluorescein eye stain test. <http://www.healthline.com/health/fluorescein-eye-stainOverview1>, February 2016.
- [33] N. Yokoi, H. Yamada, Mizukusa. Y, A. J. Bron, J. M. Tiffany, T. Kato, and S. Kinoshita. Rheology of tear film lipid spread in normal and aqueous teardeficient dry eyes. *Investigative Ophthalmology & Visual Science*, 49(12):5319–5324, December 2008.

## **Building a Custom Microscope – An Advanced Lab to Study Brownian Motion**

**Hunter Seyforth**

**Advisor: Wylie Ahmed, Ph.D.**

*Department of Physics, California State University, Fullerton*

### **ABSTRACT**

The process of building a microscope from scratch provides the students with a basic understanding of each individual component of the optical set-up. Subsequent digital image recording and data analysis provide an introduction to image processing and statistical analysis. Our goal is to create an advanced laboratory module for students to build an optical microscope, calibrate it, and make precise measurements of Brownian motion. We constructed an optical microscope based on the design by Kemp et al. (arXiv:1606.03052). Then, using a 40x objective, we study the Brownian motion of 1 micron colloidal particles. A digital camera is used to record videos of colloidal motion, ImageJ is used to post-process the images, and Matlab is used to calculate the diffusion coefficient of the particles. We use these measurements as an opportunity to explore error quantification in measurements of Brownian motion (Catipovic et al. AJP 81(7) 2013). Our advanced lab module is intended to be an introduction to physics research, fortify concepts from optics and statistical physics, and give students hands-on experience in building optical systems and analyzing noisy data.

# **Nonequilibrium Dynamics of Active Colloids**

**Paris Blaisdell-Pijuan<sup>1</sup>, Mauricio Gomez<sup>1</sup>, and Ngoc La<sup>1,2</sup>**

**Advisor: Wylie Ahmed, Ph.D.<sup>1</sup>**

<sup>1</sup>*Department of Physics, California State University, Fullerton*

<sup>2</sup>*Department of Physical Sciences, Golden West College*

## **ABSTRACT**

Self-propelled colloids are an example of an active matter system that can be precisely controlled to investigate their nonequilibrium behavior. Under blue-light illumination, the asymmetric colloids generate phoretic and osmotic driving forces that cause self-propulsion and deviate their dynamics from non-active equilibrium particles. Here, we study the thermal and non-thermal diffusion of the colloids using video microscopy, image analysis, and approaches from statistical mechanics. Using a mean-squared displacement (MSD) analysis we characterize the motion of these colloids as directed and non-directed. The velocity autocorrelation function (VACF) was also studied to investigate directional persistence. The diffusion coefficient of these colloids was calculated using both methods (MSD and VACF), and compared to the expected diffusion coefficient for particles in equilibrium. Active and thermal diffusion have been characterized to help study the transition between random and directed motion. This has allowed us to investigate the relationship between active diffusion and directed motion. We have examined the efficiency of the active colloids by comparing the energy provided and dissipated in the system. The characterization of this non-equilibrium colloidal system will help set the foundation for understanding the fundamental physics of active matter and diffusive systems.

## **Visualizing Fluid Physics of Microswimmers**

**Sarah Al Bassri**

**Advisor: Wylie Ahmed, Ph.D.**

*Department of Physics, California State University, Fullerton*

### **ABSTRACT**

Microscopic swimming organisms must generate forces that result in fluid flows to facilitate their motion and feeding. Studying the flow physics of swimming microorganisms is important to have a better understanding of their thermodynamics and interactions with their environment. Therefore, we developed an analysis based on the visualization of fluid flow using the flowtrace algorithm in ImageJ/Fiji. This allows us to quantify universal fluid flow patterns generated by a variety of organisms. So far, we observed that organisms generate vortices via ciliary beating. The average velocity of the vortex exhibited a characteristic decay with distance from the cilia. Additionally, in organisms that vary in size by nearly 10 times, we found that the ratio of vortex size to cilia length is conserved, with a value of  $5.00 \pm 0.86$  (mean  $\pm$ SD). This observation suggests the underlying flow physics may follow a scaling behavior for organisms of different sizes as they generate vortices for feeding.

**Keywords:** *Microswimmers, fluid physics, microorganisms, feeding, thermodynamics, and vortex.*

## **Authors and Editors**



### **ADRIAN ESCOBAR**

Adrian R. Escobar is a senior majoring in Geology. He is working alongside Dr. Richard Laton to determine if ground source heat pumps can be implemented on the CSUF campus to improve its green footprint by reducing energy needs. Adrian has spent the last year as president of the Geology Club working to grow and strengthen students through promoting engagement opportunities within the geosciences. After graduation this spring, he intends to pursue a graduate degree focusing on structural geology.



### **AIDA DADASHZADEH**

Aida Dadashzadeh is a fourth year biochemistry major graduating Fall 2018. She has worked in Dr. Fry-Petit's lab as an undergraduate researcher since 2016. In the future, she plans on going to dental school and pursuing a career in cosmetic dentistry. When she isn't working in Dr. Fry-Petit's lab she spends time working as the Volunteer and Outreach coordinator of the Pre-Dental Society.



### **ANGELICA ARREDONDO**

Angelica Arredondo is a mathematics major with a concentration in applied mathematics. She is currently involved in the Prime math club and also part of a program called the Graduate Readiness and Access in Mathematics (GRAM) Scholars. Angelica conducts research with Dr. Nicholas Brubaker and Breanna Mcbean studying the shapes of bubbles.



### **ARIANA MCKENZIE**

Ariana is a biology student with a concentration in ecology and evolutionary biology. She has enjoyed the last two years studying the demographic structure of urban coyotes under the guidance of Dr. Paul Stapp and plans to further her education with a master's degree. Overall, her goal is to pursue a career in conservation and animal health as a wildlife veterinarian.



### **BREANNA MCBEAN**

Breanna McBean is a third year applied mathematics major and computer science minor. She is a GRAM Scholar working under the guidance of Dr. Nicholas Brubaker and a member of the University Honors Program working with Dr. Anael Verdugo. She is also an executive officer for the Math Club, SMART Girls Club, and PRIME Club. This is her first semester as a Dimensions editor.



### **BRIAN AUSTIN MAGUMCIA**

Brian is currently a senior at Cal State University, Fullerton majoring in Geological Sciences. He is involved in the Geology club on campus and spends time working with Dr. Diane Clemens-Knott trying to understand the overall history of the Sierra Nevadas. In the future, he plans to apply to graduate school for Geology and hopefully work in the mining industry.



### **CHEYANNE RAMON**

Cheyenne Ramon is the Graduate Student Assistant for the College of Natural Sciences and Mathematics. She is a first year student in the Master of Science in Education, Higher Education Emphasis (MSHE) Program. Her background in science (B.S. in Biology from UC Riverside) has shaped her interests in higher education such as supporting traditionally underrepresented students in STEM. After her master's program, Cheyanne would like to work at a four-year university and pursue her Ph.D.



### **CHRISTIAN DO**

Christian has a love of both mathematics and music, especially theoretical aspects of both. His math interests include algebra and number theory. On the musical side, he enjoys percussion, and has some experience in both teaching and composing music. Christian plans to attend graduate school and become a professor to conduct research on group theory and music theory.



### **COLLIN MARSHALL**

Collin is a biochemistry major with a molecular biology minor at Cal State Fullerton. He works in the lab of Dr. Niroshika Keppetipola studying an RNA binding protein that regulates alternative splicing. He plans to pursue graduate studies in cell and molecular biology at a PhD-granting institution beginning in fall 2018. Some extracurricular activities that he participates in include exercising at the SRC, hiking, and trying new foods.



### **CONNOR FREDERICKSON**

Connor Frederickson is a senior majoring in Geology at CSUF. He is currently working on completing his undergraduate thesis under Dr. Sean Loyd. His research focuses on the relationship between geochemical and physical properties in calcites as expressed through carbon isotope composition and crystal habit. After graduation, he hopes to continue his studies in a graduate program with a focus on environmental geochemistry.



### **CRYSTAL RODELA**

Crystal Rodela is a senior majoring in Liberal Studies with a focus in multiple subject teaching. She will graduate in the spring of 2019 and has the ultimate goal of completing the credential program at Cal State Fullerton and becoming a well-rounded, multicultural teacher.



### **DESIRÉE LUCAS**

Desirée is currently pursuing a degree in Earth Sciences with a minor in Geology. She has worked as a Student Assistant in the Geology department at CSUF. Desirée's current research focuses on volcanic-plutonic connections in Yosemite National Park. Desirée is a Member at Large for the College of NSM's Interclub Council which provides funding to students to travel to research conferences. She is also the Geological Sciences Editor for DIMENSIONS. Her goal in life is to one day open her own museum.



### **ERICK VALDEZ**

Erick Valdez is a senior pursuing a Bachelor of Science Degree in Biological Science with a concentration in Ecology and Evolutionary biology and a Minor in Chemistry. He's involved in Dr. Abraham's research lab where he studies item format effects on performance and perceived difficulty of English Language Learners and native English speaking undergraduate biology students. After graduation, he plans to pursue a teaching credential to teach Biology and Chemistry at the high school level.



### **HUNTER SEYFORTH**

Hunter is a third year Physics Major at Cal State Fullerton. He joined the SLAM lab in the summer of 2017 where he has been working on a microscope project ever since. Hunter plans to graduate in the spring of 2019.



### **JACQUELINE ESTRADA**

Jacqueline Estrada is a senior majoring in biochemistry with a minor in psychology at CSUF who will be graduating this Spring, 2018. Jacqueline's undergraduate research is based on studying the molecular interactions between ascorbic acid (vitamin C) and a catalyst, Pd. She used a computational quantum mechanical model known as density function theory (DFT) to investigate the binding energy of atoms to a metal surface. After graduation, Jacqueline will be pursuing a degree in clinical science.



### **JAMES SHADE**

James is a CSUF President's Scholar and GRAM scholar majoring in pure mathematics and minoring in computer science. He has studied abroad in Germany and Uzbekistan, and has published articles in College Math Journal, Dimensions, and Uzbekistan Mathematical Journal. His research interests include algebra and number theory. Other than mathematics, his interests include programming, writing, and reading. James plans to attend graduate school to earn a Ph.D. in mathematics and become a professor.



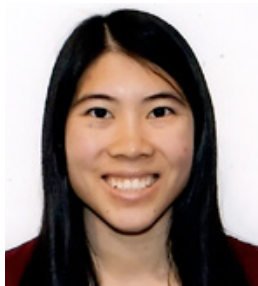
### **JAMIE HAYWARD**

"Jamie Hayward is pursuing a Bachelor of Science in Geology at California State University, Fullerton. She works under the guidance of Dr. Joe Carlin on coastal and marine geology and holds a part time position at the Southern California Coastal Water Research Project (SCCWRP). She also is the current social media coordinator for the Geology Club on campus. After graduation, Jamie plans to attend graduate school and pursue a career in research."



### **JOHN AYERS**

John Ayers is a senior undergraduate student currently finishing up his final semester at CSUF. He is also working on his undergraduate senior thesis with Dr. Memeti researching compositional variations within the equigranular Half Dome granodiorite unit of the Tuolumne Intrusive Complex in Yosemite National Park, California. His research includes field mapping, petrography, and XRF whole rock geochemical analysis. John's professional goal is to teach geoscience at the college level.



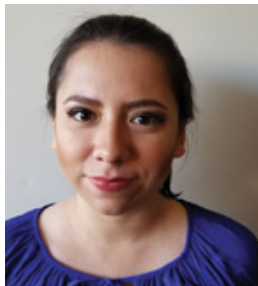
### **KAREN TOM**

Karen is a fourth year undergraduate majoring in Biochemistry. She has been in the Fry-Petit inorganic chemistry lab since Fall 2015, working on the rational design of alternative battery materials. After graduating this spring, Karen will attend the University of Southern California, pursuing a doctorate degree in pharmacy. Karen hopes to either work in the pharmaceutical industry or become a clinical pharmacist developing medication therapies for patients.



### **KILLIAN WOOD**

Following the completion of his summer work Exploring the p-Adic Numbers: A Brief Overview, Killian transitioned to Applied Mathematics to pursue his newfound interest in Mathematical and Computational Biology. His future projects will expand upon his work the Repressilator model—covering the updated model in the 2016 study of a new Repressilator formulation. Going forward, Killian will pursue a Ph.D. in a program that reflects these interests in hopes of attaining a private research position.



### **KIMBERLY M. ZAVALA**

Kimberly M. Zavala is a transfer student from East Los Angeles Community College. It is her second year at Cal State Fullerton and she is majoring in Liberal Studies and American Studies. After graduation she is going to enter the credential program from CSU Fullerton and has high hopes to become an elementary teacher in the near future. She also desires to apply everything she has learned from the new common core standards and weave them into her classroom to make a more challenging and rich class curriculum.



### **ISABEL GUINTO**

Isabel Guinto is a senior undergraduate majoring in geology at Cal State Fullerton. Under the advisement of Natalie Bursztyn, she is developing a narrative about the plutonic history of Yosemite National Park to be taught through a downloadable app. She is also an active member of the Geology Club and all it has to offer. After graduation, she looks forward to a fulfilling career while continuing to give back to the community.



### **LEAH WIITABLKE**

Leah Wiitablake is a double major earning her B.S. in Geology and B.F.A. in Animation at California State University, Fullerton. She presented her undergraduate thesis on developing a molecular mineralogy app at the Geological Society of America Conference in Denver, CO, in the Fall 2016. She is currently Vice President of the Cal State Fullerton Association for Women Geoscientists Student Chapter, which is working towards introducing children to the sciences through outreach events.



### **LIZ HITCH**

Liz Hitch is a junior biology major at California State University, Fullerton and this is her first semester being involved in LSAMP. She is currently conducting research in Dr. Fry-Petit's Solid State Inorganic Chemistry Lab and has been working on her project that involves synthesizing perovskite compounds for oxygen transport membranes. Her research has progressed into synthesizing other perovskites with varying stoichiometries at a higher mass. Liz hopes to apply for graduate school and obtain a Ph.D. in an area of Biology.



### **LUIS GAMEZ**

Luis Gamez is a biochemistry student at Cal State University Fullerton who works in Dr. Fry-Petit's inorganic research lab. He has been at CSUF for 5 years, constantly learning about biochemistry and himself. Luis plans to go into industry after obtaining his degree; hopefully, landing a position in quality control. He loves riding the train and observing the southern California clouds.



### **MADISON CHEEK**

Madison Cheek is majoring in Biological Sciences with a concentration in Molecular and Biotechnology. She works in Dr. Parvin Shahrestani's *Drosophila melanogaster* lab, and in the future she hopes to work in the Forensic Science Unit at the Orange County Crime Lab. Her passion for lab work was first discovered while working with fruit flies. Therefore, making them a model organism that she holds near and dear to her heart.



### **MAUREEN KELLEY**

Maureen Kelley is a senior pursuing a bachelor's degree in Biology, with a concentration on Ecology and Evolutionary Biology. She is currently a member of Dr. Christopher R. Tracy's Herpetology Research Lab and Dr. Ryan P. Walter's Molecular Ecology Lab. Biology has been her passion since she was four years old, when she would hunt for lizards and insects. Her future plans include obtaining a master's degree in ecology and working for an ecological survey company, wildlife sanctuary, or zoo.



### **MELANIE GARCIA**

Melanie Garcia is an undergraduate student at CSUF double majoring in Biology and French. She is currently involved in Dr. Parvin Shahrestani's evolutionary research lab as a student research assistant and lab manager. Working in this lab has opened up so many opportunities and has really given her the motivation and inspiration necessary to continue to grad school. She aspires to pursue a career in the medical field as a medical examiner while still continuing research.



### **MIKAYLA MAYS**

Mikayla Mays is a first-year graduate student in the physics department and a TA for undergraduate physics labs. She graduated last year from CSUF with her B.S. in Physics, and stayed on in the Master's program to continue her research in Physics Education. Once she graduates she hopes to pursue a Ph.D. and eventually a faculty position at a university.



### **NANCY CASTELLANOS**

Nancy Castellanos is a senior at California State University Fullerton, where she is majoring in Biological Sciences with a concentration in Molecular and Biotechnology. She is currently working in Dr. Ramirez's research lab, analyzing the interaction between various *A. baumannii* and *S. aureus* strains.



### **NATALIE LINCOLN**

Natalie Lincoln is currently in the CSUF Multiple Subject Teaching Credential. She received her undergraduate degree also from Fullerton as a Liberal Studies Major. She hopes to enter the workforce as an elementary school teacher in the fall with a focus on STEM curriculum.



### **NEEKA FARNOUDI**

After completing her B.S. in Human Biology from UC Santa Cruz in 2014, Neeka entered CSUF as a pre-med post-baccalaureate student. In 2016, she began working in Dr. Parvin Shahrestani's ecology/evolutionary laboratory where she is currently the experimental leader of the Sex-Specific Mating and Immunity project. The team aims to uncover how reproduction can reduce immune defense of female *Drosophila melanogaster* after fungal infection. She is excited for the future of the project, and as for her personal goals, she hopes to enter medical school this upcoming year.



### NICHOLAS KELLAS

Nicholas Kellas is an active volunteer on campus driven by a family history of volunteering for the Boy Scouts and other children's organizations. At csuf, Nicholas was an officer for the Math club and Chemistry and Biochemistry Club and is this year's Math Club president. In 2017, Nicholas was awarded the Lyle Wallace Service Award for service to the Chemistry department. Now, Nicholas is conducting research in computational chemistry under Dr. Michael Groves.



### PARIS BLAISDELL-PIJUAN

Paris Blaisdell-Pijuan is a senior physics major in Dr. Wylie Ahmed's SLAMlab, working on nonequilibrium dynamics of active colloids. He has held research positions at Argonne National Lab and NASA/Caltech JPL, researching ZnO quantum dots and radiation hardened memory devices, respectively. In the fall he will start his Ph.D in Electrical Engineering (Applied Physics, Materials, and Devices) at Princeton University and begin work on spin systems in diamond for quantum information processes.



### RANDALL ORTEGA

Randall Ortega is the Chemistry and Biochemistry section editor for Dimensions. He is a senior majoring in Biochemistry and minoring in Economics. His research involves the purification and crystallization of a dihydromethanopterin reductase, vital in tetrahydromethanopterin biosynthesis in *Methylobacterium extorquens*. He enjoys spreading his love for science on and off campus as the president of the Chemistry and Biochemistry Club. He plans on attending law school to become an intellectual property lawyer.



### RODRIGO AVILES

Rodrigo is a senior at California State University, Fullerton majoring in Geological Science. His thesis advisor is Dr. Diane Clemens-Knott. They are trying to confirm the ages of a low-silica gabbro and a high-silica granite. If Late Cretaceous in age, assumed age, then they will see if they are related to the Independence dike swarm. His future plans are to apply for graduate school and work towards a Ph.D.



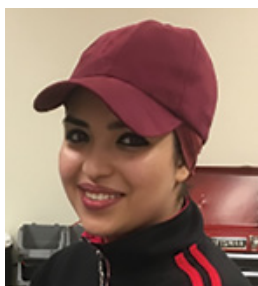
### **SABEECA VADAKKAN**

Sabeeca Vadakkan is currently a college sophomore majoring in biology. She has been working in Dr. Parvin Shahrestani's lab for the past year as a volunteer. In the future, she plans to attend medical school and have a career in medical research.



### **SABRINA GREEN**

Sabrina Green is majoring in geology. Mentored by Dr. Vali Memeti, Sabrina is interested in investigating the chemical relationship between volcanic and plutonic rocks to better understand the processes that occur in the magma plumbing system. She will graduate this summer with an interest in working in the private sector.



### **SARAH AL BASSRI**

Sara Al Bassri is a senior Biochemistry major with a Physics minor at California State University, Fullerton, who got involved in LSAMP in Fall 2017. Sara is currently participating in a biophysics research with Dr. Wylie Ahmed as an LSAMP Research Scholar to monitor the fluid physics of micro-swimmers. The goal of this project is to explore flowfield patterns similarities and differences among different organisms. Sara's career goal includes obtaining a Ph.D. in Biomedical Engineering, and hope to develop devices that can be used in the medical field.



### **SEAN ZULUETA**

Sean Zulueta is pursuing a Bachelor of Science degree in Biological Science with a concentration in Ecology and Evolutionary Biology. He is a Southern California Ecosystems Research Program (SCERP) scholar and works under the guidance of Dr. Kristy Forsgren describing the gonadal development of the black-bellied dragonfish. After graduation, Sean intends to pursue a graduate degree to obtain a career that revolves around his interests in ecological conservation and restoration.



### **SHAYNA AVILA**

Shayna Avila is currently pursuing a BS in Geology. She is also the President of the AWG student chapter. Shayna is employed as an Instructional Student Assistant for the CSUF University Learning Center, and the Teacher Pathway Partnership, as well as a research assistant for CSUF. She plans to graduate and attend geology field camp in May 2018, and go on to become a professional geologist in the future.



### **TERRINDA ALONZO**

Terrinda Alonzo is a senior in the Department of Geological Sciences, focusing in the field of hydrogeology with Dr. Richard Laton. Her work in the field of Hydrogeology stems from her interest to further investigate and contribute to the understanding of various physical phenomena encountered in Geology and its role when it interjects with today's society. Her goal is to become a hydrogeologist, where she can work with the occurrence and distribution of underground water.



### **TILLY DUONG**

Tilly Duong is an undergraduate senior pursuing a major in biological sciences, with a concentration focus in plant biology. In addition to her work with Dr. Joel Abraham, Tilly is a LSAMP participant, and a scholar in the STEER and University Honors Program at California State University, Fullerton. She plans to continue her path in research by furthering her education in a graduate program, with a goal to teach in higher education.



### **TRINI NGUYEN**

Trini is a Mathematics graduating senior. Her academic career includes being a Maximizing Access to Research Career (MARC) Program scholar, in which, under the mentorship of Dr. Charles Lee, she is developing mathematical models to detect dry-eye diseases and has won three presentation awards for this project. Her other research experience includes a bioinformatics project at the University of California, San Diego. In Fall 2018, she will begin a Ph.D. program in the Applied Mathematics.



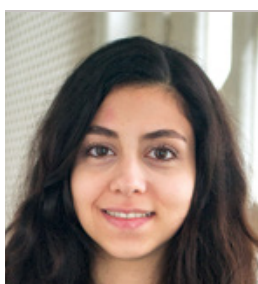
### **VICTORIA SEVERIN**

Victoria Severin is a senior Geology undergraduate at California State University, Fullerton and will be graduating this spring. Her research is in marine and coastal processes under the advisement of Dr. Joe Carlin at the Coastal and Marine Geology Lab. After graduation she plans to pursue a master's degree in Environmental Science with a focus in management of water quality and conservation in drought prone areas.



### **WASEEFA AHMED**

Waseefa Ahmed recently graduated with a Bachelor of Science Degree in Biochemistry in Fall of 2017. She worked in Dr. Michael Groves' lab studying the decomposition of ethylamine for chiral modification. She intends to further her studies in another interest of hers, computer science.



### **YASAMIN HAJY HEYDARY**

Yasamin Hajy Heydary is a third year Biology major with a concentration in cellular and developmental biology. She has been a part of Dr. Parvin Shahrestani's evolutionary genetics lab since Fall 2017. Their research team is working on the intestinal microbiota composition of *Drosophila melanogaster* as they age, and the evolutionary relationship between the gut microbiota and their host. She is a pre-med student and I am interested in pursuing a career in medicine.